The Dissertation Committee for Akhilesh Jain Certifies that this is the approved version of the following dissertation:

Simulation of UV Nanoimprint Lithography on Rigid and Flexible Substrates

Committee:

Roger T. Bonnecaze, Supervisor

S. V. Sreenivasan

Carlton Grant Willson

Venkat Ganesan

P. Randall Schunk

Simulation of UV Nanoimprint Lithography on Rigid and Flexible Substrates

by

Akhilesh Jain, B. Tech., M. Tech.

Dissertation

Presented to the Faculty of the Graduate School of
The University of Texas at Austin
in Partial Fulfillment
of the Requirements
for the Degree of

Doctor of Philosophy

The University of Texas at Austin
December 2016

To my father who gave me the roots,

to my mother who gave me the wings,

&

to Gunja who gave me the heart to do this.

Acknowledgements

The years I spent at the University of Texas at Austin have been the most transformative and enjoyable years of my life. For that, I would like to thank the people I met here. My advisor, Prof. Roger Bonnecaze guided me during my PhD with great enthusiasm and patience. I will always cherish the discussions we had during our meetings and I would like to thank him for being a great mentor. I am extremely grateful to Dr. Andrew Spann who helped in parallelization and speed-up of the simulations. Without his skills and enthusiasm, my dissertation would not have reached its full scope. I would like to thank Prof. Randy Schunk from University of New Mexico, Albuquerque and his students, Andrew Cochrane and Dr. Kristianto Tjiptowidjojo. Collaborating and brainstorming with them helped significantly in understanding and modeling the process. I would also like to thank Prof. S. V. Sreenivasan and Dr. Shrawan Singhal who gave critical input for my research based on the experiments.

I shared office space with some very inspiring and helpful group members. I would like to thank Lavanya Mohan, Benjamin Huntington, Shruti Jain, Meghali Chopra, Talha Arshad, Mark Ferraro, Stephanie Liu, Mohammadreza Shafiei, Mike Clements and Parag Katira who were always there for guidance and to share lighter moments in the office. It was a great pleasure knowing them. I was the President of the NASCENT Student Council 2014-15. Prabhakar Marepalli, Shruti Jain and Craig Milroy formed the absolute best team to work with. They showed me how delightful and productive working in a functional team can be. I would like to thank them for the exciting times we had while organizing and attending events. I believe I have forged a lifelong friendship working with them. It was also a great pleasure working with the NASCENT staff: Larry Dunn, Risa Hartman, Darlene Yanez and Janet Monaco.

I made friends with some very interesting and passionate people during my years at Austin. I would like to thank Paras Ajay, Shilpi Goel, Siddharth Jain, Garima Jain, Aniruddha Dasgupta, Pallavi Dasgupta, Shravya Donkada, Akshay Singh, Vineet Singh, Aarti Punase, Dylan Kipp, Vaidyanathan Sethuraman, Santosh Mogurampelly, Anand Surada, Spandana Remarsu, Sucheta Arora, Avni Jain, Neha Mohan, Aaron Sherraden, Abhishek Baradia and Rachit Agarwal for the amazing times together. Their friendship and generosity never ceased to amaze me. I would especially like to thank Amey Puranik who I was friends with from the first day of PhD. I would also like to thank Samuel Cohn and Lynn Wallisch for looking after my well-being and sharing their wisdom.

I cannot express enough gratitude for my wife, my friend and fellow UT ChemE, Gunja Pandav, who was always there for encouragement, support and inspiration. I cannot imagine my years at Austin without her. Lastly I would like to thank my brother Piyush, my parents Anil and Sapna Jain, my parents-in-law Rajesh and Rama Pandav and my adorable family who cheered me all the way to the end.

Simulation of UV Nanoimprint Lithography on Rigid and Flexible Substrates

Akhilesh Jain, Ph. D.

The University of Texas at Austin, 2016

Supervisor: Roger T. Bonnecaze

Nanoimprint lithography (NIL) is a low cost, high throughput process used to replicate sub-20 nm feature from a patterned template to a rigid or flexible substrate. Various configurations for NIL are analyzed and classified based on type of template and substrate. The steps involved in pattern transfer using roller template based NIL are identified and models to study these steps are proposed. Important process parameters such as maximum web speed possible, required UV intensity, minimum droplet size and pitch and required force on the roller are calculated. The advantages, disadvantages and optimal process window for the different configurations are identified.

Droplet spreading is simulated in NIL with rigid substrates in order to study the effect of droplet size, droplet placement error, gas diffusion and template pattern on throughput and defectivity. Square arrangement is found to be the optimum arrangement for achieving minimum throughput. Large droplet-free regions on the substrate edge and error in droplet placement error have significant impact on the throughput. A fluid flow model with average flow permeability is presented to account for flow in the template patterns. Optimum droplet dispensing for multi-patterned templates is achieved by distributing droplet volume according to local filling requirements.

Non-fill defects in NIL are classified into pocket, edge and channel defects. A model to predict the size of non-fill defects based on imprint time and droplet size is presented. Defect characterization is presented for various pattern-types. A model is presented to determine the time required for the encapsulated gas to diffuse into the resist.

The coupled fluid-structure interaction in NIL with flexible substrate is studied by simulating the web deformation as the droplet spreads on the substrate. It is found that the flexible substrate can be modeled as a membrane due to the lack of rigidity. RLT variation reduces as the number of droplets or the web tension increases. For the magnitude of RLT variation, thinner residual layers require higher web tension. The position of the template on the substrate is important and template positioned at the corner of the substrate is found to provide the least RLT variation.

Table of Contents

List of Tables

List of Figures

Chapter 1: Introduction

1.1. NANOIMPRINT LITHOGRAPHY

The market for flexible electronics is growing rapidly with huge demand for next generation devices such as large area flexible displays, flexible solar panels, printed RFID and e-paper [1]. The current market for the printed and flexible electronics is $26.5 billion and is expected to grow to $69 billion in 2026 [2]. Roll-to-roll (R2R) manufacturing methods are required to fabricate nano-enabled devices at high volume and low cost. Nanoimprint lithography (NIL) is a low cost, high throughput process able to replicate sub-20 nm patterns from a template on to a substrate. NIL has shown great potential for high precision patterning and is being proposed for high volume manufacturing of semiconductor device and high density bit patterned media [3, 4]. Roll-to-roll nanoimprint lithography or R2RNIL is a term used for replicating micro- or nano- patterns continuously on a flexible or rigid substrate using NIL. It has been shown that R2RNIL can be successfully merged with roll-to-roll processing to pattern flexible substrates for fabricating devices like lab-on-a-chip [5], solar cells [6], polarizers [7], and OLEDs [8].

NIL was proposed by Chou *et al.* in 1995 as a pattern replication technique for manufacturing integrated circuits in the semiconductor devices [4]. The schematic for nanoimprint lithography process proposed by Chou *et al.* is shown in Figure 1.1 [4]. A substrate is coated with a thin layer of thermoplastic polymer. A template with patterns (also called a mask or mold) is pressed into this polymer layer. The polymer is heated to a temperature above its glass transition temperature so that it may flow like a viscous fluid and the polymer conforms to the pattern on the template. After the template is pressed into the polymer, it is removed leaving the pattern of the template replicated in the polymer. The residual layer of the cooled film is removed by an anisotropic oxygen plasma etching process to complete the pattern transfer. This process of using nanoimprint at high temperature for pattern replication is often referred to as thermal NIL or hot embossing. Similar imprint techniques for pattern replication were also proposed by Whitesides [9, 10] and Philips Research [11].

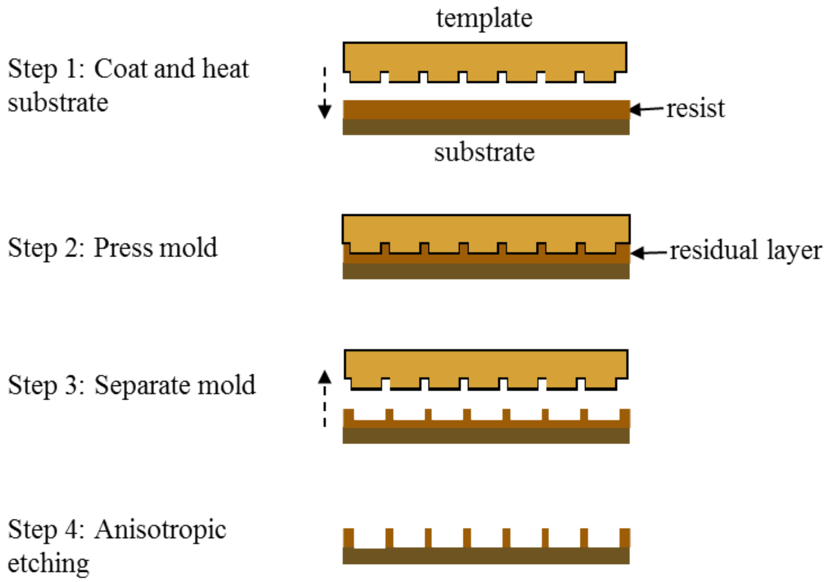

Figure 1.1: Schematic of the nanoimprint lithography process.

Soon after, Colburn *et al.* described the “step and flash imprint lithography” or SFIL (as shown in Figure 1.2) [12, 13]. In the SFIL process, droplets of a low viscosity, photo-polymerizable monomer are dispensed on a substrate with a transfer layer. The template is lowered on to the droplets and the fluid fills the gap by a combination of viscous and capillary forces. Once the desired residual layer thickness is reached, ultraviolet (UV) light is irradiated through the transparent template to photocure the monomer. The template is then lifted, leaving the patterns on the coated substrate. An oxygen reactive ion etch (RIE) etch through the polymer and the transfer layer is used to create a high aspect ratio pattern on the substrate. The drops are placed using inkjets and this imprinting process is sometimes termed “jet and flash imprint lithography” or JFIL [14, 15]. Nanoimprint processes using UV curing instead of thermal curing are broadly classified under the term “UV nanoimprint lithography” or UV NIL.

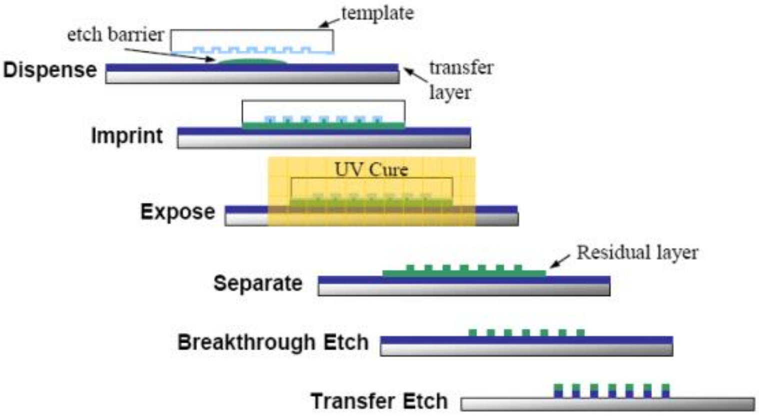

Figure 1.2: Schematic of the step and flash imprint lithography process.

1.2. ROLL-TO-ROLL NANOIMPRINT LITHOGRAPHY

R2RNIL provides an opportunity to merge the existing roll-to-roll process with nanoimprint lithography and fabricate highly functional devices such as wire-grid polarizers [7, 16], plasmonic devices [17], multi-functional optical films [18-21], photovoltaic cells [6, 22] in high volume. R2RNIL was first demonstrated more than a decade ago by Tan *et al*. who replicated sub-100 nm patterns on PMMA resist using thermal curing [23]. A schematic of one embodiment of a R2RNIL system with a roller template is illustrated in Figure 1.3. It includes a roller with patterned template, a flexible or rigid substrate, an imprint dispenser unit and a thermal or UV curing module. The flexible substrate is sometimes also referred to as the web. For thermal curing, the imprint material used is a thermoplastic polymer like PMMA [23-25] and for UV curing, there are UV-curable resins like acrylics [21, 26] and epoxysilicones [7, 27], for example. A pretreated substrate is coated with a layer of imprint material by roller coating [27-29], inkjetting [30] or knife coating [18] process. The imprint material moves along with the substrate and comes in contact with the roller template. As the fluid fills the features on the template, it is cured by a thermal or UV-source, thus replicating the patterns on the template on the roller. After the pattern is transferred, the cured resist is peeled from the roller.

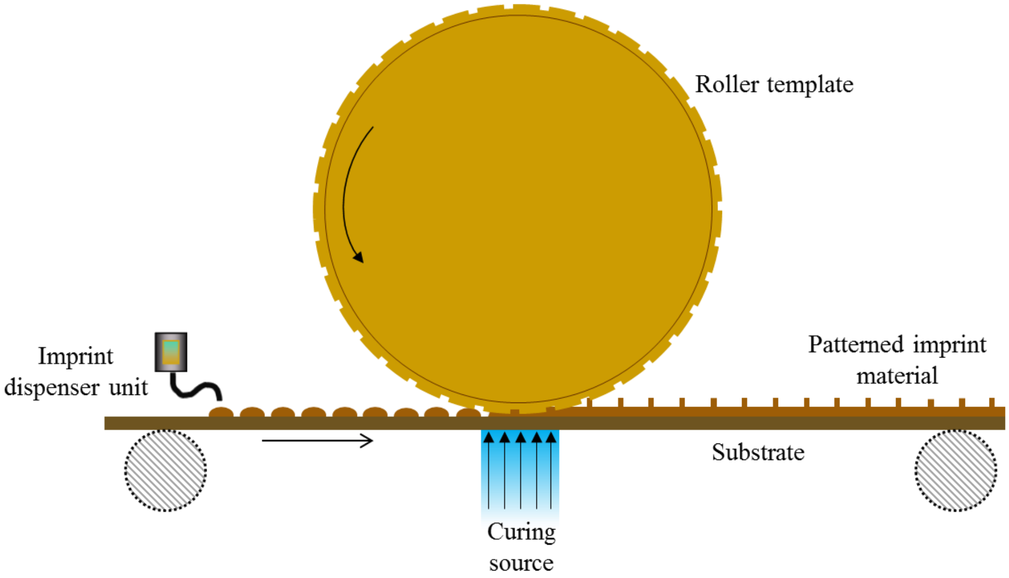

Figure 1.3: Schematic of roll-to-roll nanoimprint lithography with a patterned roller template, an inkjet dispenser, a substrate and a UV/thermal curing source. A curable imprint material is ink-jetted as droplets on the substrate which forms a patterned resist layer after curing.

Various systems using thermal or UV curing have been developed to realize R2RNIL. Tan *et al.* introduced two simple methods for R2RNIL with thermal curing [23]. In the first method, a nickel mold with 700 nm wide, 60 nm deep line patterns was wrapped around a cylinder mold as shown in Figure 1.4(a). The mold was rolled on a 220 nm thick polymethylmethacralate (PMMA) layer coated on a flat silicon wafer for pattern transfer. In the second method, a silicon wafer mold with patterns of 190 nm period and 180 nm height is placed directly on the substrate as shown in Figure 1.4(b). A roller is pressed and rolled over the mold and the patterns on the mold transfer to the PMMA resist. In both the methods, the roller template is heated above the glass transition temperature (170-200 °C) while the temperature of the platform is set below the glass transition temperature (about 50 °C). The resist in contact with the heated roller flows and conforms to the patterns on the template. The roller speed was varied between 0.5-1.5 cm/min and the estimated pressure was between 2-32 MPa. Inspection using optical microscope and AFM showed that the best results were reported at roller temperature of

170-200°C and platform temperature of around 50°C for the cylinder mold method and 70°C for the flat mold method.

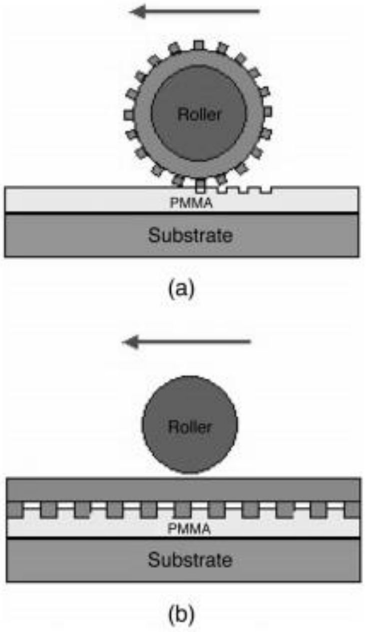

Figure 1.4: Schematic of two methods for thermal R2RNIL proposed by Tan *et al.*[23]: (a) cylinder mold method; (b) flat mold method.

Ahn *et al.* was the first to propose R2RNIL with UV curing since thermal curing required high pressure and temperature [20, 26]. The set up included an imprint dispensing unit, a pair of flattening roller to maintain a uniform coat of polymer, a UV source, a roller template and a rigid or flexible substrate as shown in Figure 1.5. A passive gap control system is used to control the thickness of the final pattern and maintain an applied pressure of 90.6 N. They presented two realizations of UV R2RNIL: one with a rigid substrate which made line contact with the roller template and another with a flexible substrate which partially wrapped around the roller to provide better contact. They patterned lines with a width of 500 nm, a pitch of 1 μm and a height of 900 nm on an 80 mm wide area at a speed of 78 cm/min.

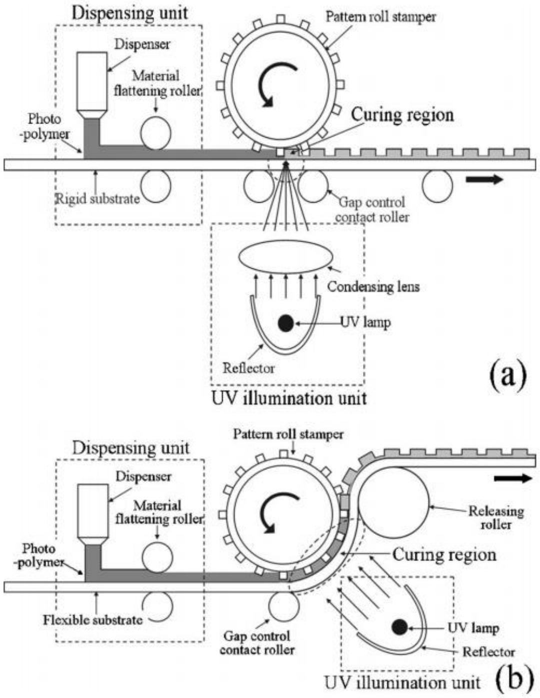

Figure 1.5: Schematic of UV R2RNIL system (a) for a rigid substrate and (b) for a flexible substrate as proposed by Ahn *et al*.[26].

Guo *et al.* presented two UV R2RNIL systems (shown in Figure 1.6) consisting of a roller coating system and a template wrapped around two rollers like a tensioned conveyor belt. This setup can be used to pattern rigid or flexible substrates. They patterned 300 nm linewidth and 600 nm pitch features on a flexible PET substrate with width 4 inches and length 12 inches [28]. They also demonstrated patterning 70 nm linewidth epoxysilicone grating on 1 cm wide substrate at a web speed of about 1 m/min using this setup [27].

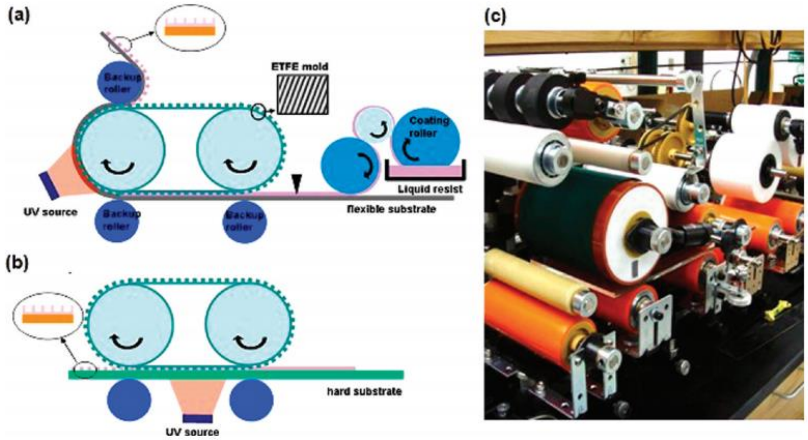

Figure 1.6: Schematic of UV R2RNIL systems proposed by Ahn *et al.* [28] for a (a) flexible or (b) rigid substrate. (c) Photograph of the R2RNIL apparatus.

A stepper template can also be used for R2RNIL. The schematic for such a system is shown in Figure 1.7. The system includes a flat template, a flexible substrate, an imprint dispenser unit, and a thermal or UV curing module. The imprint dispenser introduces imprint material on the substrate by roll coating, ink-jetting or knife coating. The template presses onto the imprint material causing it to fill the features on the template. When the desired residual layer thickness is reached, the imprint material is cured using heat or UV light. The template is peeled off from the resist leaving the patterns on the substrate. The substrate rolls forward and these steps are repeated. The process is semi-continuous because of the starting and stopping of the rollers.

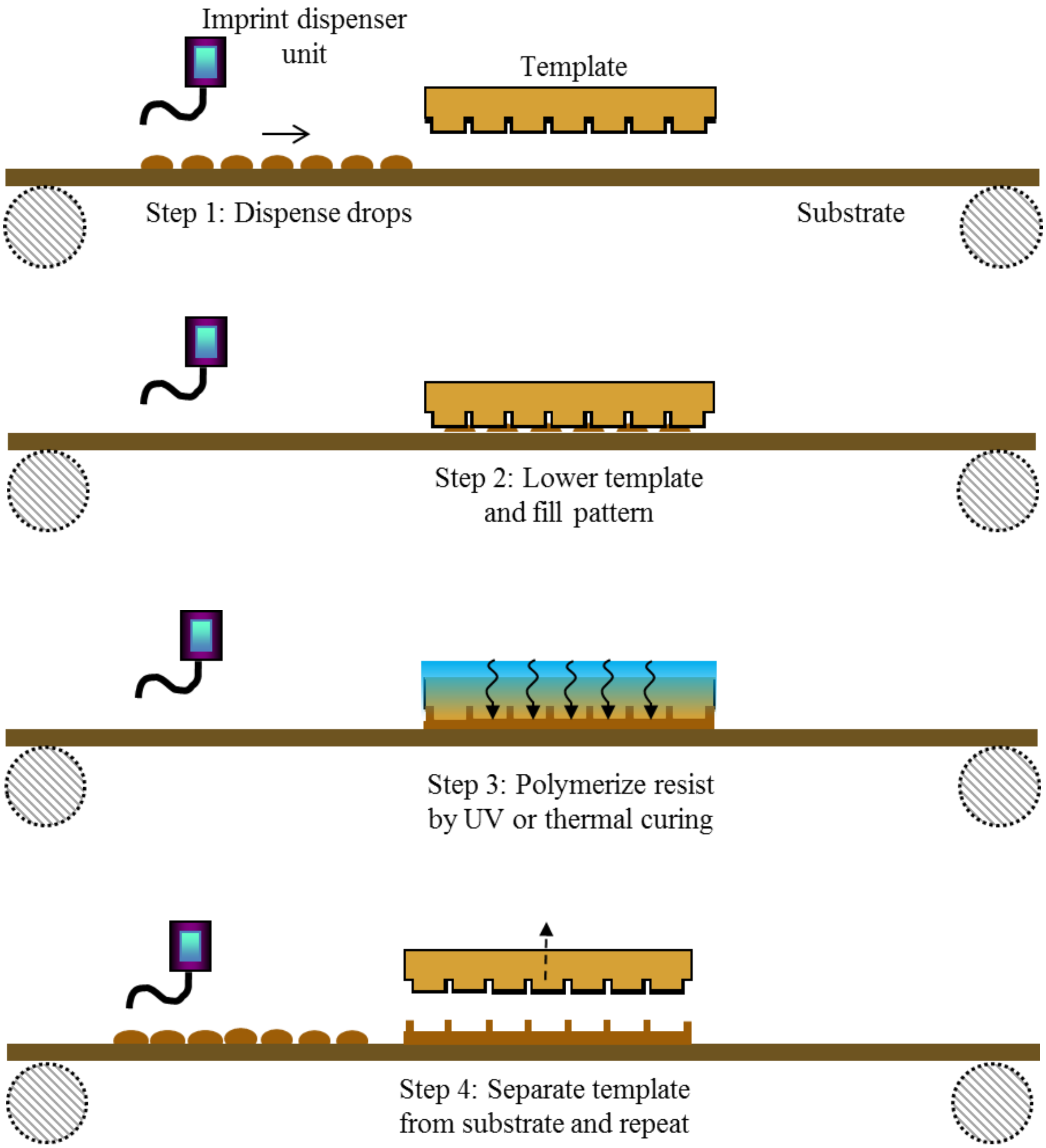

Figure 1.7: Schematic showing steps involved in roll-to-roll nanoimprint lithography on a flexible substrate with a stepper template.

Table 1.1: Recent achievements in UV and thermal R2RNIL

Citation	R2RNIL system type	Critical dimension	RLT	Web width	Web speed	Throughput	Pattern accuracy
Thesen *et al*. [31, 32]	UV R2RNIL with roller template	Line gratings 500 nm width, 200 nm height	N.R.	300 mm	30 m/min	9 m^2/min	94%
Wu *et al*. [33]	UV R2RNIL with roller template	Line gratings 50 nm width, 180 nm height	66 nm	50 mm	1 m/min	0.05 m^2/min	95%
Inanami *et al*. [34]	UV R2RNIL with roller template	Line gratings 24 nm width, 58 nm height	13 μm	70 mm	1 m/min	0.07 m^2/min	N.R.
Ahn *et al*. [35]	UV R2RNIL with stepper template	Line gratings 50 nm width	N.R.	300 mm	>1 m/min	0.3 m^2/min	N.R.
Ahn *et al*. [16]	UV R2RNIL with stepper template	Line gratings 50 nm width	12 nm	80 mm	N.R.	625 mm^2/min	N.R.
Makela *et al*. [36]	Thermal R2RNIL with roller template	Line gratings 400 nm width, 230 nm height	N.R.	50 mm	20 m/min	1 m^2/min	50%
Sohn *et al*.[37]	Thermal R2RNIL with roller template	Line gratings 5 μm width	N.R.	150 mm	1.8 m/min	0.27 m^2/min	N.R.

N.R.: Not reported

1.3 CHALLENGES FOR ROLL-TO-ROLL NANOIMPRINT LITHOGRAPHY

R2RNIL has a considerable advantage over batch nanoimprint lithography. Some of the recent achievements in terms of critical dimensions, minimum RLT, web speed and patterned area using UV and thermal R2RNIL are listed in Table 1.1. However, there are several challenges in improving throughput, residual layer thickness and defectivity that need to be addressed before the process can be successfully implemented in the industry. The challenges involved in improving these metrics are discussed in this section.

1.3.1. Throughput

One of the most appealing features of the R2RNIL is the ability to process rolls of patterned substrate continuously. R2RNIL offers high throughput by imprinting large area substrates at high speed. The speed of continuous imprinting is given by [24]

$$web\ speed = \frac{L_{contact}}{t_{contact}}, \tag{1.1}$$

where $L_{contact}$ is the length of contact between the roller and substrate and $t_{contact}$ is the time for which roller and the substrate are in contact. In thermal R2RNIL, $t_{contact}$ is dictated by the filling time t_{fill} required for the imprint material to spread to the features on the template. Insufficient filling time can cause no-fill defects in the pattern. The filling time is dependent on the viscosity and thickness of the imprint material, the size of the cavity on the template and pressure applied [24, 38]. For thermal R2RNIL, filling time is given by [24]

$$t_{fill} = \frac{6\mu H^2}{PW^2} \tag{1.2}$$

where μ is viscosity of the imprint material, H is the feature height, W is feature width, and P is the pressure applied at the entrance of the feature. This model assumes that feature dimensions H and W are much smaller than the roller radius and contact length between the roller and the substrate. It also assumes that the pressure distribution is uniform along the contact length and the fluid flow is purely viscous. Near the glass transition temperature the typical value of viscosity μ is of the order of 1-10 MPa.s. The high viscosity of thermoplastic fluids leads to long filling times. While increasing temperature to reduce the viscosity also reduces the filling time, the speed is limited by the temperature at which plastic deformation occurs on the flexible substrate [23]. Currently, the typical web speed achieved with thermal R2RNIL is 0.05-1 m/min which may not be suitable for many high volume manufacturing requirements [24, 38, 39].

In UV R2RNIL, filling time depends on the time required for the resist to spread on the substrate. Ahn *et al.* presented a simple model to calculate spreading time for UV R2RNIL with roller template as the resist is squeezed under the roller [28]. The spreading time model is given by

$$t_{fill} = \frac{\mu a^3 L}{2F}\left(\frac{1}{H_f^2} - \frac{1}{H_o^2}\right) \tag{1.3}$$

where, μ is viscosity of the imprint material, a is the roller contact width, L is the substrate width, F is the applied force, H_o is the initial resist film thickness and H_f is the final residual layer thickness. Typically, the viscosity of UV curable resins ranges from 10-500 mPa.s. For a resist viscosity of 10 mPa.s, contact width of 1 mm, substrate width of 10 cm, initial resist thickness of 1μm, final residual layer thickness of 10 nm and an applied force of 100 N, the typical spreading time is calculated using Equation 1.3 to be about 0.5 s. The typical curing time is of the order of 1-10 seconds for typical UV dosage requirements and UV intensity [40]. Thus for UV R2RNIL with roller template, $t_{contact}$ is dependent on curing time and not the filling time. Insufficient curing time can cause the replicated patterns to deform after pattern release [41]. Thesen *et al*. have demonstrated the highest throughput from UV R2RNIL process with a roller template. They fabricated wire-grid polarizers using newly developed inkjetable and photo-curable NIL resists and a UV R2RNIL apparatus with roller template manufactured by Joanneum Research Material, Austria [31, 32]. They imprinted line gratings of width 500 -750 nm and aspect ratio 0.33 - 0.5 on a resist mr-UVCur27SF XP at a web speed of up to 30 m/min. The imprinted area was 250 mm wide. The pattern accuracy was 94% and 98% at a web speed of 30 m/min and 20 m/min. The process needs to be optimized for web speed and applied UV dosage to achieve pattern fidelity at high throughput.

For SFIL with rigid substrates, the exposure time and template/resist separation steps are well understood and typical time for these steps is 0.1 to 0.2 seconds for a template of size 6 inches x 6 inches [42]. For drop volumes of 1.5 to 0.9 picoliters, the filling time on rigid substrate ranges from 1.5 seconds to 2.5 seconds [42]. Thus, for SFIL on rigid substrates, the filling step is the key limiting step [43]. Therefore, $t_{contact}$ is dependent on filling time. Similar curing and filling time can be expected when R2RNIL with a stepper template is used. Ahn *et al.* have reported the highest throughput for this process by using LithoFlex 350. LithoFlex 350 is an inkjet based nanopatterning tool which can imprint 300 mm area on flexible substrates using a stepper template. Ahn *et al.* created 300 mm wide flexible wire-grid polarizers (extinction ratio 50,000:1, average transmission 44%) using this tool by patterning 50 nm line gratings on polycarbonate web at web speed greater than 1 m/min (Figure 1.8) [35].

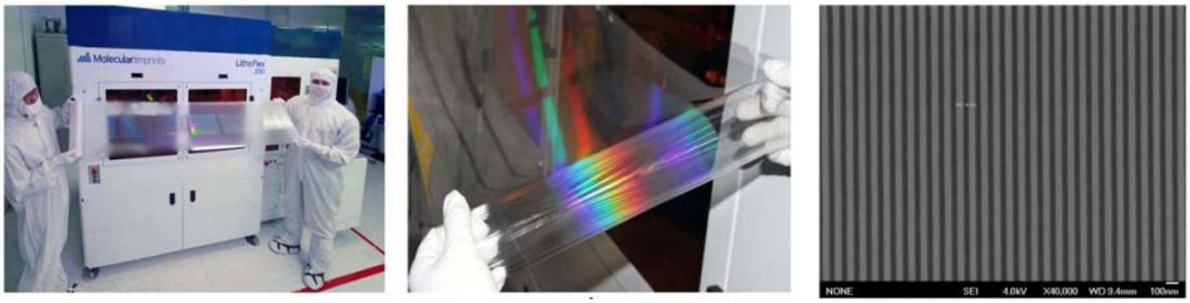

(a) **(b)** **(c)**

Figure 1.8: (a) Multiple fields of 300 mm width on a 350 mm polycarbonate film patterned using LithoFlex 350. (b) Close up of the imprinted pattern. (c) 50 nm half pitch line grating for application in wire grid polarizers. (adapted from Ahn *et al.*[35])

A technology roadmap projects industrial manufacturing of flexible displays of area 3000 cm^2 by 2019 to meet market demand [44]. The throughput of the R2RNIL needs to be improved by imprinting larger area and increasing web speed while maintaining pattern quality. For thermal R2RNIL with roller template and UV R2RNIL with stepper template, the throughput is limited by fluid filling and spreading step. For UV R2RNIL with roller template, the throughput is limited by UV curing step. Understanding these steps in the light of the fluid flow, structural mechanics and operating parameters like pressure, temperature, UV intensity etc. is the key to improving the throughput.

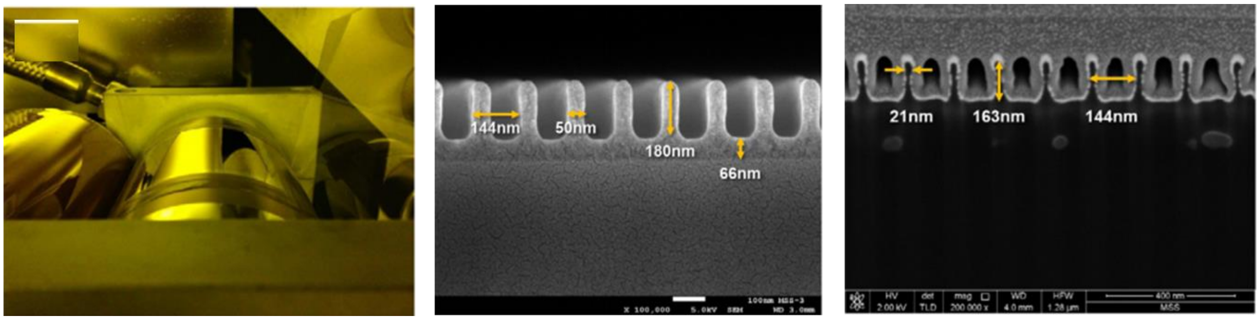

(a) (b) (c)

Figure 1.9: (a) Photograph of the nickel stamp mounted onto the imprint roller (b) SEM image of imprinted resist gratings on a glass substrate with a linewidth of 50 nm and a height of 180 nm. (c) R2R imprinted resist gratings on a PET substrate with a linewidth of 21 nm after plasma trimming. (Adapted from Wu *et al.* [33])

1.3.2. Residual Layer Thickness and Uniformity

The residual layer thickness (RLT) is a layer of resist left behind after the imprinting process. This layer is etched after the imprinting step which affects the critical dimensions of the features. Non-uniform residual layer thickness also leads to pattern transfer difficulties when using etch processes [35, 45]. Thus, achieving thin and uniform RLTs is an important technical challenge. Wu *et al.* described a process to achieve a RLT of 66 nm (before plasma trimming) which is the smallest RLT reported using R2RNIL with a roller template [Figure 1.9(b)]. They patterned sub-30-nm wide line gratings with high aspect ratio up to 16:1 using R2RNIL followed by plasma trimming to fabricate high optical performance (extinction ratio 12000:1, average transmission 82%) flexible wire-grid polarizers [33]. A nickel stamp (line width 50 nm, depth 180 nm) mounted on an imprint roller (8 cm diameter) was used as the template. PAK-02 (Toyo Gosei Co., Ltd) was used as the imprint resist on PET substrate of size 5 cm x 5 cm (A4300 125 μm, Toyobo Co., Ltd) [Figure 1.9(a,b)]. The process conditions of R2RNIL were 1 m/min web speed, 50 N imprinting force, and 25 °C isothermal imprinting temperature. After plasma trimming, sub-30 nm wide line gratings and a RLT of 26-48 nm was achieved [Figure 1.9(c)].

Ahn *et al.* used LithoFlex 100 to fabricate bilayer wire grid polarizers (extinction ratio 4500:1, average transmission 80%) by patterning 50 nm half pitch line gratings with aspect ratio 3:1 on a flexible substrate of 25 mm x 25 mm area. The tool uses a 25 mm x 25 mm stepper template to pattern flexible substrates up to 80 mm wide. They achieved a RLT of 12 nm which is the smallest RLT achieved with stepper R2RNIL. The throughput of the system was about 180 imprints/hour [16]. Achieving small RLT and maintaining RLT uniformity is huge challenge especially when imprinting on flexible substrates which deform easily under pressure. Guo *et al.* conducted experiments to show that for UV R2RNIL with roller template, the RLT decreases with increasing force. They also provided a theoretical model to support this relation using a dynamic elastic-roller contact model [28]. Various factors can influence residual layer thickness and uniformity like web tension, fluid dispensing scheme, position of the template on the substrate, applied pressure etc. Fluid spreading on flexible substrate needs to be studied to understand the RLT variation during the R2RNIL process.

For thermal R2RNIL, the force required to achieve thin RLT are higher because of the high viscosity of the imprint material. The high pressure can damage the template posing a huge disadvantage when using thermal R2RNIL.

1.3.3. Defect Rate

Defects during pattern transfer strongly impact the device performance and it is important to reduce or eliminate them altogether. In R2RNIL, common sources of defects are (i) non-filling of features and (ii) inadequate UV or thermal curing. Non-filling defects can occur when air gets trapped in the imprint material creating bubbles or if the imprint material does not have enough time to spread and fill the gap between the substrate and the resist. For R2RNIL, more defects due to bubble trapping occur at higher web speeds and for high viscosity resist [46]. This happens because it is difficult for the air in the resist to escape if the resist moves rapidly or if the resist has high viscosity. Figure 1.10 shows the defects due to bubble trapping that occurred during replicating micro-pyramids from a Ni roller onto a PET substrate using UV R2RNIL [46]. A process window with optimum web speed and temperature can reduce bubble trapping while maintaining throughput. In UV R2RNIL with stepper template, the air dissolves quickly in the imprint material and bubble trapping is not the main cause of no-fill defects [47]. In this process, non-filling occurs due to long filling times required to spread to the features and gap between the template and the substrate [42]. Dispensing resist material with very small size and optimizing the drop pattern has shown to reduce defect rate while maintaining high throughput [42]. Allowing the resist to spread for longer will also reduce the no-fill defects but that lowers the process throughput creating a challenge for R2RNIL.

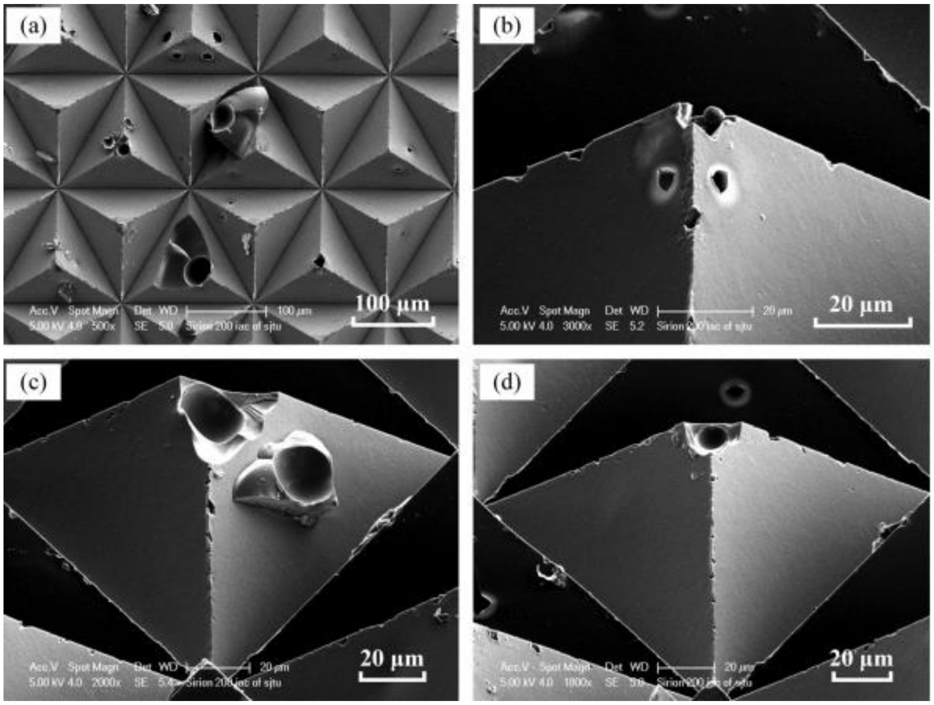

Figure 1.10: SEM images of pyramid arrays with bubble defects: (a) vertical view of multiple structures with various bubble defects; side view of single pyramid structure (b) with bubble on top, (c) with bubble just exposed and (d) with bubble fully exposed. (adapted from Wu *et al.* [46])

The other factor influencing defect rate is UV or thermal curing. In thermal R2RNIL, the embossing is carried out at a temperature higher than the glass transition temperature of the imprint material [23]. Thus, the operating temperature can be as high as 100 - 300 °C [38]. If the imprint material is not cooled below the glass temperature rapidly, the lack of applied pressure and the absence of mold subjects the pattern to distortions during the releasing. There may also be undesired viscoelastic recovery after pattern releasing. The high temperature makes it difficult to cool the thermoplastic film rapidly before demolding. Effective active cooling and heating strategies are required to avoid pattern distortion in thermal R2RNIL [24].

In UV R2RNIL with a roller template, the UV curable resin is exposed to UV light for a short time while it is pressed by the template. Adequate UV curing is extremely critical as incomplete UV curing will cause the replicated pattern to deform after the pattern release while over-exposure will make the pattern brittle causing potential damage to both the template and replicated pattern during pattern release [48]. UV dosage depends on the web speed and UV intensity thus the required UV dosage puts a limit on the maximum web speed available for a R2RNIL system. Taniguchi *et al.* conducted experiments to show the effect of UV dosage on pattern quality. They carried out UV R2RNIL with different UV doses by varying the web speed and UV intensity and found that there exists a critical UV dosage below which the patterns collapse. PAK-01 was used as the UV-curable resin and UV light emitting diode (ZUV-C20H, Omron Co., wavelength 365 nm) was used as the UV light source. Figure 1.11 (a) shows the UV R2RNIL system used by Taniguchi *et al.* Figure 1.11 (b) and (c) show a 10 mm x 10 mm area with line and space patterns (100 nm width, 200 nm depth) on a polyester film at two different UV dosages. At web speed of 9 m/min and UV intensity of 52.4 mW/cm^2, the resin was exposed to UV dosage of 5.59 mJ/cm^2 which was lower than the required UV dosage resulting in pattern collapse due to insufficient UV dosage. At web speed of 6 m/min and UV intensity of 524 mW/cm^2, the resin was exposed to a higher dose of 83.8 mJ/cm^2 which results in pattern transfer without failure. By conducting the experiment at various web speeds and UV intensity, they have shown that UV dosage is an important factor for successful pattern transfer. UV curing needs to be studied further in the context of required UV dosage for the imprint material, desired throughput and the intensity of the UV source to attain quality pattern replication. UV R2RNIL overcomes these challenges by utilizing low viscosity resin, enabling low pressure processing (about ~100 kPa) at room temperature. The low viscosity of the imprint results in spreading and filling times which are orders of magnitude shorter than thermal R2RNIL. Unlike thermoplastic fluids, UV curable resins do not have a glass transition temperature thus the patterns do not suffer from viscoelastic recovery at elevated temperature. The process is carried out at low pressure and room temperature which helps avoid undesired stresses in the template, thus improving template lifetime and overall pattern quality. Thus, UV R2RNIL presents many advantages over thermal R2RNIL and is comparatively more suitable for high throughput patterning. For UV R2RNIL with roller template, the throughput is limited by the curing time while for UV R2RNIL with a stepper template it is limited by the spreading time. Other than throughput, improvement in RLT uniformity and low defectivity are the main challenges for UV R2RNIL. Many realizations of UV R2RNIL have been demonstrated to overcome these challenges. The cost and complexity of R2RNIL setup make it difficult to acquire and study these systems. Process modeling and simulation of R2RNIL has been proposed as an effective and inexpensive approach. Recent efforts in modeling and simulating the R2RNIL are discussed in the next section.

These issues with throughput, residual layer thickness and defectivity need to be addressed before R2RNIL can be successfully implemented in the industry for high volume manufacturing. The development of thermal R2RNIL is hindered by the extreme operating conditions for temperature and pressure requirements. High temperature (typically from 100^{o}C to 300^{o}C) and high pressure (of atleast 5 MPa) are required to lower the viscosity of the thermoplastic fluid for pattern replication [38]. Increasing the temperature and pressure helps fluid to spread faster leading to higher throughput; however, the throughput is limited by the temperature at which plastic deformation occurs on the flexible substrate. The pattern needs to be cooled before demolding to avoid deformation due to viscoelastic recovery. High pressure and temperature gradient generate stresses in the template that can damage the template and reduce template longevity. The high viscosity of the thermoplastic fluid and the high temperature and pressure requirements make thermal R2RNIL inherently unsuitable for high throughput manufacturing.

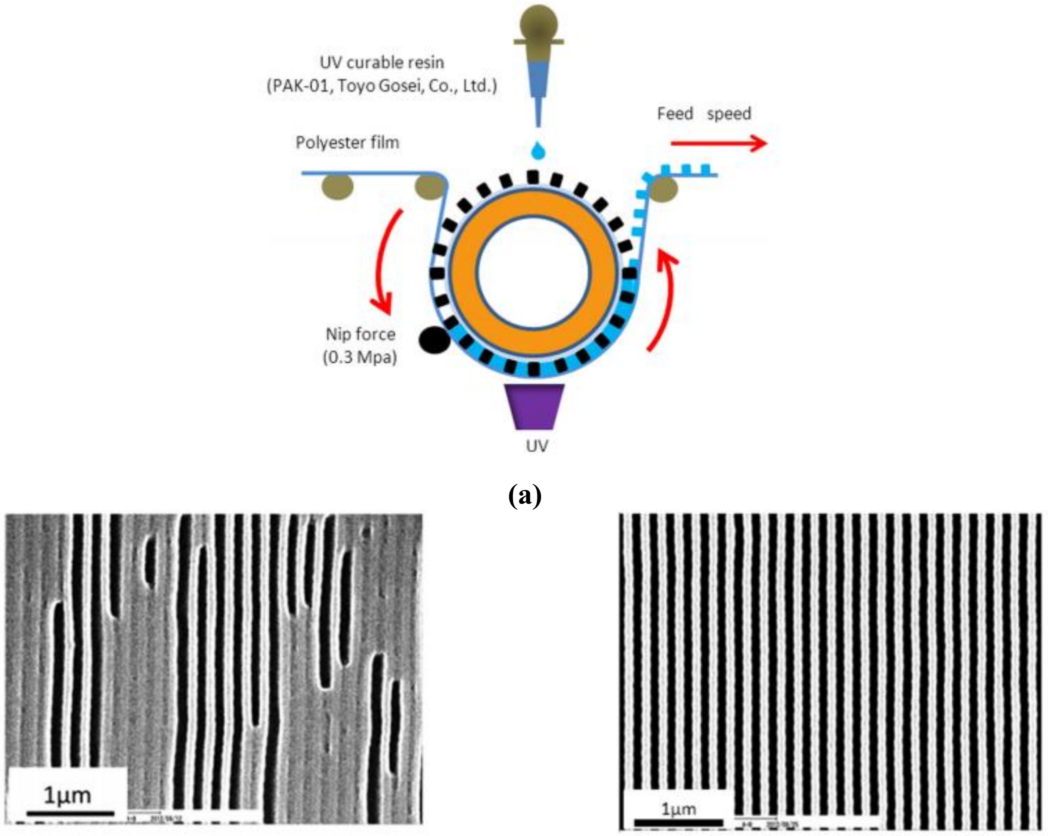

(a)

(b) **(c)**

Figure 1.11: (a) UV R2RNIL setup used by Taniguchi *et al*. [41]. SEM photos of the top view of patterns transferred via RTR UV-NIL under conditions of (b) 9 m/min web speed, 52.4 mW/cm^2 UV intensity and 5.59 mJ/cm^2 UV dose and (c) 6 m/min web speed, 524 mW/cm^2 UV intensity and 83.8 mJ/cm^2 UV dose. In Figure (b), the pattern collapse due to insufficient UV dosage at high web speed. In Figure (c), the pattern transfer is successful due to sufficient UV dose at reduced web speed.

1.5 MODELING AND SIMULATION IN NANOIMPRINT LITHOGRAPHY

Several different realizations of R2RNIL process have been designed; however, there is a lack of standardized infrastructure to understand and test these systems. The elaborate R2R systems are expensive and difficult to set up. Designing and conducting experiments is expensive because of the complexity of the R2RNIL process and the large number of parameters involved. Metrology and inspection incorporating in-line optical techniques are being developed, but significant challenges remain for real-time monitoring of high throughput processes having nanoscale features. This has led to very slow process development. The potential and the limitations of R2R imprinting have not been explored thoroughly, especially in the context of defect rate, throughput and resist layer uniformity. A lack of validated, multi-scale simulation and design models has been identified as one of the main barriers to realize high volume R2R nano-manufacturing [49]. Modeling and simulation tools can be very helpful in understanding the fundamentals of the different steps involved in the R2RNIL process. Computational tools have been very successful in the past for studying NIL and some of them are presented here.

Many efforts have been made previously to model the fluid flow during imprint spreading and feature filling to improve process throughput and reducing defectivity. Colburn *et al.* studied the spreading of droplets between a template and a substrate for UV imprint lithography [50]. They evaluated several template control schemes theoretically and experimentally. Lubrication theory approximations were proposed to describe the fluid behavior as the template is actuated with a fixed velocity, fixed pressure or constant applied force. They found that when imprinting with a constant volume and fixed force, the force required reduces as the number of drops increases. Reddy *et al.* presented a dynamic, multi-drop simulation based on lubrication theory proposed by Colburn *et al*. The volume of fluid method is used to handle the merging of droplets and interfaces in the simulation. They modeled the flow and coalescence of multiple fluid drops for the case of zero and non-zero applied force. The simulation of 5 drops spreading on the substrate with net zero force acting on the template is shown in Figure 1.12. They found that the imprint time decreases with increasing number of drops or with an applied force on the template [51].

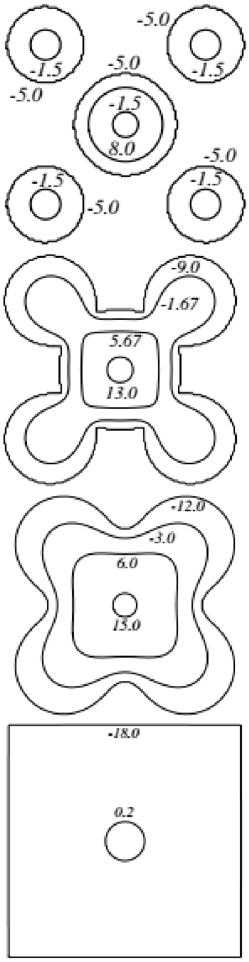

Figure 1.12: (a) Pressure contours for merging of five drops at different times *t* = 0, *t* = 0.02, *t* = 0.06, *t* = 1.05. No external force is being applied on the template. The template moves to balance the capillary force generated by the droplet interface. The coalesced drops behave as a single drop with high interior pressure immediately after the drops merge. The lowest contour at each time step corresponds to the fluid-air interface. (adapted from Reddy *et al.*[51])

Sirotkin *et al*. have presented a coarse-grain method for simultaneous calculation of the resist viscous flow in nanoimprint lithography and the deformation of stamp and substrate [52-56]. They simulated the residual layer thickness and pressure distribution for two templates with a complex layout where structure size and distribution vary locally over the surface of the template. Figure 1.13 shows the distribution of the elastic deformation of stamp/substrate for "MEMS" structure with resist mr-1 8000 at 180°C. For the calculation of the stamp/substrate deformation, elastic properties of stamp and substrate used are: modulus of elasticity 10^{11} Pa and

Poisson's ratio 0.2. The resist dynamic viscosity is taken to be of the order of 10^4 Pa.s. The initial resist thickness and cavity depth is 318 nm and 315 nm respectively. They compared the simulated and experimental results and were able to predict the residual layer thickness variation with 10% precision [54].

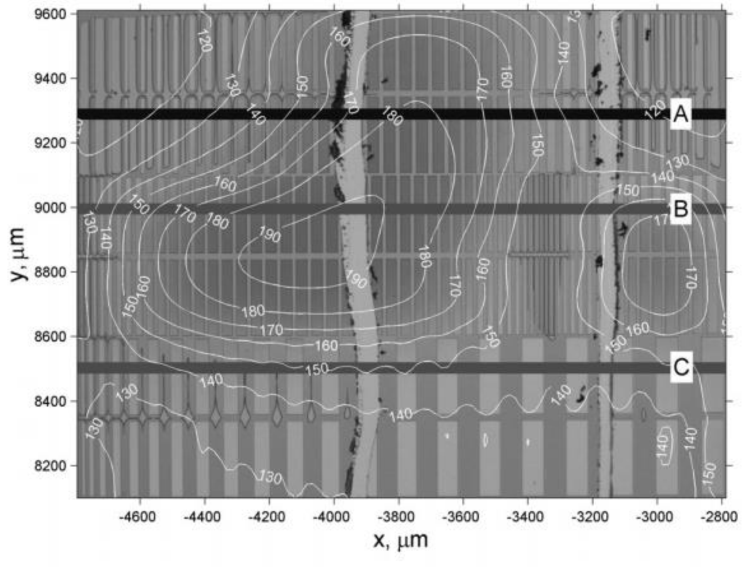

Figure 1.13: The calculated distribution of the stamp/substrate deformation is shown in white isolines numbered by values of the elastic displacement in nanometers. The optical microscopy image of the imprinted test structure is shown in the background. (adapted from Sirotkin *et al*.[54])

Reddy *et al*. proposed a mechanism for interface advancement at low capillary number through sharp rectangular features [57]. A two-dimensional simulation is presented to model the fluid as it flows through channel between the template and substrate and the fluid–air interface encounters a rectangular feature with some height greater than the channel gap. Capillary number *Ca* is the ratio between the viscous and surface tension forces. Figure 1.14 shows a time trace of the fluid-air interface as it moves through a feature under low Capillary number condition with $Ca = 10^{-3}$.They were able to predict incomplete feature filling for a given channel height, feature height and feature width.

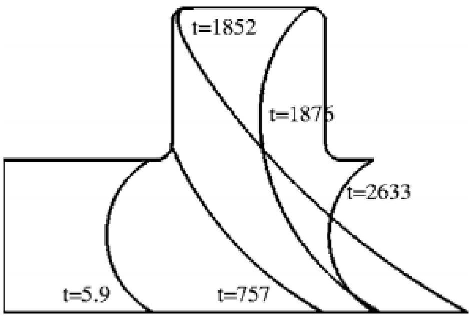

Figure 1.14: Time trace of the interface motion through a feature at *Ca*=10^{-3}. Times are denoted for each interfacial position shown. (adapted from Reddy *et al.*[57])

Chauhan *et al*. dealt with the issue of pinning which can also lead to non-filling of the features [58]. Pinning occurs when the pressure at the air-liquid interface reaches the pressure of the bulk liquid as shown in Figure 1.15 (i). At this condition, there is no pressure gradient or driving force to move the liquid and fill the feature. They analyzed the effect of several parameters for pinning on a trench feature: residual layer thickness, wettability of the feature edge, applied force on the template, and radius of curvature of the feature edge. The analysis demonstrates that larger width features require thicker residual layers to fill without pinning. It is shown that pinning should be more favorable at the mesa edge than the feature edge for better feature filling.

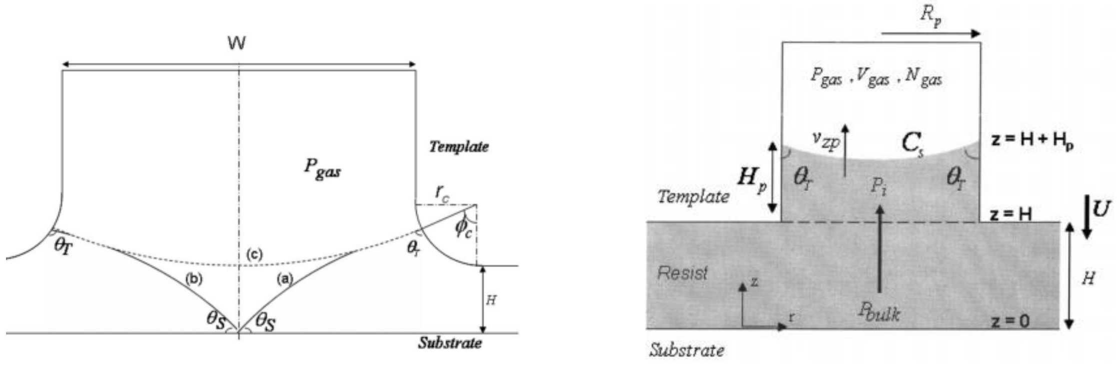

(i) **(ii)**

Figure 1.15: (i) Schematic of pinning at both the edges of a trench. The lower contact lines of two interfaces (a) and (b) can meet to form an upward facing concave meniscus (c). (adapted from Chauhan *et al.*[58]) (ii) Schematic of gas entrapment in a pore of radius R_p with liquid level H_p. P_{gas}, V_{gas}, and C_s represent the pressure, volume, and the surface concentration of an entrapped gas, respectively. V_{zp} represents the velocity of the liquid interface (filling rate) inside the pore. (adapted from Chauhan *et al.*[47])

Chauhan *et al*. alsoanalyzed the feature filling phenomenon for step and flash imprint lithography (SFIL) via diffusion of gas entrapped in the features [as shown in Figure 1.15 (ii)] [47]. Several factors including the gas concentration profile across the liquid resist drop, the filling progression, and the total filling time for different pattern configurations are investigated to quantify feature filling. Their simulation predicts a rapid pressure controlled filling of features initially followed by a slower diffusion controlled process. They also found that the absolute time for diffusion of a gas, entrapped in features is very short and gas diffusion will not cause non-filling of features during the SFIL.

Rowland *et al.* have presented simulations of viscous polymer deformation during NIL embossing with a non-uniform embossing template [59-61]. They modeled the polymer as a viscous Newtonian liquid and used the finite element code GOMA to model the moving boundary polymer surface in NIL. The schematic of a cavity during NIL embossing with the boundary conditions used by Rowland *et al*. is shown in Figure 1.16. The cavity has an indenter width S, cavity height h_c and cavity width W. They examined the location and size of polymer deformation peaks and cavity filling time by variation of template geometry and polymer thickness. They found that as cavity width increases, the deformation mode changes from single peak to dual peak deformation, as shown in Figure 1.16(b). The polymer deformation also transitions from single to dual peak as the initial polymer film thickness decreases, as shown in Figure 1.16(c) [61]. For the largest cavity widths and thinnest polymer layers, the two peaks are highly localized near the vertical cavity walls and do not interact. They also found that for an embossing template with non-uniform cavities, the smaller cavity sizes will fill before the larger cavity sizes [60]. These simulations enable design of imprint templates capable of distributing pressure evenly across the mold surface and facilitating symmetric polymer flow over large areas to prevent mold deformation and non-uniform residual layer thickness.

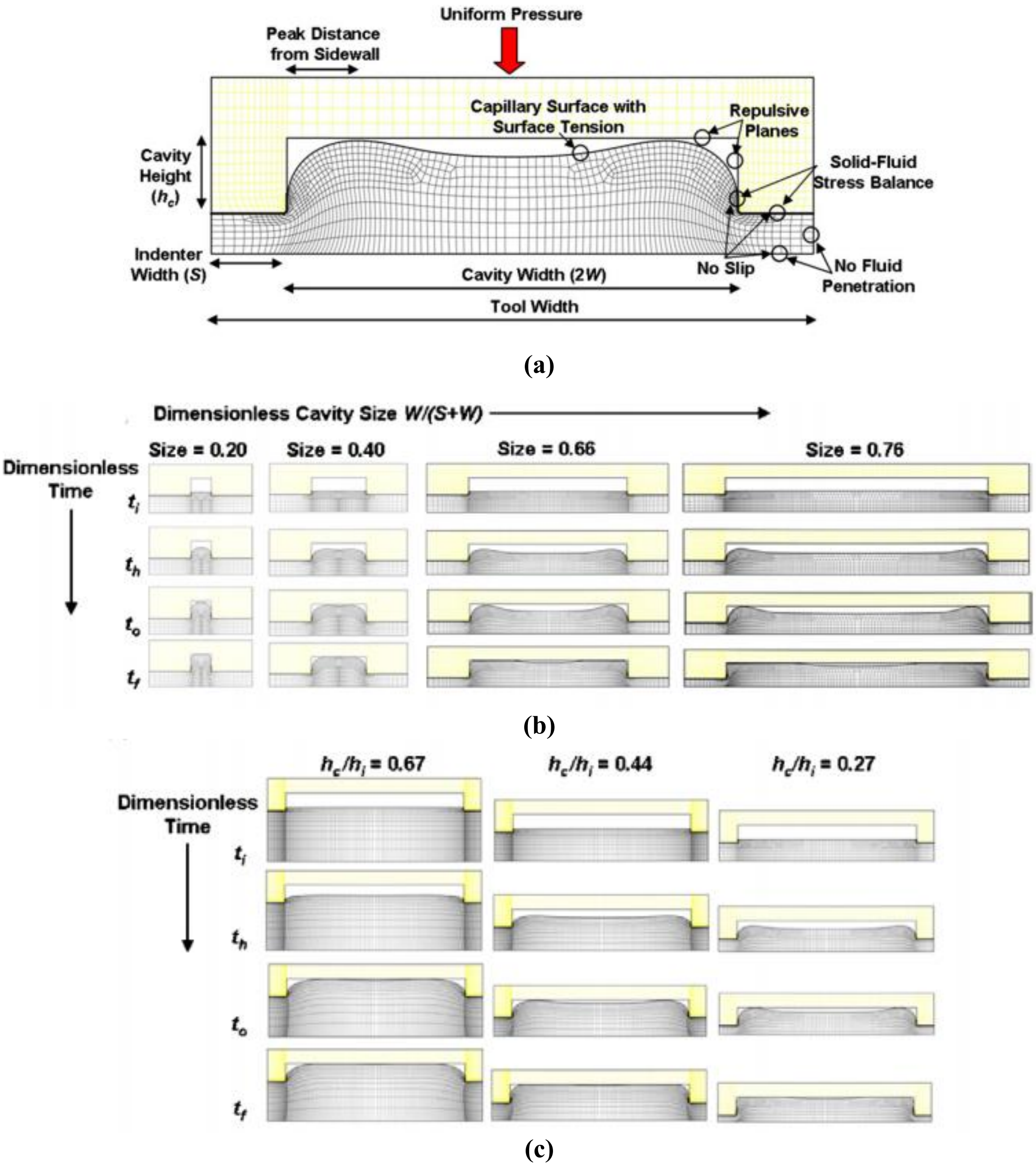

Figure 1.16: (a) Nanoimprint lithography cavity and deforming polymer, showing simulation boundary conditions, geometry variables and polymer peak deformation location measurement. (b) Deformation profiles for increasing cavity width (*W*) holding indenter width and film thickness constant. (c) Deformation profiles for decreasing film thickness (h_i) holding cavity geometry constant.

NIL has generated great interest in the last two decades which has resulted in development of sophisticated metrology and simulation tools to study the process [62, 63]. The focus on R2RNIL is relatively recent and adequate tools to understand the process are still under development. R2RNIL can benefit considerably from modeling and simulation efforts; however, processing large area flexible substrates at very high throughput creates interesting challenges in creating new models. Some of the existing gaps in modeling and simulation and the objective of this dissertation are presented in the next section.

1.6 RESEARCH OBJECTIVES

Pattern replication with various configurations of R2RNIL has been proposed; however, the various steps involved in the pattern transfer are not well understood. The scale-up of these systems requires design rules based on different steps involved the process. A comparative study of the benefits and limitations of these systems is required to determine the most suitable setup for any application. In this dissertation, we present models of different steps in R2RNIL and propose design rules that can help scale-up and optimize the process.

Achieving high throughput and low defect rate is the main challenge in SFIL. Throughput and defectivity in SFIL are dictated by droplet spreading. Studying the fluid dynamics in SFIL during droplet spreading can help in identifying the main factors limiting fast droplet spreading and pattern fidelity. However, the high density of droplets, patterns on the template and many possible schemes for template control and droplet dispensing pose a huge challenge in studying the fluid flow. We present models for dynamic simulation of thousands of droplets spreading in SFIL in order to overcome to these challenges. A method to calculate bulk flow permeability is proposed to take fluid flow around features into account. Defect characterization in SFIL is presented. A gas diffusion model to study the impact of gas trapping in SFIL on throughput is presented. The objective is to analyze different droplet dispensing schemes and template patterns in SFIL in order to determine optimum conditions to achieve high throughput and low defectivity.

RLT variation in nanoimprint lithography with flexible substrate greatly impacts the pattern fidelity. The coupled fluid-structure mechanics in nanoimprint lithography with flexible substrates needs to be studied to completely understand the underlying physics. We propose a model to calculate residual layer thickness in the process based on droplet spreading and various important factors such as web tension and template position.

The computational study presented in this dissertation would provide insight into the physics of various steps involved in nanoimprinting on rigid and flexible substrates and help make design decisions for optimum pattern fidelity and throughput.

Chapter 2: Models for Roll-to-roll Nanoimprint Lithography with a Roller Template

2.1. INTRODUCTION

Roll-to-roll nanoimprint lithography (R2RNIL) is a process based on batch nanoimprint lithography to replicate nano- and micro-scale patterns from the surface of a patterned mold to a large area, flexible or rigid substrate. R2RNIL was first demonstrated more than a decade ago by Chou et al. [23] who replicated sub-100 nm patterns on PMMA resist using thermal curing. Since then, R2RNIL has been proposed as a cost-effective route to manufacture lab-on-a-chip [5], solar cells [6], polarizers [7], and OLEDs [8]. To design and evaluate the viability of such a manufacturing system, the process parameters and their effect on throughput, residual layer thickness (RLT) and defectivity are needed. Here we present different configurations of R2RNIL and an analysis of R2RNIL for ink-jetted, UV curable liquids on a rigid substrate for patterning by a roller.

A R2RNIL setup is illustrated in Figure 2.1, and it includes a roller with patterned template, a flexible or rigid substrate, an imprint dispenser unit, imprint material, and a heating or UV curing module. For thermal curing, the imprint material used is a thermoplastic polymer like PMMA [23-25] and for UV curing, there are UV-curable resins like acrylics [21, 26] and epoxysilicone [7, 27]. A pretreated substrate is coated with a layer of imprint material by roller coating [27-29], inkjet [30] or knife coating [18] process. The pattern transfer takes place by application of pressure from the roller, as the imprint material spreads along with the substrate. The imprint material is cured by a thermal or UV-source as it fills the features on the template, thus replicating the patterns on the template on the roller permanently. R2RNIL provides a considerable advantage over batch nanoimprint lithography by offering higher throughput, lower cost and the ability to pattern large area of flexible or rigid substrate. However, there are several challenges to overcome before the process can be successfully implemented in the industry.

A. Jain and R. T. Bonnecaze, "Fluid management in roll-to-roll nanoimprint lithography," *Journal of Applied Physics,* vol. 113, 2013.
Prinicipal research was carried out by A. Jain. The research was supervised by R. T. Bonnecaze.

Thermal R2RNIL suffer from long thermal cycles in which the heated resist is embossed by the mold and then cooled before the mold is peeled off making it a very time consuming process [38]. Mold fabrication is an expensive process and heating and cooling cycle of the mold can lead to high thermal stresses and consequently short life of the mold [27]. Slight misalignment of the substrate and mold can also lead to waste of the entire batch.

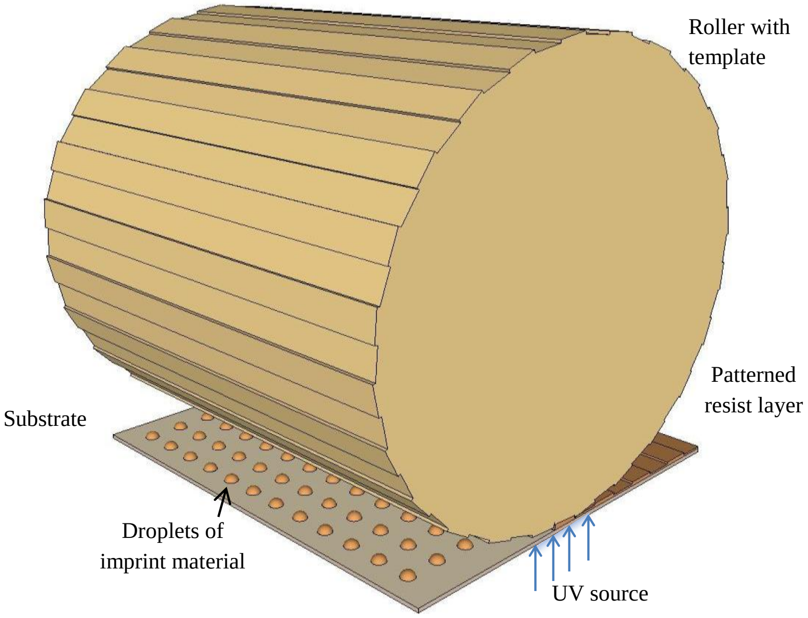

Figure 2.1: Schematic of a roll-to-roll nanoimprint lithography setup showing a roller of radius *R* with patterned template, a rigid substrate and a UV source. UV curable imprint material is ink-jetted as droplets on the substrate which forms a patterned resist layer after UV-curing.

Ahn et al. proposed using UV curing instead of thermal curing to improve the imprinting rate of the substrate [26]. Low viscosity imprint material used in UV curing requires a shorter filling time as compared to thermally cured materials [24, 64]. The low viscosity of UV-curable imprint material also lead to low forces in the process which reduces the defects in the pattern and increase the life of the mold [38]. Since the introduction of the R2RNIL process, many modifications have been suggested to improve the quality of the pattern replication and the overall processing time [8, 24, 26, 64-67]. Most of these suggestions include improvement in the setup of the process like introduction of a conveyor mold to improve the speed of thermal R2RNIL [24], use of a cheaper flexible mold to reduce the cost of the mold fabrication [64], and automatic stamp release to reduce the pattern distortion [66]. Some of these systems have been described in Section 1.2. The R2RNIL systems can be classified into four main configurations: (i) Basic R2R (ii) Wrapped R2R (iii) Belt R2R and (iv) Step R2R as shown in Figure 2.2.

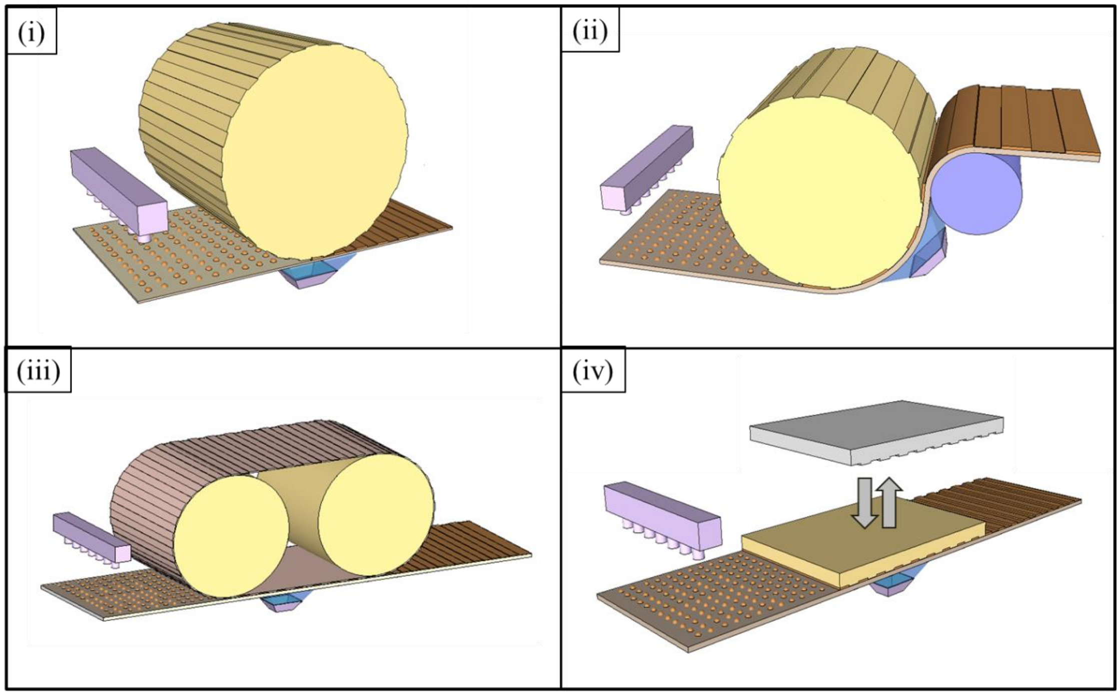

Figure 2.2: Configurations for R2RNIL (i) Basic (ii) Wrapped (iii) Belt and (iv) Step.

(i) Basic R2R: In Basic R2R configuration, a patterned template is wrapped around a roller. The roller template imprints on a flexible or rigid substrate making a line contact as shown in Figure 2.2(i) [26, 68, 69]. This system was designed to pattern continuously on a large substrate with low forces and pattern uniformity [23]. This roll-to-roll nanoimprint apparatus has the simplest design among the configurations with roller template.

(ii) Wrapped R2R: This configuration is used to pattern a large area flexible substrate with a roller template. In this configuration, a flexible substrate partially wraps around the roller. This set up provides larger contact area between the roller and substrate and more stability to the system as shown in Figure 2.2(ii). Wrapped R2R configuration is the most widely used configuration for R2RNIL [7, 18, 20, 21, 26-28, 41, 70-79]. However, unlike the other three configurations, Wrapped R2R configuration can only pattern a flexible substrate.

(iii) Belt R2R: In Belt R2R configuration, a patterned template is wrapped around two rollers partially or completely [28, 80, 81]. A schematic of a Belt R2R configuration with template completely wrapped around two rollers is shown in Figure 2.2(iii). This arrangement provides larger contact area between template and substrate and works with both rigid and flexible substrate. It is especially useful in thermal R2RNIL since it allows adjustable cooling time between the two rollers.

(iv) Step R2R: Step R2R configuration has a stepper template instead of a roller template. It can pattern a flexible or a rigid substrate as shown in Figure 2.2(iv) [12, 16, 35]. In this configuration, imprinting can be single-step imprinting or multi-step imprinting. In single-step imprinting the entire imprint area is imprinted in one step and the size of patterned area is same as the size of the patterned area on the stepper template. In multi-step imprinting, smaller stepper template makes multiple imprints on the substrate in the form of a matrix.

The imprinting process needs to be studied to identify the advantages, disadvantages and operational limits of the different configurations. There is also a lack of understanding of the quantitative effects of the process parameters and material properties on the dynamics of the imprinting process. A thorough understanding of the behavior of the imprint material can help optimal design and control of the process.

This work focuses on modeling the roll-to-roll nanoimprint lithography process using the Basic R2R configuration with UV curing and inkjet dispensing on a rigid substrate. Inkjets dispense calculated volumes of imprint material at specified positions providing conformity and minimal waste. These droplets of imprint material merge and spread on the substrate as they come in contact with the template on the roller forming a continuous resist layer. The resist layer is then cured by the UV-source as it conforms to the features on the template. The feature filling is facilitated by the pressure from the roller. The resist layer gets peeled off from the roller once the process is complete. We present the fluid dynamics of the resist layer as the entire process of merging of droplets, UV-curing and peel-off of the patterned resist layer takes place. We derive a model for the roll-to-roll nanoimprint process and study the flow of imprint material as it is UV-cured during the imprint process by using a Maxwell model to describe the viscoelastic nature of the imprint material. We study the effect of the UV dosage for sufficient UV curing on the maximum web speed possible. Further, we calculate various process parameters like the point of merging of droplets, the point of peel-off of the resist layer, the available exposure time, the pressure profile of the imprint layer, the normal and shear forces on the substrate and the torque on the roller based on the input parameters and material properties.

Table 2.1: Classification of R2RNIL systems based on configuration

Roller template				**Stepper template**
Basic	***Wrapped***		***Belt***	***Step***
Ahn et al. (2006)[26] Chang et al. (2006)[68] Yang et al. (2006)[69]	Ahn et al. (2006)[26] Ahn et al. (2007)[7] Bessonov et al. (2011)[21] Unno et al. (2011)[72] Inanami et al. (2012)[34] Taniguchi et al. (2012)[41] Kooy et al. (2013)[82]	Tsai et al. (2013)[79] Wu et al. (2013)[33] Yoshikawa et al. (2013)[33, 74] Inanami et al. (2014)[75] Liu et al. (2014)[77] Sabik et al. (2014)[78]	Ahn et al. (2009)[28] Seo et al. (2006) †[64] Ogino et al. (2013) †[83]	Ahn et al. (2012)[16] Ahn et al. (2014)[35] Thesen et al. (2014)[31, 32]

†Thermal R2RNIL

2.2 DROPLET MANAGEMENT AND RESIST BEHAVIOR

One of the most appealing features of the R2RNIL is the ability to process continuous rolls of patterned substrate. Previously, pattern transfer using R2RNIL has been demonstrated at web-speed of 0.3 m/min to 0.84 m/min [18, 26, 68]. This feature along with high web speed can result in higher throughput compared to batch nanoimprint process. However, high web speed has been attributed to cause defects in the pattern size due to incomplete feature filling and incomplete curing of the imprint material [68]. The exposure time is critical to the quality of the replicated pattern as an uncured resist will produce defects due to inability to keep the shape while excessive curing will damage the mold with excessive demolding force [48]. Thus, the throughput of the process and the quality of pattern replication is governed by process parameters, peel-off mechanism, forces on the substrate and the roller and UV-exposure time. In the following sections we discuss in details various aspects of the R2RNIL process using the Basic configuration with focus on droplet arrangement, peel-off mechanism and forces involved in the process.

2.2.1 Process Parameters

Here we identify important design and operating parameter which will be used throughout the chapter. Consider the roll-to-roll nanoimprint process illustrated in Figure 2.3. Figure 2.3(a) shows the overall process with a roller of radius R, the substrate and the UV source. The roller and the substrate both move at speed u_o to minimize the shear stress on the imprint material. The inset in Figure 2.3(a) shows the imprint material dispensed on the substrate as droplets of radius r_d with distance d between them. Figure 2.3(b) shows the process in further detail along with the important process parameters. The droplets merge to form a continuous layer at the point of merging $x = x_m$. The imprint material is cured from a viscous liquid to an elastic resist from $x = x_m$ to $x = 0$ by the UV source. After the pattern transfer is complete, the resist layer detaches from the template on the roller at the point of peel-off $x = x_p$. Thus, the imprint material behaves as a viscoelastic fluid from $x = x_{\mathrm{m}}$ to $x = 0$ and as an elastic solid from $x = 0$ to $x = x_{\mathrm{p}}$.

At $x = 0$, the gap between the roller and the substrate is minimum. Since the radius of the roller R is very large compared to the minimum gap thickness h_o, the shape of the roller can be described by the following equation

$$y = h(x) = h_o + \frac{x^2}{2R}\,. \tag{2.1}$$

Note that, at $x = 0$, $h = h_o$. Each droplet has a radius r_d and makes a contact angle θ with the substrate. The droplets have a distance d between them as shown in the inset of Figure 2.3(a). The droplet volume is given by

$$q_v = \frac{\pi}{3}\frac{\left(2 - 3\cos\theta + \cos^3\theta\right)}{\sin^3\theta} r_d^3 \tag{2.2}$$

The flow rate per unit width of the substrate is then given by,

$$q = u_o \frac{q_v}{\left(2r_d + d\right)^2} \tag{2.3}$$

The residual layer thickness of the imprint material can be of the order of a few microns or nanometers depending on the volume of droplet dispensed and the distance between them. A mass balance between the volume of the droplets and the patterned imprint material gives the residual layer thickness of the imprint material, h_f as:

$$h_f = \frac{q_v}{\left(2r_d + d\right)^2} = \frac{q}{u_o} \tag{2.4}$$

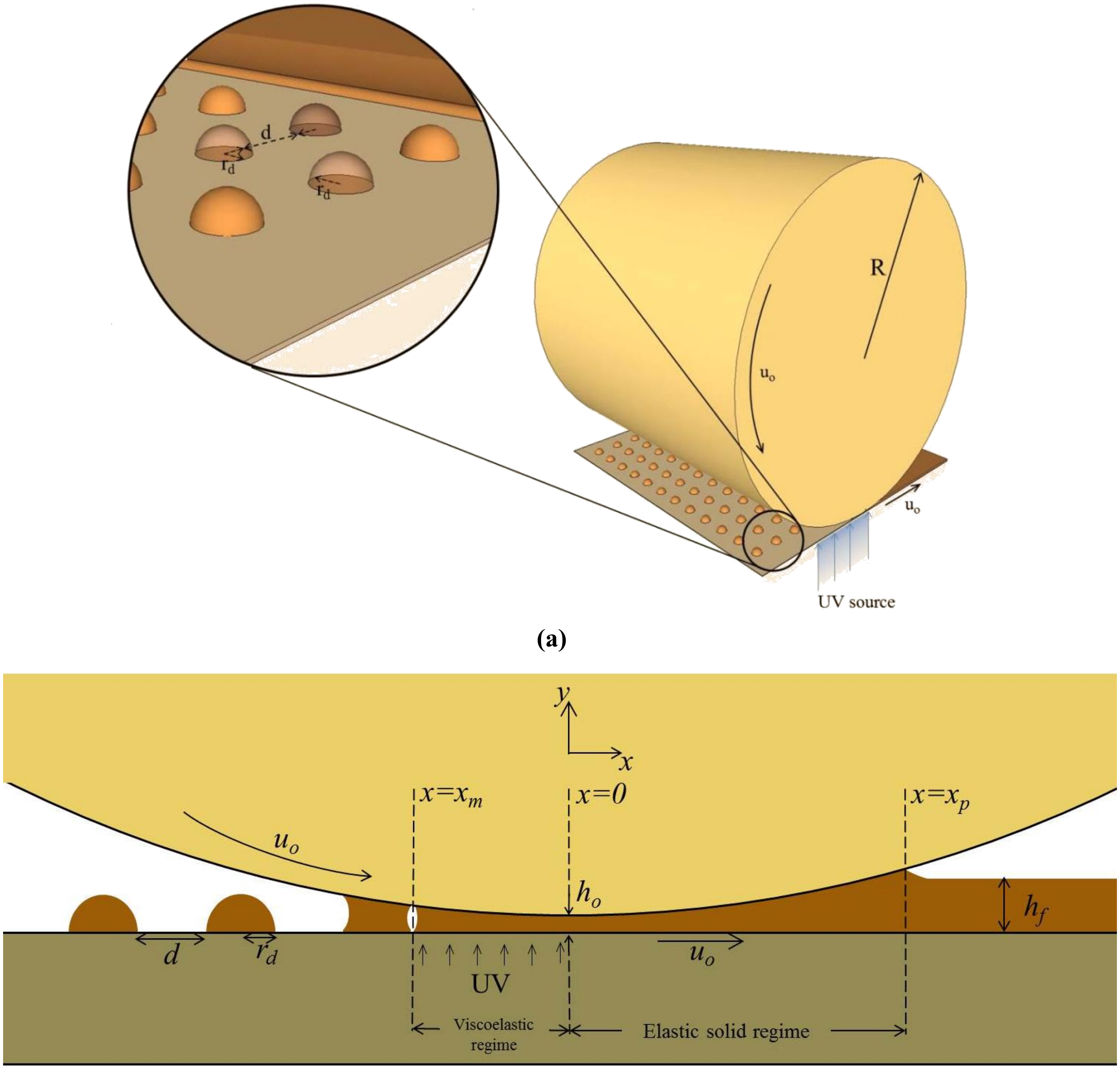

(a)

(b)

Figure 2.3: Our model for the R2RNIL shows the roller with radius *R* and the substrate, both moving with a speed u_o. (a) The inset shows the imprint droplets of radius r_d with distance *d* between them. (b) A further simplified view of the process. Figure shows the droplets move in the positive *x* direction along with the roller and the substrate. The droplets merge at $x = x_m$ to form a continuous resist layer of thickness h_f. The patterned imprint layer peels off from the roller at $x = x_p$. The minimum gap between the roller and substrate is h_o at $x = 0$.

2.2.2 Point of Merging

Figure 2.4(a) shows the different positions of a droplet as it merges into a continuous film of imprint material under the roller. The point of merging can be calculated based on the design parameters of the process. At the point of merging, the continuous film is completely conformed to the shape of the template and the merging droplet is assumed to have a cylindrical shape as shown in Figure 2.4(b). It is assumed that the shear stress from the roller or the substrate does not cause the center of the droplets to shift from their original position since the roller and substrate are moving at the same speed.

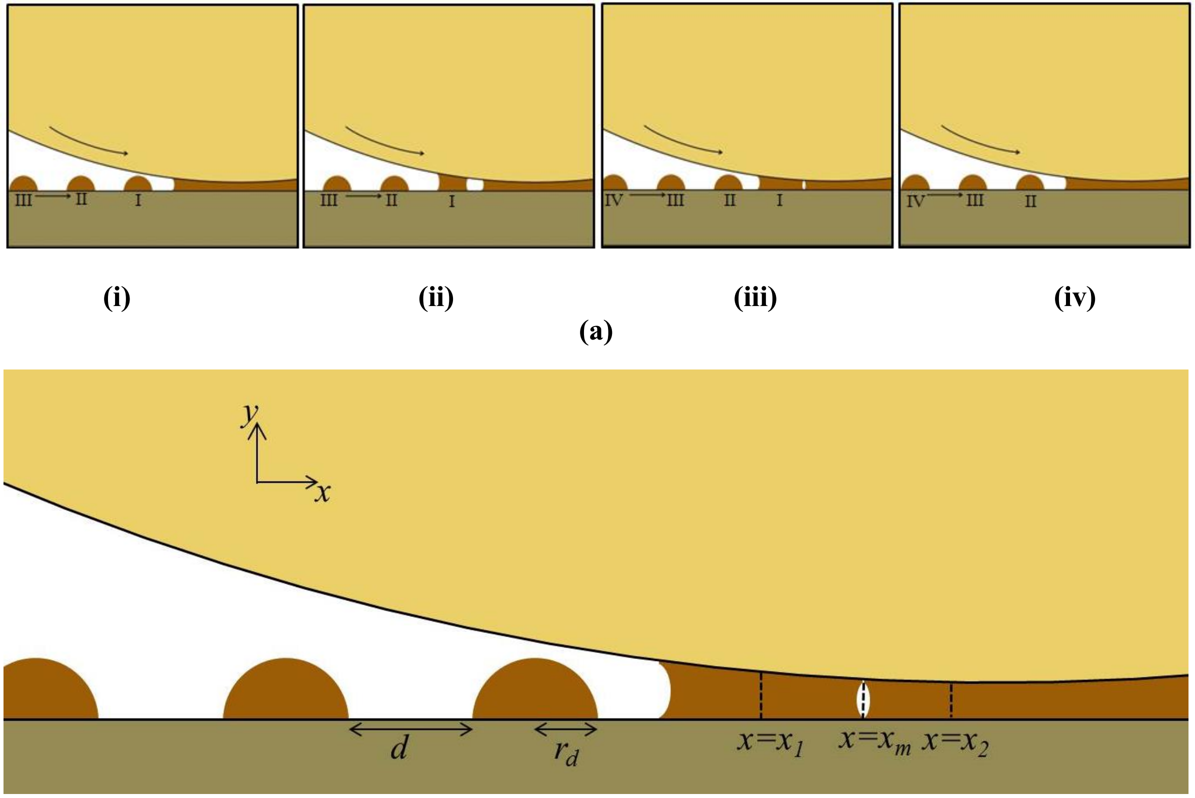

(i) **(ii)** **(iii)** **(iv)**

(a)

(b)

Figure 2.4: (a) Schematic diagram showing merging of droplets to the continuous film of imprint material. (i) a continuous film of imprint material and the droplets I, II and III. (ii) droplet I coming in contact with the roller as it moves forward. (iii) droplet I about to merge with the film. (iv) droplet I completely merges into the film and droplet II merges next. (b) An enlarged view of Figure 2.4(a) (iii) showing the position of droplets at the point of merging $x = x_m$. The shape of droplet at $x = x_1$ can be approximated to be cylindrical. The droplet at $x = x_2$ is a part of the continuous film and completely conformed to the shape of the roller.

Figure 2.4(b) shows the position of a droplet at $x = x_1$ merging with the continuous film at the point of merging $x = x_m$. The droplet at $x = x_1$ has a constant volume q_v and assuming that its shape is cylindrical, q_v can be written as:

$$q_v \approx \pi (x_m - x_1)^2 \left(h_o + \frac{x_1^2 + x_m^2}{4R} \right) \tag{2.5}$$

Since, $h_o >> \frac{x_1^2}{2R}, \frac{x_m^2}{2R}$ the above equation can be simplified to give:

$$x_1 = x_m - \left(\frac{c_2}{x_m^2 + c_1} \right)^{1/2}, \text{ where } c_1 = 2Rh_o \text{ and } c_2 = \frac{2Rq_v}{\pi}. \tag{2.6}$$

Since the shear stress is negligible and the positions of the center of the droplets do not change, it can be assumed there is a droplet at $x = x_2$ which has merged completely with the continuous film and conformed to the shape of the roller. The volume of droplet at $x = x_2$ is given by:

$$q_v \approx 2(2r_d + d) \left[h_o (x_2 - x_m) + \left(\frac{x_2^3 + x_m^3}{6R} \right) \right] \tag{2.7}$$

For $h_o >> \frac{x_2^2}{2R}, \frac{x_m^2}{2R}$, the above equation can be simplified to give

$$x_2 = x_m + \left(\frac{c_3}{x_m^2 + c_1} \right), \text{ where, } c_1 = 2Rh_o \text{ and } c_3 = \frac{Rq_v}{2r_d + d}. \tag{2.8}$$

Since the distance between the droplets is d and the centers of the droplets are at $x = x_1$ and $x = x_2$, the distance between the centers of the droplets is given by

$$x_2 - x_1 = 2r_d + d. \tag{2.9}$$

Solving Equations (2.6), (2.8), (2.9) and using the expression (2.4) we find that the point of merging x_m is given by,

$$\frac{x_m}{\sqrt{2Rh_o}} \approx \left(1.09 \frac{h_f}{h_o} - 1 \right)^{1/2}. \tag{2.10}$$

2.2.3. Required UV Dosage and Maximum Web Speed

In this section, a model is created to calculate the UV dose based on the residual layer thickness h_o and the exposure length. From Beer Lambert's law, we know that the UV intensity at a thickness d is given by

$$I = I_o e^{-d/d_p}, \tag{2.11}$$

where, I_o is UV light intensity and d_p is the penetration depth. The typical value of penetration depth is about 100 μm. The penetration depth for 365nm UV-LED used in experiments by Yoshikawa et al. is 88 μm [84]. The total UV exposure dose to the photopolymer of thickness h_o in time t is

$$J = I_o\left(1-e^{-h_o/d_p}\right)t. \tag{2.12}$$

Total exposure time, t is given by

$$t = \frac{L}{u_o}, \tag{2.13}$$

where, L is the exposure length and u_o is the web speed. Thus the UV exposure dose, J, is given by

$$J = I_o\left(1-e^{-h_o/d_p}\right)\frac{L}{u_o}. \tag{2.14}$$

The minimum required UV dose is a significant parameter as it dictates the maximum web speed possible. If the required exposure dose J is known, the web speed can be calculated using

$$u_o = I_o\left(1-e^{-h_o/d_p}\right)\frac{L}{J}. \tag{2.15}$$

The exposure length L can be calculated based on the point of merging of droplets. Once the droplets have merged to form a continuous film, the imprint material is cured from $x = x_m$ to $x = 0$. For high quality pattern replication, the imprint material must be cured into an elastic solid at x

= *0* where it is at maximum compression from the roller as shown in Figure 2.3(b). Thus, the exposure length *L* for Basic R2R is given by

$$L = -x_m \tag{2.16}$$

and exposure time *t* is given by

$$t = \frac{-x_m}{u_o} . \tag{2.17}$$

--

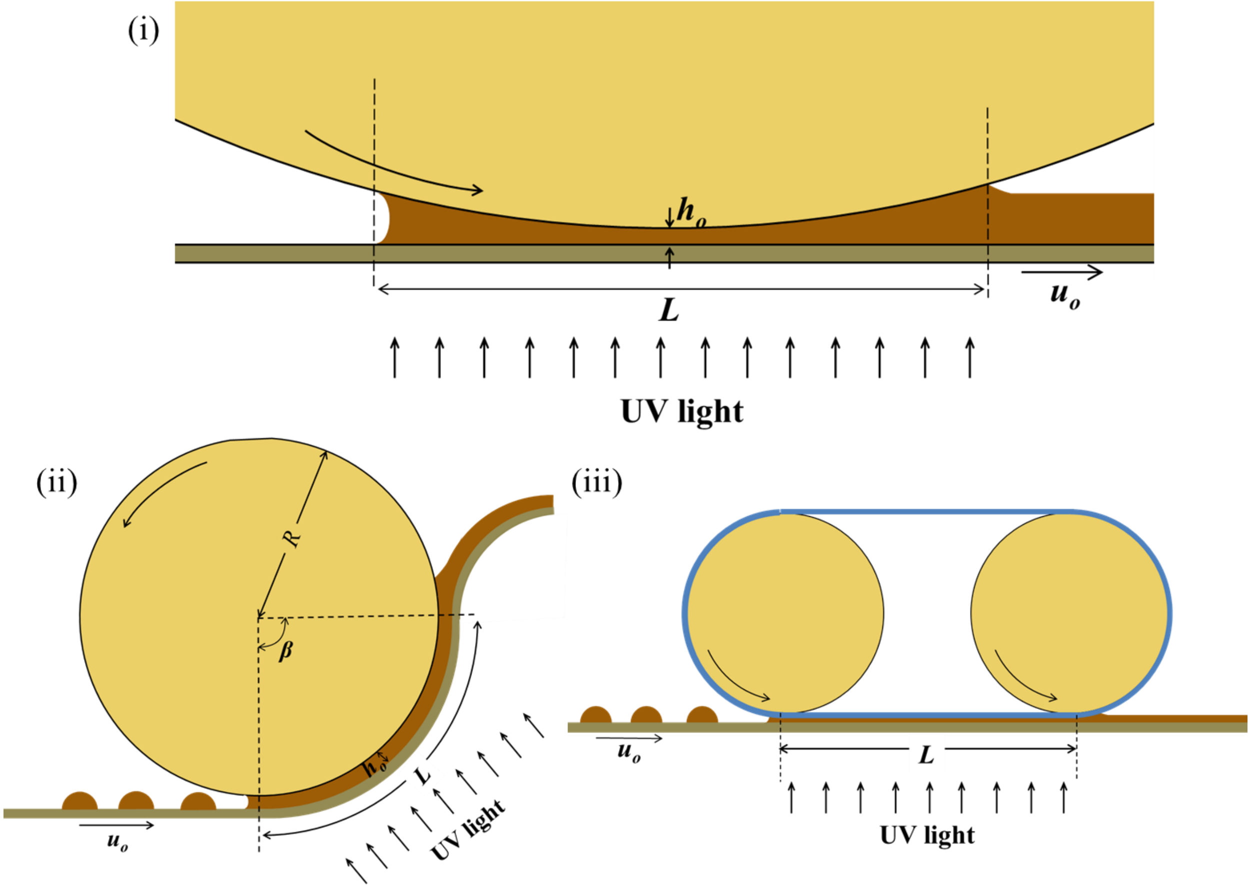

Figure 2.5: Schematic showing exposure length *L* for different configurations of R2RNIL (i) Basic R2R (ii) Wrapped R2R (iii) Belt R2R.

The maximum web speed for a fixed UV dosage can also be calculated for the Wrapped and Belt configurations using the exposure length. For Wrapped R2R configuration, the exposure length is the length of substrate wrapping the roller and it is of the order of $R\beta$ where, R is the roller radius and β is the fraction of roller circumference covered by the substrate. For Belt R2R configuration, the exposure length is the distance between the rollers. The schematic of the exposure length for the three roller-based configurations are shown in Figure 2.5.

2.2.4. Point of Peel-off

The peel-off takes place as the surface energy of the contact region between the roller and the resist is balanced by the strain energy in the tensile region of the imprint layer [85]. Once the pattern transfer is complete, the resist layer is peeled off from the roller at the point of peel-off $x = x_p$ as shown in Figure 2.3(b). Here, the resist layer is modeled as an elastic solid with residual layer thickness h_f. Figure 2.6(a) describes our problem for values of h_f greater than h_o. The imprint layer experiences maximum compressive force at $x = 0$ where the gap between the roller and the substrate is minimum. As the imprint layer moves forward it relaxes and eventually experiences tensile stress from template because of adhesion between roller and the imprint material, and ultimately peels off the roller.

The roller surface is defined as before by Equation (2.1) and the local deformation of the imprint layer at any point is given by,

$$\delta(x) = h_f - h(x). \tag{2.18}$$

The shear effects on the elastic solid can be neglected because the roller and the substrate are moving at the same speed u_o. Neglecting the shear effects, the elastic solid can be modeled as a Winkler foundation [86] and the contact pressure at any point x as a function of the elastic modulus E, the Poisson's ratio v, residual layer thickness h_f is given by

$$p_e(x) = \frac{(1-\nu)E}{(1+\nu)(1-2\nu)}\frac{\delta(x)}{h_f} = C\delta(x), \tag{2.19}$$

where, C is the resulting stiffness. This expression gives a positive pressure for compressive stress ($h(x) < h_f$) and negative pressure for tensile stress ($h(x) > h_f$). The reaction force F_E acting on a width W of the substrate up to a point x_p can be calculated by integrating pressure p_e from $x = 0$ to $x = x_p$, so that

$$F_E = \int_0^{x_p} p_e W dx = CWx_p\left(\frac{x_p^2}{3R} - h_e\right) = CW\left(2R(\Delta h + h_e)\right)^{1/2}\left(\frac{2\Delta h - h_e}{3}\right), \tag{2.20}$$

where, $\Delta h = h_f - h_o$ and $h_e + \Delta h = \dfrac{x_p^2}{2R}$.

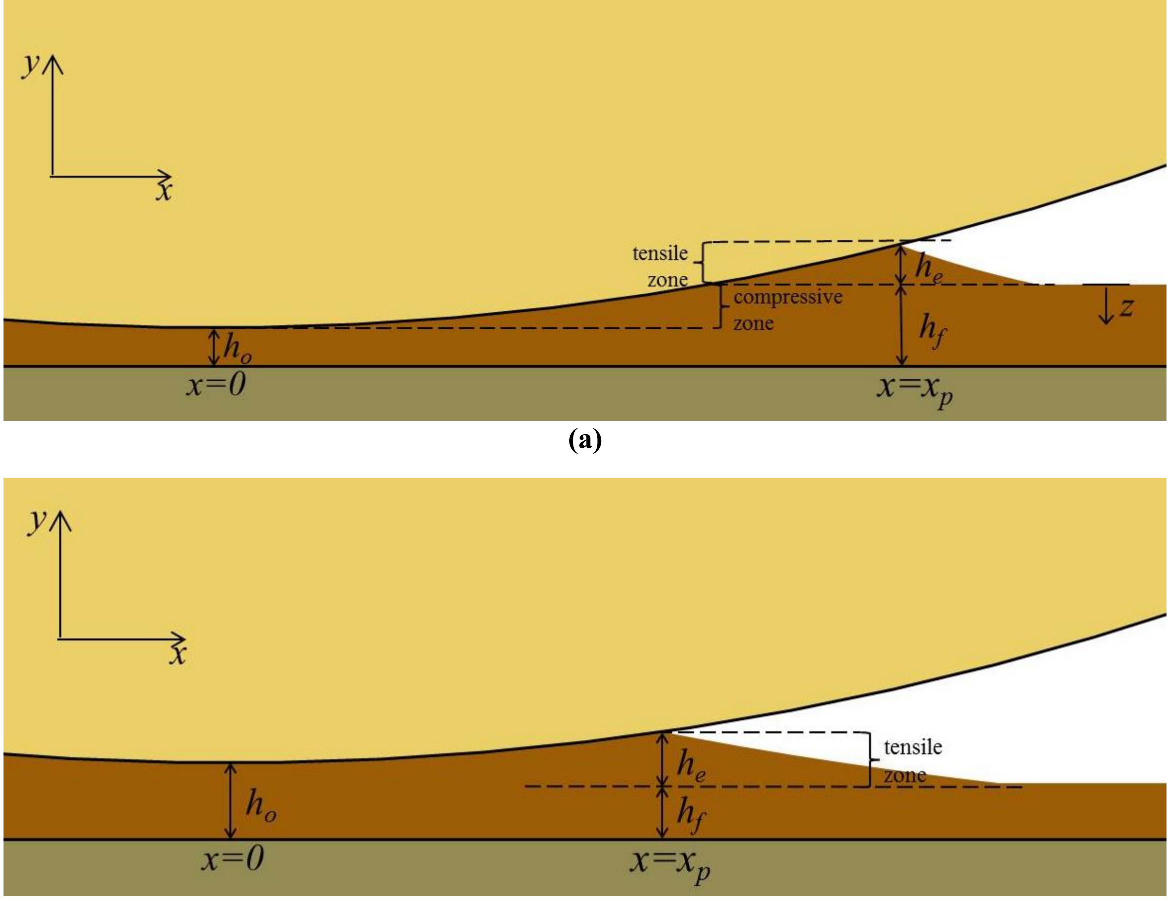

(a)

(b)

Figure 2.6: Schematic showing the final resist peeling off from the roller as the tensile energy in the resist balances the surface energy due to adhesion in the contact region. (a) $h_f > h_o$ (b)$h_f < h_o$. For $h_f < h_o$, there is no compression zone in the resist layer and the total strain is only due to the tensile zone.

To calculate the strain energy in the tensile region, we calculate the strain energy in the compressive region without adhesion (U_o) and subtract it from the total strain energy (U_T). In the absence of the adhesion, the force on the imprint layer is purely compressive (i.e. $h_e = 0$). U_o can be calculated by integrating the force on the imprint layer from $z = 0$ to $z = \Delta h$, where z is the penetration of the roller into the resist layer. Equation (2.21) gives U_o in terms of the final penetration Δh. (Recall that Equation (2.20) gives the reaction force for $z = \Delta h$.)

$$U_o = \int_{z=0}^{z=\Delta h} CW(2Rz)^{\frac{1}{2}}\left(\frac{2z}{3}\right)dz = \frac{4}{15}CW(2R)^{\frac{1}{2}}\Delta h^{\frac{5}{2}} \ . \tag{2.21}$$

The total strain energy (U_T) includes the strain energy in both the compressive and tensile region of the imprint layer. A direct integration of the contact force through the contact will fail to give the correct expression of U_T because of the deformation history of the imprint layer. U_T is given by subtracting the energy released due to stress relaxation in the tensile region from the strain energy at maximum penetration (U_{max}) at a fixed x_p. Thus, U_{max} at maximum penetration $z = z_{max} = \Delta h + h_e$ is given by

$$U_{\max} = \int_{z=0}^{z=\Delta h+h_e} CW(2Rz)^{\frac{1}{2}}\left(\frac{2z}{3}\right)dz = \frac{4}{15}CW(2R)^{\frac{1}{2}}(\Delta h + h_e)^{\frac{5}{2}} \ . \tag{2.22}$$

The recovered energy released due to tensile stress can be calculating integrating Equation (2.20) for no adhesion from $h' = 0$ to $h' = h_e$. The following equation gives the total strain energy U_T as follows:

$$U_T = U_{\max} - \int_0^{h_e} CWx_p\left(\frac{x_p^2}{3R} - h'\right)dh' = U_{\max} - \frac{h_e}{6}CW(2R)^{\frac{1}{2}}(4\Delta h + h_e)(\Delta h + h_e)^{\frac{1}{2}} \ . \tag{2.23}$$

The strain energy in the tensile zone is given by the difference between the total strain energy U_T and the strain energy in the compressive zone U_o. At the point of peel-off, the tensile energy is balanced by the change in surface energy of the contact area of the tensile zone, U_S, i.e.

$$U_T - U_o = U_s \tag{2.24}$$

The surface energy U_S for the contact area in the tensile zone ΔA is given by,

$$U_s = \gamma \Delta A = \gamma W\left\{x_p + \frac{x_p^3}{6R^2} - \sqrt{2R\Delta h}\left(1 + \frac{\Delta h}{3R}\right)\right\}. \tag{2.25}$$

Combining Equations (2.21-2.25), we find

$$\begin{aligned}&(\Delta h+h_e)^{5/2}-\frac{5}{8}h_e\left(4\Delta h+h_e\right)\left(\Delta h+h_e\right)^{1/2}-\Delta h^{5/2}\\&=\frac{15}{4}\frac{\gamma}{C(2R)^{1/2}}\left\{x_p+\frac{x_p^3}{6R^2}-\sqrt{2R\Delta h}\left(1+\frac{\Delta h}{3R}\right)\right\}\end{aligned}. \tag{2.26}$$

This equation can be solved to find the point of peel-off x_p. This analysis was done for $h_f > h_o$. For $h_f < h_o$, the same analysis can be carried out again, the only difference being the strain energy for compressive zone, U_o will be equal to zero as shown in Figure 2.6(b).

2.2.5. Liquid Resist Behavior and Pressure Analysis

The rheological properties of the liquid resist, such as viscosity and elasticity, change considerably during the curing process [27, 87-90]. During the UV curing process, the imprint material changes from a viscous liquid at $x = x_m$ to an elastic solid at $x = 0$ and the rheology of the imprint material in this region can best be described as a viscoelastic fluid as shown in Figure 2.7. The rheology of photopolymer in fast UV curing process has been extensively studied previously [84, 88, 89, 91, 92]. Based on these studies, the viscosity and elastic modulus of the imprint material as a function of x as follows:

$$\eta(x)=\eta_o\Phi(x)=\eta_o\exp(\phi x). \tag{2.27}$$

$$G(x)=G_o\Psi(x)=G_o\exp(\psi x). \tag{2.28}$$

The fluid dynamics of the process must be determined to calculate the force applied on the substrate and the torque on the roller. To this end we need a model to describe the rheology of the imprint material and governing equations to describe its flow. Figure 2.7 shows our two dimensional problem in which the imprint flows in the narrow gap between the roller and the substrate, both moving a constant velocity u_o. The viscoelastic characteristic of the imprint material can be modeled by the upper convected Maxwell constitutive equation having varying rheological properties as given in Equations (2.27) and (2.28) [93, 94]. The governing equations and boundary conditions for the flow of the imprint material have been described in details in the appendix. Solving the equations using lubrication approximation and perturbation analysis, we find that the pressure profile is given by (see Appendix)

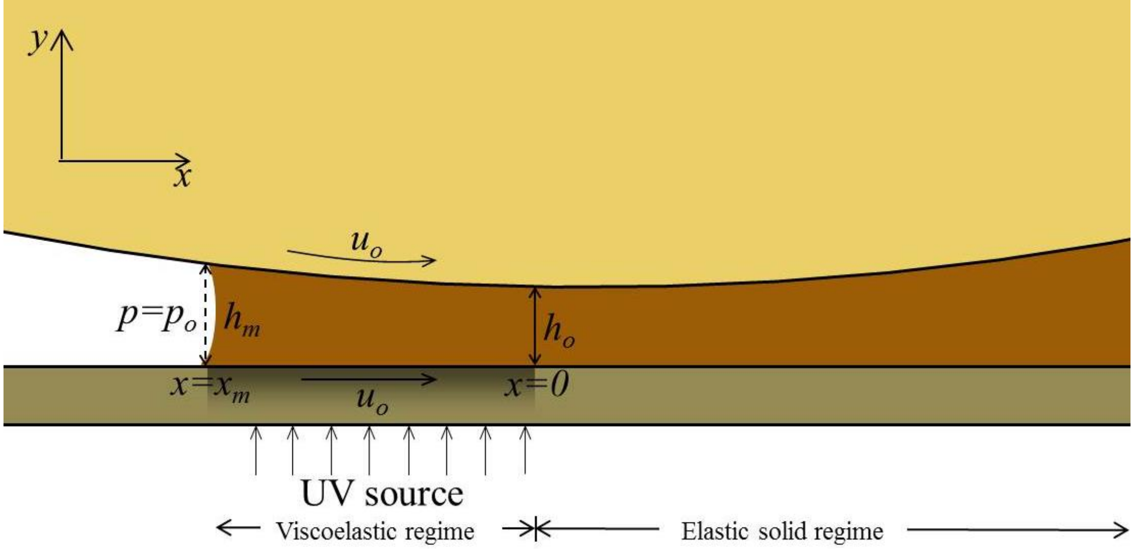

Figure 2.7: The imprint material behaves as a viscoelastic fluid as it is cured by the UV source. After complete curing the imprint material can be modeled as an elastic solid. The figure also shows the boundary conditions governing the flow.

$$\frac{dp_\eta}{dx}=\frac{12\eta u_o\left(h-h_f\right)}{h^3}-\frac{12\eta u_o}{h^3}De\left[L\frac{\Phi}{\Psi}\left\{\begin{array}{l} h'\left(1+6\frac{h_f^2}{h^2}\left(1-\frac{h}{h_f}\right)\right) \\ +\frac{h_f^2}{h}\frac{\Phi'}{\Phi}\left(\frac{6}{5}-\frac{27}{5}\frac{h}{h_f}+\frac{31}{5}\frac{h^2}{h_f^2}-2\frac{h^3}{h_f^3}\right)\end{array}\right\}+h_d\right] \tag{2.29}$$

In this expression, Φ,Ψ and h are functions of x and $De=\frac{\lambda_o u_o}{L}$. This expression is numerically integrated to determine the pressure profile of the imprint material in the viscoelastic regime. The pressure profile for the imprint material after it is completely cured i.e. from $x = 0$ to $x = x_p$ is given by Equation (2.29).

There are two forces acting on the substrate: the normal force because of the pressure of the imprint material, and the shear force from the imprint material. The normal force F applied on substrate can be calculated by integrating the pressure in the viscoelastic regime (from $x = x_m$ to $x = 0$) and the elastic regime (from $x = 0$ to $x = x_p$) over the length of the substrate as follows:

$$f_n = \int_{x_m}^{x_p} p dx = \int_{x_m}^{0} p_\eta dx + \int_{0}^{x_p} p_e dx , \tag{2.30}$$

where, the expression for pressure in the viscoelastic regime and the elastic regime is given in Equations (2.29) and (2.19) respectively.

The shear force per unit length of the substrate is given by solving the governing equations for the shear stress on the imprint material (τ_{xy}) at $y = 0$ and integrating over the length $x = x_m$ to $x = 0$. The expression for the shear stress, τ_{xy} at $y = 0$ is given by:

$$\tau_{xy}\left(y=0\right) = \frac{6\eta u_o\left(h-h_f\right)}{h^2} + De\left[\frac{h}{2}\frac{dp^{[d]}}{dx} + 12\frac{\eta u_o L}{h}\frac{\Phi}{\Psi}\left\{\begin{array}{l} \frac{h'}{h}\left(1-4\frac{h_f}{h}+3\frac{h_f^2}{h^2}\right)+ \\ \left(\frac{\Phi'}{\Phi}-2\frac{m'}{m}\right)\left(1-2\frac{h_f}{h}+\frac{h_f^2}{h^2}\right) \end{array}\right\}\Bigg]\right], \tag{2.31}$$

where, $\frac{dp^{[d]}}{dx}$ is given by Equation (2.A23). The torque (T) on the roller is calculated by taking the product of the shear force on the roller and the radius of the roller.

2.3. RESULTS AND DISCUSSION

2.3.1. Point of Merging

The size and position of the droplets dispensed on the substrate are critical process parameters because all the future steps of pattern transfer including feature filling, curing and peel-off depend on it. Moreover, if the droplets are too small or far apart, the droplets might not spread enough to make a continuous film for patterning. If the droplets are too large, the excess imprint material will be wasted and might cause irregular pressure distribution. The point where the droplets merge is important for calculating the total exposure time and deciding the position of the UV source. Equation (2.10) gives the point of merging of the droplets x_m as the distance from $x = 0$, in terms of the residual layer thickness h_f, the minimum gap h_o and the roller radius R. Figure 2.8 shows the relationship between the point of merging x_m and the process parameters

h_o, h_f and R. We observe that for a particular value of h_o and R, the distance of point of merging increases as the residual layer thickness increases. The increase in the residual layer thickness requires increase in the size of the droplet (r_d) or decrease in the distance between the droplets (d). This explains x_m tending to 0 as we lower the value of h_f. If we lower the value of h_f further (i.e. we decrease r_d or increase d), the droplets do not merge, leaving a discontinuous resist film. Thus, there exists a minimum value of r_d and maximum value of d beyond which the droplets will fail to merge. These values are deduced from Equation (2.10). For real values of x_m,

$$\frac{h_f}{h_o} \geq 0.92 \Rightarrow \frac{q_v}{\left(2r_d + d\right)^2 h_o} \geq 0.92 \tag{2.32}$$

For a fixed value of r_d and gap h_o, this inequality gives a maximum value of d, beyond which the droplets will fail to merge. Likewise, for a fixed value of d and minimum gap h_o, this inequality gives a minimum value of r_d, beyond which the droplets will fail to merge.

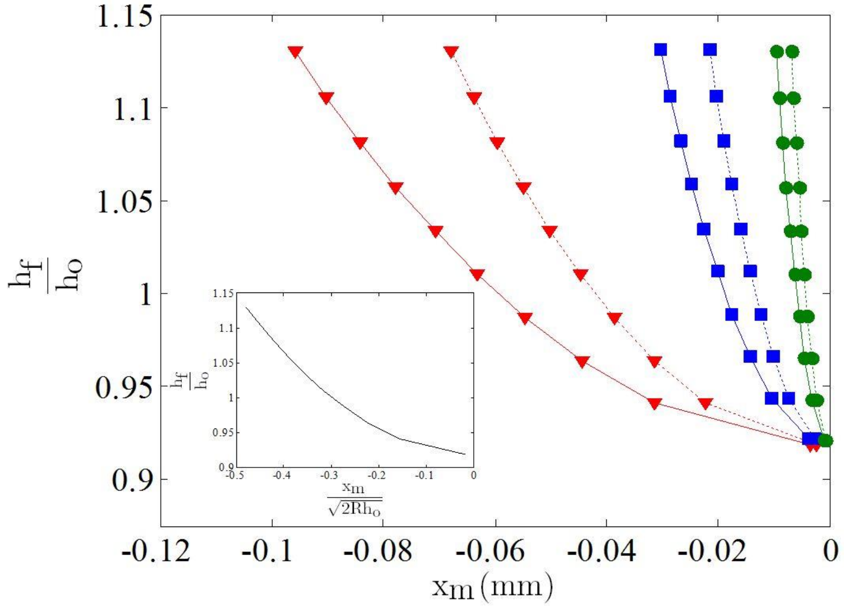

Figure 2.8: The plot showing the point of merging of the droplets x_m as a function of h_f/h_o for different values of R and h_o at u_o = 1 m/min. The inset shows the plot between non-dimensionalized x_m and non-dimensionalized h_f. (▼):h_o = 1 µm; (■):h_o = 100 nm; (●):h_o = 10 nm; (—): R = 2 cm; (---): R = 1 cm.

2.3.2. Point of Peel-off

The point of peel-off of the resist x_p is calculated by balancing the strain energy in the tensile zone in the resist layer and the surface energy in the contact area. Figure 2.9 shows the plot of point of peel-off of the resist as a function of h_f for different h_o and R, based on the solution of Equation (2.26) and its equivalent for $h_f < h_o$. The calculations are carried out with elastic modulus (E) = 10^6 Pa, surface energy (γ) = 46 mJ/m^2 and Poisson's ration (v) = 0.4. The inset shows the plot of non-dimensionalized x_p with non-dimensionalized h_f. It is observed that the slope of the profile is less steep for $h_f / h_0 < 1$. The change in the slope of the profile at $h_f / h_0 = 1$ suggests that the peel-off occurs more rapidly as we decrease the final thickness of the resist h_f. For values of h_f less than h_o, the compressive energy in the resist layer is zero as shown in Figure 2.6(b) where as there is both compressive and tensile energy in the resist layer for h_f greater than h_o as shown in Figure 2.6(a). The additional compressive force applied on the resist for $h_f > h_o$ during pattern transfer can improve the replication quality [26, 68]. Also, we have observed that for h_f below a critical value, the droplets might not merge to form a continuous resist layer. Based on these results, it can be concluded that the process should be carried at a value of h_f slightly higher than h_o to ensure a continuous resist layer and to provide compressive force on the imprint material for better replication quality.

2.3.3. Exposure Time and Maximum Web Speed

The intensity of UV source should be high enough so that imprint material is completely cured between $x = x_m$ and $x = 0$. If the imprint layer is under-exposed, it might cause defects in the patterns at peel off. The exposure time is calculated based on Equation (2.17) which gives an expression of exposure time as function of x_m and u_o. Fig. 8 shows the exposure time as a function of h_f/h_o for different values of h_o and R. The available exposure time, a key metric in R2RNIL, is found to be $O\left(\sqrt{Rh_o}/u_o\right)$. Ahn et al. have reported that an exposure dosage of 180 mJ/cm^2 is sufficient for complete polymerization of a urethane acrylate photopolymer of residual layer thickness 100μm [26]. It can be assumed that the same exposure dosage will be sufficient for residual layer thickness less than100 μm. Fig. 8 shows that the available exposure time decreases as the residual layer thickness is reduced. High values of web-speed might not allow enough time for complete photo-polymerization of the resist. High web speed can be compensated by either increasing the size of the roller or the power of the UV source [20]. Table 2.2 gives the process window for providing an exposure dosage of 180 mJ/cm^2 based on expression for available exposure time calculated in [11]. h_f/h_o is set to unity for all calculations. I *is* the minimum intensity of the UV source required for curing and is equal to the required exposure dosage/ available exposure time t. Typical UV source intensity is 10 W/cm^2 to 100 W/cm^2 and typical radius of the roller is 2.5 cm to 3 cm [20, 26, 27, 70, 95]. Evidently for values of h_o of the order of 100nm and lower, providing sufficient exposure will become challenging due to high UV intensity requirement even for large roller sizes. For such cases, other imprint configurations need to be considered.

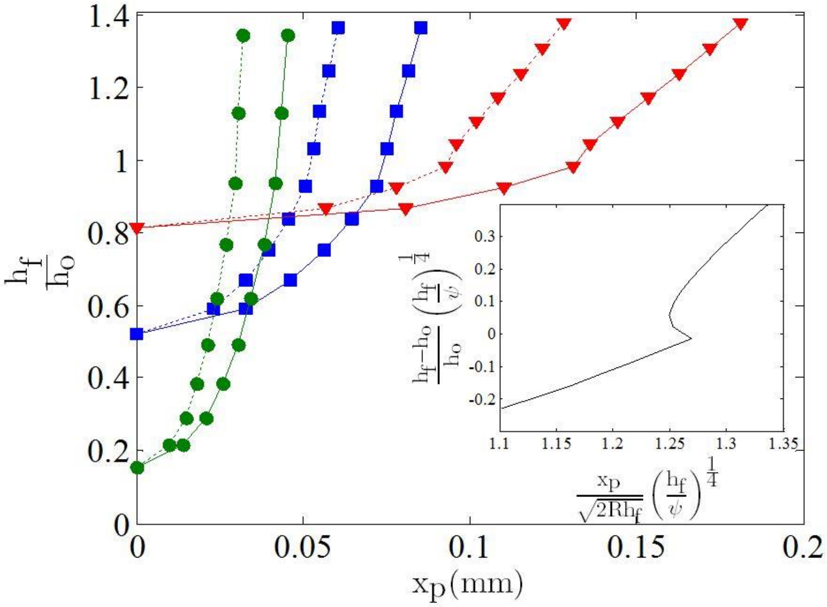

Figure 2.9: The plot showing the point of peel-off of the resist from the roller x_p as a function of h_f/h_o for different values of R and h_o at $u_o = 1$ m/min. The inset shows the plot between non-dimensionalized x_p and non-dimensionalized h_f. (▼): $h_o = 1$ µm; (■): $h_o = 100$ nm; (●): $h_o = 10$ nm; (—): $R = 2$ cm; (---): $R = 1$ cm.

Table 2.2: Estimated minimum UV intensity, *I* (W/cm^2) required for curing.

h_o (μm)	**u_o(m/min)**	**R(cm)**	**I (W/cm^2)**
100	1	1	4.7
100	1	2	3.4
100	0.5	1	2.4
1	1	1	47.5
1	1	2	33.6
1	0.5	1	23.8
0.1	1	1	150.4
0.1	1	2	106.3
0.1	0.5	1	75.2

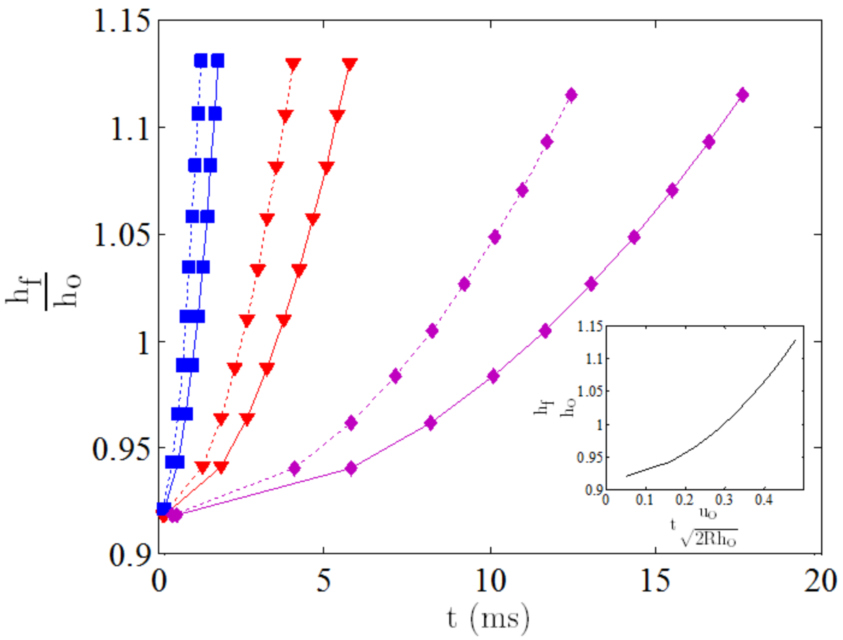

Figure 2.10: The plot showing the exposure time of the resist layer *t* as a function of h_f/h_o for different values of *R* and h_o at u_o = 1 m/min. The inset shows the plot between non-dimensionalized t and non-dimensionalized hf. (♦): h_o = 10 µm; (▼): h_o = 1 µm; (■): h_o = 100 nm; (—): *R* = 2 cm; (---): *R* = 1 cm.

The maximum web speed for different configurations for a fixed UV dosage can be calculated based on Equation (2.15). Figure 2.11 shows the maximum web speed u_o when applying a UV dose of 8 mJ/cm^2 as a function of RLT h_o for different R2R configurations. The calculations were done for an imprint roller with radius 75 mm and UV intensities of 46 mW/cm^2 (solid line) and 460 mW/cm^2 (broken line). The graph shows that for a given UV intensity and RLT, the Basic R2R needs to be run at a lower web speed compared to Wrapped and Belt R2R to apply the same UV dose. This is due to the smaller exposure length available for Basic R2R compared to Wrapped and Belt configurations. The exposure length greatly limits the maximum web speed possible for the Basic R2R configuration. Web speeds greater than 1 m/min has never been reported using the Basic configuration of UV R2RNIL. Chang et al. tried to fabricate micro-lens array of diameter 100 µm using Basic R2RNIL at roller speed of 0.5-2 mm/sec and demonstrated that the photopolymer does not cure completely at higher roller speeds [68].

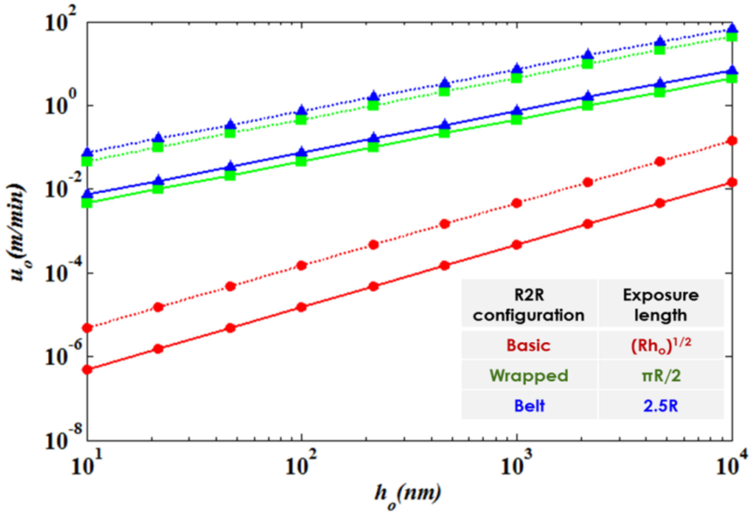

Figure 2.11: Web speed, u_o vs. RLT, h_o for Basic (•), Wrapped (■) and Belt (▲) R2R configurations. UV intensity is 46 mW/cm2 and 460 mW/cm2 for solid and broken lines respectively. Required UV dose 8 mJ/ cm^2 and a roller radius 75 mm.

The exposure time is also the time available for the imprint material to squeeze through the gap between the roller and the substrate and fill the features on the template. The feature filling time needs to be considerably smaller than the exposure time to allow for complete feature filling before photocuring of the imprint material takes place. The feature filling time for UV and thermal nanoimprint lithography has been calculated previously taking into account gas dissolution, gas diffusion, different feature sizes and fluid properties like surface tension and viscosity [47, 59-61, 96, 97]. Chauhan et al. found the rate of feature filling through a constant circular cross section feature to be of the order of $\sim O\left(R_p^2 \Delta P / 8\mu H_p\right)$ where R_p and H_p are the radius and height of the feature respectively and ΔP is the pressure difference between the fluid bulk and fluid interface [47]. This expression suggests that for feature sizes of the order of the residual layer thickness, the feature filling time will be negligible compared to the exposure time. Our model has been designed assuming an flat template, however, it is also valid for the aforementioned cases in which the feature sizes are less than or equal to the order of the residual layer thickness.

2.3.4. Pressure Profile

The pressure profile of the viscoelastic resist as it flows in the gap between the roller and the substrate is given by Equation (2.29). The viscosity and the elastic modulus of the imprint material increase according to the Equations (2.27) and (2.28). Figure 2.12 shows that the pressure in the viscoelastic regime (from $x = x_m$ to $x = 0$) as function of x for $u_o = 1$ m/min and R = 1cm and different values of h_f/h_o. In our calculations, the viscosity and the elastic modulus change from 0.02 Pa.s and 200 Pa for completely viscous fluid (at $x = x_m$) to 200 Pa.s and 10^6 Pa completely for elastic solid (at $x = 0$) respectively. The pressure increases as the imprint material reaches the minimum gap h_o. For values of h_f/h_o lower than 1, we observe cavitation in the system. The model also predicts that for lower values of h_o, higher pressure is generated which implies that operating at very low values of h_o may cause sharp increase in pressure which may lead to deformation of the template on the roller.

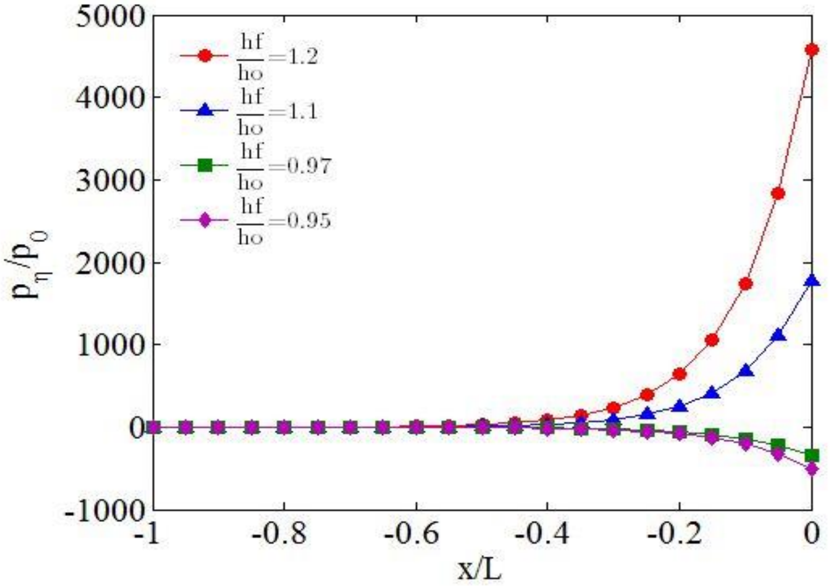

Figure 2.12: The pressure profile in the viscoelastic regime of the resist layer as a function of distance x for $h_o = 100$ nm, $R = 1$ cm, $u_o = 1$ m/min and different values of h_o.

It is assumed that the resist is completely cured to an elastic solid by the time it reaches the minimum gap h_o at $x = 0$. Figure 2.13 shows the pressure in the elastic region (from $x = 0$ to x

= x_p) as a function of x for $u_o = 1$ m/min and $h_o = 1$ μm and different values of R. A positive pressure implies a compressive force on the resist while a negative pressure implies a tensile force on the resist. For values of h_f less than h_o, the resist only experiences a tensile force (as discussed in section 2.2.4), however for values of h_f greater than h_o the resist experiences maximum compression at the minimum gap ($x = 0$). As the resist moves away from the center, it experiences a tensile strain due to adhesion from the roller until it is peeled-off from the roller surface at $x = x_p$. Also, the compressive force is zero for $h_f < h_o$ which we can observe in the graph. The quality of pattern transfer improves if there is compressive force from the roller on the resist during pattern transfer. The lack of compressive force may cause poor pattern transfer so it is suggested that the process is carried out for h_f greater than h_o.

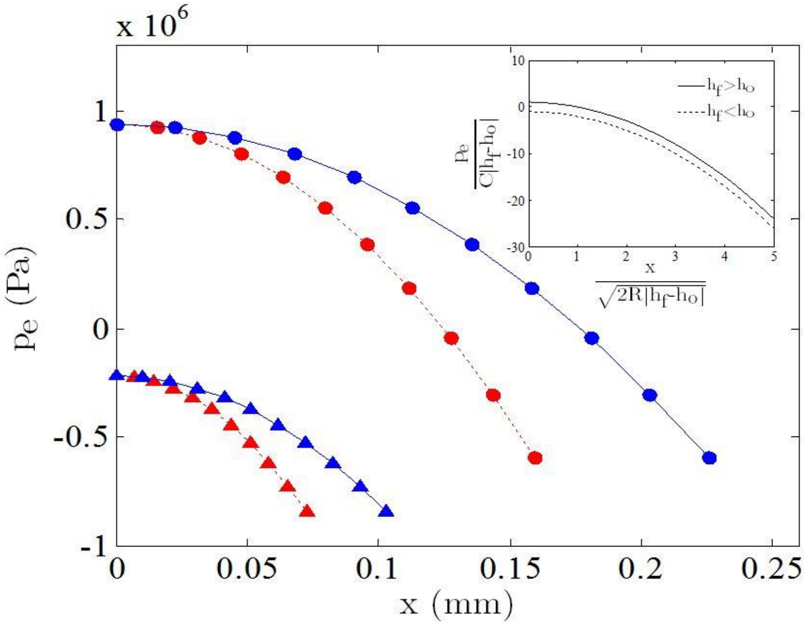

Figure 2.13: The pressure in the elastic region of the resist layer from $x = 0$ to $x = x_p$ for $u_o = 1$ m/min, $h_o = 1$ μm. A positive pressure implies a compressive force while a negative pressure implies tensile strain in the resist layer. (▼):$h_f/h_o = 0.9$; (●):$h_f/h_o = 1.8$; (—): $R = 2$ cm; (---): $R = 1$ cm.

2.3.5. Force on the Substrate and Torque on the Roller

High normal force on the substrate can result in high tension in flexible substrate and might damage rigid substrates. The normal force f_n can be calculated by integrating the pressure over the viscoelastic and elastic regime of the resist as shown in Equation (2.30). Figure 2.14 shows the normal force per unit width f_n acting on the substrate as a function of h_o for $u_o = 1$ m/min and different values of R and h_f/h_o. The model predicts higher normal force for smaller values of h_o which has also been observed experimentally [28]. The large normal force for small h_o can be explained by the high pressure generated in the gap at nanometer scale.

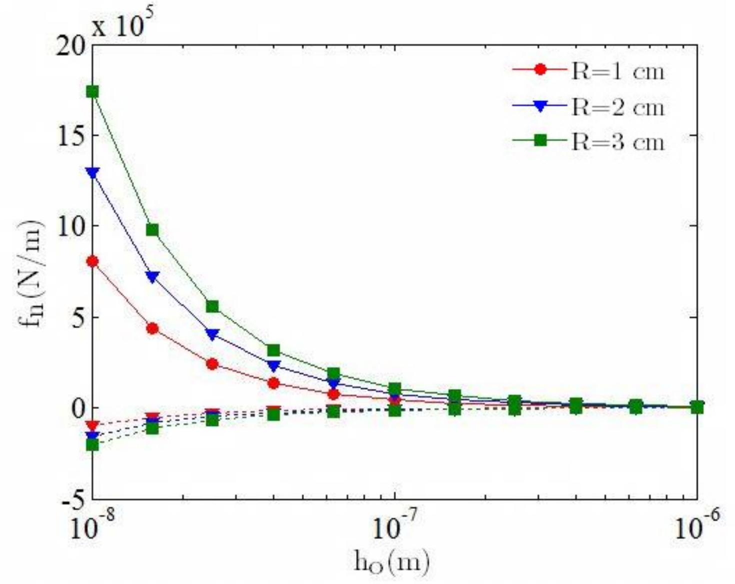

Figure 2.14: The force per unit width on the substrate as function of h_o at $u_o = 1$m/min for different values of R and h_f/h_o. (—):$h_f/h_o = 1.1$ (---):$h_f/h_o = 0.98$.

Figure 2.14 and 2.15 show the shear force per unit width (f_s) acting on the substrate and the torque per unit width (T) acting on the roller as a function of h_o at different values of h_f/h_o for $u_o = 1$ m/min and $R = 1$, respectively. The shear force on the substrate and the torque on the roller are higher for smaller values of h_o. Thus, the model predicts that higher forces are required to achieve smaller residual layer thickness. The negative forces for h_f/h_o less than can be explained by the cavitation pressure due to a starved inlet feed and the tensile force acting in the elastic resist. From Figures 2.13- 2.15, we conclude that high forces are required to achieve small residual layer thickness. All calculations assume a frictionless conveyor system.

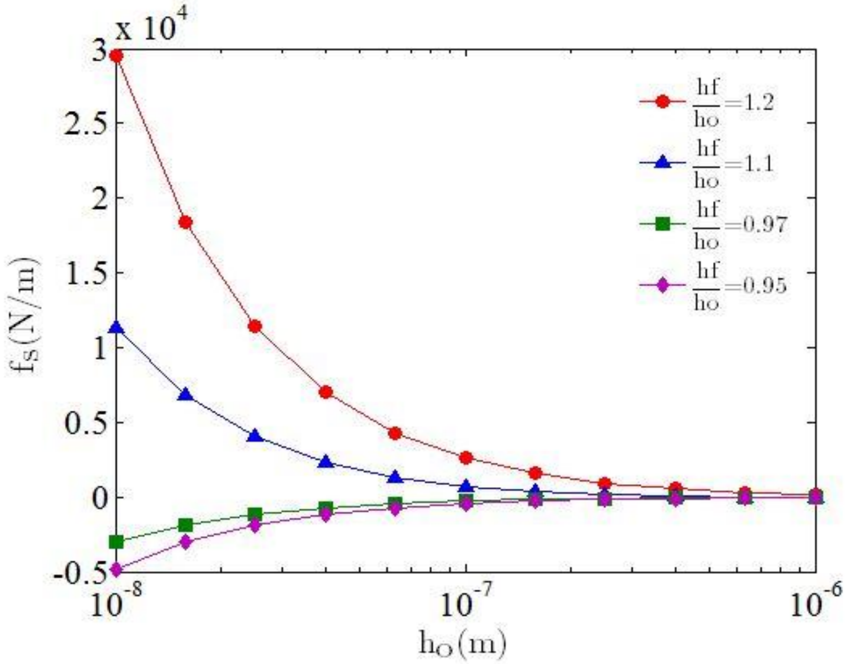

Figure 2.15: The shear force per unit width (f_s) on the substrate as function of h_o at u_o = 1 m/min for R = 1 cm and different values of h_f/h_o.

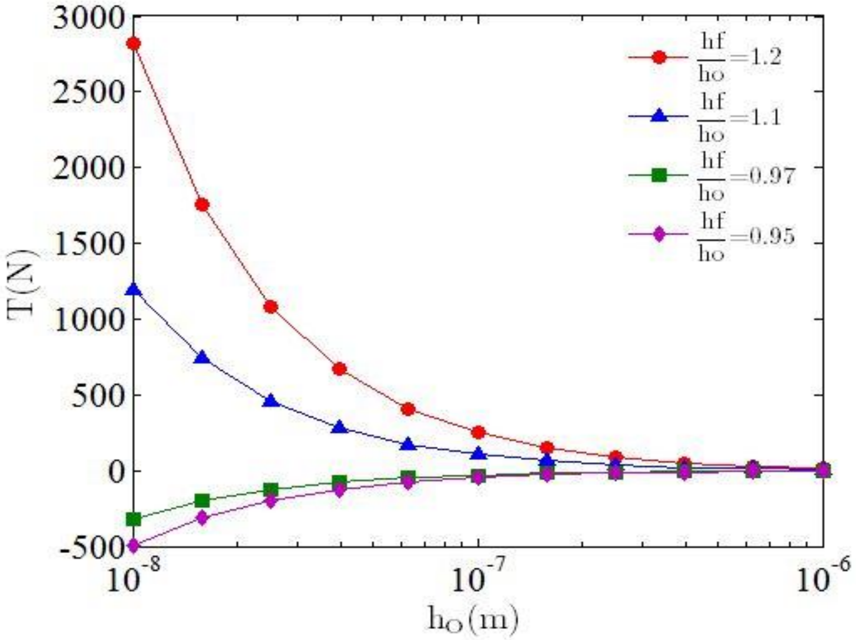

Figure 2.16: The torque per unit width (*T*) on the roller as function of h_o at u_o = 1 m/min for *R* = 1 cm and different values of h_f/h_o.

2.4. CONCLUSIONS

Roll-to-roll nanoimprint lithography is a multi-step process involving merging of droplets to form a continuous film, curing of imprint material, pattern transfer and peel-off for template detachment. Since all of these steps occur in an interval of seconds, it is crucial to understand each of these steps individually for high quality pattern replication. We study the dynamics of the imprint material and identified critical process parameters. The merging of imprint droplets is modeled and it is found that small size of droplets and large distance between the droplets can lead to incomplete merging and discontinuous resist layer. A residual layer thickness larger than the minimum gap between the roller and substrate will ensure a continuous resist layer. It is observed that the available exposure time is $O\left(\sqrt{Rh_o}/u_o\right)$. To apply sufficient exposure dosage, high web speed can be compensated by either increasing the size of the roller or the intensity of the UV source. High intensity UV source is required to photo-polymerize residual layer thickness less than 100 nm due to the low available exposure time. A theory for the peel-off mechanism relating the elastic modulus of the resist and the adhesion between the template and the resist us also proposed. The viscoelasticity of the imprint material is described using a Maxwell model and the normal and shear forces on the substrate and the torque on the roller are calculated. The UV R2RNIL process with inkjet dispensing is modeled for a rigid substrate and it will be interesting to apply the model to flexible substrate and deformable roller. The classification of R2RNIL into different configurations helps identify their drawbacks and helps in deciding the best arrangement for a given application. A comparative study of the four main R2R configurations is presented in Table 2.3.

Table 2.3: A comparison of Basic, Wrapped, Belt and Step R2RNIL configurations

	Basic R2R	Wrapped R2R	Belt R2R	Step R2R
Web speed	$O(\sqrt{Rh_o}/J)$ Web speed limited by exposure dose requirement	$O(R\beta/J)$ Web speed limited by system vibrations and high UV intensity requirement at high web speeds	$O(L/J)$ Web speed limited by system vibrations and high UV intensity requirement at high web speeds	Negligible dependence on required UV dose
Substrate handling	Flexible and rigid	Flexible only	Flexible and rigid	Flexible and rigid
UV Intensity	Needs high UV intensity at high web speed and small RLT	Low UV intensity requirement	Low UV intensity requirement	Low UV intensity requirement
Advantages	- Lower force requirement due to line contact - Reduced effect of thickness unevenness and dust on surrounding area due to line contact	- Large UV exposure area. - High throughput	- Large UV exposure area - High throughput. - Can pattern both flexible and rigid substrates	- Leverages existing wafer scale UV imprint lithography - High throughput. Highly stable
Challenges	- High UV intensity requirement - Incomplete UV curing at high web speed	- Can only pattern flexible substrate - System vibrations at high web speeds	- Roller alignment on moving substrate - Creation of roller template - System vibrations at high web speeds	- Achieving high throughput - Patterning large area with multi-step wafer template

Separate groups have demonstrated imprinting at speed of 30 m/min on a 250 mm wide area [31, 32] and a RLT of less than 70 nm [33] using Wrapped R2R configuration. This arrangement also allows greater stability. The web speed in this arrangement is only limited by system vibrations and high UV intensity requirement at high web speeds. Wrapped R2R configuration is clearly the most commonly used configuration. However, Wrapped R2R can only process a flexible substrate. Large substrates with limited flexibility e.g. thin glass can break under high web speed. Belt R2R and Basic R2R configurations can pattern flexible and rigid substrates. Alignment and system vibrations are huge challenges when dealing with two rollers in Belt R2R configuration. If these challenges are addressed, Belt R2R configuration can be used for high volume R2R nanofabrication. Basic R2R however does not have the capacity for high volume manufacturing as high web speeds (>1 m/min) are not possible with this configuration without use of high UV intensity. Step R2R configuration is already established in patterning rigid substrate. Step R2R has demonstrated imprinting 300 mm wide substrate on a flexible substrate however the throughput remains low. The throughput with Step R2R can be improved by understanding the fluid flow during the imprinting process on a flexible substrate. We believe that this work will help in determining the optimal operating conditions for roll-to-roll nanoimprint lithography process.

2.5. APPENDIX

The upper convected Maxwell (UCM) model for the viscoelastic regime of the resist material from $x = x_m$ to $x = 0$ is given by

$$\lambda \overset{\triangledown}{\overline{\boldsymbol{\tau}}} + \overline{\boldsymbol{\tau}} = 2\eta\overline{\boldsymbol{D}}\,, \tag{2.A1}$$

where η is the viscosity of the imprint material, λ is the characteristic relaxation time of the fluid given by the ratio of viscosity $\eta(x)$ and elastic modulus $G(x)$,

$$\lambda = \frac{\eta(x)}{G(x)} = \frac{\eta_o \Phi(x)}{G_o \Psi(x)} = \lambda_o \frac{\Phi(x)}{\Psi(x)}\,, \tag{2.A2}$$

$\overline{\boldsymbol{D}}$ is the deformation tensor given by

$$\overline{\boldsymbol{D}} = \frac{1}{2}\left(\nabla\overline{\boldsymbol{v}} + \left(\nabla\overline{\boldsymbol{v}}\right)^T\right), \tag{2.A3}$$

where $\bar{v} = (u,v)$ is the velocity vector,

$\overline{\boldsymbol{\tau}}$ is the extra stress tensor and $\overset{\nabla}{\overline{\boldsymbol{\tau}}}$ is the upper convected derivative defined as

$$\overset{\nabla}{\overline{\boldsymbol{\tau}}} = \frac{\partial\overline{\boldsymbol{\tau}}}{\partial t} + \overline{\boldsymbol{v}}.\nabla\overline{\boldsymbol{\tau}} - (\nabla\overline{\boldsymbol{v}}).\overline{\boldsymbol{\tau}} - \overline{\boldsymbol{\tau}}.(\nabla\overline{\boldsymbol{v}})^T . \tag{2.A4}$$

Thus, the constitutive equations for the deviatoric stress components for the UCM model can be rewritten as:

$$\tau_{xx} + \lambda\left(u\frac{\partial\tau_{xx}}{\partial x} + v\frac{\partial\tau_{xx}}{\partial y} - 2\frac{\partial u}{\partial y}\tau_{xy} - 2\frac{\partial u}{\partial x}\tau_{xx}\right) = -2\eta\frac{\partial u}{\partial x}, \tag{2.A5-a}$$

$$\tau_{xy} + \lambda\left(u\frac{\partial\tau_{xy}}{\partial x} + v\frac{\partial\tau_{xy}}{\partial y} - 2\frac{\partial u}{\partial y}\tau_{yy} - 2\frac{\partial v}{\partial x}\tau_{xx}\right) = -\eta\left(\frac{\partial u}{\partial y} + \frac{\partial v}{\partial x}\right), \tag{2.A5-b}$$

$$\tau_{yy} + \lambda\left(u\frac{\partial\tau_{yy}}{\partial x} + v\frac{\partial\tau_{yy}}{\partial y} - 2\frac{\partial v}{\partial y}\tau_{yy} - 2\frac{\partial v}{\partial x}\tau_{xy}\right) = -2\eta\frac{\partial v}{\partial y}, \tag{2.A5-c}$$

The equation of continuity and the equation of motion for unsteady incompressible fluid are given by:

$$\nabla.\overline{\boldsymbol{v}} = 0, \tag{2.A6}$$

$$\rho\left(\frac{\partial\overline{\boldsymbol{v}}}{\partial t} + \overline{\boldsymbol{v}}.\nabla\overline{\boldsymbol{v}}\right) = \overline{\boldsymbol{b}} - \nabla p + \nabla.\overline{\boldsymbol{\tau}}, \tag{2.A7}$$

where, p is the isotropic pressure, $\overline{\boldsymbol{b}}$ is the body force and ρ is the density. (For our problem, body force $\overline{\boldsymbol{b}}$ is assumed to be zero.) Assuming two-dimensional steady state flow, the component form of equations of continuity and momentum (Equations (2.A5) and (2.A6)) can be rewritten as

$$\frac{\partial u}{\partial x}+\frac{\partial v}{\partial y}=0, \qquad (2.A8)$$

$$\frac{\partial \tau_{xx}}{\partial x}+\frac{\partial \tau_{xy}}{\partial y}+\frac{\partial p}{\partial x}=0, \qquad (2.A9\text{-a})$$

$$\frac{\partial \tau_{xy}}{\partial x}+\frac{\partial \tau_{yy}}{\partial y}+\frac{\partial p}{\partial y}=0, \qquad (2.A9\text{-b})$$

with boundary conditions:

$$u=u_o, v=0 \text{ at } y=0, \qquad (2.A10\text{-a})$$

$$u=u_o, v=0 \text{ at } y=h(x), \qquad (2.A10\text{-b})$$

$$p=p_o=\frac{Ca}{h(x_m)/2} \text{ at } x=x_m, \qquad (2.A10\text{-c})$$

where $h(x_m)$ is given by Equation (2.1) and *Ca* is the capillary number.

These governing equations and the boundary conditions can be expressed in a non-dimensional form by using the following non-dimensional quantities as follows:

$$\begin{gathered} x^*=\frac{x}{L},\ y^*=\frac{y}{h_o},\ u^*=\frac{u}{u_o},\ v^*=\frac{v}{u_o h_o/L}, \\ \tau_{xx}^*=\frac{\tau_{xx}}{\eta u_o L/h_o^2},\ \tau_{xy}^*=\frac{\tau_{xy}}{\eta u_o/h_o},\ \tau_{yy}^*=\frac{\tau_{yy}}{\eta u_o/L},\ p^*=\frac{p}{\eta u_o L/h_o^2}, \\ De=\frac{\lambda_o u_o}{L},\ \varepsilon=\frac{h_o}{L},\ h^*(x)=\frac{h(x)}{h_o}. \end{gathered} \qquad (2.A11)$$

We assume L to be the characteristic length in the *x*-direction and h_o to be the characteristic length in the *y*-direction. In a non-dimensional form, the governing equations can be written as: (For convenience the asterisks have been dropped.)

$$\frac{\partial u}{\partial x}+\frac{\partial v}{\partial y}=0, \qquad (2.A12\text{-a})$$

$$\frac{\partial \tau_{xx}}{\partial x}+\frac{\partial \tau_{xy}}{\partial y}+\frac{\partial p}{\partial x}=0, \tag{2.A12-b}$$

$$\varepsilon^2\left(\frac{\partial \tau_{xy}}{\partial x}+\frac{\partial \tau_{yy}}{\partial y}\right)+\frac{\partial p}{\partial y}=0, \tag{2.A12-c}$$

$$\tau_{xx}+De\frac{\Phi}{\Psi}\left(u\frac{\partial \tau_{xx}}{\partial x}+v\frac{\partial \tau_{xx}}{\partial y}-2\frac{\partial u}{\partial y}\tau_{xy}-2\frac{\partial u}{\partial x}\tau_{xx}\right)=-2\Phi\varepsilon^2\frac{\partial u}{\partial x}, \tag{2.A12-d}$$

$$\tau_{xy}+De\frac{\Phi}{\Psi}\left(u\frac{\partial \tau_{xy}}{\partial x}+v\frac{\partial \tau_{xy}}{\partial y}-2\frac{\partial u}{\partial y}\tau_{yy}-2\frac{\partial v}{\partial x}\tau_{xx}\right)=-\Phi\left(\frac{\partial u}{\partial y}+\varepsilon^2\frac{\partial v}{\partial x}\right), \tag{2.A12-e}$$

$$\tau_{yy}+De\frac{\Phi}{\Psi}\left(u\frac{\partial \tau_{yy}}{\partial x}+v\frac{\partial \tau_{yy}}{\partial y}-2\frac{\partial v}{\partial y}\tau_{yy}-2\frac{\partial v}{\partial x}\tau_{xy}\right)=-2\Phi\frac{\partial v}{\partial y}, \tag{2.A12-f}$$

where, $\Phi \equiv \Phi(x)$ and $\Psi \equiv \Psi(x)$, with boundary conditions:

$$u=1, v=0 \text{ at } y=0, \tag{2.A13-a}$$

$$u=1, v=0 \text{ at } y=h(x), \tag{2.A13-b}$$

$$p=\frac{p_o}{\eta u_o L/h_o^2} \text{ at } x=1. \tag{2.A13-c}$$

For our problem, L is set equal to the distance of point of merging from the origin x_m. $L \gg h_o$ so the lubrication approximation will be applicable. For $\varepsilon \to 0$, we can write the Equation (2.A12) as follows:

$$\frac{\partial u}{\partial x}+\frac{\partial v}{\partial y}=0, \tag{2.A14-a}$$

$$\frac{\partial \tau_{xx}}{\partial x}+\frac{\partial \tau_{xy}}{\partial y}+\frac{\partial p}{\partial x}=0, \tag{2.A14-b}$$

$$\frac{\partial p}{\partial y} = 0\,, \qquad \text{(2.A14-c)}$$

$$\tau_{xx} + De\frac{\Phi}{\Psi}\left(u\frac{\partial \tau_{xx}}{\partial x} + v\frac{\partial \tau_{xx}}{\partial y} - 2\frac{\partial u}{\partial y}\tau_{xy} - 2\frac{\partial u}{\partial x}\tau_{xx} \right) = 0\,, \qquad \text{(2.A14-d)}$$

$$\tau_{xy} + De\frac{\Phi}{\Psi}\left(u\frac{\partial \tau_{xy}}{\partial x} + v\frac{\partial \tau_{xy}}{\partial y} - 2\frac{\partial u}{\partial y}\tau_{yy} - 2\frac{\partial v}{\partial x}\tau_{xx} \right) = -\Phi\frac{\partial u}{\partial y}\,, \qquad \text{(2.A14-e)}$$

$$\tau_{yy} + De\frac{\Phi}{\Psi}\left(u\frac{\partial \tau_{yy}}{\partial x} + v\frac{\partial \tau_{yy}}{\partial y} - 2\frac{\partial v}{\partial y}\tau_{yy} - 2\frac{\partial v}{\partial x}\tau_{xy} \right) = -2\Phi\frac{\partial v}{\partial y}\,. \qquad \text{(2.A14-f)}$$

Now we analyze Equation (2.A14) by a regular perturbation expansion of the variables as a power series of *De*, where 0<*De*<<1. In Equation (2.A15), the leading term gives the conventional lubrication solution and is denoted by the subscript [*l*]. The perturbation correction due to the viscoelasticity is denoted by [*D*].

$$u = u^{[l]} + De \cdot u^{[D]} + O\left(De^2\right), \qquad \text{(2.A15-a)}$$

$$v = v^{[l]} + De \cdot v^{[D]} + O\left(De^2\right), \qquad \text{(2.A15-b)}$$

$$\tau_{xx} = {\tau_{xx}}^{[l]} + De \cdot {\tau_{xx}}^{[D]} + O\left(De^2\right), \qquad \text{(2.A15-c)}$$

$$\tau_{xy} = {\tau_{xy}}^{[l]} + De \cdot {\tau_{xy}}^{[D]} + O\left(De^2\right), \qquad \text{(2.A15-d)}$$

$$\tau_{yy} = {\tau_{yy}}^{[l]} + De \cdot {\tau_{yy}}^{[D]} + O\left(De^2\right), \qquad \text{(2.A15-e)}$$

$$p = p^{[l]} + De \cdot p^{[D]} + O\left(De^2\right). \qquad \text{(2.A15-f)}$$

Substituting (A15) into (A14), the leading order terms result in the following equations:

$$\frac{\partial u^{[l]}}{\partial x}+\frac{\partial v^{[l]}}{\partial y}=0\,, \tag{2. A16-a}$$

$$\frac{\partial \tau_{xx}^{[l]}}{\partial x}+\frac{\partial \tau_{xy}^{[l]}}{\partial y}+\frac{\partial p^{[l]}}{\partial x}=0\,, \tag{2. A16-b}$$

$$\frac{\partial p^{[l]}}{\partial y}=0\,, \tag{2.A16-c}$$

$$\tau_{xx}^{l}=0\,, \tag{2.A16-d}$$

$$\tau_{xy}^{l}=-\Phi\frac{\partial u^{[l]}}{\partial y}\,, \tag{2.A16-e}$$

$$\tau_{yy}^{l}=-2\Phi\frac{\partial v^{[l]}}{\partial y}\,. \tag{2.A16-f}$$

The boundary conditions for the leading terms are given by:

$$u^{[l]}=1, v^{[l]}=0 \text{ at } y=0\,, \tag{2.A17-a}$$

$$u^{[l]}=1, v^{[l]}=0 \text{ at } y=h(x)\,, \tag{2.A17-b}$$

Solving we get:

$$u^{[l]}=\frac{1}{2\Phi}\frac{\partial p^{[l]}}{\partial x}\left(y^{2}-hy\right)+1\,. \tag{2.A18}$$

Since the inflow rate of imprint is known (Equation (2.4)), we get,

$$\int_{0}^{h}u^{[l]}dy=\frac{q}{u_{o}h_{o}}\,. \tag{2.A19}$$

Using the above expression in Equation (2.A18) and simplifying, we find:

$$\frac{\partial p^{[l]}}{\partial x}=\frac{12\Phi\left(h-h_f\right)}{h^3}, \qquad (2.A20)$$

where h_f is in its non-dimensional form.Similarly substituting (2.A15) into (2.A14), and collecting *De*-order terms we get the following equations:

$$\frac{\partial u^{[D]}}{\partial x}+\frac{\partial v^{[D]}}{\partial y}=0, \qquad (2.A21\text{-a})$$

$$\frac{\partial \tau_{xx}^{[D]}}{\partial x}+\frac{\partial \tau_{xy}^{[D]}}{\partial y}+\frac{\partial p^{[D]}}{\partial x}=0, \qquad (2.A21\text{-b})$$

$$\frac{\partial p^{[D]}}{\partial y}=0, \qquad (2.A21\text{-c})$$

$$\tau_{xx}^{[D]}+\frac{\Phi}{\Psi}\left(-2\frac{\partial u^{l}}{\partial y}\tau_{xy}^{[l]}\right)=0, \qquad (2.A21\text{-d})$$

$$\tau_{xy}^{[D]}+\frac{\Phi}{\Psi}\left(u^{[l]}\frac{\partial \tau_{xy}^{[l]}}{\partial x}+v^{[l]}\frac{\partial \tau_{xy}^{[l]}}{\partial y}-2\frac{\partial u^{[l]}}{\partial y}\tau_{xy}^{[l]}\right)=-\Phi\frac{\partial u^{[D]}}{\partial y}, \qquad (2.A21\text{-e})$$

$$\tau_{yy}^{[D]}+\frac{\Phi}{\Psi}\left(u^{[l]}\frac{\partial \tau_{yy}^{[l]}}{\partial x}+v^{[l]}\frac{\partial \tau_{yy}^{[l]}}{\partial y}-2\frac{\partial v^{[l]}}{\partial y}\tau_{yy}^{[l]}-2\frac{\partial v^{[l]}}{\partial x}\tau_{xy}^{[l]}\right)=-2\Phi\frac{\partial v^{[l]}}{\partial y}. \qquad (2.A21\text{-f})$$

The boundary conditions that need to be satisfied by the above equations are given by:

$$u^{[D]}=0, v^{[D]}=0 \text{ at } y=0, \qquad (2.\ A22\text{-a})$$

$$u^{[D]}=0, v^{[D]}=0 \text{ at } y=h(x), \qquad (2.A22\text{-b})$$

$$p^{[D]}=0 \text{ at } x=0. \qquad (2.A22\text{-c})$$

Solving the above equations gives the following expression for pressure for *De*-order term:

$$\frac{\partial p^{[D]}}{\partial x}=-\frac{12\eta u_o}{h^3}De\left[L\frac{\Phi}{\Psi}\left\{\begin{array}{l}h'\left(1+6\frac{h_f^2}{h^2}\left(1-\frac{h}{h_f}\right)\right)+\\ \frac{h_f^2}{h}\frac{\Phi'}{\Phi}\left(\frac{6}{5}-\frac{27}{5}\frac{h}{h_f}+\frac{31}{5}\frac{h^2}{h_f^2}-2\frac{h^3}{h_f^3}\right)\end{array}\right\}+h_d\right], \tag{2.A23}$$

where h_d can be solved using Equation (2.A22-c). Since

$$\frac{\partial p}{\partial x}=\frac{\partial p^{[I]}}{\partial x}+De\frac{\partial p^{[D]}}{\partial x}, \tag{2.A24}$$

combining Equations (2.A20) and (2.A23) we find the pressure gradient for imprint material under the roller for the viscoelastic regime from $x = x_m$ to $x = 0$ can be written as follows:

$$\begin{aligned}\frac{\partial p}{\partial x}=\frac{\partial p_\eta}{\partial x}=&\frac{12\eta u_o\left(h-h_f\right)}{h^3}\\ &-\frac{12\eta u_o}{h^3}De\left[L\frac{\Phi}{\Psi}\left\{\begin{array}{l}h'\left(1+6\frac{h_f^2}{h^2}\left(1-\frac{h}{h_f}\right)\right)+\\ \frac{h_f^2}{h}\frac{\Phi'}{\Phi}\left(\frac{6}{5}-\frac{27}{5}\frac{h}{h_f}+\frac{31}{5}\frac{h^2}{h_f^2}-2\frac{h^3}{h_f^3}\right)\end{array}\right\}+h_d\right].\end{aligned} \tag{2.A25}$$

Chapter 3: The Effect of Droplet Size and Placement on Throughput and Defect Rate in Step and Flash Imprint Lithography

3.1. INTRODUCTION

Step and Flash Imprint Lithography (SFIL) is a low cost, high throughput process to replicate high resolution nano- and micro- patterns from a template onto a rigid substrate [12]. SFIL has been used for nano-fabrication of many applications such as high density bit pattern media [98, 99], photonic applications [100, 101] and displays [102]. Lithography techniques like immersion and EUV lithography also provide high resolution patterning; however, these techniques are more expensive with lower throughput [103]. Pattern resolution in these techniques is limited by the wavelength of light and the numerical aperture of the optical system. Patterning sub-100 nm structures require complicated optical elements which increases the cost of exposure tools. SFIL does not have these limitations and has the following competitive advantages over other lithography techniques such as immersion and EUV lithography: (i) pattern resolution in SFIL is essentially only limited by the resolution of the template pattern [104, 105]; (ii) SFIL has demonstrated sub-100 nm pattern replication for features with high aspect ratios [106]; and (iii) the cost of ownership per wafer is significantly lower for SFIL compared to photolithography and EUV [107, 108].

The set up for SFIL includes a transparent template (also called a mask or mold), a rigid (glass or silicon) substrate, an inkjet dispenser and a UV light source as shown in Figure 3.1. The stepper template is patterned with micro- or nano- features of the same size as the final pattern [109]. The nanoimprint process begins with the inkjet dispenser dispensing low viscosity photo-curable resist droplets on the substrate. The inkjet dispenser is capable of dispensing droplets of volume as low as one picoliter (10^{-15} m^3) at a variable pitch ranging from 85 μm to 150 μm [110, 111]. The droplet density and arrangement depend on the volume of resist required to fill the local cavities on the template and achieve a homogeneous residual layer thickness (RLT). The stepper template is then lowered on the droplets until they merge together to form a uniform resist film. Once the fluid spreading is complete and the entire template is filled, UV light is irradiated on the resist through the transparent template. The UV light photo-polymerizes the monomer resist to create a solid film. The exposure dose and time depends on the resist material and RLT [41, 112]. Once the resist is completely cured, the template is peeled off from the resist through a precise and controlled movement of the template. The surface of the template has considerably low surface energy compared to the substrate, which allows the resist to preferentially adhere to the substrate. This process is repeated multiple times on different portions of the substrate to imprint a large wafer.

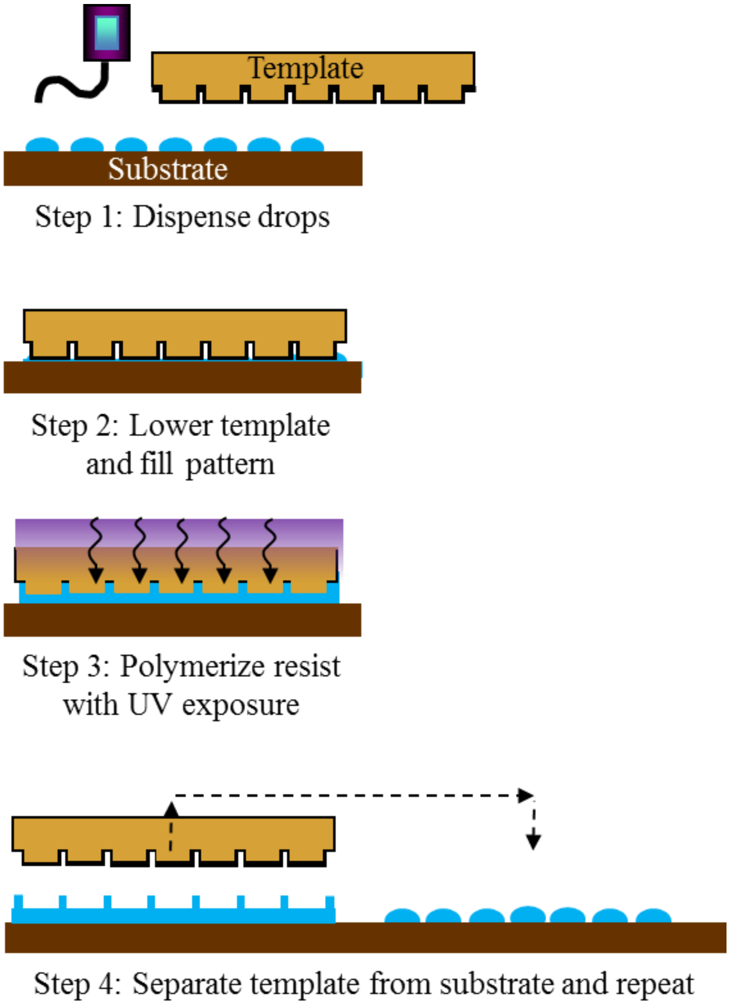

Figure 3.1: Schematic showing the main steps for pattern replication in Step and Flash Imprint Lithography.

High throughput and low defectivity are critical for high volume manufacturing of devices such as flash memory using SFIL [43, 62]. A recent cost of ownership calculations shows that a four-imprint tool system needs to produce 15 wafers per hour per imprint station at a defect density of 0.1 defects/cm^2 to compete with a single ArH self-aligned quadruple patterning tool [62]. This cost advantage was calculated for 15 nm half pitch grating. With current SFIL technology, five wafers of size 300 mm can be imprinted per hour per imprint station [42, 43]. This implies that a three-fold increase in process throughput is required. In SFIL, UV exposure and template/resist separation typically require 0.1 to 0.2 seconds for a template of size 6 in x 6 in [43]. UV exposure and template/resist separation are well understood and are not the throughput limiting step. The throughput is limited by fluid filling which takes about 1 to 5 seconds depending on the droplet size and surface energy of the substrate and template [42].

Fluid filling involves resist spreading over the entire wafer and the surrounding gas escaping from the features on the template as the resist fills these features. High throughput may lead to non-fill defects in the final pattern since the resist may not have sufficient time to fill the features or the gas may not escape the feature completely. By optimizing droplet size and allowed spreading time, defectivity of the imprint process can be improved. Khusnatdinov *et al.* conducted nanoimprinting with varying drop volume and spread times to demonstrate their effect on defect density [42]. They demonstrated a ten-fold improvement in defect rate by reducing the drop volume from 1.5 pL to 0.9 pL when nanoimprinting with a 28 nm half pitch imprint mask. They also demonstrated a 100 fold improvement in defect rate by increasing the spread time from 0.7 seconds to 1 second. Thus, non-fill defectivity needs to be considered in the context of throughput [43].

Conducting experiments to identify optimum droplet size and arrangement for different template patterns can be expensive and laborious. Previously, modeling and simulation has been effective in studying fluid behavior and gas trapping during droplet spreading in SFIL. Colburn *et al.* studied the spreading of droplets between a template and a substrate for UV imprint lithography under several template control schemes [50]. They proposed models for pressure distribution and imprint time for the droplets as the template is actuated with a fixed velocity, fixed pressure or constant applied force. Reddy *et al.* presented a dynamic, multi-drop simulation based on lubrication theory and simulated spreading of up to 49 drops with a pattern-free template [51]. Various mechanisms for interface advancement have been described to predict incomplete feature filling leading to air trapping. Local effect of sharp features on interface advancement with patterned template has been explored [57, 113, 114]. Chauhan *et al*. analyzed the diffusion of gas entrapped in the features through liquid imprint resist and found that the absolute time for diffusion of a gas, entrapped in features is very short and gas diffusion is not a cause for non-filling of features during the SFIL [47].

We simulate multi-drop spreading in SFIL with a pattern-free template to study the effect of various factors such as droplet size, droplet arrangement, droplet placement error, gas diffusion that influence throughput and defectivity in the SFIL process. We explore three droplet arrangements: (a) square and (b) hexagonal and (c) modified hexagonal (as shown in Figure 3.2). We also study the effect of error in droplet placement by the inkjet dispenser on the imprint time for different droplet sizes. For the same final RLT, if the size of the droplets is reduced, more droplets need to be dispensed in order to fill the template completely. We perform simulations with up to 1024 droplets. The objective is to understand the effect of droplet arrangement, droplet placement accuracy and drop size on throughput and identify the optimum droplet arrangement for minimum throughput. In order to understand defectivity in SFIL, we analyze non-fill defects in SFIL and propose a model to predict the defect size based on gap height and imprint time. We also propose a model to study the diffusion of gas encapsulated between droplets into the resist and identify parameters which determine whether the defect size is controlled by gas diffusion or hydrodynamic spreading. Studying these factors can help us optimize the SFIL process and significantly improve the throughput and defect rate.

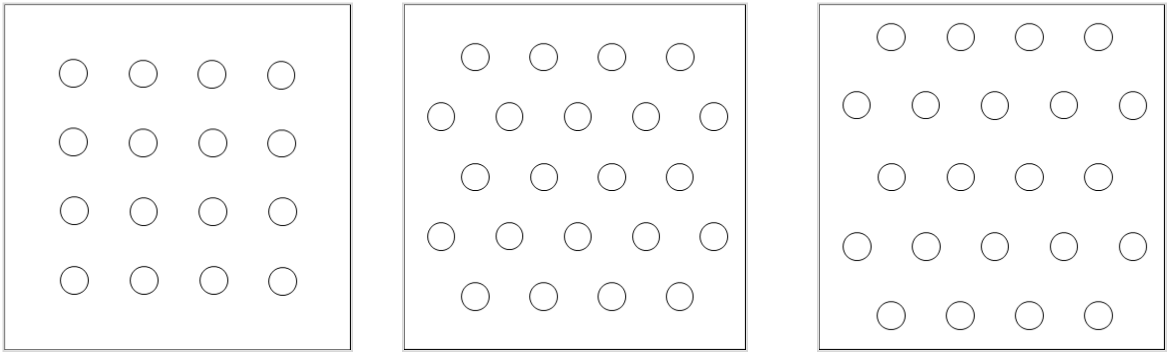
(a) (b) (c)

Figure 3.2: Schematic showing top view of droplets on a substrate. The droplets are dispensed in (a) square and (b) hexagonal and (c) modified hexagonal arrangements.

3.2. SIMULATION METHOD

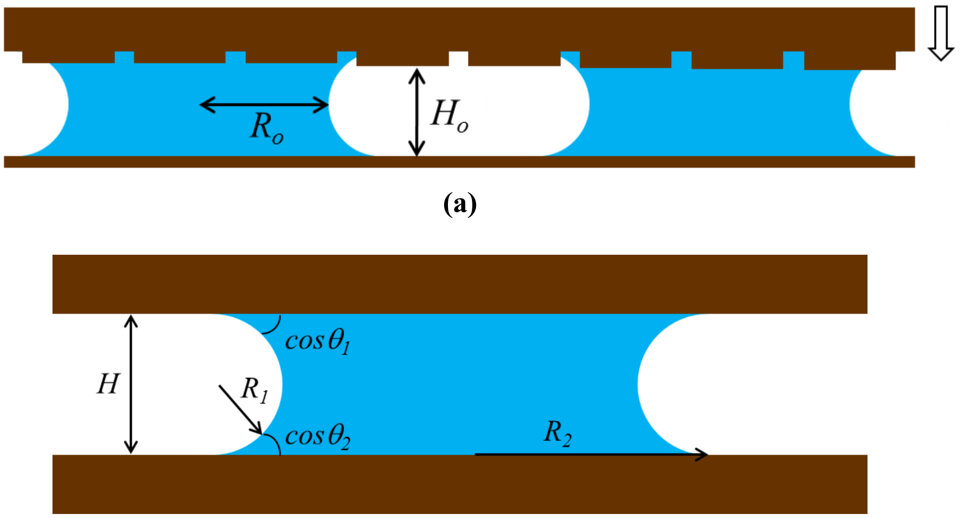

Figure 3.3: (a) Droplets between a substrate and a template. The initial radius of the drop is R_o and the initial height is H_o. (b) Schematic shows the radius of the liquid meniscus R_1 and the radius R_2 of one of several droplets between the template and the substrate. H is the gap between the top and bottom surface at any time. θ_1 and θ_2 are the contact angles of the liquid with the top and bottom surface.

A schematic of droplets with initial radius R_o in a gap of height H_o between a template and a substrate is shown in Figure 3.3(a). The template can be controlled to move with a constant velocity, constant pressure or applied force [50]. As the template approaches the substrate, the liquid-air interface of the droplet exerts capillary force on the template. The fluid flow in the gap results in viscous force. This viscous force in the fluid balances the capillary force due to the liquid-air interface and any externally applied force.

The typical size of the template L used in SFIL is 2.5 – 15 cm [42, 115]. During SFIL the gap H between the template and the substrate reduces from a few microns to finally a few nanometers. Thus, the size of the gap for fluid flow is much smaller than the transverse length scale. Reynolds' lubrication theory is a simplified form of Navier-Stokes equations that can be used to describe this flow of thin fluid films[116, 117]. The governing equations describing the pressure and velocity fields in the drop using Reynolds' lubrication theory are

$$\frac{\partial H}{\partial T} = \nabla \cdot \left(\frac{H^3}{12\mu} \nabla P \right), \tag{3.1}$$

$$\mathbf{U} = -\frac{H^2}{12\mu} \nabla P, \tag{3.2}$$

where H is the gap between substrate and template, P is the pressure in the droplet, $\mathbf{U}$ is the vertically averaged fluid velocity and μ is the viscosity of the imprint resist. The pressure distribution in the fluid is calculated using Equation 3.1. The capillary pressure at the droplet interface is used as boundary condition to solve the pressure field. The imprint material used in SFIL is highly wetting and it makes small contact angles θ_1 and θ_2 with the template and the substrate as shown in Figure 3.3(b). The pressure at the liquid-air interface is given by

$$P_{interface} = P_{atm} - \gamma \left(\frac{1}{R_1} + \frac{1}{R_2} \right), \tag{3.3}$$

where R_1 is the radius of the liquid meniscus, R_2 is the radius of the droplet and γ is the surface tension of the imprint. R_1 can be written in terms of gap H as $R_1 = H/\left(cos\,\theta_1 + cos\,\theta_2\right)$. In the imprinting process, the gap H is much smaller than the drop radius R_2, therefore $R_1^{-1} >> R_2^{-1}$. We find that the capillary pressure at the interface depends only on the radius of curvature R_1 and can be written as

$$P_{interface} = P_{atm} - \frac{2\hat{\gamma}}{H}, \tag{3.4}$$

where P_{atm} is the atmospheric pressure, $\hat{\gamma} = \gamma\left(\cos\theta_1 + \cos\theta_2\right)/2$ and γ is the surface tension of the imprint resist. θ_1 and θ_2 are the contact angles made by the fluid with the template and the substrate respectively. Here we assume that SFIL is being carried out in vacuum or in a gas which is highly soluble in imprint material and so the gas release and gas trapping can be neglected. The rate of gas dissolution will be considered later in this chapter. The imprint process begins with the droplets making contact with both the substrate and the template. We also assume that the feature filling is instantaneous as the feature fill time is negligible compared to the time required for the fluid to spread in the gap [47]. The typical values of the parameters used for the SFIL process can be found in Table 3.1.

Table 3.1: Typical values of the parameters used for the SFIL process

Parameter	**Symbol**	**Typical value**
Surface tension	γ	30 dyne/cm
Viscosity	μ	0.003 - 0.005 Pa.s
Template width	L	10 cm
Substrate width	L	10 cm
Feature height	ΔH	10-100 nm
Initial gap	H_o	1 μm
Final gap	H_f	5 nm
Resist contact angle	$\theta_{1,2}$	5 - 10^o
Initial drop height	H_{drop}	1 μm
Initial drop radius	R_o	5 mm (1 droplet, H_{drop} = 1 μm) 500 μm (100 droplets, H_{drop} = 1 μm) 200 μm (1024 droplets, H_{drop} = 1 μm)

The governing equations and boundary condition [Equation (3.1-3.3)] are non-dimensionalized using following characteristic values of the variables: $P_c = 2\hat{\gamma}/H_o$, $H_c = H_o$, $T_c = 6\mu L^2/\hat{\gamma}H_o$, $V_c = \hat{\gamma}H_o^2/6\mu L^2$ and $U_c = \hat{\gamma}H_o/6\mu L$ where H_o is the initial gap. The x and y coordinates are non-dimensionalized using the length of the template L. The dimensionless governing equations are given by

$$\nabla\cdot\left(h^3\nabla p\right) = -v \tag{3.5}$$

$$\mathbf{u} = -h^2\nabla p \tag{3.6}$$

where, $p = P/P_c$, $h = H/H_c$, $v = V/V_c = \partial h/\partial t$ and $\mathbf{u} = \mathbf{U}/U_c$. v is the dimensionless template velocity. The dimensionless pressure boundary condition is

$$p_{interface} = -\frac{1}{h} \tag{3.7}$$

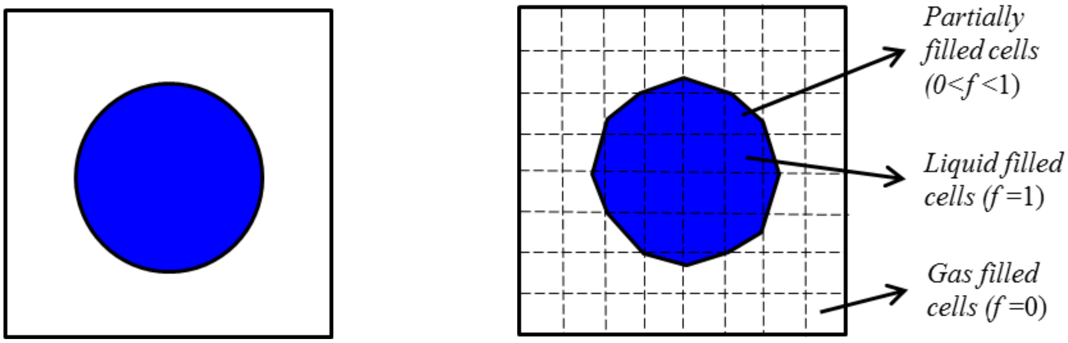

Figure 3.4: Schematic shows one droplet on a substrate (left). The domain is discretized into cells and the fluid content in each cell is tracked based on a characteristic function *f* (right). *f* is 1 and 0 for cells completely filled liquid and gas respectively. For cells partially filled with liquid, *f* is between 0 and 1.

The equations are solved using the Volume of Fluid (VOF) method [118]. The domain is discretized into cells and the fluid content in each cell is tracked based on a characteristic function *f*. This function is defined as 1 for liquid and 0 for gas (as shown in Figure 3.4). A value of *f* between 0 and 1 implies that the cell is partially filled and contains the droplet interface

[119-122]. Several interface reconstruction algorithms were explored to define the droplet interface efficiently and accurately. Efficient least squares VOF interface reconstruction algorithm (ELVIRA) described by Pilliod et al. [119] is used in our simulations because it is second order accurate and fast. In order to solve for the pressure field, Equation (3.5) is discretized using a second order finite difference scheme. The typical grid size for one droplet in the simulation is 64 x 64 cells to ensure volume loss is less than 1%. The simulation is stable if the time step is chosen using the Courant-Friedrichs-Lewy (CFL) condition which states that a fluid particle may not travel further than one cell during one time step, i.e. $|u\Delta t|<\Delta x$.

A guess for template velocity v is used to initiate the simulation. Generalized minimal residual method (GMRES) method [123] which is an iterative method to solve non-symmetric linear systems is used to numerically calculate the pressure field in Equation (3.5) at every time step. The total force on the template is calculated by integrating the pressure over the entire substrate. Then the template velocity is adjusted such that the viscous force balances the capillary force and any externally applied force. The pressure field is then recalculated. Once the pressure field is known, the total fluid fluxes in the x and y directions are determined using Equation (3.6). Immersed boundary methods are used to extrapolate the pressure field and accurately determine the fluid flux at the interfacial cells [124]. Once the velocity field is known, the fluid is advanced using the VOF method and the template is lowered. At every time step, the liquid-air interface is reconstructed based on f. The simulation is stopped once the desired gap is reached and the fluid fills the entire domain.

Simulation of large number of droplets in SFIL is computationally expensive and time consuming since the size of the domain scales as the number of droplets in the process. The pressure calculation has been found to be the slowest step in the simulation using a single processor. A parallel implementation of GMRES method is used for fast computation of the pressure field. The simulation also becomes computationally more expensive as the droplet size increases since droplet interface, velocity flux and pressure need to be calculated on a larger domain. To circumvent this problem and achieve faster simulation, the domain is remeshed with one-fourth of the initial number of cells every time the radius of the droplet doubles.

Simulations are carried out droplets dispensed in square, hexagonal and modified hexagonal arrangements. The droplet placement in a square arrangement is shown in Figure 3.5(a). The shaded region in Figure 3.5(a) shows the droplet-free region between the droplets and the edge of the substrate. This region is 16% of the total imprint area for 100 drops in square arrangement. Figure 3.5(b) shows droplets dispensed in a hexagonal arrangement where $l_h/l_b \approx \sqrt{3}/2$ (=0.866). The figure illustrates that the droplet-free region (shaded) is 26% of the total imprint area. Figure 3.5(c) shows droplets dispensed in a modified hexagonal arrangement where $l_h^*/l_b^* = 0.893$. In this arrangement, the droplet-free region at the edge is reduced by increasing the distance between the droplets. Droplets are added at the corner to reduce the droplet-free region. Figure 3.5(c) shows that the droplet-free region (shaded) at the edge reduces from 26% of the substrate in hexagonal arrangement to 16% in the modified hexagonal arrangement. In all the simulations, the gap between the substrate and the template closes from a gap of $h = 1$ to a final gap of $h = 0.01$. The total volume of droplets in all arrangements is equal to the volume required to fill the gap between the template and the substrate when the desired final gap ($h = h_f = 0.01$) is reached.

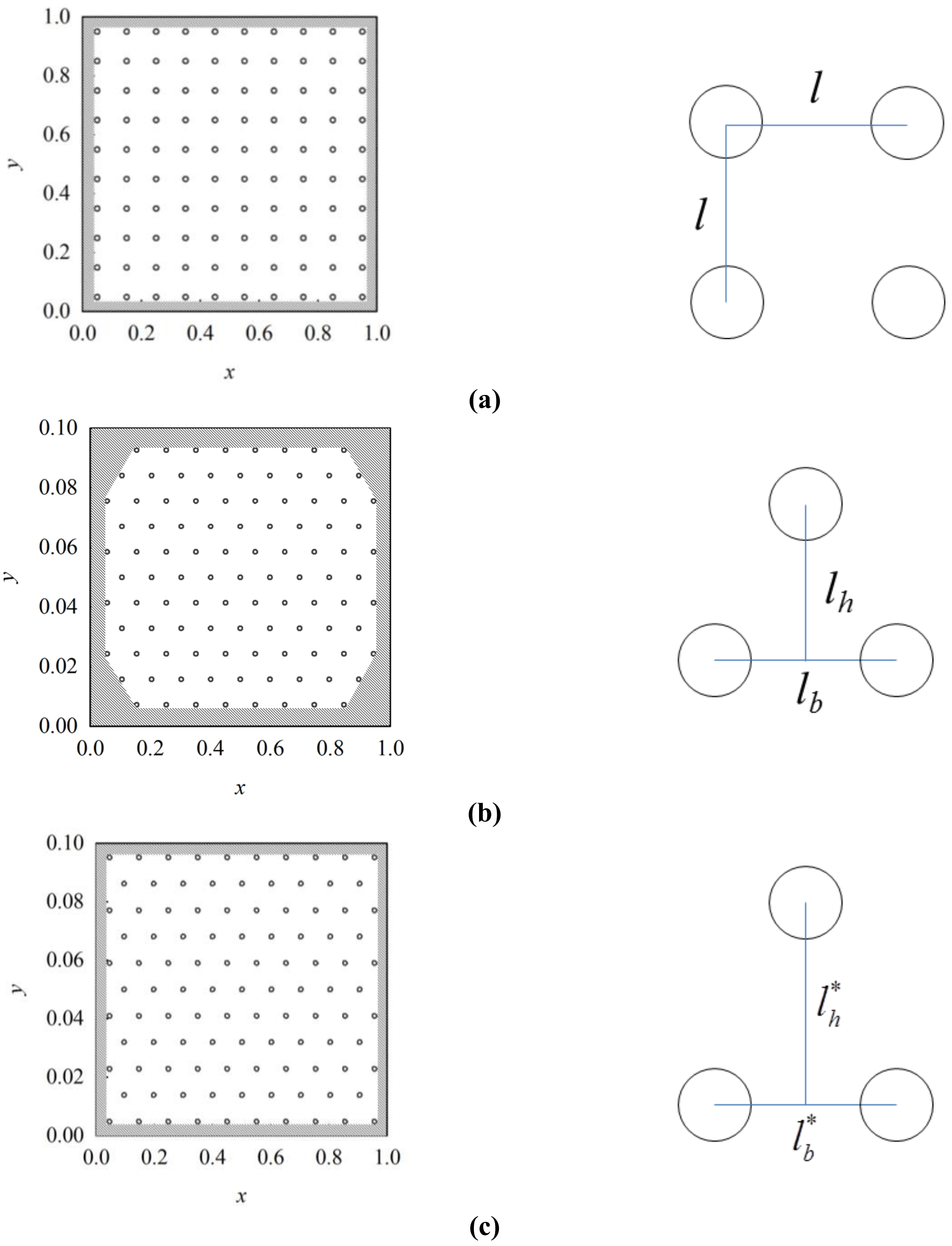

Figure 3.5: Schematic showing top view of 100 droplets dispensed on a substrate. The droplets are dispensed in a (a) square, (b) hexagonal and (c) modified hexagonal arrangement. The shaded region represents the droplet-free region between the droplets and the edge of the substrate. The droplet-free region at the edge is 16%, 26% and 16% of the substrate in the square, hexagonal and modified hexagonal arrangement respectively. The droplet placement in the different arrangements is shown in the right column. The value of l_h/l_b and l_h^*/l_b^* is 0.866 and 0.893 respectively.

3.3. RESULTS

Figure 3.6 shows the spreading of a single droplet, including the location of the interface and the pressure field within the droplet. The droplet spreads on the substrate as a pattern-free template approaches the substrate. The template is driven by the capillary forces in the droplet and has no external force acting on it. The pressure is negative at the liquid-air interface because of the capillary pressure and positive at the center because of the viscous component of the pressure. The capillary pressure is very low towards the end when the gap is very small. At all time, the net viscous force balances the net capillary force creating a net zero force on the template.

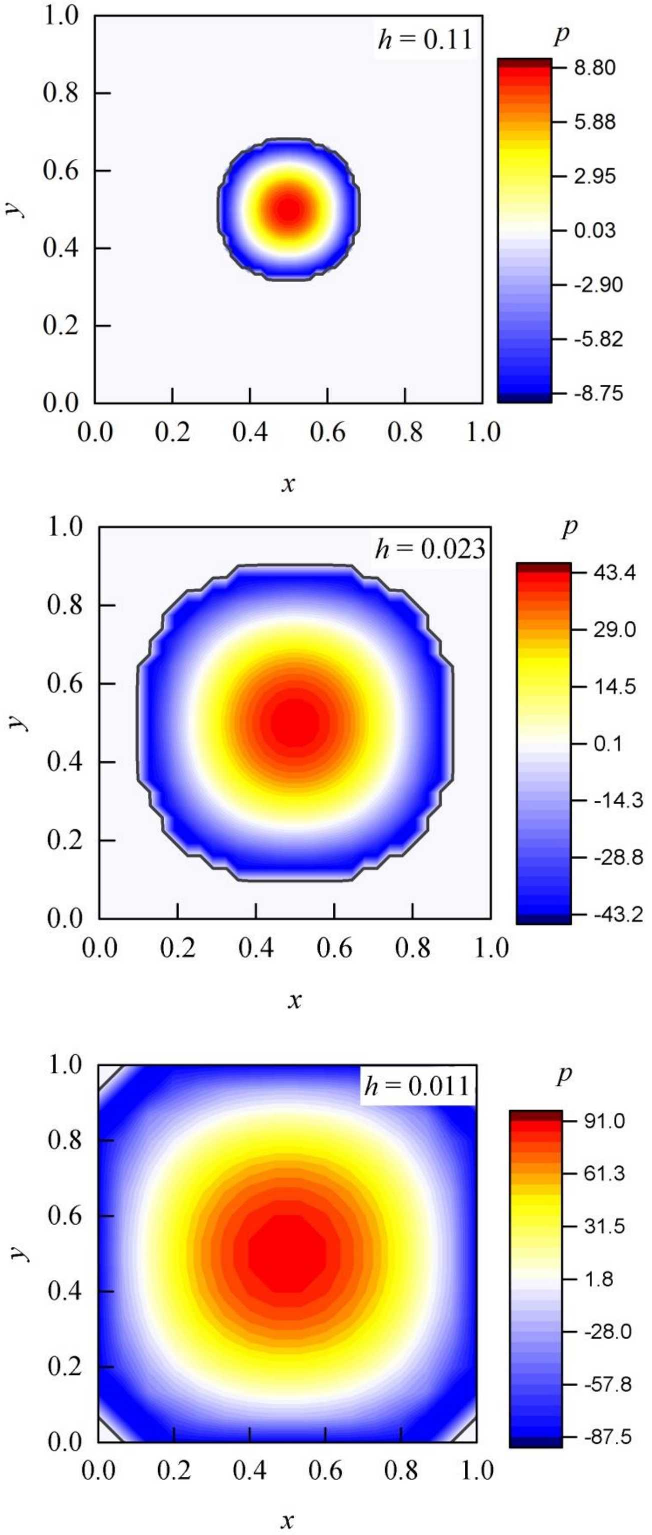

Figure 3.6: Contour map showing pressure field for a drop spreading on a substrate at *h* = 0.11, *h* = 0.023 and *h* = 0.011. The template is pattern-free and has net zero force acting on it.

The simulation is repeated for multi-drop SFIL with pattern-free template with zero force acting on it. Figure 3.7 shows spreading of about 100 droplets that are dispensed in (a) square, (b) hexagonal and (c) modified hexagonal arrangement. The desired final gap is $h = 0.01$. The droplets spread as the gap between the template and the substrate closes. At very small gap, the neighboring droplets merge together and spread to the edge of the substrate forming unfilled edge regions. Figure 3.7 (a), (b) and (c) show these unfilled edges for the three arrangements. We find that the unfilled edge in the hexagonal arrangement is significantly larger than the unfilled edge in the square or modified hexagonal arrangement. At $h = 0.01$, the gap is completely filled with the resist.

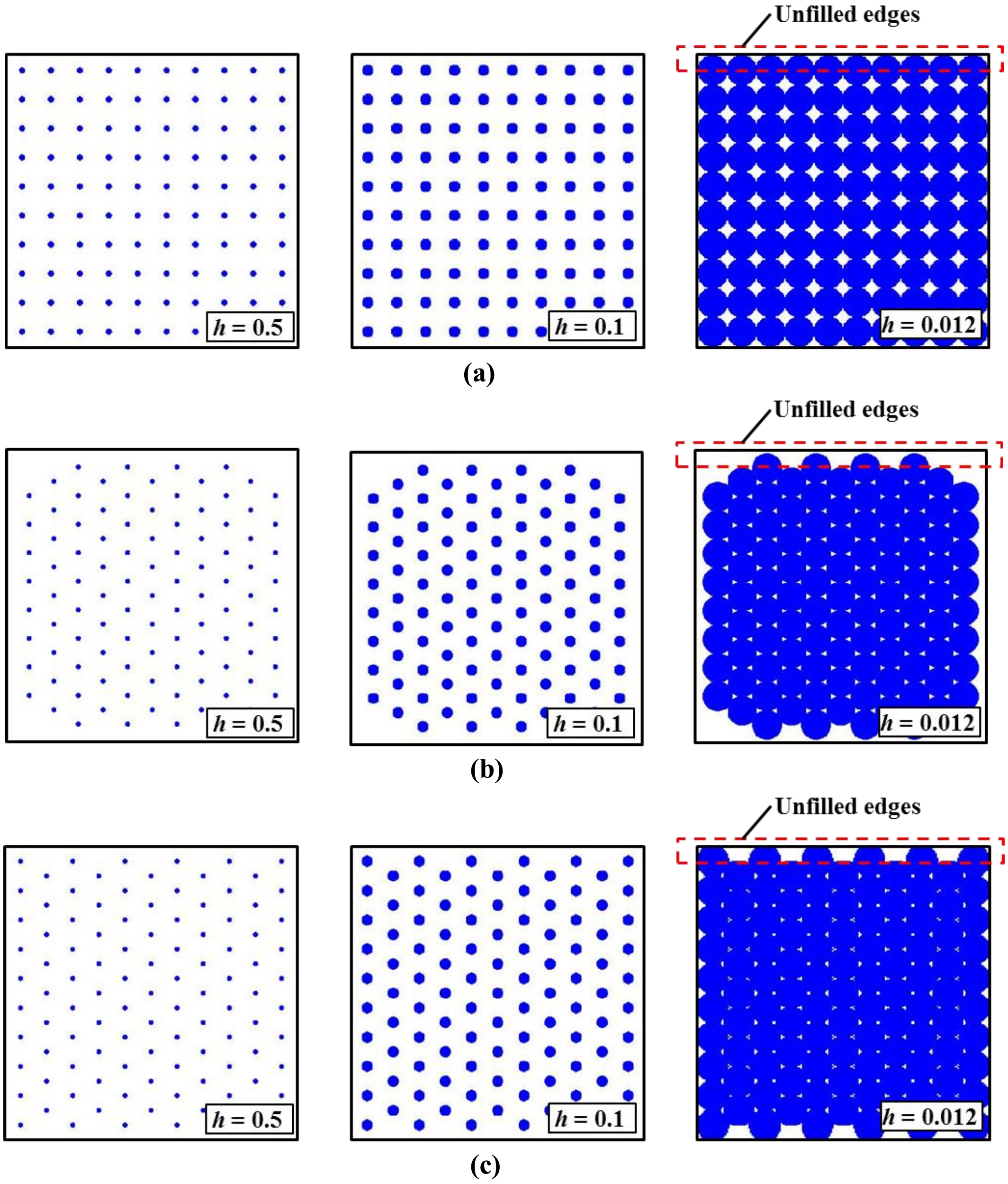

Figure 3.7: Simulation of SFIL with about 100 droplets dispensed in (a) square arrangement (b) hexagonal arrangement and (c) modified hexagonal arrangement. The droplets reach the edge of the substrate towards the end of the process creating unfilled edges at small gaps. The gap is completely filled with resist at *h* = 0.01.

3.3.1 Throughput for Square, Hexagonal and Modified Hexagonal Droplet Arrangement

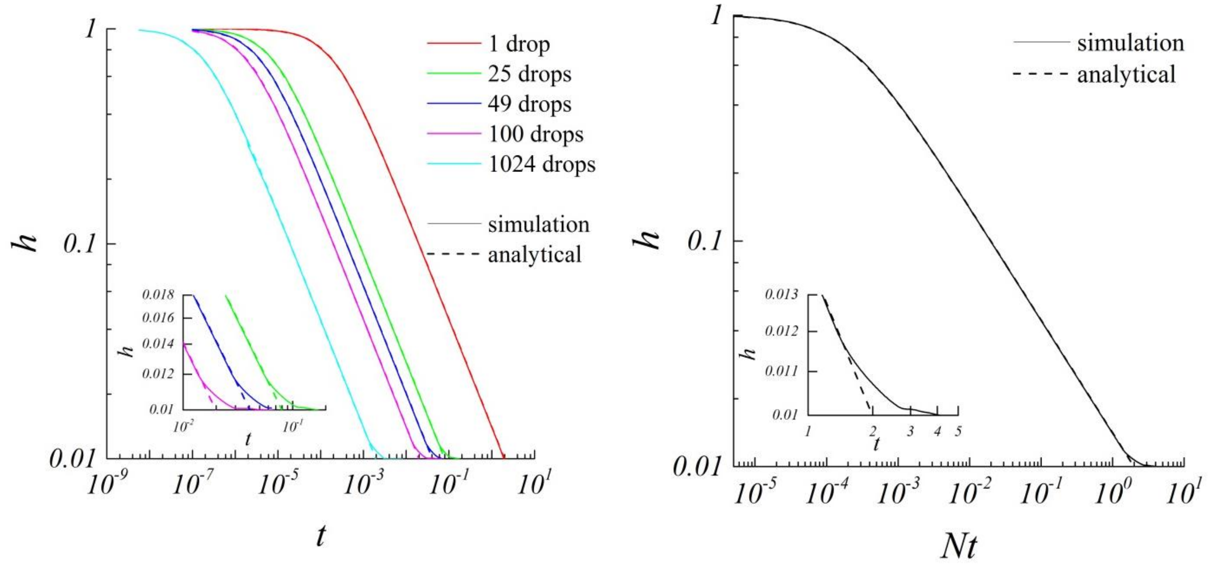

(a) **(b)**

Figure 3.8: (a) Imprint time for multiple droplets dispensed in a square arrangement. The template is pattern-free and has net zero force acting on it. The analytic solution for the gap height is shown in dashed line. The inset plot shows the imprint time close to the time of droplet merging. (b) The plot collapses into a single curve when gap height *h* is plotted against *Nt*. This shows that imprint time scales as 1/*N*. Thus, the total imprint time decreases as number of drops increases.

Figure 3.8 shows the gap height h as a function of time t for SFIL with square droplet arrangement. As the number of droplets is increased, the overall imprint time reduces. An analytical expression for the gap height h as a function of time t has previously been derived for multiple droplets spreading on a substrate with net zero force on the template [50, 51]. Governing equation for pressure distribution is described in Equation (3.1). Integrating Equation (3.1) and applying the pressure boundary condition given by Equation (3.4), we find that the dimensionless pressure in a single droplet at a distance $\bar{r}$ from the center of the droplet is given by

$$P = -\frac{1}{h} + \frac{v}{4h^3}\left(r^2 - \bar{r}^2\right), \tag{3.8}$$

where, r is the droplet radius. The dimensionless force f_{app} applied on the template can be calculated by integrating the pressure over the template. f_{app} is found to be

$$f_{app} = \left(-\frac{1}{h} + \frac{vr^2}{8h^3} \right) N\pi r^2 , \tag{3.9}$$

where, N is the total number of drops. For a net zero force on the template, $f_{app} = 0$. The template velocity v for zero force on the template is given by

$$v = \frac{8h^2}{r^2} . \tag{3.10}$$

Since the total volume of the droplets q is equal to the volume of resist required to fill the gap at $h = h_f$,

$$q = N\pi r^2 h = h_f . \tag{3.11}$$

Thus, v can be written as

$$v = 8N\pi \frac{h^3}{h_f} . \tag{3.12}$$

Putting $v = -\frac{dh}{dt}$ and integrating we find that the time t can be written in terms of gap h as follows

$$t = \frac{h_f}{16\pi N} \left(\frac{1}{h^2} - 1 \right) . \tag{3.13}$$

The gap h from the analytical solution is shown in Figure 3.8 by dashed lines. Figure 3.8(a) shows that the imprint time for a single drop from simulation results matches the analytical solution exactly. Figure 3.8(b) shows that the plot for gap height h against Nt results in a single curve for different number of droplets suggesting that t scales as $1/N$. Thus, the total imprint time decreases as number of drops increases. However, this analytical expression is only valid for droplets spreading without merging. We find that, as the droplets merge at very small gap height, the simulated imprint time starts to deviate from this analytical solution. This deviation can be attributed to the formation of a larger droplet due to droplet merging. From Equation (3.11) and (3.12), we find that the template velocity scales as

$$v \sim \frac{1}{r^6}. \tag{3.14}$$

As the droplets merge, the droplet size increases and r becomes large. Increase in r results in a decrease in template velocity. Thus, after merging, the resist flows more slowly resulting in an overall imprint time which is higher than that predicted by the analytical solution.

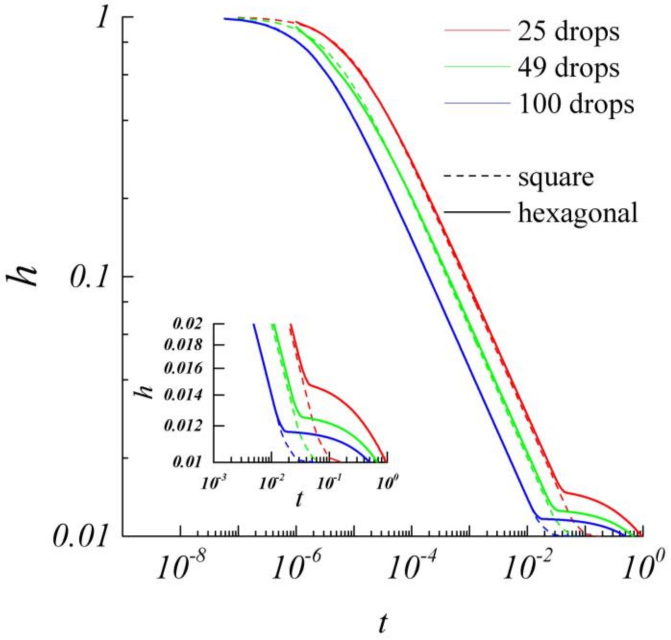

Figure 3.9: Imprint time for multiple droplets dispensed in a hexagonal arrangement. The template is pattern-free and has net zero force acting on it. The imprint time for droplets arranged in a square arrangement is shown in dashed line. The inset plot shows the imprint time close to the time of droplet merging.

Figure 3.9 shows the gap height h as a function of imprint time t for hexagonal droplet arrangement. The imprint time for the same number of droplets in square arrangement is shown in dashed lines. Similar to square arrangement, the time scales as $1/Nh^2$ except at the end of the process when the gap is very small (as shown in the inset of Figure 3.9). For the same number of droplets, the overall imprint time for hexagonal arrangement is found to be longer than that for square arrangement. This can be attributed to the different size of unfilled edge regions in square arrangement (shown in Figure 3.7(a) (right)) and hexagonal arrangement (shown in Figure 3.7(b) (right)). A plot of the area of the unfilled edge as function of *h* for square and hexagonal droplet arrangement is shown in Figure 3.10. The unfilled area is larger in hexagonal arrangement compared to square arrangement. In the previous section, we discussed that the resist spreads slowly after droplet merging due to reduced template velocity. After droplet merging, the resist keeps spreading until it reaches the edge of the substrate and fills the entire gap. The larger unfilled region in hexagonal arrangement requires longer time to fill compared to the square arrangement resulting in longer overall imprint time. Thus the combined effect of droplet merging and unfilled edges leads to longer overall imprint time for hexagonal arrangement.

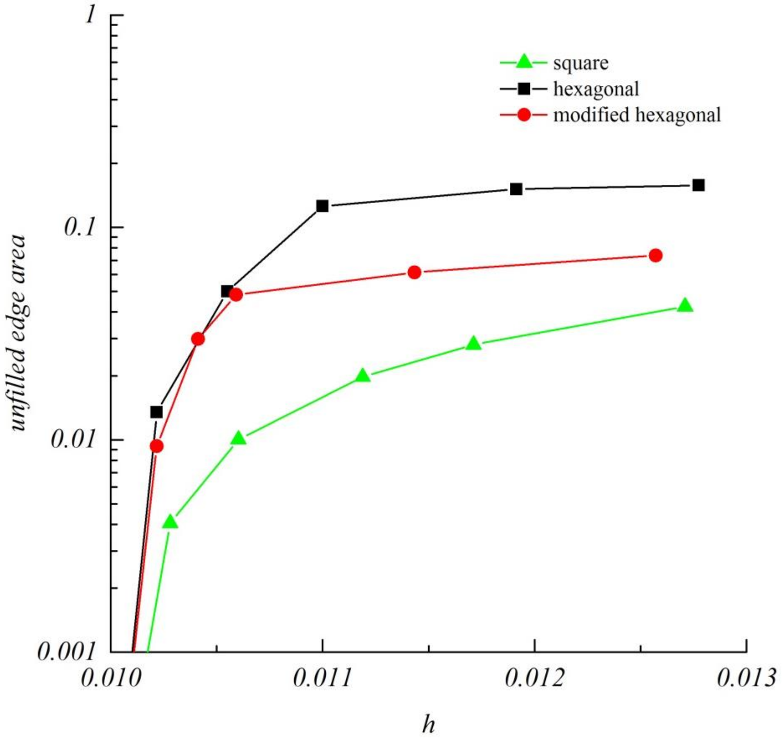

Figure 3.10: The area of unfilled edge region for square, hexagonal and modified arrangement of droplets at different gap heights. The hexagonal arrangement has the largest unfilled edge area while square arrangement has the smallest area.

By studying the droplet spreading in square and hexagonal arrangement of droplets, we find that droplet merging and the size of the unfilled edge region have a significant impact on the imprint time. A modified hexagonal arrangement is proposed in which the size of the unfilled region has been reduced by spreading the droplets in hexagonal arrangement towards the edges and adding more droplets at the corner. The area of droplet-free region between the droplets and the edge of the substrate in modified hexagonal arrangement of droplets is 16% of the total imprint area compared to 26% in hexagonal arrangement (as shown in Figure 3.5). Figure 3.11 shows the imprint time for SFIL with about 100 droplets dispensed in square, hexagonal and modified hexagonal arrangement. We find that the modified hexagonal arrangement provides a 0.56 times reduction in imprint time compared to the hexagonal arrangement. However, the imprint time is still longer than square droplet arrangement. The unfilled edge is largest for hexagonal arrangement and smallest for the square arrangement (as shown in Figure 3.10). Thus by reducing unfilled edge region, the overall imprint time can be reduced. The square droplet arrangement is found to be the optimum drop dispensing pattern to achieve minimum imprint time.

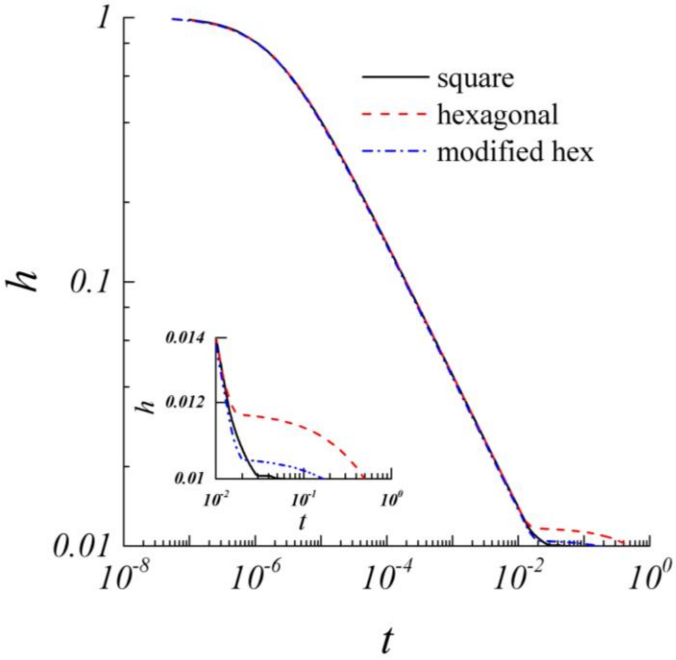

Figure 3.11: The gap height *h* as a function of imprint time *t* for about 100 droplets dispensed in square (solid), hexagonal (dash) and modified hexagonal (dash-dot) arrangements. The inset plot shows the imprint time close to the time of droplet merging. The modified hexagonal arrangement provides a 0.56 times reduction in imprint time compared to hexagonal arrangement. The overall imprint time is least for droplets dispensed in a square arrangement.

3.3.2. Effect of Droplet Placement Error

There is error in droplet placement during dispensing based on the size of the droplet and distance between the imprint head from the substrate. This error can manifest itself in droplet spreading and overall imprint time. The normalized placement error ε is defined as

$$\varepsilon = \frac{\text{error in droplet placement}}{L}, \tag{3.15}$$

where L is the length of the substrate. Figure 3.12 shows droplets (blue) placed in a square arrangement with ε = 0.02. Droplets dispensed with zero placement error are shown with red circles in Figure 3.12.

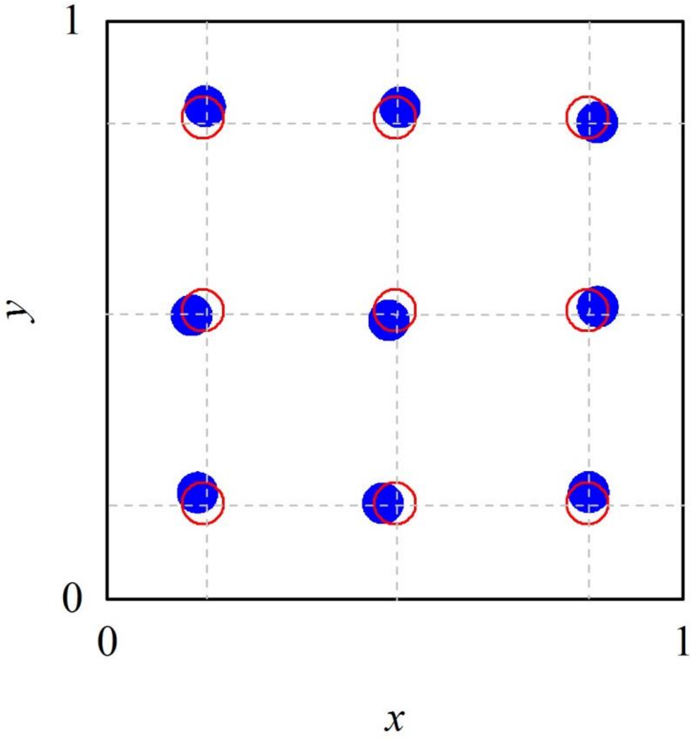

Figure 3.12: Blue circles show droplets dispensed in a square arrangement with a normalized placement error ε = 0.02. Red circles show droplets dispensed in a square pattern with ε = 0.

The imprint time required for the gap height to close from h = 1 to h = 0.01 is simulated for droplets dispensed in a square arrangement with different values of placement error. Figure 3.13 shows spreading of 81 droplets dispensed in a square arrangement with ε = 0.02. Unlike square or hexagonal arrangements, the unfilled regions are randomly spread over the substrate due to the droplet placement error as shown in Figure 3.13. The resist completely fills the gap between the template and the substrate at $h = 0.01$.

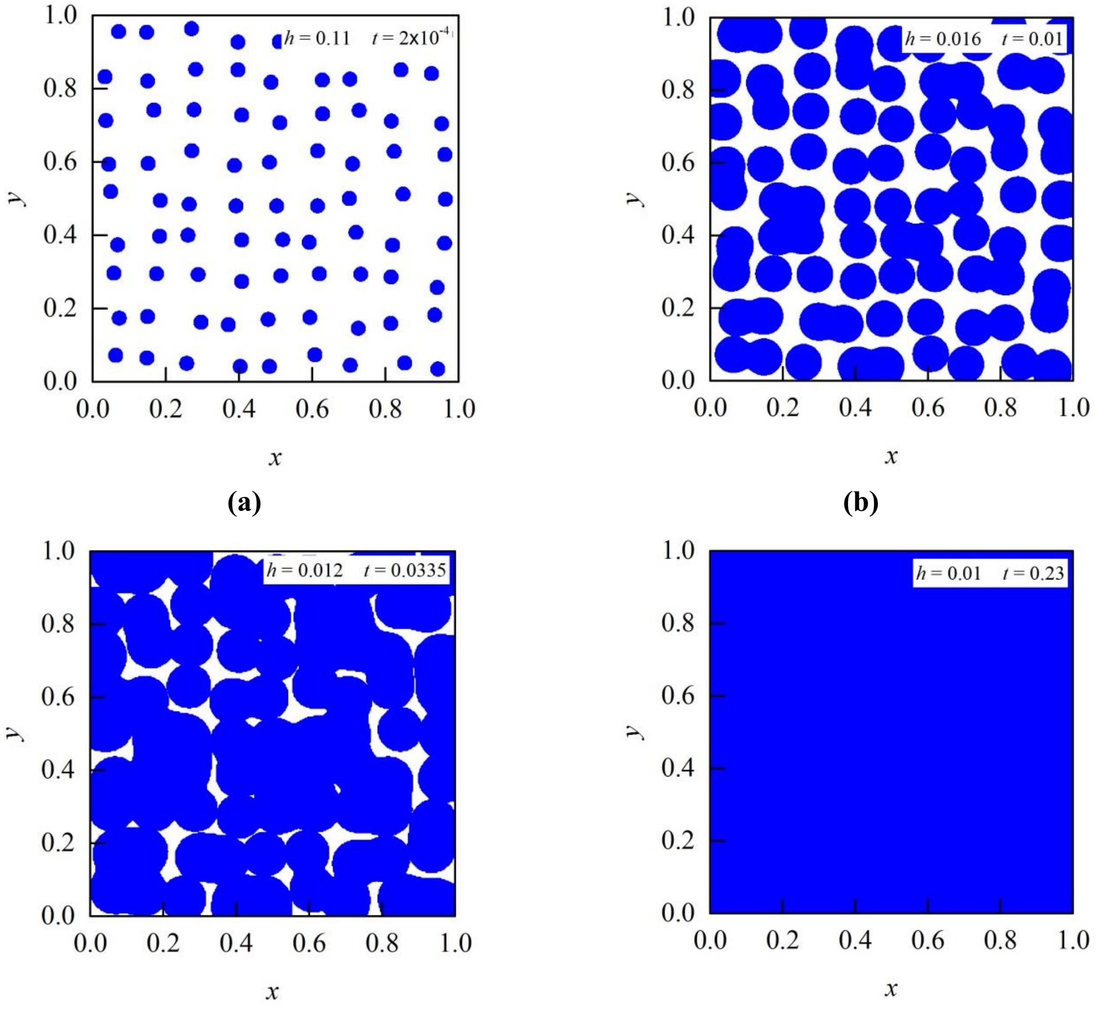

(a) (b)

(c) (d)

Figure 3.13: Simulation of SFIL with 81 droplets dispensed in a square arrangement with a droplet placement error $\varepsilon = 0.02$ at (a) $t = 2\text{x}10^{-4}$, (b) $t = 0.01$, (c) $t = 0.0335$ and (d) $t = 0.23$. The gap closes from $h = 1$ to $h = 0.01$.

Figure 3.14 shows gap height as a function of time for different values of droplet placement error. Figure 3.15 shows the overall total imprint time (t_i) required for the gap to close from $h = 1$ to $h = 0.01$ for different values of ε and number of droplets N. We find that the imprint time increases as the placement error increases. As the placement error increases, the droplets start merging sooner creating larger droplets. Since larger droplets lead to longer imprint time, early droplet merging leads to longer imprint time. Figure 3.16 shows the ratio $t_{i,\varepsilon}/t_{i,0}$ as function of ε where $t_{i,\varepsilon}$ is the imprint time with droplet error placement ε. $t_{i,0}$ is the imprint time with error placement $\varepsilon = 0$. We find that for a fixed ε, $t_{i,\varepsilon}/t_{i,0}$ is larger for higher number of droplets indicating that the imprint time is more sensitive to ε when droplet size is smaller. The imprint time increases significantly for $\varepsilon > 10^{-4}$ for more than 100 droplets.

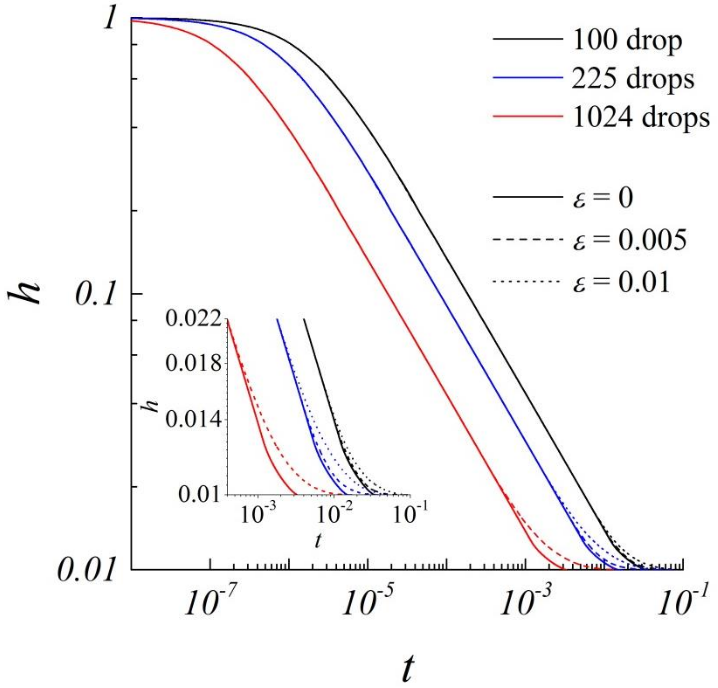

Figure 3.14: Gap height *h* as a function of imprint time *t* for multiple droplets dispensed in a square arrangement with droplet placement error ε = 0, 0.005 and 0.01. The inset plot shows the imprint time close to the time of droplet merging. Larger error in droplet placement leads to longer imprint time.

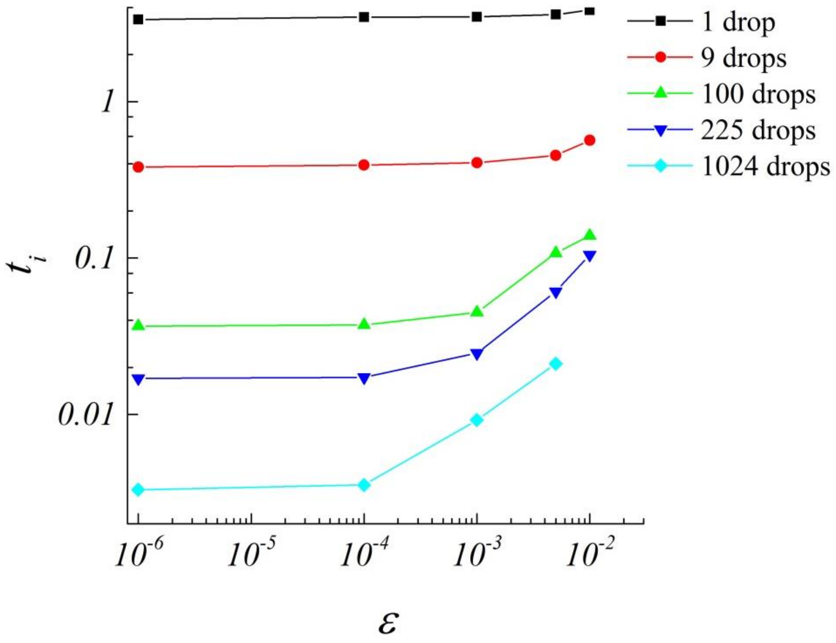

Figure 3.15: The total imprint time t_i required for the gap height to reduce from h = 1 to h = 0.01 as a function of droplet placement error ε. The total imprint time increases as ε increases.

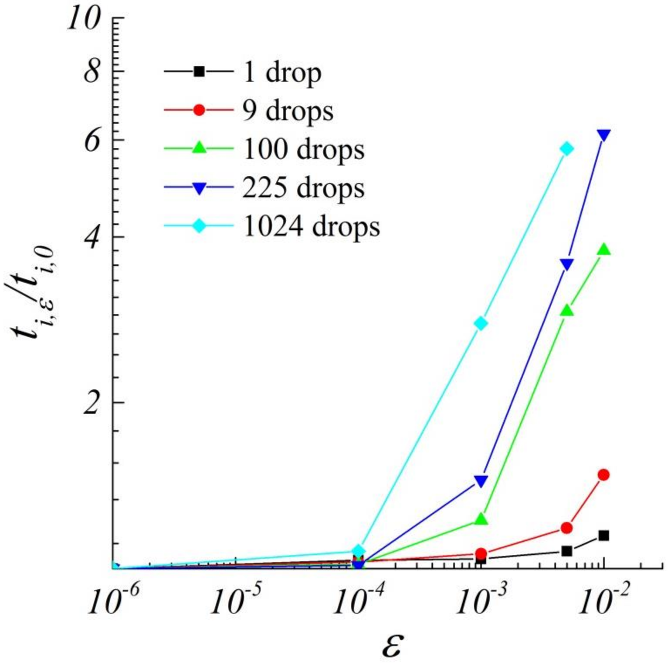

Figure 3.16: Figure shows the ratio $t_{i,\varepsilon}/t_{i,0}$ as function of ε where $t_{i,\varepsilon}$ is the imprint time required for the gap to close from h = 1 to h = 0.01 with droplet error placement ε. $t_{i,0}$ is the imprint time with ε = 0. For the same ε, $t_{i,\varepsilon}/t_{i,0}$ is larger for higher number of droplets. This indicates that the SFIL is more sensitive to error in droplet dispensing when smaller droplets are used.

3.3.3. Defect Analysis

As the gap between the template and the substrate closes, the droplets spread and start merging with each other. For square arrangement, droplets begin merging at $h = 4h_f/\pi$. At this point, multiple unfilled regions are formed on the substrate. Figure 3.17 shows these unfilled regions for simulation of SFIL with 100 drops in square arrangement at $h = 4h_f/\pi$. As the gap closes further, these unfilled regions become smaller until the entire substrate is covered by the resist. Imprint time lower than the time required for the resist to spread over the entire substrate leads to non-filling defects in the final pattern. These defects can be classified into two types: unfilled edges which are formed at the edge of the substrate and unfilled pockets which are pockets of gas encapsulated between the droplets. The unfilled edges and pockets formed simulated with 100 droplets are shown in Figure 3.17. In these simulations, droplet spreading is due to hydrodynamic effects and gas diffusion is neglected.

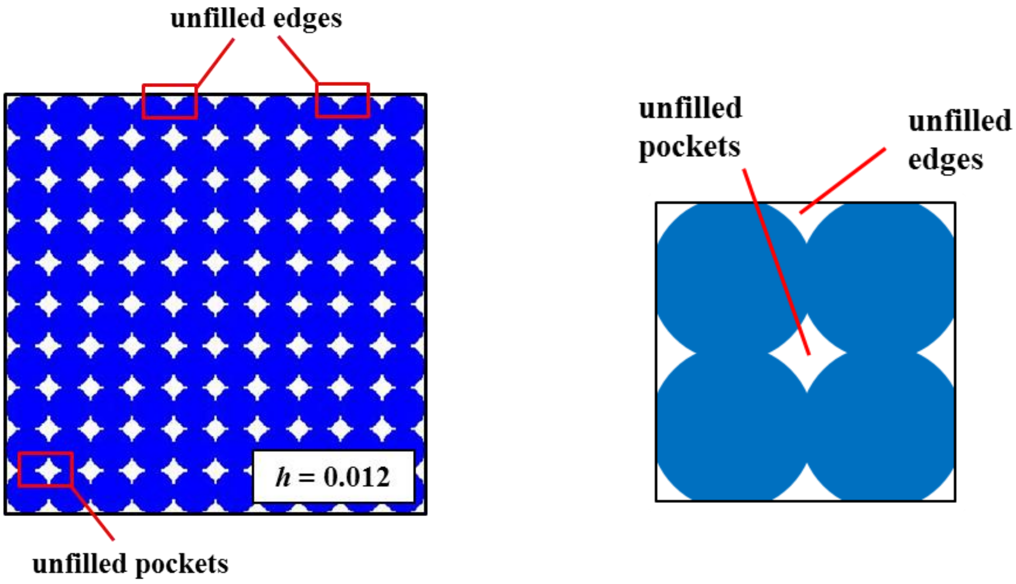

(a)

(b)

Figure 3.17: (a) Figure shows 100 droplets in square arrangement in SFIL. At $h = 4h_f/\pi = 0.012$, the droplets come in contact with each other to form unfilled edges and pockets. (b) Schematic shows unfilled pockets and edges in SFIL. The size of unfilled edges is half of the size of the pockets.

For SFIL with N droplets, the number of unfilled pockets, $n_{pockets}$ is

$$n_{pockets} = \left(N^{1/2} - 1\right)^2 \tag{3.16}$$

and number of unfilled edge defects, n_{edge} is

$$n_{edge} = 4N^{1/2}\,. \tag{3.17}$$

The total number of defects is given by

$$n_{defects} = n_{edge} + n_{pockets} = \left(N^{1/2} + 1\right)^2. \tag{3.18}$$

The dimensionless volume of each unfilled pocket, $s_{pockets}$ is

$$s_{pockets} = N^{-1}\left(h - h_f\right) \tag{3.19}$$

and the dimensionless volume of each unfilled edge defect, s_{edge} is

$$s_{edge} = 0.5N^{-1}\left(h - h_f\right) \tag{3.20}$$

From Equations (3.16)-(3.20), we find that average volume of defects, s_d is

$$s_d = \frac{n_{pockets}s_{pockets} + n_{edge}s_{edge}}{n_{pockets} + n_{edge}} = \frac{h - h_f}{\left(N^{1/2} + 1\right)^2} \tag{3.21}$$

The model shows that the number of defects increase and the defect size reduces as the number of droplet increases.

Figure 3.18 shows the volume of unfilled edges, pockets and average volume of unfilled defects formed in SFIL with 100 drops in a square arrangement from simulations compared with the results from Equations (3.19)-(3.21). The simulations strongly agree with the predicted modeling results. This model can be used to predict the size and number of defects at any given time or gap height.

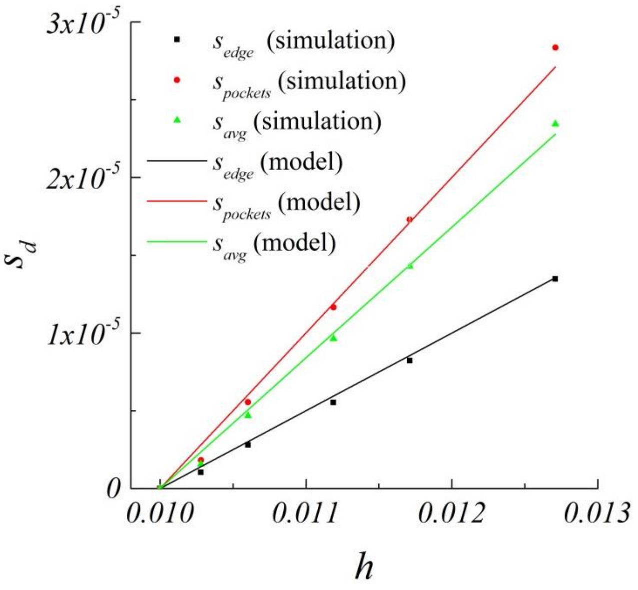

Figure 3.18: Figure shows the volume of unfilled edges (s_{edge}), pockets ($s_{pockets}$) and average volume of unfilled regions (s_d) formed in SFIL with 100 drops in a square arrangement from simulations and the predicted results from modeling.

Figure 3.19 shows s_d at different gap height and time from simulation of SFIL with droplets dispensed in a square arrangement. For any number of droplets, the defects are formed at $h = 4h_f/\pi$ (= 0.0127 for h_f = 0.01) and their volume reduces as the gap closes ultimately becoming zero at h = 0.01 as shown in Figure 3.19(a). s_d from simulations is compared with the results from Equation (3.21) in Figure 3.19(a) (right). There is good agreement between the simulations and analytical solution confirming that defect size reduces as the number of droplets increases.

A plot of s_d with t in 3.19 (b) (right) shows that

$$\left(N^{1/2}+1\right)^2\left(s_d - s_d^o\right) \sim 10^{-3} N\left(t_o - t\right), \tag{3.22}$$

where s_d^o is the volume of the defect at the time of formation $t = t_o$. Since, the defect is formed at $h = 4h_f/\pi$, from Equation (3.21) we find that

$$s_d^o = \left(\frac{4}{\pi} - 1\right)\frac{h_f}{\left(N^{1/2}+1\right)^2} = \frac{0.273h_f}{\left(N^{1/2}+1\right)^2}, \tag{3.23}$$

From Equations (3.22) and (3.23), the total time Δt_{fill} required for the defect to fill completely can be written as

$$\Delta t_{fill} = t_o - t \sim \frac{s_d^o \left(N^{1/2}+1\right)^2}{10^{-3}N} = \frac{273}{N} h_f \ . \tag{3.24}$$

Thus, Δt_{fill} reduces as the number of droplets increases. The defect volume is non-dimensionalized by L^2H_o and t by characteristic time, $T_c = 6\mu L^2 / \hat{\gamma} H_o$. For SFIL with substrate length L = 10 cm, initial gap height of H_o = 1 μm, resist viscosity μ = 0.001 Pa.s and surface tension γ = 70 dyne/cm, T_c = 857 seconds and $L^2H_o = 10^{-8}$ m^3. Figure 3.19 shows that for SFIL with 100 droplets, a defect of volume 2.34x10^{-13} m^3 is formed at gap height H = 12.7 nm and time T_o = 10.52 seconds. The defect fills in about 20 seconds as the resist spreads. For SFIL with 1024 droplets, a defect of volume 2.77x10^{-14} m^3 is formed at H = 12.7 nm and T_o = 1.02 second. This defect fills in about 1 second. The time required to fill the defects as predicted by Equation (3.24) is 23 seconds and 2.28 seconds for 100 droplets and 1024 droplets respectively. These results are close to the results from the simulations.

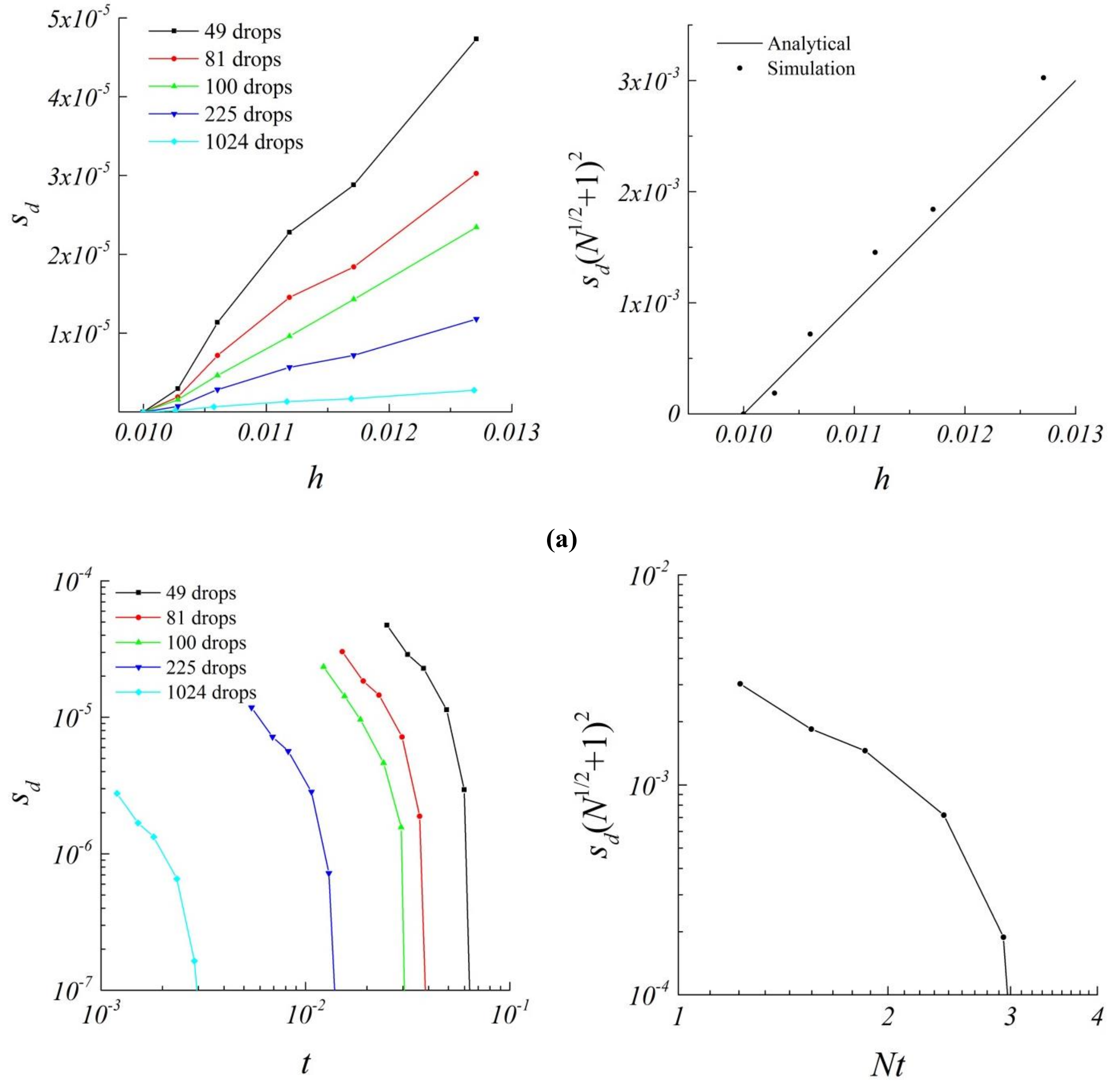

(a)

(b)

Figure 3.19: Figure shows average defect volume s_d at different (a) gap height and (b) time for droplets dispensed in a square arrangement. The defect volume reduces as the gap reduces ultimately becoming zero at h = 0.01. The defect size also decreases as the number of droplets is increased. The reduction in defect size is purely due to hydrodynamic spreading of the resist as these simulation results do not account for gas diffusion.

3.3.4 Gas Diffusion in Non-fill Defects

The simulations assume that diffusion of gas in the encapsulated pockets is faster than the hydrodynamic spreading of the resist. Thus, the instantaneous size of the defects is dictated only by hydrodynamic spreading of the resist. However, if the rate of gas diffusion is slower than the hydrodynamic spreading of the resist, the effect of gas diffusion on the size of the defects needs to be taken into account. We model this gas diffusion to determine whether the defect size is dictated by gas diffusion or hydrodynamic spreading of the resist.

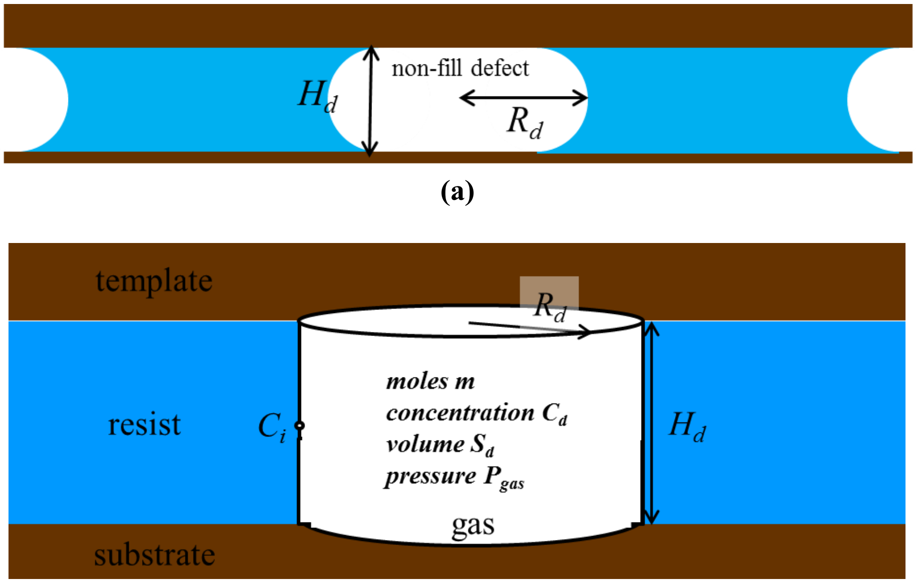

(a)

(b)

Figure 3.20: (a) Schematic showing a pocket defect trapped between droplets. (b) The pocket defect is modeled as a cylinder of radius R_d and height of H_d. The gas concentration is C_d inside the defect and C_i at the gas-liquid interface.

Figure 3.20 shows a schematic for a pocket defect formed during the SFIL process. The defect can be modeled as a cylinder of radius R_d and height H_d. C_d is the gas concentration inside the defect, m is the number of moles and C_i is the gas concentration at the gas-liquid interface.

The gas-liquid interfacial area A_d and defect volume S_d are given by

$$A_d = 2\pi R_d H_d \, . \tag{3.25}$$

and

$$S_d = \frac{m}{C_d} = \pi R_d^2 H_d \tag{3.26}$$

The volume of the total gap between the template and the substrate L^2H is given by

$$L^2 H = n_{defects} S_d + L^2 H_f \tag{3.27}$$

where $n_{defects}$ is the number of defects given by Equation (3.18) and $L^2 h_f$ is the total liquid volume in the gap at any time. Rearranging, we get

$$\left(\frac{R_d}{L}\right)^2 = \frac{H_d - H_f}{n_{defects} \pi H_d} \tag{3.28}$$

The rate at which moles of gas in the defect deplete can be written as

$$\frac{dm}{dT} = -DA_d \left.\frac{dC}{dX}\right|_{int\,erface}, \tag{3.29}$$

where D is the diffusion constant. The concentration gradient profile in the resist can be written as [125]

$$\left.\frac{dC}{dX}\right|_{int\,erface} = \frac{C_i - C_{bulk}}{R_d}, \tag{3.30}$$

where C_{bulk} is the gas concentration in the bulk of the liquid. C_{bulk} can be assumed to be negligible. C_i can be determined using Henry's law [47]:

$$C_i = C_d \frac{RT_s}{k_H}, \tag{3.31}$$

where R is the gas constant, T_s is the surrounding temperature and k_H is the Henry's law constant. Applying Equations (3.31) and (3.30) into (3.29), we find

$$\frac{dm}{dT} = -DA_d \frac{m}{S_d} \frac{RT_s}{R_d k_H} \tag{3.32}$$

Applying Equation (3.25) in Equation (3.32), we find

$$\frac{dm}{dT} = -2\pi \frac{mH_d}{S_d} \frac{DRT_s}{k_H} \tag{3.33}$$

Using the ideal gas law, the gas pressure P_{gas} is given by

$$P_{gas} = \frac{mRT_s}{S_d} \tag{3.34}$$

We can non-dimensionalize Equations (3.26), (3.28), (3.33) and (3.34) using $r_d = R_d/L$, $h_d = H_d/H_c$, $p_{gas} = P_{gas}/P_c$, $t = T/T_c$, and $s_d = S_d/L^2H_o$. The characteristic values of the variables H_c, P_c and T_c are given by $H_c = H_o$, $P_c = 2\hat{\gamma}/H_o$ and $T_c = 6\mu L^2/\hat{\gamma}H_o$. The dimensionless equations are given by

$$r_d^2 = \frac{h_d - h_f}{n_{defects}\pi h_d} \tag{3.35}$$

$$s_d = \pi r_d^2 h_d \tag{3.36}$$

$$\frac{dm}{dt} = -\alpha \frac{mh_d}{s_d} \tag{3.37}$$

$$p_{gas} = \frac{m}{s_d} \frac{RT_s}{2\hat{\gamma}L^2} \tag{3.38}$$

where

$$\alpha = \frac{12\pi\mu D}{\hat{\gamma}H_o} \frac{RT_s}{k_H} \tag{3.39}$$

The dimensionless force f_{app} applied on the template taking into account gas pressure is given by

$$f_{app} = \left(-\frac{1}{h} + \frac{vr^2}{8h^3}\right) N\pi r^2 + p_{gas}\,. \tag{3.40}$$

$f_{app} = 0$ when there is no force acting on the template. Assuming net zero force on the template and using Equation (3.11), we get

$$v = \frac{dh}{dt} = 8N\pi \frac{h^3}{h_f}\left(1 - p_{gas}\frac{h^2}{h_f}\right). \tag{3.41}$$

When $p_{gas} = 0$, we get back the template velocity in the absence of gas pressure given by Equation (3.12).

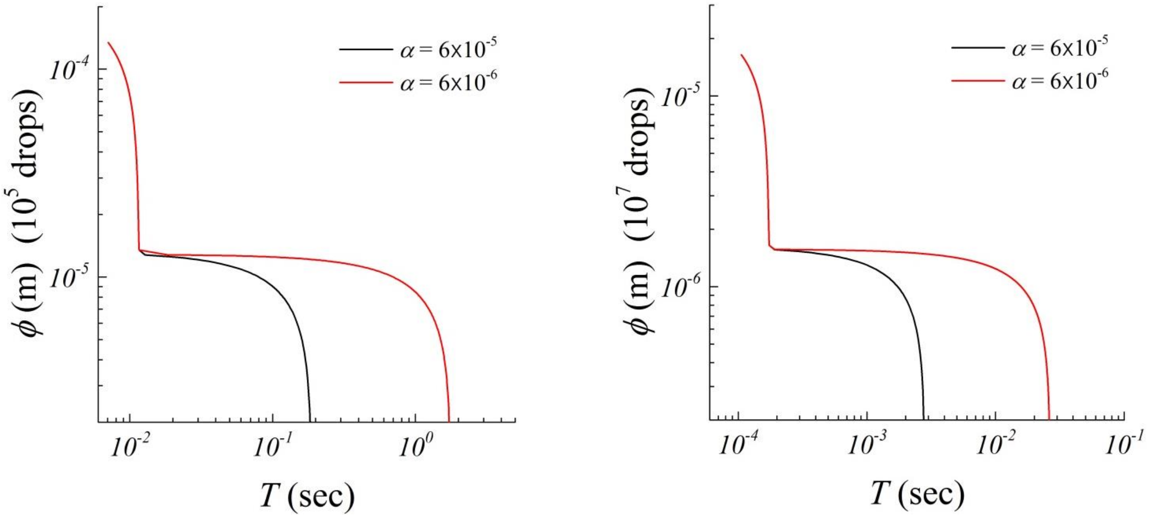

(a) **(b)**

Figure 3.21: Figure shows the plot for defect diameter ϕ (in meters) as function of time T (in seconds) for two initial defect sizes: 100 μm and 10 μm. For 100 cm^2 substrate and a desired final gap of 10 nm, initial ϕ is 100 μm for $N = 10^5$ droplets (left) and ϕ is 10 μm for $N = 10^7$ droplets (right). The results indicate that as α increases, the defect volume reduces faster.

The unknowns r_d, h_d, s_d, m and p_{gas} are solved numerically using Equations (3.35-3.39) and (3.41). The typical value of R = 8.314 Pa.m^{3}K^{-1}mol^{-1}; T_s= 300 K; D = 10^{-9} m^{2}s^{-1} and k_H = 1x10^4 Pa.m^{3}mol^{-1}. If the substrate size is 100 cm^2 and desired final gap is 10 nm, the initial defect size is 100 μm when 10^5 droplets are dispensed and 10 μm when 10^7 droplets are dispensed. Typically hundreds of thousands of droplets are dispensed in SFIL, so the initial defect size is between 10-100 μm. The diameter of the defects at different times as it shrinks from an initial size of 100 μm (left) and 10 μm (right) is shown in Figure 3.21 for α = 6x10^{-5} and 6x10^{-6}. We find that as α decreases the overall time required for the defect to fill increases. The figure also illustrates that the initial defect filling is orders of magnitude faster compared to the remainder of the defect filling process. Initially, the gas pressure inside the defect is about the same as the atmospheric pressure. The gas diffusion is slow during this time due to low gas pressure. As the template lowers, the defect size reduces and the gas pressure and concentration increase. The increase in gas pressure slows down the template and the high gas concentration leads to a higher gas diffusion rate. As the gas diffuses into the resist, the defect slowly fills. $\Delta T_{diffusion}$, the total time required for defects to fill by diffusion is illustrated in Figure 3.22. The plot shows that $\Delta T_{diffusion}$ decreases as α increases or diffusion constant, D increases. $\Delta T_{diffusion}$ also becomes shorter as the initial defect size ϕ decreases. For sub-100 μm defects and $\alpha > 10^{-7}$, the diffusion time is less than a second. For SFIL, the typical value of α is about 10^{-6} - 10^{-4} for $R = 8.314$ Pa.m^{3}K^{-1}mol^{-1}; $T_s = 300$ K; $D = 10^{-10}$ - 10^{-8} m^{2}s^{-1} and $k_H = 1\text{x}10^4$ Pa.m^{3}mol^{-1}.

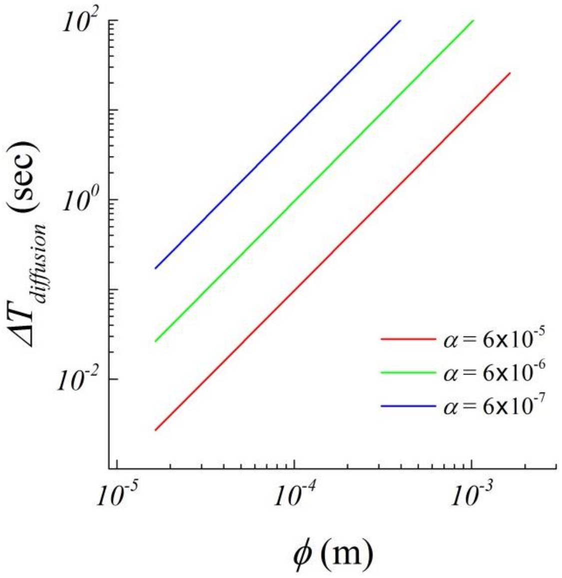

Figure 3.22: Plot for the total time required for defects to fill by diffusion, $\Delta T_{diffusion}$ (in seconds) as a function of initial defect diameter ϕ (in meters) for different values of α. The plot shows that $\Delta T_{diffusion}$ decreases as α increases. $\Delta T_{diffusion}$ also becomes shorter as the initial defect size ϕ decreases. For sub-100 μm defects, the diffusion time is less than a second for values of $\alpha > 10^{-7}$.

Figure 3.23 shows the plot of dimensionless defect volume s_d with time for different values of α. The black line shows results if gas diffusion is neglected and the filling only took place by hydrodynamic droplet spreading. For values of $\alpha > 1x10^{-4}$, the time required for the defect to completely disappear by hydrodynamic droplet spreading is longer compared to the time required by the gas to diffuse. This implies that for $\alpha > 1x10^{-4}$, the non-filling defects in SFIL are only a result of hydrodynamic non-filling and not gas diffusion. However for $\alpha < 1x10^{-4}$, the gas diffusion is a very slow process and may lead to non-filling defects. Thus for low values of α, defect size is diffusion-controlled while for high values, it is hydrodynamically-controlled. Since the typical value of α in SFIL is $10^{-6} – 10^{-4}$, gas diffusion is important when considering imprint time. For cases in which diffusion is very slow, the template is slightly bent at the center while being lowered so that the droplets start spreading outwards allowing the gas to escape easily.

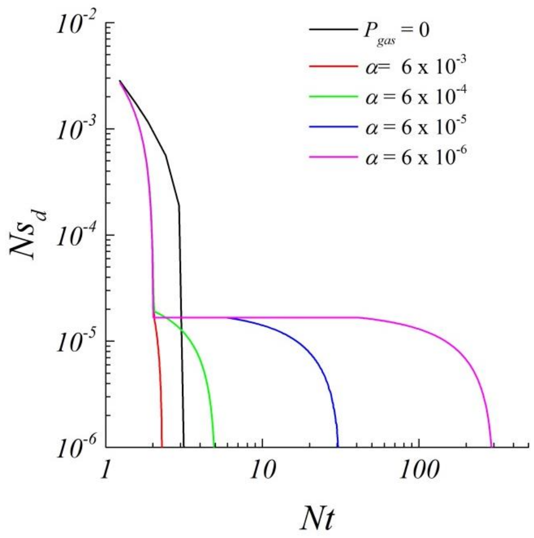

Figure 3.23: Figure shows the plot for dimensionless defect volume s_d as function of time t for different values of α. The results indicate that as α increases, indicating faster gas diffusion, the defect volume reduces faster. The black line shows the dimensionless defect volume if gas is neglected and the filling took place by hydrodynamic droplet spreading only.

3.4. CONCLUSIONS

Multi-drop spreading is simulated for SFIL with pattern free template and droplets ink-jetted in square, hexagonal and modified hexagonal arrangements. Lubrication theory is used to describe the pressure and velocity field for the fluid flow. VOF method is used to track fluid interface. No external force is applied on the template during the imprint process. We find that droplet size, droplet arrangement and droplet placement accuracy are critical to achieving high throughput in SFIL. Large unfilled edge regions increase the imprint time for hexagonal and modified hexagonal droplet arrangement. The modified hexagonal droplet arrangement provides an imprint time lower than the hexagonal arrangement by a factor of 0.56 for SFIL with 100 droplets. For the same size of droplets, the square arrangement is found to be the optimum arrangement as it provides lower imprint time than both hexagonal and modified hexagonal droplet arrangement. The effect of droplet placement error by inkjet system on the imprint time is observed. The imprint time increases significantly for $\varepsilon > 10^{-4}$ and more than 100 droplets. The imprint time increases with the magnitude of droplet placement error and SFIL with smaller droplets is more sensitive to droplet placement error. A non-fill defect analysis is presented based on simulation of SFIL with droplets dispensed in a square arrangement. The non-fill defects are formed at $h = 4h_f/\pi$ when droplets come in contact with each other and reduce in size as the resist spreads. The defects are categorized into unfilled edges and unfilled pockets. A model is proposed to predict the defect size and number of these defects based on gap height and imprint time. The model predicts that smaller droplets lead to smaller defect size. However, the number of defects increases as the droplet size reduces. The results from this model strongly agree with the simulations. We also propose a model to study the diffusion of gas encapsulated between droplets into the resist. The defect size can be diffusion–controlled or hydrodynamics-controlled based on a parameter α which scales as $\sim \mu D / k_H \gamma H_o$. For values of $\alpha < 1\text{x}10^{-4}$, gas diffusion is slow and defect size is diffusion-controlled while for higher values, it is hydrodynamically-controlled. We also find that for sub-100 μm defects, the diffusion time is less than a second for values of $\alpha > 10^{-7}$. Droplet size, droplet arrangement, droplet placement accuracy and non-filling are some of the most critical factors affecting throughput and defect rate. We have successfully presented the effect of these factors on SFIL process. Designing the SFIL process based on the proposed models can significantly improve the throughput and the defect rate for the process.

Chapter 4: Fluid Flow and Defect Characterization in Step and Flash Imprint Lithography with Multi-patterned Template

4.1. INTRODUCTION

High throughput and low defectivity in Step and Flash Imprint Lithography (SFIL) are important to achieve high volume manufacturing for applications such as flash memory. These factors depend strongly on the template control scheme [50, 51], droplet distribution [51] and template pattern [51, 60]. The effect of template control scheme and droplet distribution on throughput of nanoimprint lithography has been explored previously using modeling and simulation [50, 51, 112, 114]. The effect of patterns on fluid flow has been studied primarily in the context of feature filling and gas trapping [47, 57, 58, 61, 113, 126, 127]. The effect of patterns on droplet spreading across the template has not been studied yet. The patterned templates used in SFIL are very high quality as defects on template patterns can result in repeating defects on the final pattern. They are fabricated from an industry standard mask blank using phase shift mask fabrication technology [108, 109]. The template fabrication process is highly precise and contributes considerably to the over-all tool cost [107, 108]. The template price for SFIL varies from \$25,000 for 90 nm node to \$82,500 for 65 nm node (2-tier template for dual damascene). The pattern size and density dictates the fluid flow behavior and can have a significant impact on throughput and defect rate. The high cost of template fabrication demands that the template design has been optimized to minimize defectivity and imprint time. We can optimize template design by gaining insight into the flow behavior for various pattern type and sizes through modeling and simulation. However, simulating the flow around individual patterns is computationally very expensive due to the high density of patterns.

Here, we propose a model for droplet spreading in SFIL with patterned template which incorporates the effect of patterns on fluid flow by calculating an average flow permeability of the template. SFIL with line and space patterned templates is studied by varying droplet size and arrangement. The average permeability accounts for the porosity due to anisotropic patterns on the imprint template. Droplet spreading is simulated with multi-patterned templates and different droplet dispensing schemes to find the optimum droplet distribution for maximum throughput. We identify and characterize different non-fill defects formed when using different patterns and predict the size, location and count of these defects.

4.2. SIMULATION METHOD

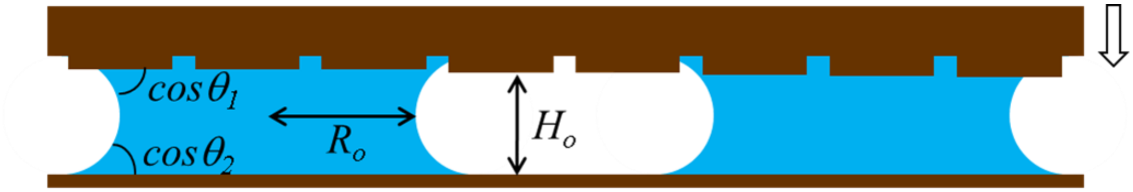

Figure 4.1: Droplets between a substrate and a template. The initial radius of the drop is R_o and the initial height is H_o. θ_1 and θ_2 are contact angles made by the imprint material with the template and the substrate respectively.

A schematic of imprint droplets with initial radii R_o and a gap of height H_o between a template and a substrate is shown in Figure 4.1. The template can be controlled to move with a constant velocity, constant pressure or applied force [50]. As the template approaches the substrate, the liquid-air interface of the droplet exerts capillary force on the template. The fluid flow in the gap results in viscous force which balances the capillary force due to the liquid interface and any externally applied force.

Typically sub-ten picoliter droplets are used in SFIL [104]. The radius of the droplets is about 10 – 100 μm. For sub-100 nm wide patterns, the droplets are many orders of magnitude larger than the patterns and each droplet cover hundreds or thousands of individual patterns. Since the resist flows over a very high density of patterns, the spreading of the droplets can be studied by calculating an average permeability. The equations describing the pressure and velocity fields in the drop for SFIL with high density patterned template are given by the Reynolds' lubrication theory:

$$\frac{\partial H}{\partial T} = \nabla \cdot \left(\mathbf{K} \cdot \frac{\nabla P}{\mu} H \right), \tag{4.1}$$

$$\mathbf{U} = -\mathbf{K}.\frac{\nabla P}{\mu}, \tag{4.2}$$

where H is the gap between substrate and template, P is the pressure in the droplet, $\mathbf{K}$ is the permeability, $\mathbf{U}$ is the vertically averaged fluid velocity and μ is the viscosity of the imprint resist. For a rigid substrate and template, $\partial H / \partial T = -V$, where V is the template velocity. The pressure distribution in the fluid is calculated using Equation 4.1 and the pressure boundary condition at the liquid – air interface. For a patterned template, the capillary pressure at the interface can be written as

$$P_{interface} = P_{atm} - \frac{\gamma\left(\cos\theta_1 + \cos\theta_2\right)}{\hat{H}}. \tag{4.3}$$

$\hat{H}$ is an averaged gap between the substrate and the template accounting for the effect of pattern roughness on the capillary pressure. An expression of $\hat{H}$ for line and space pattern is presented in the appendix. P_{atm} is the atmospheric pressure and γ is the surface tension of the imprint resist. θ_1 and θ_2 are contact angles made by the imprint material with the template and the substrate respectively (as shown in Figure 4.1). Imprint material used in SFIL is highly wetting and for our simulations we assume that $\theta_1 = \theta_2 = 0$, so, $P_{interface} = P_{atm} - 2\gamma/\hat{H}$. In our model, we assume that SFIL is being carried out in vacuum or in a gas which is highly soluble in imprint material and so gas release and trapping can be neglected. The imprint process begins with the droplets making contact with both the substrate and the template. We also assume that the feature filling is instantaneous as the feature fill time is negligible compared to the time required for the fluid to spread in the gap.

The governing equations and boundary condition [Equations (4.1), (4.2) and (4.3)] can be non-dimensionalized using the characteristic values of pressure, gap thickness, time and velocity. These values are given by: $P_c = 2\gamma/H_o$, $H_c = H_o$, $T_c = 6\mu L^2/\gamma H_o$, $V_c = \gamma H_o^2/6\mu L^2$ and $U_c = \gamma H_o/6\mu L$ where H_o is the initial gap. The x and y coordinates are non-dimensionalized using the width of the template L. The dimensionless governing equations are given by

$$-v = \nabla \cdot \left(\left(\mathbf{k} \cdot \nabla p \right) h \right) \tag{4.4}$$

$$\mathbf{u} = -\mathbf{k} \cdot \nabla p \tag{4.5}$$

where, $h = H/H_c$, $v = V/V_c = \partial h / \partial t$, $p = P/P_c$, and $\mathbf{u} = \mathbf{U}/U_c$. v is the dimensionless template velocity. The dimensionless pressure boundary condition is given by

$$p_{interface} = -\frac{1}{\hat{h}} \tag{4.6}$$

where $\hat{h}$ is the dimensionless averaged gap between the substrate and the template accounting for the effect of pattern roughness on the capillary pressure.

Figure 4.2 shows a schematic of a nanoimprint template with line and space patterns. The feature height of the pattern is ΔH and the minimum and maximum gap between the substrate and the template at any time is H and $H+\Delta H$ respectively. The width of lines and spaces is d_1 and d_2 respectively. The lines and spaces in Figure 4.2 (a) are parallel to the X direction and into the plane. The resist completely fills the features and the gap between the template and the substrate at the end of the imprinting process to form a continuous resist layer. The total volume of resist Q required to fill the gap is given in dimensional form by

$$Q = L^2 \left(H_f + \Delta H \frac{d}{1+d} \right) \tag{4.7}$$

where, H_f is the final resist thickness and $d = d_2/d_1$. Typically the pattern height ΔH is less than 100 nm.

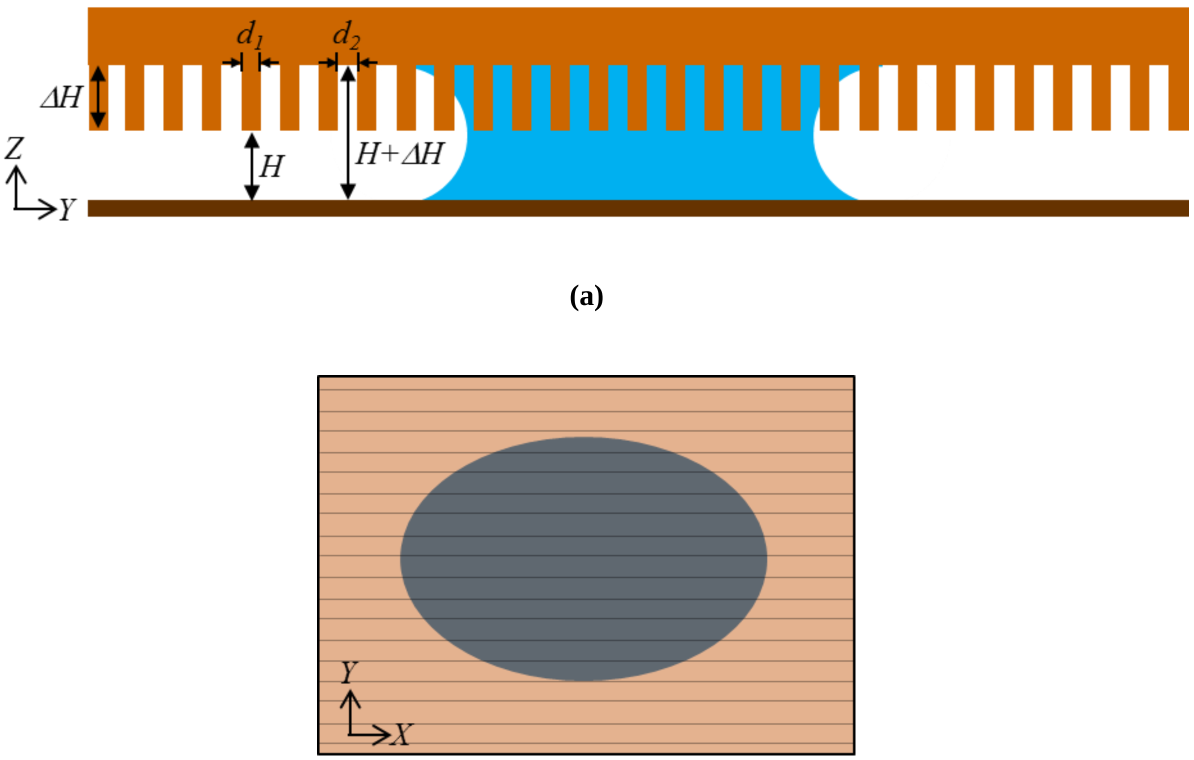

(a)

(b)

Figure 4.2: Schematic of a nanoimprint template with line and space patterns. (a) Side view of the template. The feature height of the pattern is Δ*H*. The minimum and the maximum gap between the substrate and the template are *H* and *H*+Δ*H* respectively. The width of the line and space pattern is d_1 and d_2 respectively. The patterns are parallel to the *x* direction. (b) Top view of the template with a droplet spreading under it. The horizontal lines show the direction of the patterns (not to scale).

The dimensionless governing Equations (4.4) and (4.5) can be written in the Cartesian coordinate system as

$$-v = \frac{\partial}{\partial x}\left(k_{xx}h_{avg}\frac{\partial p}{\partial x}\right)+\frac{\partial}{\partial y}\left(k_{yy}h_{avg}\frac{\partial p}{\partial y}\right), \tag{4.8}$$

$$u_x = -k_{xx}\nabla p \tag{4.9}$$

and

$$u_y = -k_{yy}\nabla p\,. \tag{4.10}$$

For line and space patterns, h_{avg}, k_{xx} and k_{yy} are given by

$$h_{avg} = h\left(\frac{1+\left(1+\Delta h/h\right)d}{1+d}\right), \tag{4.11}$$

$$k_{xx} = h^2\frac{1+\left(1+\Delta h/h\right)^3 d}{1+d\left(1+\Delta h/h\right)}, \tag{4.12}$$

and

$$k_{yy} = h^2\left(\frac{1+d}{1+\left(1+\Delta h/h\right)^{-3} d}\right)\left(\frac{1+d}{1+\left(1+\Delta h/h\right)d}\right) \tag{4.13}$$

where $d = d_2/d_1$ and $\Delta h = \Delta H/H_c$. The dimensionless pressure boundary condition is given by

$$p_{interface} = -\frac{1}{h}\frac{1}{1+d}\left(1+\frac{d}{1+\left(\Delta h/h\right)}\right) \tag{4.14}$$

The derivation of these expressions is shown in the appendix. For these expressions, the effect of sidewalls on fluid flow is neglected. The effect of sidewalls on fluid flow is discussed later in the chapter. These equations are solved using the Volume of Fluid (VOF) method described in Chapter 3.

4.3. RESULTS

4.3.1. SFIL using Template with Line and Space Patterns

The droplet spreading and merging is simulated as the gap between the substrate and the template closes from an initial gap of $h = 1$ to a final gap of $h = 0.01$. The template has zero net force acting on it and the feature height is $\Delta h = 0.1$. For initial gap $H_o = 1$ μm, $h = 1$ and $\Delta h = 0.1$ corresponds to a dimensional gap of $H = 1$ μm and a feature height of $\Delta H = 100$ nm respectively as shown in Figure 4.2(a). For a pattern width 100 nm and substrate width 10 cm, each drop spans about 10,000 gratings for 9 drops and 3000 gratings for 100 drops. The width of lines and spaces are equal i.e. $d = 1$. The patterns are parallel to the x-direction. The initial volume of the droplet is selected based on the number of droplets and Equation (4.7) so that the resist completely fills the features forming a uniform continuous film at $h = 0.01$.

Simulation of SFIL using a template with line and space patterns with 9 droplets and 100 droplets are shown in Figures 4.3 and 4.4 respectively. The droplets form non-circular shapes when SFIL is carried out with templates having line and space patterns. The non-circular shape is a result of the difference in flow permeability in x and y directions. Figure 4.5 shows the plot between permeability k_{xx} and k_{yy} in the x and y direction as the gap closes from $h = 1$ to $h = 0.01$ for $\Delta h = 0$, 0.01 and 0.1. For $\Delta h = 0$ (pattern-free template), both k_{xx} and k_{yy} scale as h^2. For $\Delta h = 0.1$, permeability k_{xx} in the x-direction becomes significantly higher than k_{yy} as the gap becomes smaller. This leads to the droplet spreading faster in the x direction compared to the y direction. The spreading of the droplets can be divided into three regimes: (i) initial circular spreading (ii) elliptical spreading before droplet merging and (ii) linear spreading after droplet merging. Initially from $h = 1$ to about $h = 0.6$, the droplets spread uniformly in the all directions as the droplets are squeezed by the template. This occurs because the permeabilities in x- and y-directions are about the same as shown in Figure 4.5. In this regime both k_{xx} and k_{yy} scale as $O(h^2)$. Thus the droplets maintain their circular shapes as shown for multiple droplets in Figure 4.3 and 4.4 (top). As the droplets are squeezed further, k_{xx} starts to increase rapidly while k_{yy} continues scaling with h^2. Thus the droplet spreads faster in the x direction compared to the y direction leading to droplets of ellipse like shape as shown in Figure 4.3 and 4.4 (center). Droplets continue spreading under this regime until they either start merging with neighboring droplets or reach the template edge. Once all the droplets in x directions merge together, they form continuous film flowing only in the y direction as shown in Figure 4.3 and 4.4 (bottom). Since k_{yy} is very small compared to k_{xx}, the fluid spreads slowly in the y direction after drop merging.

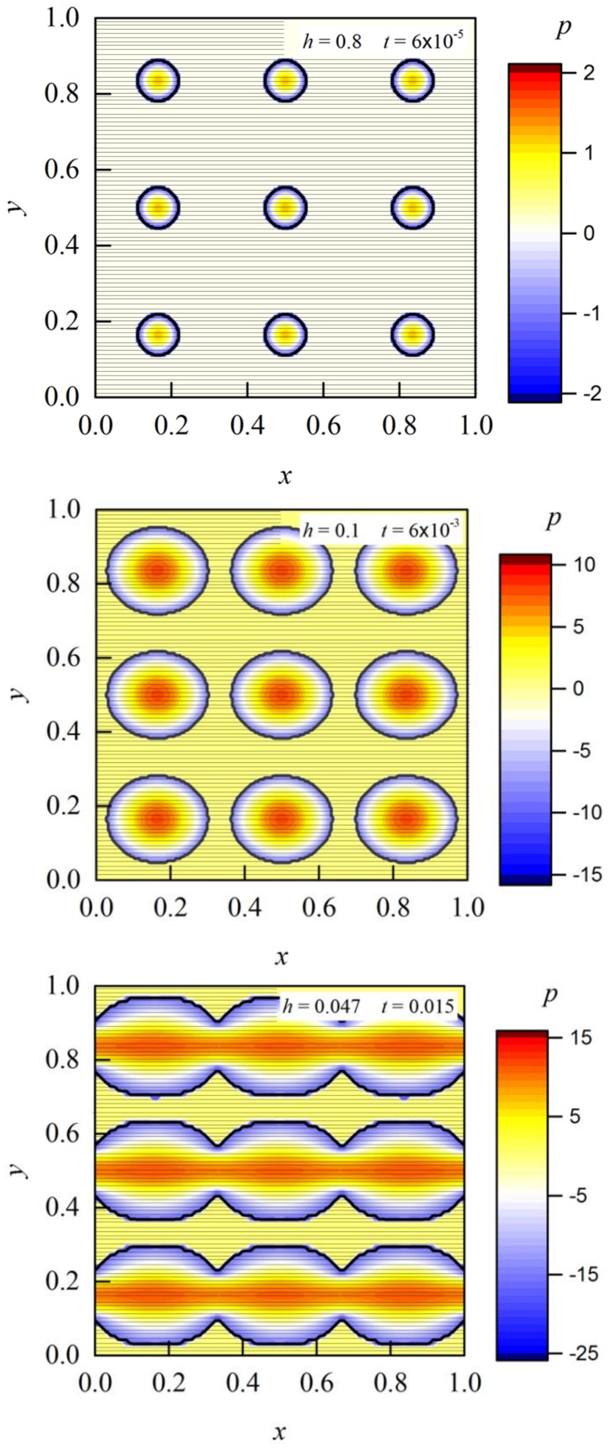

Figure 4.3: Contour map showing pressure field for nine drops spreading on a substrate at *h* = 0.8, *h* = 0.1 and *h* = 0.047. The template has line and space patterns and has net zero force acting on it. The grey horizontal lines show the direction of the patterns (not to scale). The droplet spreads faster in the *x* direction compared to *y* direction. The feature height Δ*h* is 0.1.

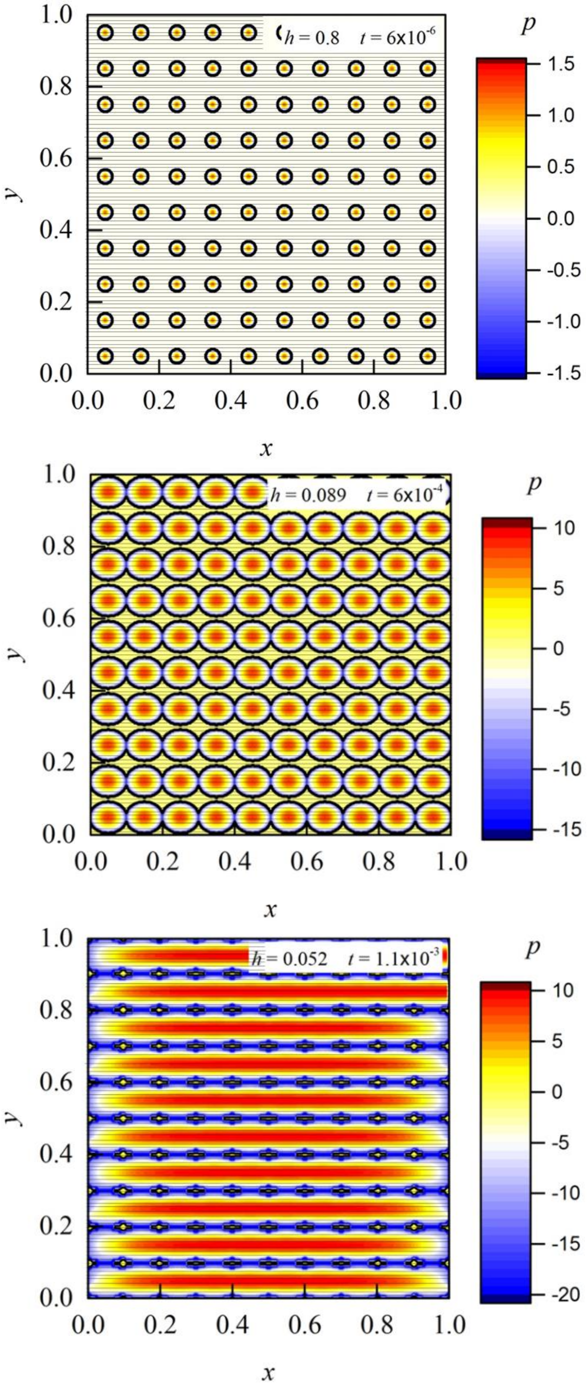

Figure 4.4: Contour map showing pressure field for 100 drops spreading on a substrate at *h* = 0.8, *h* = 0.089 and *h* = 0.052. The template has line and space patterns and has net zero force acting on it. The grey horizontal lines show the direction of the line and space patterns (not to scale). The droplet spreads faster in the *x* direction compared to *y* direction. The feature height Δ*h* is 0.1.

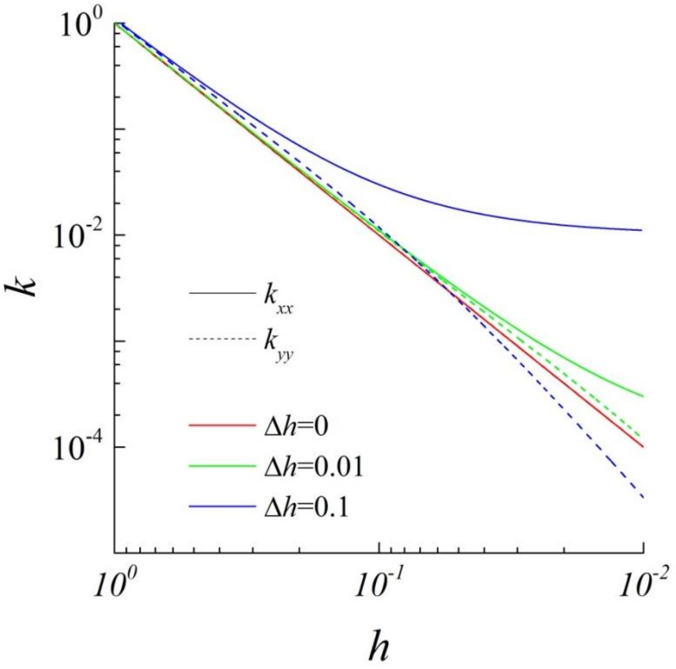

Figure 4.5: Permeability k_{xx} and k_{yy} in the x and y direction respectively for pattern height Δh = 0, 0.01 and 0.1. k_{xx} and k_{yy} are equal for pattern-free template and scale as h^2. For Δh = 0.1, the permeability becomes significantly higher in the x direction compared to y direction as the gap closes.

The droplet merging simulation is repeated with multiple droplets in a square arrangement (as shown in Figure 4.6(a)) and three pattern heights Δh = 0, 0.01 and 0.1. The dimensionless volume of resist required to fill entire gap at $h = h_f$ is given by

$$q = h_f + \Delta h \frac{d}{1+d} . \tag{4.15}$$

Thus, q increases as Δh increases.

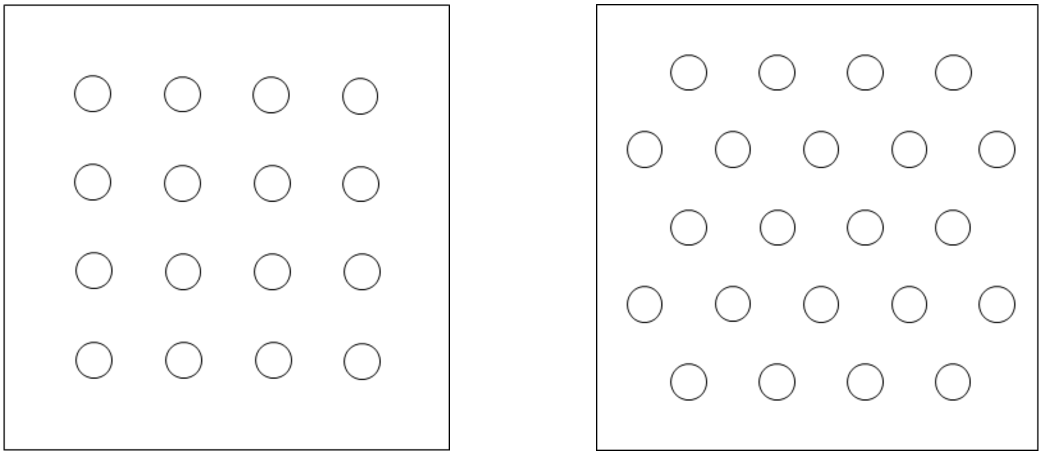

(a) **(b)**

Figure 4.6: Schematic showing top view of droplets on a substrate. The droplets are dispensed in two arrangements: (a) square and (b) hexagonal.

The dimensionless gap height h as a function of dimensionless imprint time t is shown for multiple droplets in Figure 4.7. The results for $\Delta h = 0$ corresponds to results for a template with no patterns. The imprint time for $\Delta h = 0$ reduces as the number of droplets increases. The imprint time required for $\Delta h = 0.01$ does not differ significantly from $\Delta h = 0$ because there is a relatively small difference in permeability for $\Delta h = 0$ and $\Delta h = 0.01$ as shown in Figure 4.5. However, a pattern height of $\Delta h = 0.1$ has significant impact on the imprint time. The imprint time is longer for $\Delta h = 0.1$ compared to $\Delta h = 0$ because of the higher volume of the resist required to fill a gap with $\Delta h = 0.1$. Initially the droplets spread more in the x direction compared to the y direction due to high relative permeability in the x direction. Once they reach the substrate edge they can no longer spread in the x direction and are forced to spread only in the y direction as shown in the Figure 4.3 and 4.4 (bottom). Since the permeability in the y direction is lower than the x direction, it leads to slow spreading and an increase in imprint time. The characteristic time for these simulation is $T_c = 6\mu L^2 / \gamma H_o$. For SFIL with substrate length L = 10 cm, initial gap height of H_o = 1 μm, resist viscosity μ = 0.001 Pa.s and surface tension γ = 70 dyne/cm, T_c = 857 seconds. Figure 4.7 shows that without pattern, the overall imprint time is about 200 seconds for 9 droplets and 44 seconds for 100 droplets. With a pattern height of 10 nm, the overall imprint time is about 220 seconds for 9 drops and about 48 seconds for 100 droplets. For larger patterns of height 100 nm, the overall imprint time increases to about 370 seconds for 9 droplets and 80 seconds for 100 droplets. Figure 4.7(b) shows that the results for multiple droplets collapse into one curve when imprint time is rescaled by the number of drops N suggesting that t scales as N^{-1} .

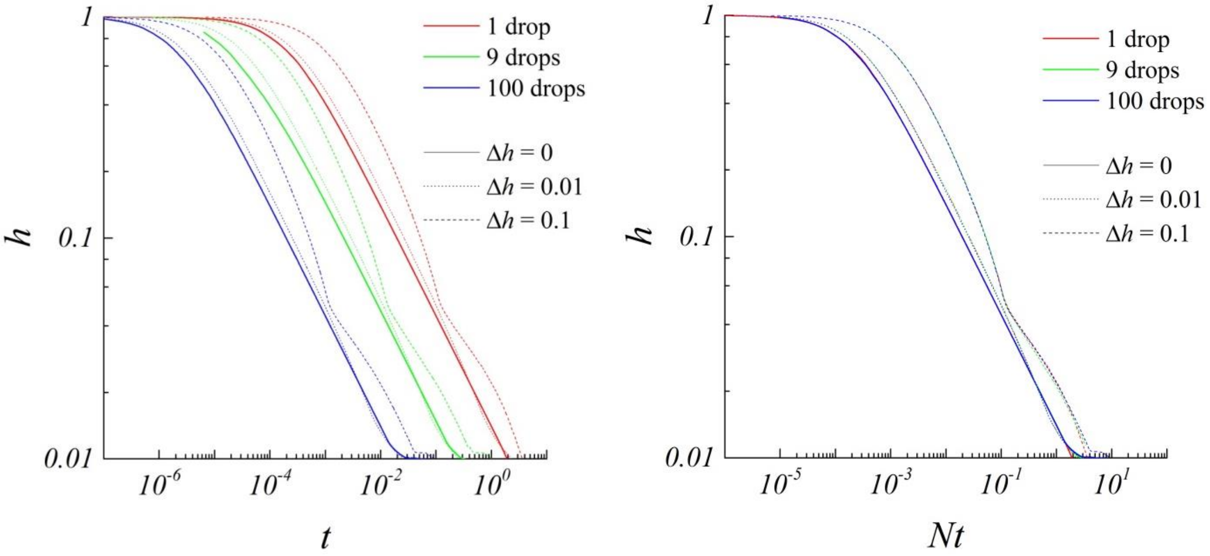

(a) **(b)**

Figure 4.7: (a) Imprint time for SFIL with multiple droplets and a template with line and space patterns of height Δh = 0, 0.01 and 0.1. The droplets are dispensed in a square arrangement. (b) Rescaling the imprint time with the number of droplets (N) collapses the results into one curve suggesting that t scales as N^{-1} .

The droplet spreading simulation is repeated with 100 droplets dispensed in a hexagonal arrangement (as shown in Figure 4.6(b)). The dimensionless gap height h as a function of dimensionless imprint time t is shown for 100 droplets in Figure 4.8. The imprint time increases as the pattern height is increased. For the same number of droplets, the imprint time is found to be higher in hexagonal arrangement compared to square arrangement. This increase in imprint time is due to the larger droplet free region at the substrate edge in hexagonal droplet arrangement as was discussed in Chapter 3.

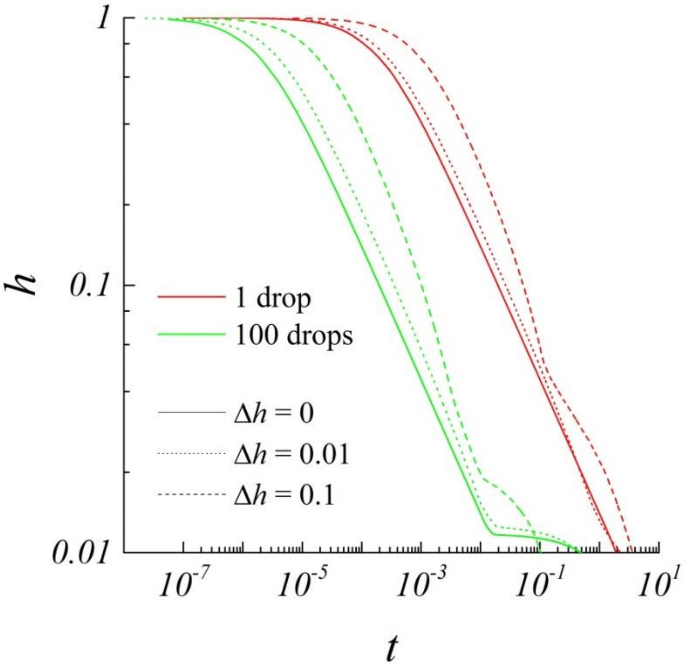

Figure 4.8: Imprint time for SFIL with multiple droplets and a template with line and space pattern for pattern height Δh = 0, 0.01 and 0.1. The droplets are dispensed in a hexagonal arrangement.

4.3.2 SFIL using Multi-patterned Template

Multi-patterned templates have varying flow permeability in different parts of the template which can lead to interesting fluid flow behavior. We have simulated drop spreading on three types of templates which are shown in Figure 4.9. In template type-I, the top half (section A) is covered with line and space patterns of height ΔH parallel to x direction and the bottom half (section B) is pattern free. In template type-II, section A is covered with lines and space patterns of height ΔH parallel to y direction and section B is pattern free. In template type-III, both section A and section B are pattern free however section A is at a height $\Delta H/2$ higher than section B as shown in Figure 4.9(c). At a fixed gap height H, same volume of resist is required to fill the gap between the template and the substrate for all three templates.

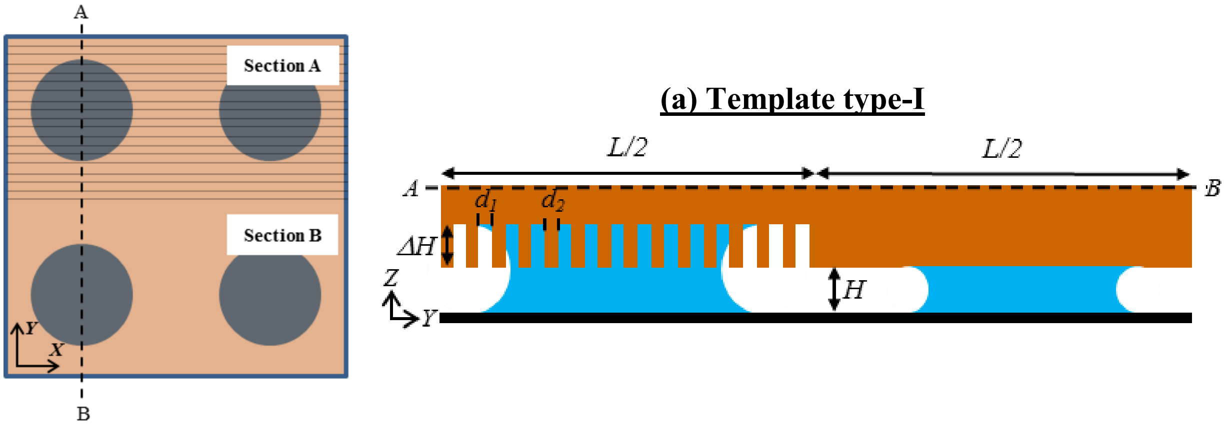

(a) Template type-I

(b) Template type-II

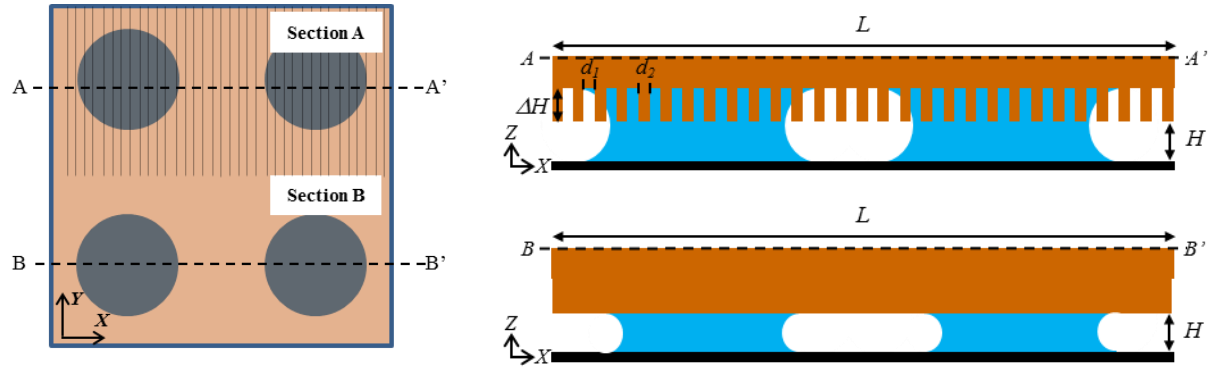

(c) Template type-III

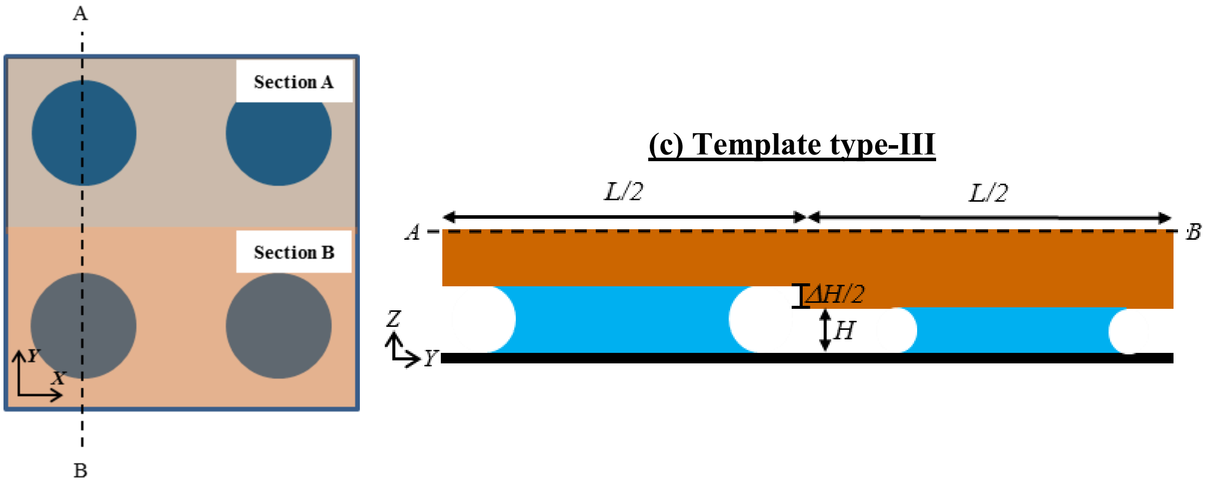

Figure 4.9: Schematic showing top view and cross-sectional view of multi-patterned template type- I, II and III. Template type-I (a) and type-II (b) have line and space patterns at the top (section A) and no pattern at the bottom (section B). The grey lines show the direction of the patterns (not to scale). The patterns are parallel to x and y direction in template I and II respectively. Template type-III does not have patterns but the gap in section A is larger than section B by $\Delta H/2$.

The permeability in sections A and B are different resulting in different flow behaviors (as shown in Figure 4.5). The spreading and merging is simulated with these multi-patterned templates as the gap between the substrate and the template closes from an initial gap of $h = 1$ to a final gap of $h = 0.01$. The template has no net force acting on it. $h = 1$ and corresponds to 1 μm. The width of lines and spaces are equal i.e. $d = 1$. Here we explore two drop pattern schemes. In drop pattern scheme 1, all the droplets have equal volume and the total volume of droplets is sufficient to fill the entire template when $h = h_f$. In drop pattern scheme 2, each section has different size of droplet such that total volume of the droplets in a section is sufficient to completely fill that section when $h = h_f$. In both schemes, the initial volume of the droplet is selected such that the resist completely fills the features and the entire substrate forming a uniform continuous film at $h = 0.01$. The total number of drops in each section is $N/2$. At the beginning of SFIL, the dimensionless height of droplets in section A and B is $(1 + 0.5\Delta h)$ and 1 respectively. The dimensionless radius of droplets used for the two sections in schemes 1 and 2 is shown in Table 4.1.

Table 4.1: Size of droplets on section A and B for drop pattern scheme 1 and 2

Section of Template I,II or III	Volume required to fill section	Droplet radius for scheme 1 (Equal drop volume)	Droplet radius for scheme 2 (Distributed drop volume)
Section A	$0.5\left(h_f + 0.5\Delta h\right)$	$\left[\dfrac{h_f + 0.25\Delta h}{N\pi\left(1+0.5\Delta h\right)}\right]^{1/2}$	$\left[\dfrac{h_f + 0.5\Delta h}{N\pi\left(1+0.5\Delta h\right)}\right]^{1/2}$
Section B	$0.5h_f$	$\left(\dfrac{h_f + 0.25\Delta h}{N\pi}\right)^{1/2}$	$\left(\dfrac{h_f}{N\pi}\right)^{1/2}$

The droplet spreading time for template I, II and III under drop pattern scheme 1 and 2 for 100 drops and feature height is $\Delta h = 0.1$ is shown in Figure 4.10. The imprint time using scheme 1 is much higher compared to scheme 2 for all three templates. The total number of droplets in each section on the template is $N/2$. The total volume of droplets in each section is calculated using Table 4.1. For scheme 1, the total volume of droplets in each section is $0.5(h_f +$

$0.25\Delta h$). The volume required to fill section A is $0.5(h_f + 0.5\Delta h)$. Thus there is a deficit of $0.125\Delta h$ in section A and excess volume of same amount in section B. This excess fluid flows from section B to section A as the gap between the template and the substrate closes to the desired height. However the gap in section A is larger than the gap in B, thus the capillary pressure in section A is higher than that in section B. The higher pressure in section A inhibits the fluid flow from section B to section A. We observe the excess fluid in section B flows to section A only after section B is completely filled. As we had observed in Chapter 3, the spreading of droplets to reach the edges is a slow step and this increases the time required to fill the section B completely. Once section B is filled, the excess fluid spreads and fills section A. The results for the different templates under the same scheme are comparable.

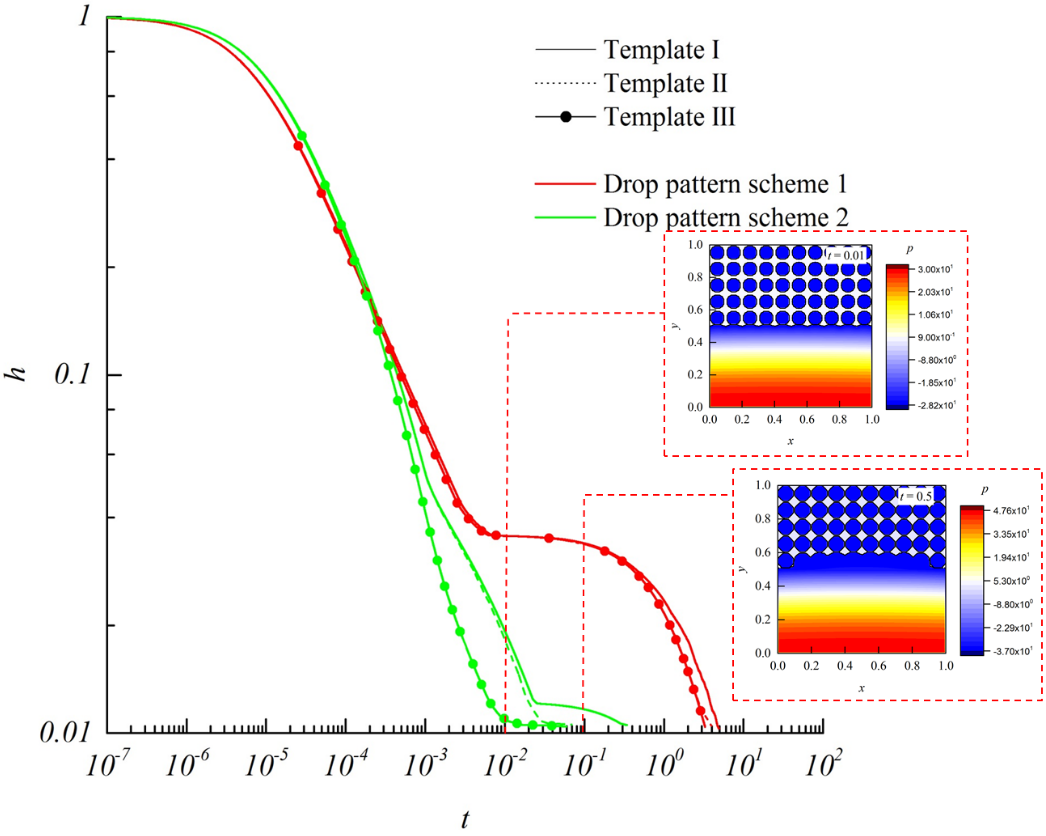

Figure 4.10: Imprint time for SFIL with 100 droplets, feature height Δh = 0.1 and templates I, II and II. Droplets are dispensed under two schemes. In drop pattern scheme 1, all droplets have equal volume. In drop pattern scheme 2, droplets in different sections of the template have different volume. The imprint time for scheme 1 is found to be much longer than scheme 2.

For scheme 2, the total volume of droplets in section A and B is $0.5(h_f + 0.5\Delta h)$ and $0.5h_f$ respectively. The volume required to fill section A and B is $0.5(h_f + 0.5\Delta h)$ and $0.5h_f$ respectively. Thus unlike scheme 1, scheme 2 provides sufficient volume of fluid in each section leading to significantly shorter imprint times.

These simulations were repeated with same type of templates but having pattern height $\Delta h = 0.01$. The imprint time as a function of gap height is shown in Figure 4.11. Drop pattern scheme 2 still provides lower imprint time than drop pattern scheme 1. It can be concluded that irrespective of pattern direction in multi-patterned templates, drop scheme 2 will provide shorter imprint time than drop scheme 2. The difference in imprint time increases with increase in the pattern height. Template type III provides slightly shorter imprint time than template type I. Based on this study we conclude that the optimum droplet dispensing scheme is distributing droplet volume based on local fluid requirement.

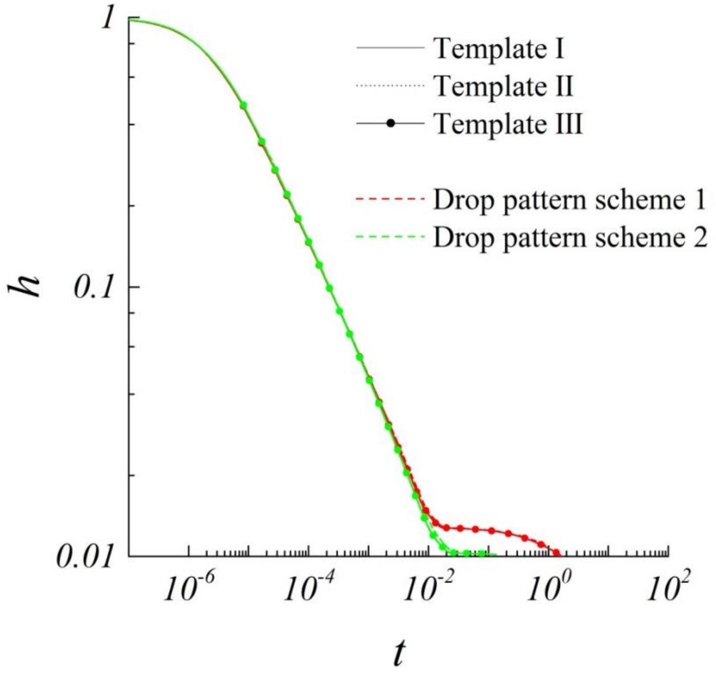

Figure 4.11: Imprint time for SFIL with 100 droplets, feature height $\Delta h = 0.01$ and templates I, II and III. Droplets are dispensed under two schemes. In drop pattern scheme 1, all droplets have equal volume. In drop pattern scheme 2, droplets in different sections of the template have different volume. The imprint time for scheme 1 is found to be much longer than scheme 2.

4.3.3 Non-fill Defect Characterization

As the gap between the template and the substrate closes, the resist spreads to the unfilled regions on the substrate eventually covering the entire substrate. If the allowed imprint time is lower than the time required for the resist to spread over the entire substrate, it leads to non-filling defects in the final pattern. Figure 4.12 shows the unfilled regions on a substrate for 100 drops with a pattern free template (Figure 4.12(a)) and a template with line and space patterns of height $\Delta h = 0.1$ (Figure 4.12(b)). The gap in both processes closes from $h = 1$ to $h = 0.01$. The unfilled regions in SFIL can be classified into three types:

(i) Unfilled edges: At the beginning of the imprint process, a large portion of the substrate is not covered with droplets. As shown in Figure 4.12, this type of non-filling covers a large fraction of the substrate and reduces in size as the imprint process progresses. As the gap closes, this unfilled region becomes smaller ultimately reducing to regions along the edges.

(ii) Unfilled pockets: These unfilled regions are formed as the droplets start to merge creating regions which are bound by resist on all sides. Typically these unfilled regions are small compared to unfilled edges and are formed only towards the end of the imprinting process.

(iii) Unfilled channels: These unfilled regions are observed only in SFIL with anisotropic patterns. The anisotropic flow due to the template results in the droplet merging only in one direction creating long and thin channels of unfilled regions which are bound by resist on two sides. The other two sides of this region can be bound by resist or template edge. Unfilled channels are typically smaller than unfilled edges and larger than unfilled pockets.

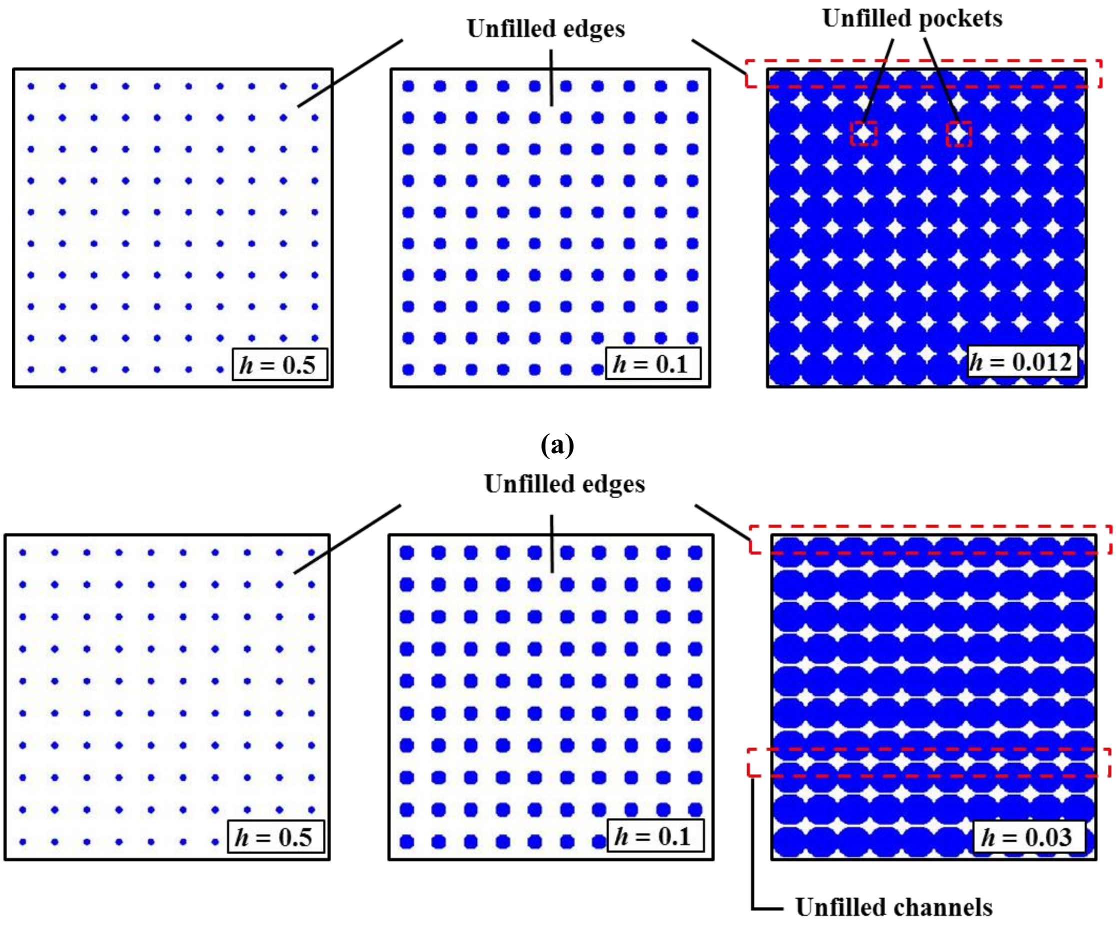

(a)

(b)

Figure 4.12: Different unfilled regions for SFIL with 100 drops and (a) a template without patterns (b) a template with line and space pattern of height Δ*h* = 0.1. The gap closes from *h* = 1 to *h* = 0.01. The different types of unfilled regions are: (i) unfilled edges (ii) unfilled pockets and (iii) unfilled channels.

Figure 4.13 shows the fraction of the substrate with unfilled region and fluid-filled region for SFIL with 100 drops and a template without patterns as the gap closes from $h = 1$ to $h = 0.01$. Initially, the substrate has fluid filled regions and unfilled edges. As the droplets spread, the fluid filled regions (blue) become larger while the unfilled edges (white) become smaller. The droplets merge at a gap slightly higher than $h = 0.01$ and create unfilled pockets (black) as shown in Figure 4.12(a)(right). These unfilled pockets are of the order of 10^{-3} in area and are filled quickly by the spreading resist. Insufficient imprint time can lead to small defects of size $O(10^{-3})$ to

O(10^{-4}) spread over the substrate. For a characteristic length scale L = 10 cm, the patterned area is 100 cm^2. A defect of size 10^{-4}- 10^{-3} corresponds to 0.01 - 0.1 cm^2.

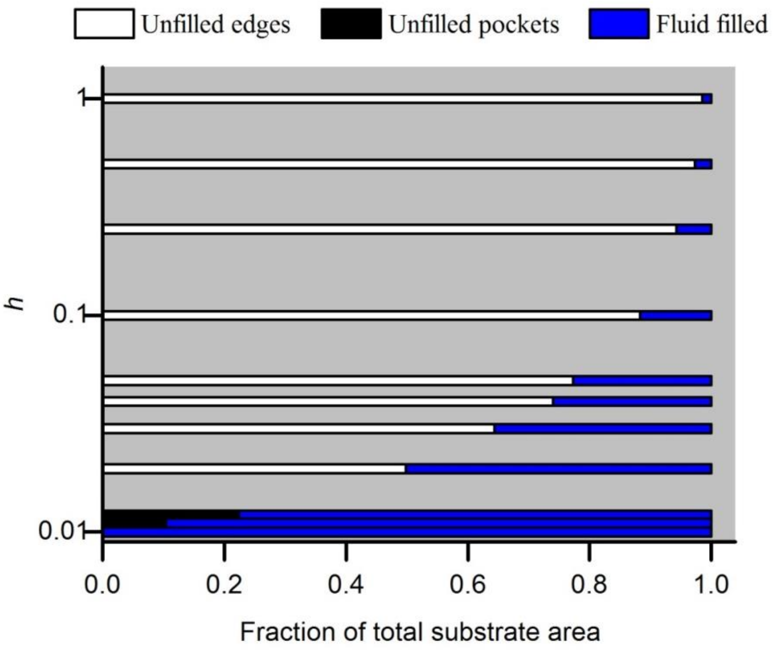

Figure 4.13: Figure shows fraction of the total substrate area with unfilled and fluid filled region for SFIL with 100 drops and a template without patterns as the gap closes from *h* = 1 to *h* = 0.01. The fraction of the area covered by unfilled pockets is shown in black.

Figure 4.14 shows the fraction of the substrate with unfilled region and fluid-filled region for SFIL with 100 drops and a template with line and space pattern of height $\Delta h = 0.1$ as the gap closes from $h = 1$ to $h = 0.01$. Initially, the substrate has fluid filled regions and unfilled edges. As the droplets spread, the fluid filled regions (blue) become larger while the unfilled edges (white) become smaller. The droplets then merge in the direction of the line pattern creating unfilled channels (gray) as shown in Figure 4.12(b)(right). These channels are of the order of 10^{-2} in area and are filled slowly as the resist spreading is slow in direction normal to the pattern. Thus these unfilled regions are present for a long period in the imprint process. Insufficient imprint time in this imprint process can lead to thin channel defects which run from edge to edge and are of size O(10^{-2}) or less. A defect of size 10^{-2} corresponds to 1 cm^2 for a 100 cm^2 patterned area.

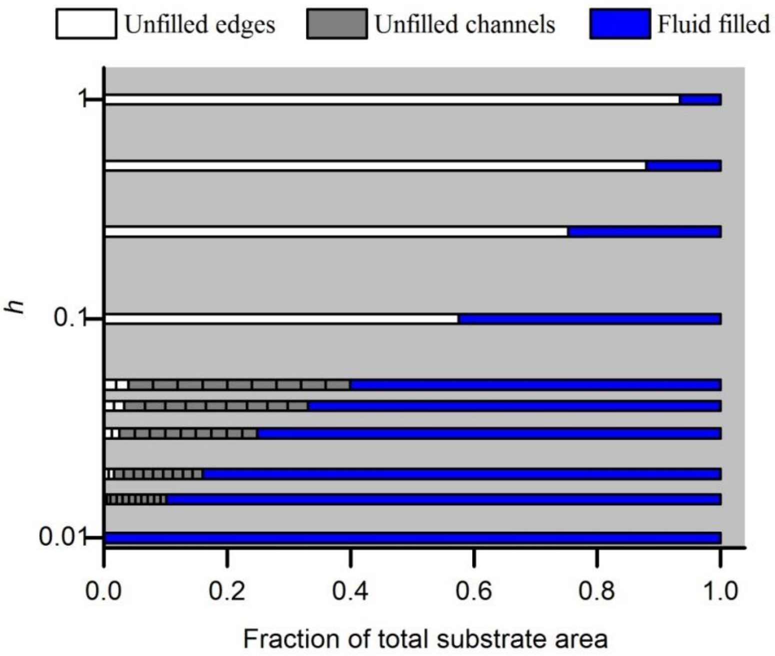

Figure 4.14: Figure shows fraction of the total substrate area covered with fluid and non – filled regions for SFIL with 100 drops and a template with line and space pattern of height Δ*h* = 0.1 as the gap closes from *h* = 1 to *h* = 0.01.

This method of defect characterization is applied to imprint process with 100 drops and multi-patterned template I in droplet pattern scheme 1 and 2. In template type-I, the top half is covered with horizontal line and space patterns of height Δ*h* = 0.1 and the bottom half is pattern free as shown in Figure 4.9(a). The gap closes from *h* = 1 to *h* = 0.01. The results for droplet scheme 1 and 2 are shown in Figure 4.15 and 4.16 respectively. Figure 4.15(a) and 4.16(a) show the fraction of the substrate with unfilled region and the fluid-filled region. Figure 4.15(b)-(g) and 4.16(b)-(g) show non-fill defect count and area of defects at different times close to the end of the imprint process. In SFIL with drop scheme 1, unfilled pockets are created at about *h* = 0.05 due to merging of droplets in the pattern free section of the template as shown in Figure 4.15(b). The total defect count is >50 and area is O(10^{-4}) to O(10^{-3}) as shown in Figure 4.15(c). These defects are filled soon as the gap becomes smaller. At about *h* = 0.04, the droplets in patterned section of the template merge creating unfilled channels. These defects are less than 10 and their size is between 10^{-1} and 10^{-2}. For a 100 cm^2 patterned area, a defect of size 10^{-1} corresponds to 10 cm^2 and 10^{-2} to 1 cm^2. These defects are comparatively larger than the unfilled pockets and take longer to fill as the fluid spreading in direction normal to the line patterns is slow.

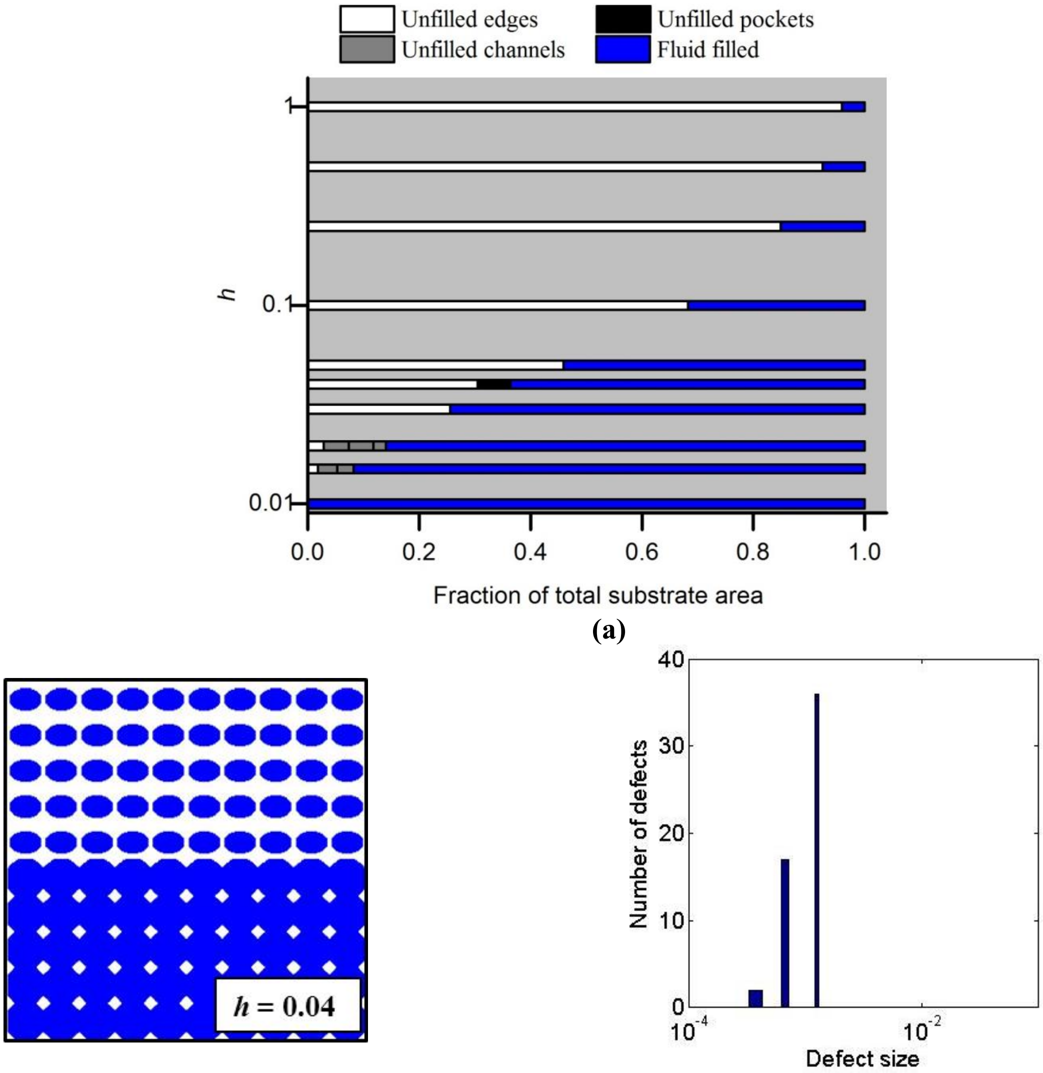

(a)

(b)

(c)

Figure 4.15: continued next page

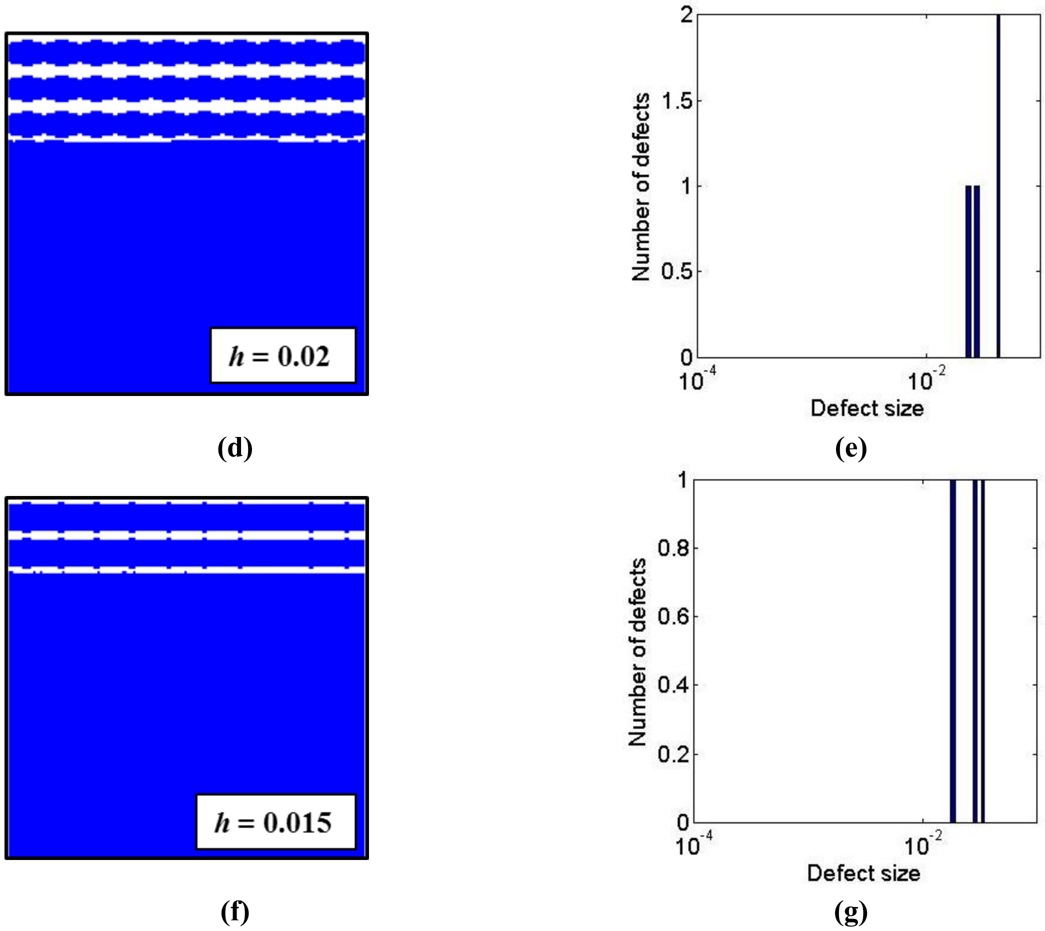

(d) (e)

(f) (g)

Figure 4.15: (a) Figure shows the fraction of the area of substrate with unfilled region and fluid-filled region for SFIL with 100 drops and template I. The droplets are dispensed under pattern scheme 1. Figures (b)-(g) show count and area of unfilled region at different times close to the end of the imprint process. The gap closes from a height *h* = 1 to *h* = 0.01 and height of the patterns in the upper section of the template Δ*h* = 0.1.

In SFIL with drop scheme 2, unfilled channels are created at about $h = 0.05$ due to merging of droplets in the upper section of the template with line patterns as shown in Figure 4.16(b). The total defect count is <10 and size is between O(10^{-1}) to O(10^{-2}) as shown in Figure 4.16(c) . These defects fill over time as the droplets spread. At about $h = 0.012$, the droplets in the section of the template with no patterns merge creating unfilled pockets. The defect count is >100 and their area is about 10^{-4} to 10^{-3}. For a 100 cm^2 patterned area, a defect of size 10^{-4} - 10^{-3} corresponds to 0.01 – 0.1 cm^2.

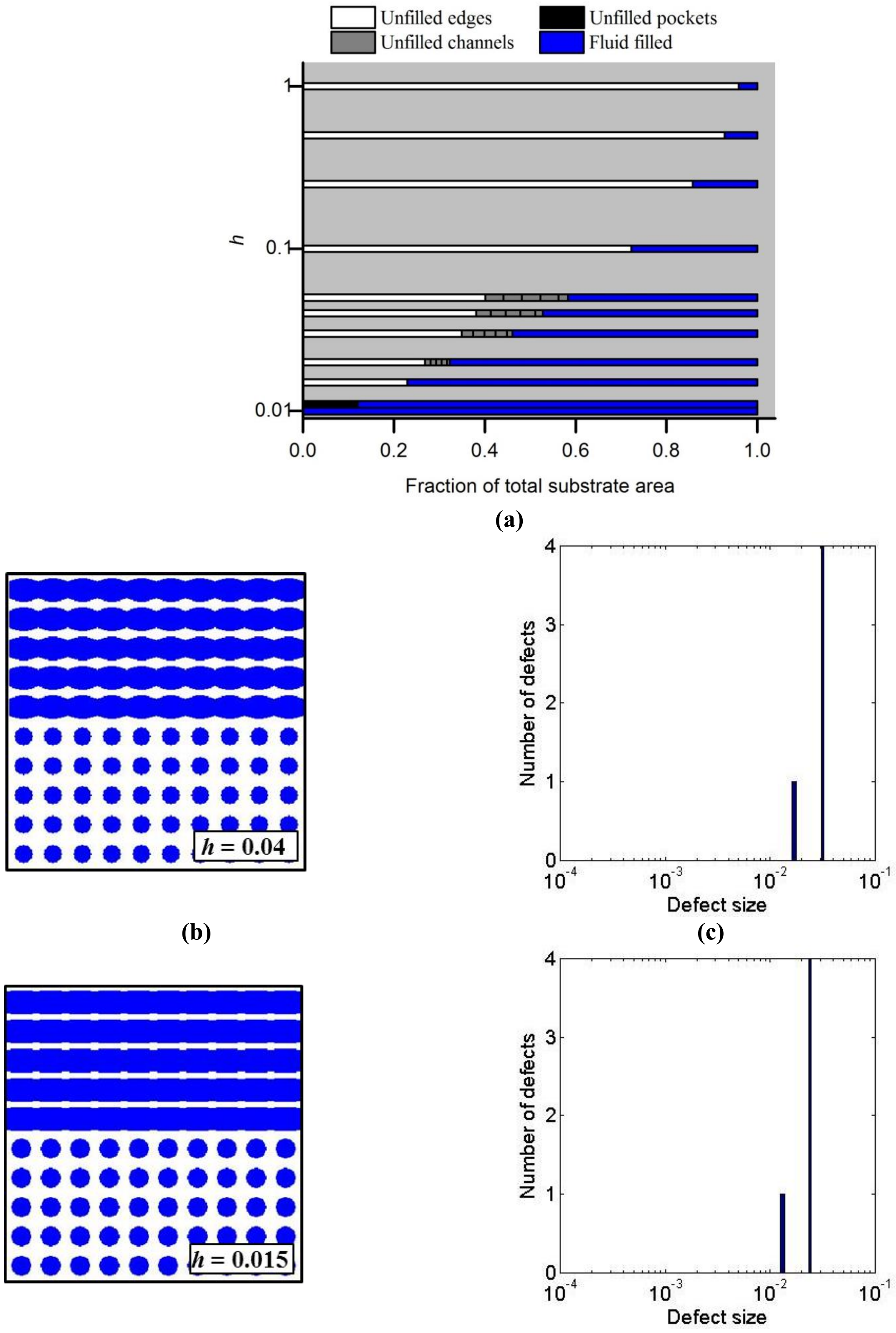

(a)

(b) **(c)**

(d) **(e)**

Figure 4.16: continued next page

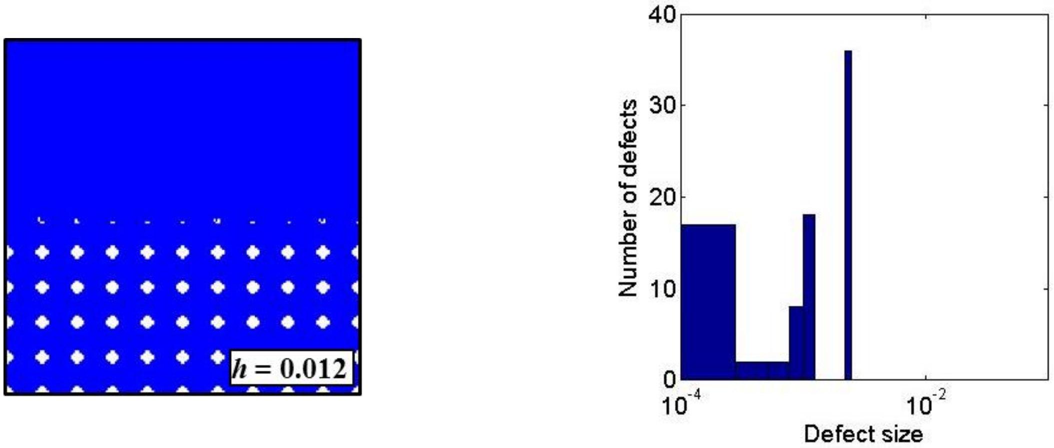

(f) (g)

Figure 4.16: (a) Figure shows the fraction of the area of substrate with unfilled region and fluid-filled region for SFIL with 100 drops and template I. The droplets are dispensed under pattern scheme 2. Figures (b)-(g) show count and area of unfilled region at different times close to the end of the imprint process. The gap closes from a height *h* = 1 to *h* = 0.01 and height of the patterns in the upper section of the template Δ*h* = 0.1.

In scheme 2, unfilled channels are created before unfilled pockets, while in scheme 1, unfilled pockets were formed first. This indicates that insufficient imprint time will lead to channel defects in the upper section of the substrate for scheme 1 and pocket defects in the lower section of the substrate for scheme 2. Channel defects are small in number but take longer to fill while pocket defects are larger in number but fill faster. Since the imprint time required for scheme 2 is shorter than that of scheme 1, if both processes were allowed the same fill time, channel defects will be present in the final pattern from scheme 1 while resultant pattern from scheme 2 will be defect free. Same result can be expected for template II under the two schemes, since the imprint time does not differ significantly between template I and II.

4.3.4 Effect of Sidewalls on Droplet Spreading

The sidewalls affect the fluid flow in a direction parallel to the line patterns as they increase the surface of contact between the fluid and the template. The flow permeability in the direction parallel to the flow is recalculated taking into account the sidewalls in the Appendix. The flow permeability is given by

$$k_{xx} = h^2 \frac{1+\left(1+\Delta h/h\right)^3 \left(d/\psi\right)}{1+d\left(1+\Delta h/h\right)}, \tag{4.16}$$

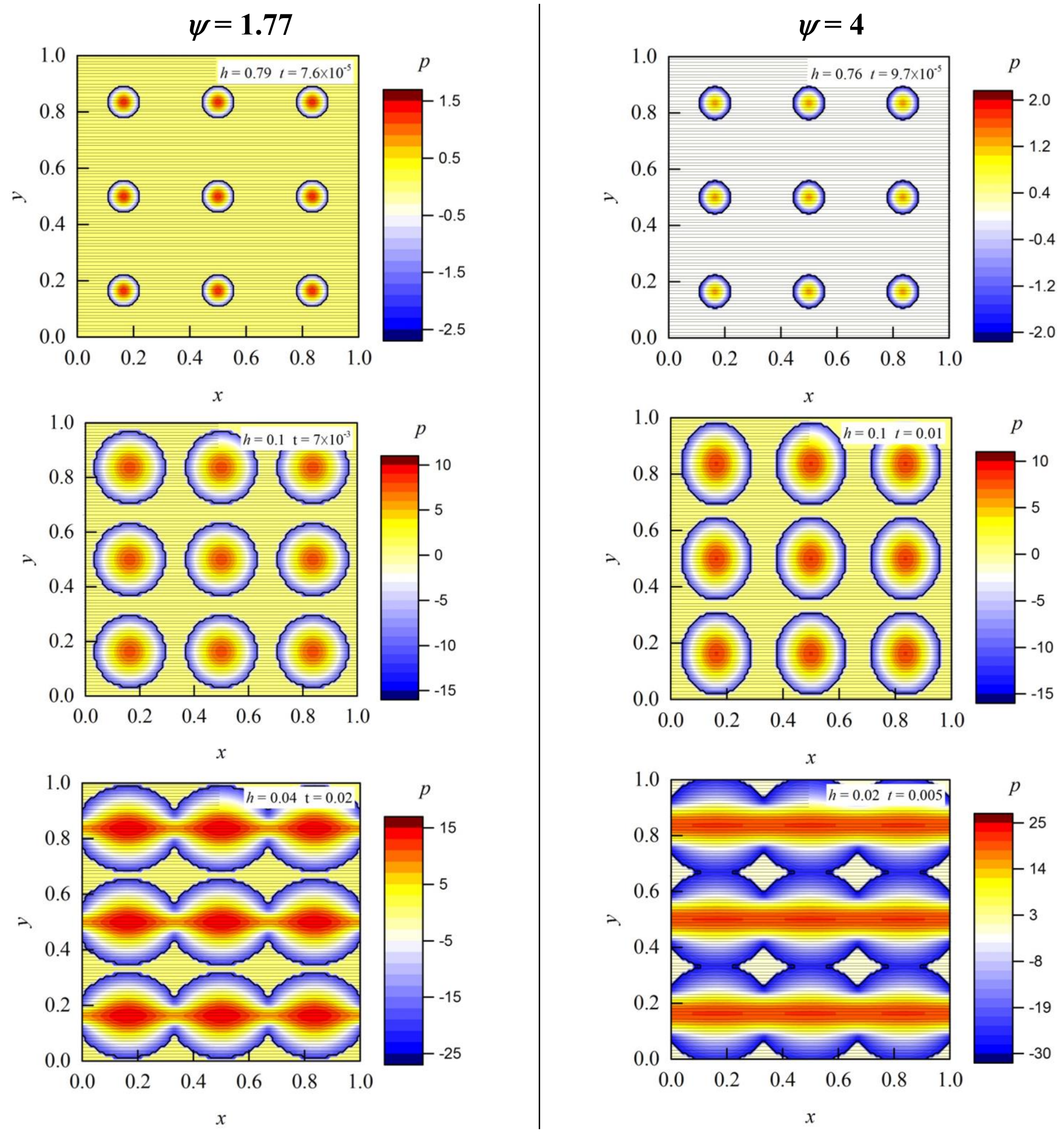

$\psi = 1.77$

$\psi = 4$

Figure 4.17: Contour map shows simulation of nine drops spreading on a substrate as the gap closes from h = 1 to h = 0.01. The feature height Δh is 0.1. The value of ψ = 1.77 (left) and ψ = 4 (right). The template has line and space patterns and has net zero force acting on it. The horizontal lines show the direction of the patterns (not to scale). The droplet spreads faster in the x direction compared to y direction.

where, $\psi = \left(1 + \left(\Delta h/\bar{d}_2\right)\left(H_o/L\right)\right)^2$. $\bar{d}_2$ is dimensionless grating width given by $\bar{d}_2 = d_2/L$ (refer to Figure 4.2 (a)). As the ratio of pattern height to pattern width increases, ψ becomes larger. When ψ = 1, we get back k_{xx} for flow without sidewalls. The effect of sidewalls on flow in the direction perpendicular to the patterns can be neglected by assuming negligible entrance and exit lengths as the fluid flows in the gaps. The permeability k_{yy} in the y direction remains the same and is given by Equation (4.13).

Figure 4.17 shows spreading of 9 droplets in SFIL with line and space patterned template with ψ = 1.77 (left) and ψ = 4 (right). When ψ = 1.77, the pattern width is three times the pattern height. When ψ = 4, the pattern width and pattern height are equal. In both cases, the pattern height is Δh = 0.1. We find that initially the flow is slightly higher in the direction perpendicular to the patterns as k_{yy} is larger than k_{xx} (as shown in Figure 4.18) As the gap closes, k_{xx} becomes significantly larger than k_{yy} resulting in faster fluid flow in the direction parallel to the patterns and merging of droplets. After this stage the droplets spread slowly in the direction normal to the pattern. Similar droplet spreading profile was observed when the sidewalls were neglected.

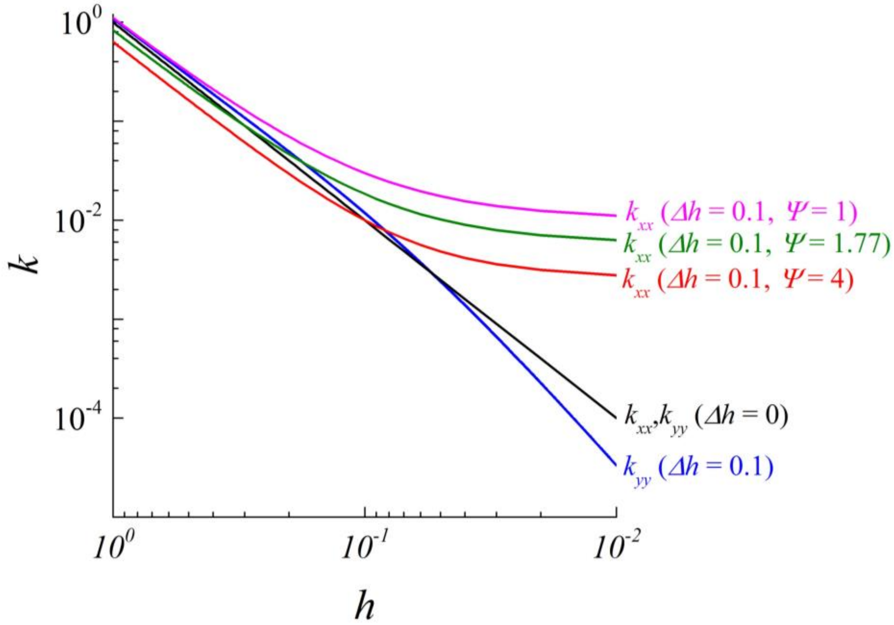

Figure 4.18: Permeability k_{xx} and k_{yy} in the x and y direction respectively with and without the effect of sidewalls. As the gap closes, k_{xx} is larger for smaller ψ suggesting that the flow in the x direction increases as ψ becomes smaller. k_{yy} is assumed to be independent of ψ.

Figure 4.19 shows the gap height at different time for $\psi = 1$, 1.77 and 4 and $\Delta h = 0.1$ (left) and 0.01 (right). The effect of sidewalls can be observed by comparing results for $\psi = 1$ (no sidewalls) with $\psi = 1.77$ and $\psi = 4$. For $\Delta h = 0.01$ and $\psi = 4$, pattern height and pattern width both are 10 nm when initial gap height $H_o = 1$ μm. For SFIL with substrate length $L = 10$ cm, resist viscosity $\mu = 0.001$ Pa.s and surface tension $\gamma = 70$ dyne/cm, characteristic time $6\mu L^2/\hat{\gamma} H_o = 857$ seconds. Figure 4.19 suggests that for $\Delta h = 0.01$, SFIL process with 100 droplets takes about 51 seconds if $\psi = 4$ and 48 seconds if $\psi = 1$. For $\Delta h = 0.1$ and $\psi = 4$, pattern height and pattern width both are 100 nm. The simulations predict that for $\Delta h = 0.1$, the overall imprint time is 66 seconds for $\psi = 4$ and 78 seconds if $\psi = 1$. This shows that sidewalls have small impact on the imprint time.

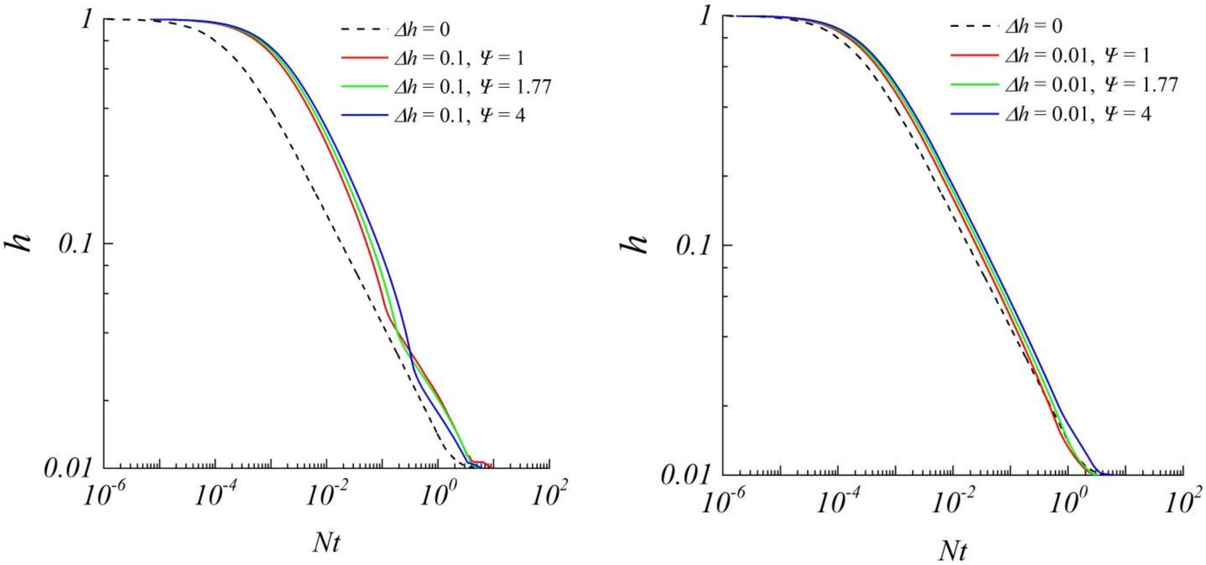

Figure 4.19: Imprint time scaled with the number of droplets in SFIL with $\psi = 1$, 1.77 and 4. A value of ψ is equivalent to neglecting the effect of sidewall. The results are shown for $\Delta h = 0.1$ (left) and $\Delta h = 0.01$ (right).

4.4. CONCLUSIONS

A model for SFIL with a patterned template is presented to simulate droplet spreading and analyze the defectivity. An average permeability is calculated to take into account the effect of fluid flow around features. For line and space patterns, the droplet spread faster in the direction parallel to the patterns due to increase in permeability while the flow in the direction normal to the patterns is slow leading to intermediate elliptical droplets and potential unfilled channel defects. The flow anisotropy and overall imprint time increase with the pattern height. Simulation is carried out for SFIL with templates which are pattern free in one half and are covered with line and space patterns on the other half. Two drop pattern schemes are explored for SFIL with these multi-patterned templates to optimize the process for minimum imprint time. It is found the dispensing the drops such that the droplets have sufficient volume to fill the gap locally leads to shorter imprint times compared to dispensing equal volumes of droplets on the entire substrate. Defect characterization for SFIL with multi-patterned template is presented. The unfilled defects can be categorized into: (i) unfilled edges that are formed at the edge of the substrate (ii) unfilled pockets that are formed when gas gets trapped within the resist and (iii) unfilled channels that are edge to edge defects formed due to anisotropic drop spreading. The type of defects, their count and size in SFIL with a multi-patterned template in two drop pattern schemes are predicted. A model to simulate flow taking into account the effect of sidewalls is also presented. It is shown that sidewalls have small impact on the imprint time and flow profile. This computational tool can help make better design decisions for creating templates and drop dispensing strategies that improve throughput and defect rate.

4.5. APPENDIX

A. Flow Permeability for Patterned Template

Figure 4.20: Schematic showing template with line and space patterns with width d_1 and d_2 respectively. The minimum and maximum gap between the template and the substrate at any time is H_1 and H_2 respectively.

Figure 4.20 shows a template with lines and space patterns. The feature height is ΔH and width of lines and spaces is d_1 and d_2 respectively. The minimum and maximum gap between the template and the substrate at any time is H_1 and H_2 respectively. At time $t = 0$, the gap $H_1 = H_o$ and $H_2 = H_o + \Delta H$. The governing Equations (4.1) and (4.2) can be written as

$$\frac{dH}{dT} = \frac{\partial}{\partial X}\left(\frac{K_{xx} H_{avg}}{\mu} \frac{\partial P}{\partial X}\right) + \frac{\partial}{\partial Y}\left(\frac{K_{yy} H_{avg}}{\mu} \frac{\partial P}{\partial Y}\right), \tag{A.1}$$

$$U_x = -\frac{K_{xx} \nabla P}{\mu}, \tag{A.2}$$

and

$$U_y = -\frac{K_{yy} \nabla P}{\mu}, \tag{A.3}$$

where U_x and U_y are vertically averaged velocities along x and y directions. The total volume flux q_x in the x direction can be written as

$$q_x = U_x H_{avg} \left(d_1 + d_2\right) \tag{A.4}$$

where,

$$H_{avg} = \frac{H_1 d_1 + H_2 d_2}{d_1 + d_2}, \tag{A.5}$$

q_x can also be written as

$$q_x = U_{1x} H_1 d_1 + U_{2x} H_2 d_2 \tag{A.6}$$

where U_{1x} and U_{2x} are vertically averaged velocity in the gap H_1 and H_2 given by

$$U_{1x} = -\frac{H_1^2}{12} \frac{\nabla P}{\mu} \tag{A.7}$$

and

$$U_{2x} = -\frac{H_2^2}{12}\frac{\nabla P}{\mu}. \tag{A.8}$$

Combining Equations (A.4)-(A.8), we get

$$U_x = -\frac{H_1^3 d_1 + H_2^3 d_2}{12\left(H_1 d_1 + H_2 d_2\right)}\frac{\nabla P}{\mu}. \tag{A.9}$$

Using Equation (A.2), we find that K_{xx} is given by

$$K_{xx} = \frac{H_1^3 d_1 + H_2^3 d_2}{12\left(H_1 d_1 + H_2 d_2\right)}. \tag{A.10}$$

The vertically averaged flow U_y in the y direction is given by

$$U_y = -\frac{H_{avg}^2}{12}\frac{\nabla P}{\mu} \tag{A.11}$$

where

$$\nabla P = \frac{d_1 \nabla P_1 + d_2 \nabla P_2}{d_1 + d_2} \tag{A.12}$$

Vertically averaged velocities in the y direction U_{1y} and U_{2y} in the gap H_1 and H_2 are given by

$$U_{1y} = -\frac{H_1^2}{12}\frac{\nabla P_1}{\mu} \tag{A.13}$$

and

$$U_{2y} = -\frac{H_2^2}{12}\frac{\nabla P_2}{\mu}. \tag{A.14}$$

For a continuous flow in the y direction,

$$U_y H_{avg} = U_{1y} H_1 = U_{2y} H_2 \tag{A.15}$$

Combining Equations (A.11)-(A.15) gives

$$U_y = \frac{1}{12 H_{avg}}\frac{d_1 + d_2}{\frac{d_1}{H_1^3} + \frac{d_2}{H_2^3}}\frac{\nabla P}{\mu} \tag{A.16}$$

Using Equation (A.3), we find that K_{yy} is given by

$$K_{yy} = \frac{1}{12H_{avg}} \frac{d_1 + d_2}{\frac{d_1}{H_1^3} + \frac{d_2}{H_2^3}} \tag{A.17}$$

The capillary pressure at the interface needs to be recalculated to take into account the effect of varying gap height. The capillary pressure at the interface in the gap H_1 and H_2 is given by

$$P_{interface} = P_{atm} - \frac{2\hat{\gamma}}{H_1} \tag{A.18}$$

and

$$P_{interface} = P_{atm} - \frac{2\hat{\gamma}}{H_2} \tag{A.19}$$

where P_{atm} is the atmospheric pressure, $\hat{\gamma}$ is $\gamma\left(cos\,\theta_1 + cos\,\theta_2\right)/2$ and γ is the surface tension of the imprint resist. θ_1 and θ_2 are the contact angles of the fluid with the template and the substrate respectively. Since each droplet spans hundreds or thousands of patterns the capillary pressure can be averaged over the template to calculate a net effect. Averaging over the pitch d_1+d_2, the capillary pressure at the interface can be written as

$$P_{interface} = P_{atm} - \frac{\frac{2\hat{\gamma}}{H_1} d_1 + \frac{2\hat{\gamma}}{H_2} d_2}{d_1 + d_2}, \tag{A.20}$$

or,

$$P_{interface} = P_{atm} - \frac{2\hat{\gamma}}{\hat{H}}, \tag{A.21}$$

where,

$$\hat{H} = \frac{d_1 + d_2}{\frac{d_1}{H_1} + \frac{d_2}{H_2}}, \tag{A.22}$$

We can non-dimensionalize the governing equations and boundary conditions putting $H_1 = H$, $H_2 = H + \Delta H$, $d = d_2/d_1$, $p = P/P_c$, $h = H/H_c$, $v = V/V_c$, $\mathbf{u} = \mathbf{U}/U_c$ and $\mathbf{k} = \mathbf{K} / H_c^2$. The characteristic values of the variables are given by : $P_c = 2\hat{\gamma}/H_o$, $H_c = H_o$, $T_c = 6\mu L^2/\hat{\gamma} H_o$, $V_c = \hat{\gamma} H_o^2 / 6\,\mu L^2$ and

$U_c = \hat{\gamma} H_o / 6 \mu L$ where H_o is the initial gap. The x and y coordinates are non-dimensionalized using the length of the template L. This gives

$$\frac{dh}{dt} = \frac{\partial}{\partial x}\left(k_{xx} h_{avg} \frac{\partial p}{\partial x} \right) + \frac{\partial}{\partial y}\left(k_{yy} h_{avg} \frac{\partial p}{\partial y} \right), \tag{A.23}$$

$$u_x = -k_{xx} \nabla p, \tag{A.24}$$

$$u_y = -k_{yy} \nabla p \tag{A.25}$$

where

$$h_{avg} = h\left(\frac{1 + (1 + \Delta h/h) d}{1 + d} \right), \tag{A.26}$$

$$k_{xx} = h^2 \frac{1 + (1 + \Delta h/h)^3 d}{1 + d(1 + \Delta h/h)}, \tag{A.27}$$

and

$$k_{yy} = h^2 \left(\frac{1 + d}{1 + (1 + \Delta h/h)^{-3} d} \right)\left(\frac{1 + d}{1 + (1 + \Delta h/h) d} \right) \tag{A.28}$$

The dimensionless pressure boundary condition is

$$p_{interface} = -\frac{1}{\hat{h}} \tag{A.29}$$

where $\hat{h}$ is given by

$$\hat{h} = h \frac{1 + d}{1 + \frac{d}{1 + (\Delta h/h)}} \tag{A.30}$$

B. The Effect of Pattern Sidewalls on Flow Permeability

The pressure gradient ∇P in a fluid with density ρ across a conduit with cross-sectional area A_c and wetting perimeter L_p is given by

$$\nabla P = \frac{\frac{1}{2}\rho U^2 f}{A_c / L_p} \tag{B.1}$$

where U is the average fluid velocity and f is the friction factor. The friction factor for laminar flow through rectangular conduits is given by

$$f = \frac{24}{Re} \tag{B.2}$$

where $Re = \rho U D_h / \mu$ and characteristic length, $D_h = 4A_c / L_p$. Applying the expression for f in Equation (B.1) we find

$$U = \frac{1}{3\mu}\left(\frac{A_c}{L_p}\right)^2 \nabla P \tag{B.3}$$

As shown in Figure 4.19, for flow through gap with width d_2 and height H_2, $A_c = H_2 d$ and $L_p = 2(d_2 + \Delta H)$. Using this expression, we can rewrite the vertically averaged velocity U_{2x} given by Equation (A.8) as

$$U_{2x} = -\frac{H_2^2}{12}\frac{1}{\left(1+\Delta H/d_2\right)^2}\frac{\nabla P}{\mu}. \tag{B.4}$$

Repeating the analysis presented in section A of the appendix with this expression for U_{2x}, we find that k_{xx} is given by

$$k_{xx} = h^2 \frac{1+\left(1+\Delta h/h\right)^3 \left(d/\psi\right)}{1+d\left(1+\Delta h/h\right)}, \tag{B.5}$$

where $\psi = \left(1+\left(\Delta h/\bar{d}_2\right)\left(H_o/L\right)\right)^2$ and $\bar{d}_2 = d_2/L$. When $\psi = 1$, we get back k_{xx} for flow without sidewalls given by Equation (A.28). The permeability k_{yy} in the y direction, remains the same and is given by Equation (A.29).

Chapter 5: Fluid-structure Interaction in Nanoimprint Lithography on a Flexible Substrate

5.1. INTRODUCTION

Flexible substrates patterned with nano- and micro-patterns enable various applications in optics [67, 69, 128], photovoltaics [70, 129, 130] and biology [131-133]. Step roll-to-roll nanoimprint lithography (R2RNIL) is a process based on batch nanoimprint lithography to replicate nano- and micro-scale patterns from the surface of a stepper template to a large area flexible substrate. A typical set up of Step R2RNIL consisting of a stepper template, a flexible substrate (also called "web"), an imprint dispenser unit, imprint material, and a UV/thermal curing module is shown in Figure 5.1. The process is very similar to Step and Flash Imprint Lithography. The inkjet dispenser dispenses photo-curable resist droplets on the substrate which is held under tension between two rollers. The patterned template is lowered on the droplets until they merge together to form a uniform resist film. Once the fluid spreading is complete and the entire template is filled, UV light is irradiated on the resist to photo-polymerize the resist monomer into a solid film. The template is then peeled off from the resist by a precise and synchronized movement of the substrate roll and the template, starting on one side and ending on the other side of the template. This process is repeated multiple times on different portions of the substrate to imprint a large area on the substrate.

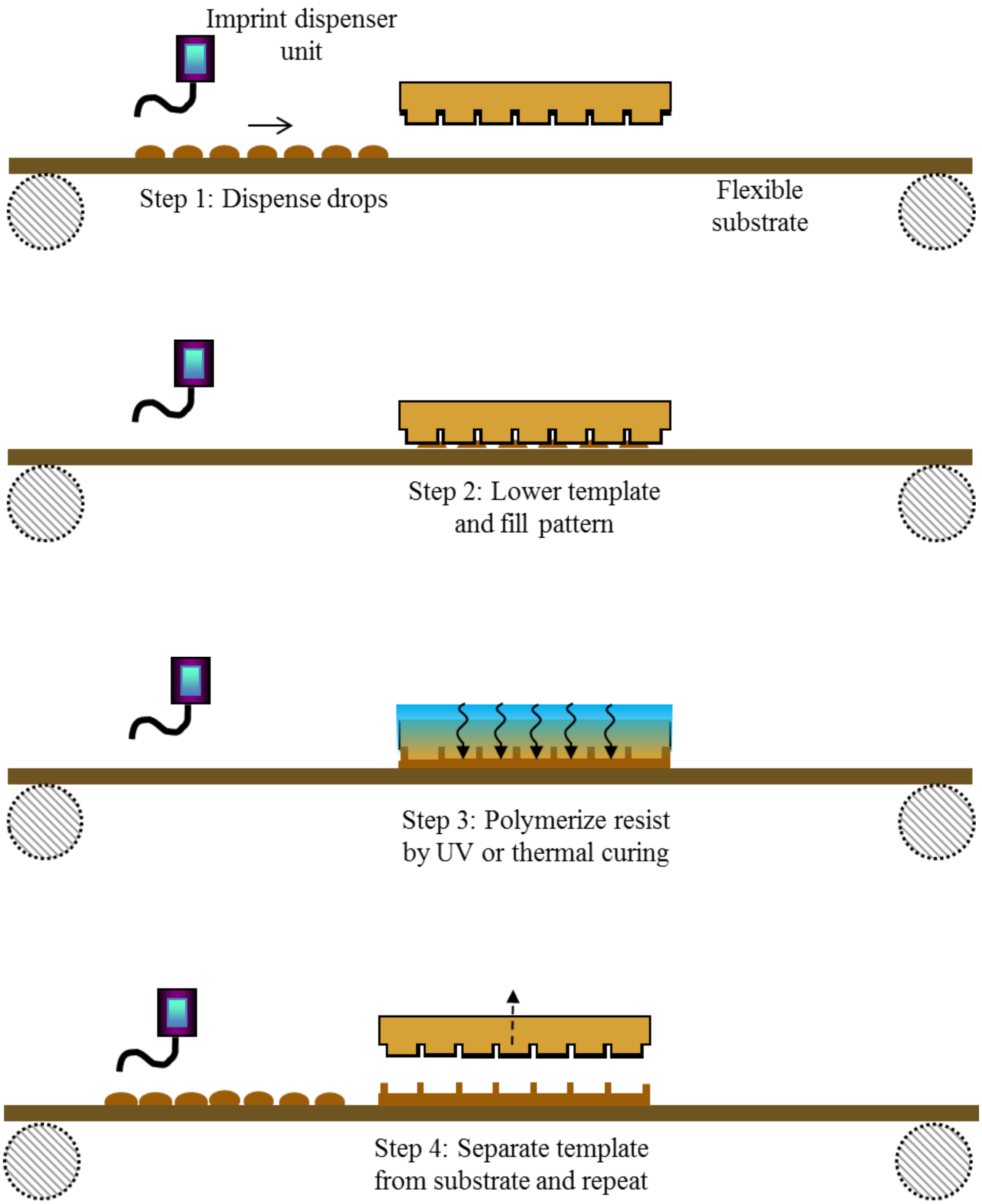

Figure 5.1: Schematic showing steps involved in roll-to-roll nanoimprint lithography with a stepper template on a flexible substrate.

Lithoflex 100 and LithoFlex 350 are Step R2RNIL tools that use inkjet dispensing and UV curing module to imprint on a polycarbonate film. Ahn *et al.* used LithoFlex 100 to fabricate bilayer wire grid polarizers by patterning 50 nm half pitch line gratings on the polycarbonate film as shown in Figure 5.2. The tool can be used with 50 mm x 50 mm or 75 mm x 75 mm stepper template to pattern flexible substrates up to 80 mm wide. They also demonstrated imprinting of 100 nm dense pillars and 25 nm holes using this tool. The throughput of the system was as much as 180 imprints per hour.

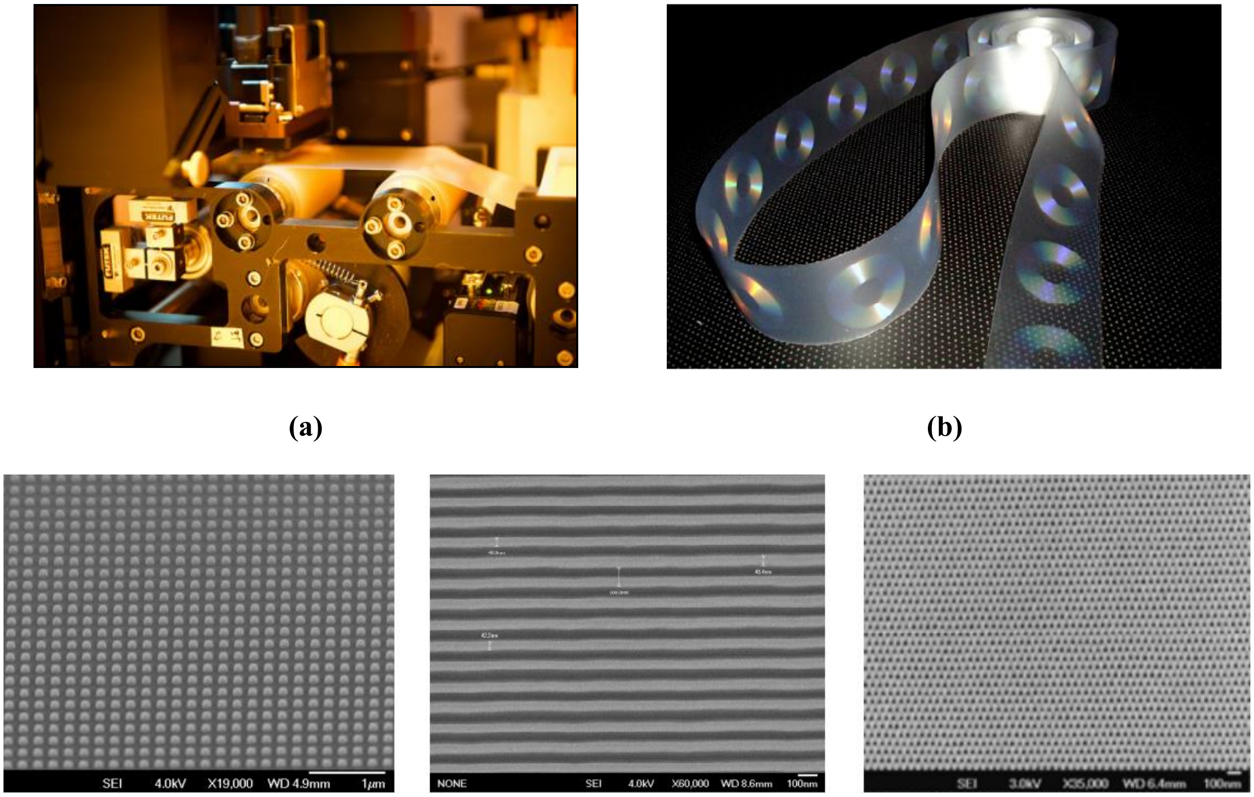

(a) **(b)**

(c) **(d)** **(e)**

Figure 5.2: (a) Step R2RNIL prototype tool Lithoflex 100 (b) 10 meters of 80 mm wide polycarbonate film patterned using Lithoflex 100. (c) 100 nm dense pillar, (d) 50 nm half pitch lines and (e) 25 nm dense holes patterned using Lithoflex 100 [16].

LithoFlex 350 has a web width of 350 mm and template width of 300 mm [35]. Ahn *et al.* created 300 mm wide flexible wire-grid polarizers using this tool by patterning 50 nm line gratings on polycarbonate web at web speed of about 1 m/min (Figure 5.3).

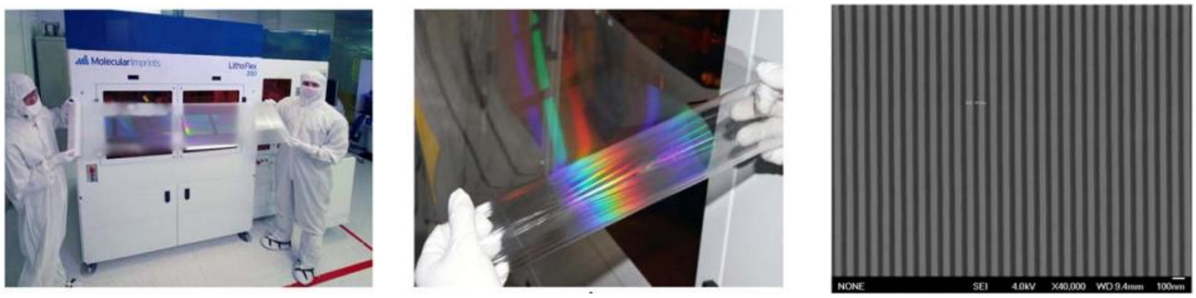

(a) (b) (c)

Figure 5.3: (a) Multiple fields of 300 mm width on a 350 mm polycarbonate film patterned using LithoFlex 350. (b) Close-up of the imprinted pattern. (c) 50 nm half pitch line grating for application in wire grid polarizers [35].

Step R2RNIL leverages existing wafer scale Step and Flash Imprint Lithography (SFIL) and demonstrates potential for high throughput pattern replication. However, considerable challenges remain in terms of throughput and residual layer thickness uniformity before the process can be successfully implemented in the industry. The throughput of 1 m/min achieved by Ahn *et al.* with a 300 mm wide substrate using LithoFlex 350 is the highest throughput reported with Step R2RNIL [35]. A technology roadmap projects industrial manufacturing of flexible displays of area 3000 cm^2 by 2019 to meet market demand [44]. The throughput of the Step R2RNIL needs to be improved by imprinting larger area and increasing web speed while maintaining pattern quality. The throughput of Step R2RNIL is limited by fluid filling and spreading. Understanding these steps in the light of the fluid flow, structural mechanics and operating parameters like pressure, temperature, UV intensity etc. is the key to improving the throughput.

The residual layer thickness (RLT) is a layer of resist left behind after the imprinting process. It is important for high quality pattern replication and performance of devices. During the etching process, the residual layer is removed. Thinner and more uniform RLT require lesser time for etching and minimize degradation of the resist pattern. Therefore, a thinner and more uniform RLT is preferred in order to minimize its impact on the pattern.

The flexibility of the substrates makes it challenging to control the residual layer during the nanoimprinting process. The RLT of 12 nm achieved by Ahn et al. on a 80 mm wide substrate is the smallest RLT reported using Step R2RNIL [16]. However the size of the imprint area is inadequate for applications which require large area substrates. Various factors can influence residual layer thickness and uniformity like web tension, fluid dispensing scheme, position of the template on the substrate, applied pressure etc. Studying fluid spreading on flexible substrate taking into account the effect of these physical parameters can help understand the RLT variation during the R2RNIL process.

Previously Sirotkin *et al*. presented a coarse-grain method for simultaneous calculation of the flow of highly viscous resist (viscosity 10^4 Pa.s) and deformation of the stamp and substrate [52-56] in nanoimprint lithography. They simulated the residual layer thickness and pressure distribution for templates with a complex layout assuming the template and the substrate to be elastic plates. They compared the simulated and experimental results and were able to predict the residual layer thickness variation with 10% precision [54].

Singhal *et al.* used thin film theory to create a 1D model for multi-scale fluid phenomena in a new process called Jet and Coat of Thin-films (JCT) which is very similar to Step and Flash Imprint Lithography (SFIL) [134]. They proposed a model incorporating thin film fluid flow, elastic bending of template and substrate deformation in order to study the time scale for imprinting process [135]. They found that lower web tensions lead to higher time scales and that changing the substrate thickness has small impact on the time scale. This model assumed periodic boundary condition for web deformation and did not take into account that the substrate is fixed at the edge. Measuring RLT variation is difficult because of metrology challenges. The index of refraction of the imprint monomer is close to the web material making optical measurements difficult. Also, unlike silica substrates, flexible substrates cannot be cleaved for cross-sectional viewing which makes metrology challenging. Kincaid *et al.* overcame these challenges by transferring the imprinted layer from the flexible substrate onto a wafer using a substrate transfer process [136]. They were able to measure the RLT and standard deviation in

RLT by examining SEM images of the resist cross-section. They performed experiments with different values of template velocity, pitch and imprint to find the optimum set of values for these parameters. The study provides an insight on the sensitivity of the process towards these process parameters; for example, a combination of low template speed, large droplet pitch and long spread time is shown to reduce error in RLT and RLT variation. However, the physics of fluid-structure interaction remains to be studied in details.

Web tension, number of droplets, position of the template on the substrate and applied pressure can have a strong influence on the deformation of the thin substrate used in Step R2RNIL. The effect of these physical parameters on the final residual layer thickness, its uniformity and the overall imprint time in Step R2RNIL is not very well understood. Here we develop a model to study the interaction of fluid spreading on a substrate under web tension. We study the effect of number of droplets and different web tension on the web deformation and RLT. In the end, we study the effect of template position relative to the substrate on RLT variation.

5.2. SIMULATION METHOD

Figure 5.4 shows a schematic of Step R2RNIL on a flexible substrate. The flexible substrate is held under uniform web tension in the X and Y direction. The droplets are inkjetted on the portion of the substrate that is to be patterned (bordered by white dashed line). As the template approaches the substrate, the droplet spreads and the pressure exerted by the droplets deforms the substrate. As the template lowers, the gap is filled completely with the resist and the deformation in the web results in a resist with non-uniform RLT.

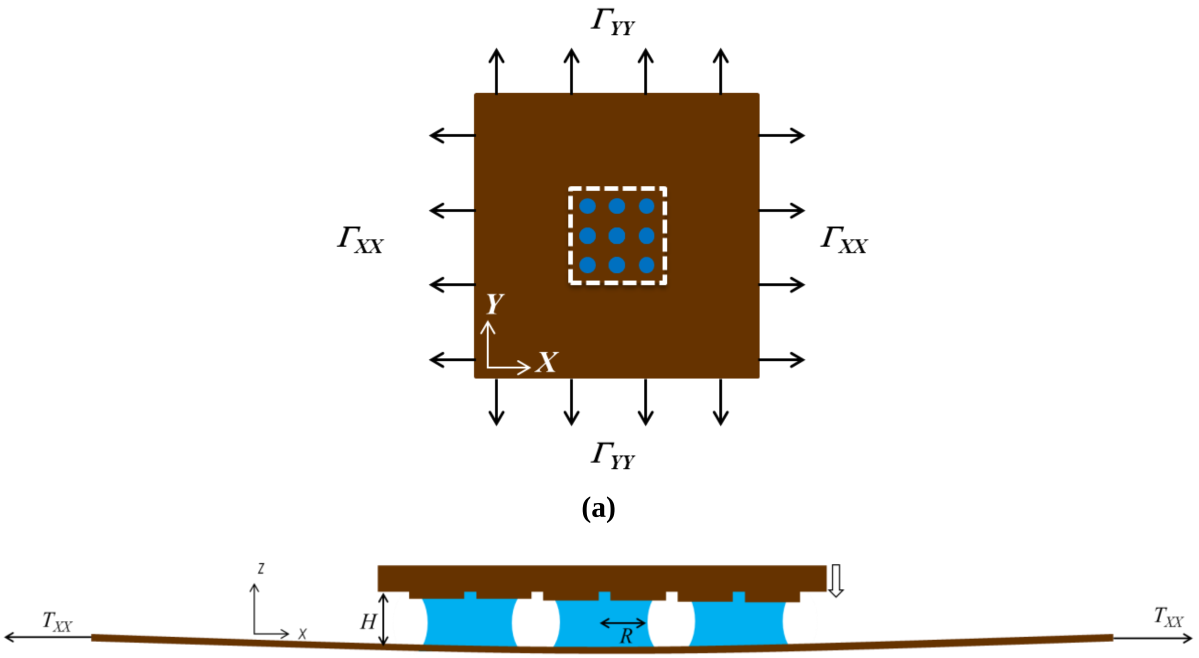

(a)

(b)

Figure 5.4: (a) Top view shows droplets dispensed on the substrate with tension Γ_{XX} and Γ_{YY} acting in the *X* and *Y* directions respectively. The white dashed line borders the area to be patterned. (b) Side view shows the droplets of radius *R* in a gap height *H(x)* between the flexible substrate and template.

A schematic of web deformation *W(X,Y)* on a substrate of length L_s is shown in Figure 5.5. The length of the template is *L* and it size is same as the patterned area. The length of the substrate L_s can be 3 to 4 times larger the length of the template *L*. The height of the gap between the template and the substrate at any time is given by

$$H = H_{edge} - W \tag{5.1}$$

where H_{edge} is the height of the template measured from the edge of the substrate. The substrate is assumed to be fixed along the edges, therefore, $W = 0$ along the edges. For a template velocity -*V*,

$$\frac{dH}{dT} = -V - \frac{dW}{dT} \tag{5.2}$$

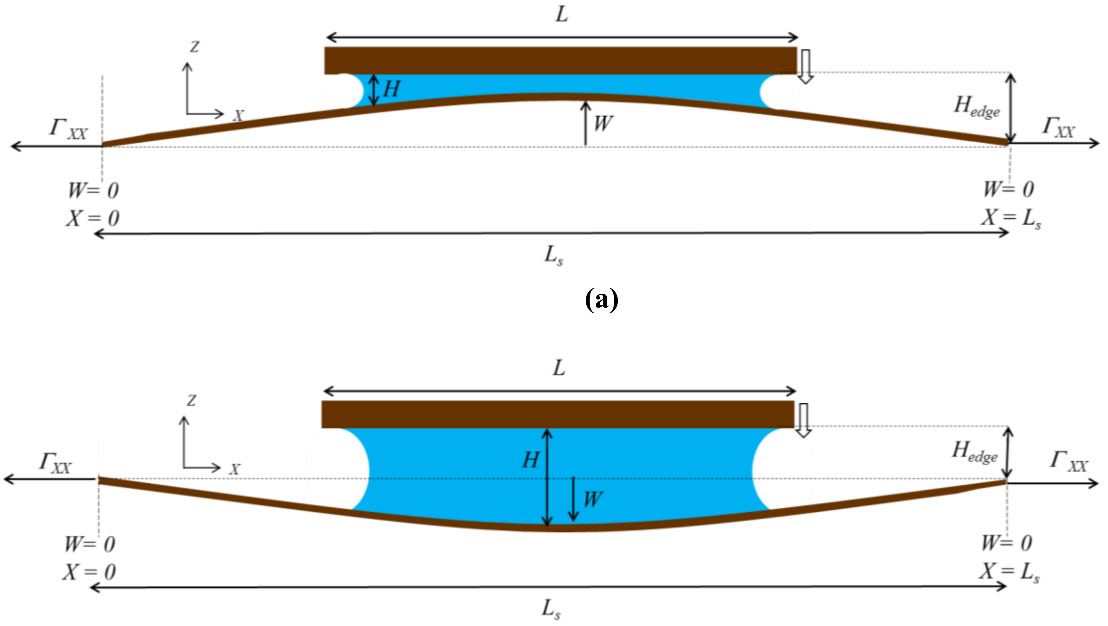

(a)

(b)

Figure 5.5: A schematic showing the gap *H* between the substrate and the template. *W* is the web deformation. The web deformation *W* = 0 at *X* = 0 and *X* = *L*. *W* is positive (a) when pressure pulls the substrate towards the template and negative (b) when it pushes the substrate away from the template. *L* and L_s are the length of the template and the substrate respectively. H_{edge} is the height of the template measured from the edge of the substrate.

An average gap height H_{av} can be calculated by averaging the gap height H over the area between the template and the substrate. When the imprint process is complete, the resist completely fills the gap between the substrate and the template and H_{av} corresponds to the final RLT of the resist. For a final RLT of $H_{av,f}$ and N droplets, the required droplet volume Q is given by

$$Q = \frac{L^2 H_{av,f}}{N}. \tag{5.3}$$

The pressure and velocity fields, described using the Reynolds' lubrication theory are

$$\frac{\partial H}{\partial T} = \nabla \cdot \left(\frac{H^3}{12\mu} \nabla P \right), \tag{5.4}$$

$$\mathbf{U} = -\frac{H^2}{12\mu}\nabla P\,, \tag{5.5}$$

where P is the pressure in the droplet and μ is the viscosity of the imprint resist, $\mathbf{U}$ is the vertically averaged fluid velocity. The pressure at the liquid-air interface is given by

$$P_{interface} = P_{atm} - \frac{2\hat{\gamma}}{H}\,, \tag{5.6}$$

where P_{atm} is the atmospheric pressure, $\hat{\gamma}$ is $\gamma\left(cos\,\theta_1 + cos\,\theta_2\right)/2$ and γ is the surface tension of the imprint resist. θ_1 and θ_2 are the contact angles made by the fluid with the template and the substrate respectively.

The deformation of the flexible substrate can be described using plate theory as following

$$D\nabla^4 W - \Gamma\nabla^2 W = -P \tag{5.7}$$

where Γ is the web tension and bending stiffness, $D = Ed^3/12\left(1-\nu^2\right)$. Here E is the Young's modulus, d is the substrate thickness and ν is the Poisson ratio. Polyethylene Teraphthalate (PET), polycarbonate or polyimide is used as material for the flexible substrate [35]. For PET, the typical value of E = 2 - 2.7 GPa and ν = 0.37 – 0.44. The membrane thickness d is about 100-125 μm. For large web tension acting on thin plates, the bending stiffness is very small and the first term in Equation (5.7) is negligible compared to the second term (as shown in the appendix). Therefore we have

$$\Gamma\nabla^2 W = P\,. \tag{5.8}$$

This equation is referred to as the membrane equation. The boundary condition for membrane deformation is

$$W\big|_{edge} = 0 \tag{5.9}$$

since the substrate is fixed at the edge. The typical values of the parameters used for the Step R2RNIL process can be found in Table 5.1.

Table 5.1: Typical values of the parameters used for the Step R2RNIL process

Parameter	**Symbol**	**Typical value**
Surface tension	γ	30 dyne/cm
Viscosity	μ	0.003 - 0.005 Pa.s
Resist contact angle	$\theta_{1,2}$	$5 - 10^{\mathrm{o}}$
Template length	L	2.5 cm
Substrate length	L_s	10 cm
Initial gap	H_o	1 μm
Final gap	H_f	10-100 nm
Initial drop height	H_{drop}	1 μm
Initial drop radius	R_o	5 mm (1 droplet, H_{drop} = 1 μm) 500 μm (100 droplets, H_{drop} = 1 μm) 200 μm (1024 droplets, H_{drop} = 1 μm)
Web Tension	Γ	200 - 1000 N/m

The governing equations and boundary conditions [Equation (5.4-9)] can be non-dimensionalized using the characteristic values of the variables: $P_c = 2\hat{\gamma}/H_o$, $H_c = H_o$, $T_c = 6\mu L^2/\hat{\gamma}H_o$, $V_c = \hat{\gamma}H_o^2/6\mu L^2$, $U_c = \hat{\gamma}H_o/6\mu L$, $W_c = H_o$ and $\tau_c = 2\hat{\gamma}L^2/H_o^2$ where H_o is the initial gap. The x and y coordinates are non-dimensionalized using the length of the template L. The dimensionless governing equations are given by

$$\nabla\left(h^3\nabla p\right) = -\nu - \frac{dw}{dt} \tag{5.10}$$

$$\mathbf{u} = -h^2\nabla p \tag{5.11}$$

$$\tau \nabla^2 w = p \tag{5.12}$$

where, $p = P/P_c$, $h = H/H_c$, $v = V/V_c$, $w = w/W_c$, $\mathbf{u} = \mathbf{U}/U_c$ and $\tau = \Gamma/\tau_c$. The dimensionless boundary condition for pressure and web deformation are given by

$$p_{interface} = -\frac{1}{h} \tag{5.13}$$

$$w\big|_{edge} = 0 . \tag{5.14}$$

l_s and l are the dimensionless substrate and template width respectively. Using Equation (5.3), the dimensionless drop volume q for N droplets and an average RLT $h_{av,f}$ is given by

$$q = \frac{h_{av,f}}{N} . \tag{5.15}$$

The governing equations for pressure p and web deformation w are coupled since the pressure field in the fluid dictates the web deformation and the web deformation changes the local gap h which determines the pressure field. Due to this coupled nature of the problem, an iterative solution scheme is required to calculate the pressure and web deformation. The simulation is initiated using a guess for dimensionless template velocity v and assuming no deformation at time $t = 0$. Equation (5.10) is solved numerically for the pressure field using generalized minimal residual method (GMRES) method [123] which is an iterative method to solve non-symmetric linear systems. The total force on the template is calculated by integrating the pressure over the entire substrate. Then the template velocity is adjusted such that the viscous forces balance the capillary force and any externally applied force. The pressure field is then recalculated. Once the pressure field has been determined, Equation (5.12) is solved using GMRES method to calculate the substrate deformation while a pressure p and dimensionless web tension τ acts on it. The gap h is then updated to account for the web deformation and the pressure is recalculated. The template velocity is updated during pressure calculations to ensure that viscous forces balance the capillary force and other externally applied force. The pressure and deformation are solved iteratively till the new web deformation is within 1% of the solution from the last iteration. Once this convergence criterion is met, the total fluid fluxes in the x and y directions are determined using Equation (5.11) and the fluid is advanced using Volume of Fluid Method as described in Chapter 3. The web tension τ is assumed to be uniform in the x and y direction. It is assumed that buckling does not occur in the web since the web tension is uniformly distributed in x- and y- directions. These simulations are performed for up to 100 droplets. Simulation of more than 100 droplets exceeds the memory limit of Texas Advanced Computing Center (TACC).

5.3. RESULTS

5.3.1. Web Deformation due to Droplets on a Flexible Substrate

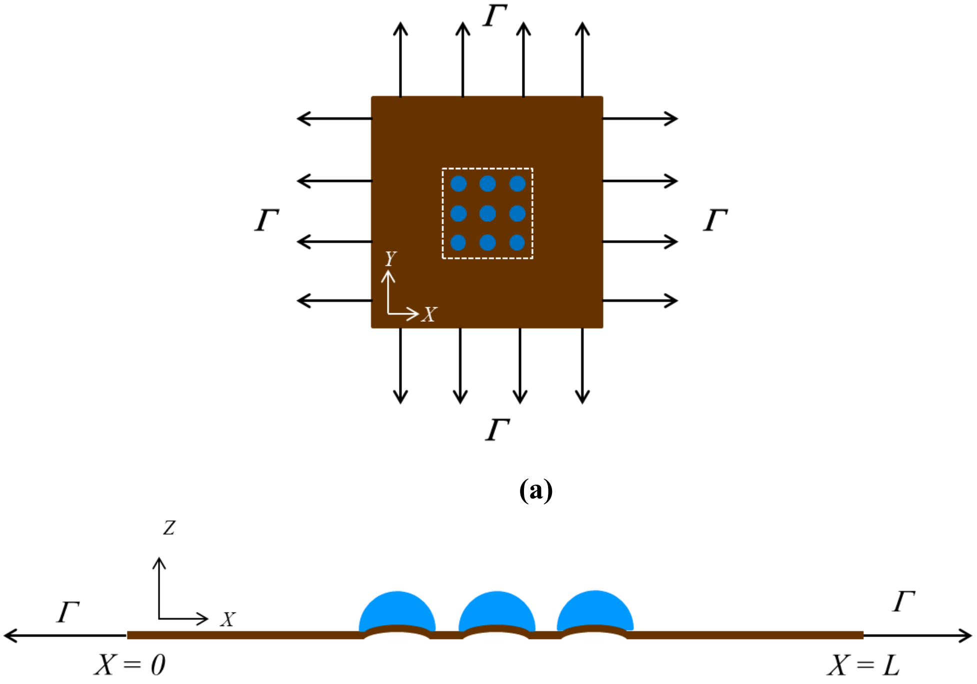

(a)

(b)

Figure 5.6: Top view (a) and side view (b) of droplets spread on a flexible substrate. The substrate has web tension Γ acting in both x and y directions.

Figure 5.6 shows the side view of droplets dispensed on a tensioned membrane. The membrane is fixed at the edge of the substrate and a web tension τ is acting in both *x*- and *y*-directions. Web deformation is calculated with different number of droplets and web tensions using Equation (5.12). The droplets are uniformly distributed at the center of the membrane in a square area of side one-third of the length of the membrane. The total volume of droplets is the same in all cases. The dimensionless pressure p inside the droplet is assumed to -1.

Figure 5.7(a) shows the deformation of the flexible substrate along y = 0.5. The web deformation decreases as the number of droplets or the web tension increases. An average web deformation over the substrate w_{av} can be calculated for each case. The plot of τw_{av} for different number of droplets in Figure 5.7 (right) shows that w_{av} decreases with increasing number of droplets. For $\Gamma = 10^6$ N/m, the average deformation w_{av} is 0.85 nm for 1 drop and 0.53 nm for 100 drop while the maximum deformation is 9.7 nm for 1 drop and 1.2 nm for 100 droplets. For $\Gamma = 10^5$ N/m, the average deformation w_{av} is 8.5 nm for 1 drop and 5.3 nm for 100 drop while the maximum deformation is 97 nm for 1 drop and 12 nm for 100 droplets. This result is important because it suggests that if simulations are carried out with a single drop and values of $\Gamma \leq 10^5$ N/m, large deformation of the web will occur. Step R2RNIL is carried out with web tension of 100 – 1000 N/m however since thousands of droplets are used the maximum deformation is small. For simulating membrane deformation with a single droplet, $\Gamma \geq 10^6$ N/m need to be used to realize realistic web deformation.

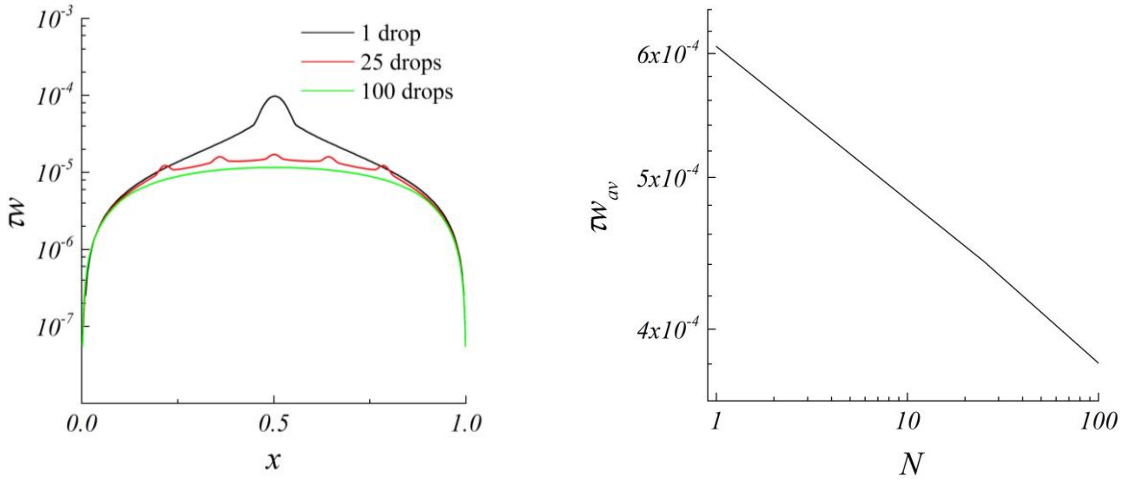

(a) **(b)**

Figure 5.7: (a) Web deformation on a flexible substrate of dimensionless length 1 along y = 0.5. The deformation decreases as the web tension and the number of drops increases. (b) The average deformation w_{av} over the substrate for different number of droplets and web tension τ. We find that as the number of droplets is increased, w_{av} decreases.

5.3.2. Web Deformation in Step R2RNIL on a Flexible Substrate

The droplet spreading and merging in Step R2RNIL is simulated as the gap between the substrate and the template closes from h = 1 to a final average gap h_{av} = 0.1. h = 1 corresponds to a gap of H = 1 μm. The initial volume of the droplet is selected such that the average RLT at completion of the SFIL process is equal to 0.1. The dimensionless web tension τ = 0.1 acts in the x and y direction. The width of the substrate L_s is three times the width of the template L i.e. l_s/l = 3. The template has zero net force acting on it. The gap height h and the pressure distribution in the droplet are plotted in Figure 5.8. The pressure is negative at the droplet interface due to the capillary pressure boundary described in Equation (5.13) and becomes positive at the center due to viscous effects. The net force from the droplet pushes the membrane outwards creating higher gap at the center of the droplet.

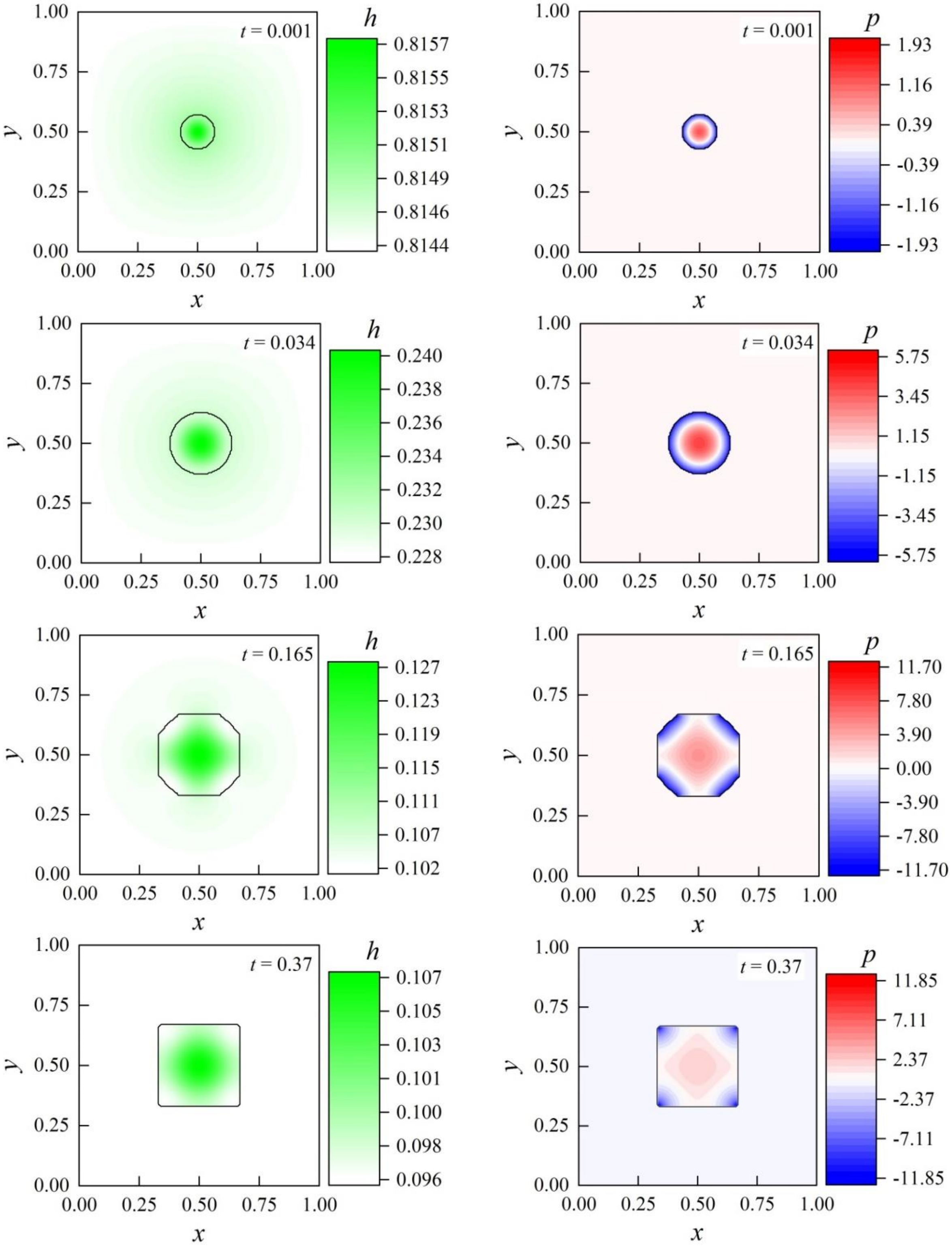

Figure 5.8: Contour map showing gap height *h* (left) and pressure *p* (right) for Step R2RNIL with one drop at time *t* = 0.001, *t* = 0.034, *t* = 0.165 and *t* = 0.37. The substrate has a web tension *τ* = 0.1 acting in *x* and *y* direction.

The plot of average gap height h_{av} over time is shown in Figure 5.9. The imprint time reduces with larger number of droplets. The inset in Figure 5.9 (a) shows that the imprint time increases as web tension reduces. For Step R2RNIL with template length L = 10 cm, initial gap height H_o = 1 μm, resist viscosity μ = 0.001 Pa.s and surface tension γ = 70 dyne/cm, characteristic time, T_c = 857 seconds. The total imprint time for SFIL with 9 drop and a rigid substrate is about 29 seconds. Imprint time for Step R2RNIL increases to 32 seconds and 36 seconds for $\Gamma = 10^9$ N/m and $5\text{x}10^7$ N/m respectively. For 100 droplets, the imprint time for rigid substrate is about 4.5 seconds and that for flexible substrate is about 3 seconds and 4 seconds for $\Gamma = 10^9$ N/m and $5\text{x}10^7$ N/m respectively.

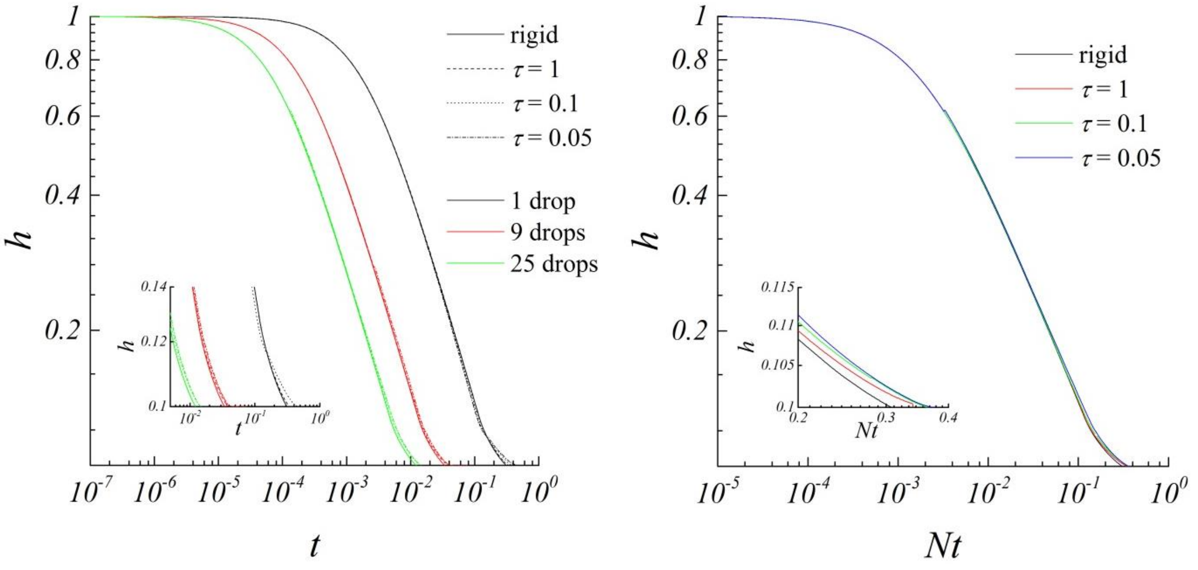

(a) **(b)**

Figure 5.9: (a) Plot of average gap height over for Step R2RNIL with multiple droplets. The simulation is carried out with τ = 1, 0.1 and 0.05. The solid line shows the imprint time for SFIL with rigid substrate. The template is pattern-free and has net zero force acting on it. The inset plot shows the imprint time close to the time of droplet merging. For a fixed number of droplets, the imprint time increases as the web tension reduces. (b) The plot of *h* vs. *Nt* shows that imprint time scales as 1/*N*. Thus, the total imprint time decreases as number of drops increases.

The plot of standard deviation of gap height σ_h with h_{av} for one droplet with τ = 1, 0.1 and 0.05 is shown in Figure 5.10(a). As the gap closes, σ_h increases until the end when σ_h reduces indicating a relatively more uniform gap. This decrease in σ_h can be explained by examining the pressure distribution. Figure 5.10(b) shows that the pressure at the droplet center p_c increases as the gap closes. Towards the end of the process, the droplets come in contact with the edge of the template and the no-flux boundary condition at the template edge leads to a more uniform and reduced pressure distribution. This results in a more uniform gap height and a reduction in σ_h.

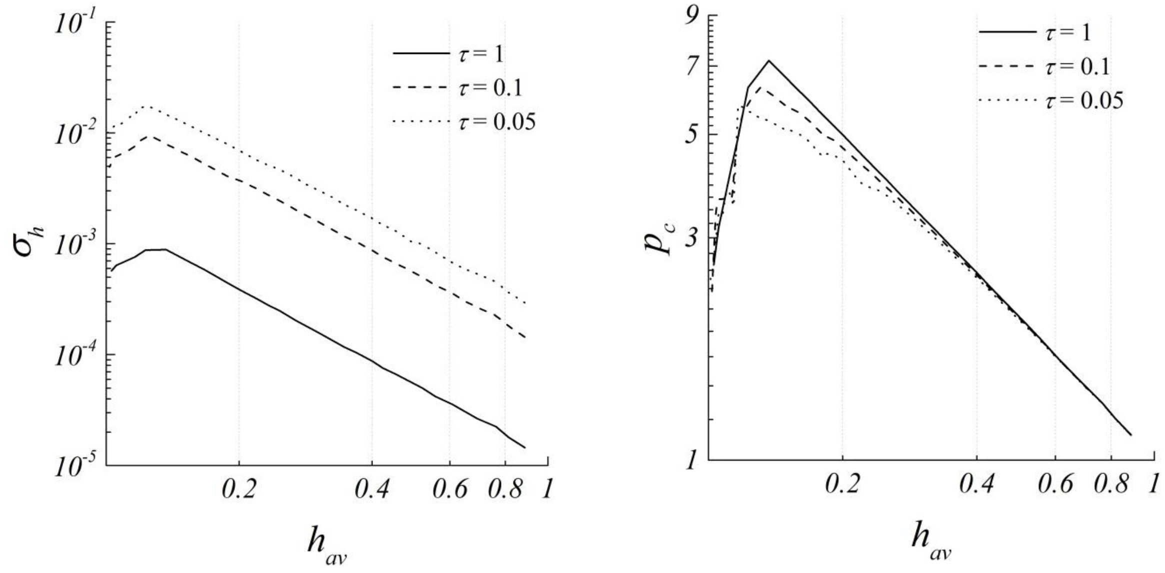

(a) **(b)**

Figure 5.10: The plot of (a) standard deviation of gap σ_h and (b) pressure at the droplet center p_c during imprinting with a single drop and τ = 1, 0.1 and 0.05. σ_h increases as the gap closes until the end when the gap becomes more uniform, resulting in a decrease in σ_h. The reduced σ_h can be attributed to a reduced and more uniform pressure distribution as the droplet makes contact with the template edge and the no-flux boundary condition is applied.

Figure 5.11 shows the plot of σ_h with multiple droplets and τ = 1, 0.1 and 0.05 for $h_{av,f}$ = 0.1. The figure suggests that for a final RLT of 100 nm and $\Gamma = 10^9$ N/m, σ_h is about 3 nm for 9 droplets and 1 nm for 25 droplets. Figure 5.11 (right) shows that for a fixed value of $N\tau$, the final σ_h is almost the same when the gap completely closes to $h_{av,f}$ = 0.1. At h_{av} = 0.1, $N\tau\sigma_h \sim 0.03$. Using Equation 5.15, we find that

$$\sigma_h \sim \frac{0.03q}{\tau h_{av,f}}. \tag{5.16}$$

Kincaid *et al.* carried out patterning on flexible PET film with a template of size 25 mm x 25 mm, 6 pl droplets and a web tension of about 1000 N/m. They reported a mean RLT of 103 nm with standard deviation 11.8 nm when patterning with 6 pl droplets and $\Gamma = 1000$ N/m [136]. For droplet volume 6 pl, $\Gamma = 1000$ N/m and final RLT of 100 nm, the predicted σ_h obtained from Equation (5.15) is about 12 nm. This shows very close agreement with the available experimental results.

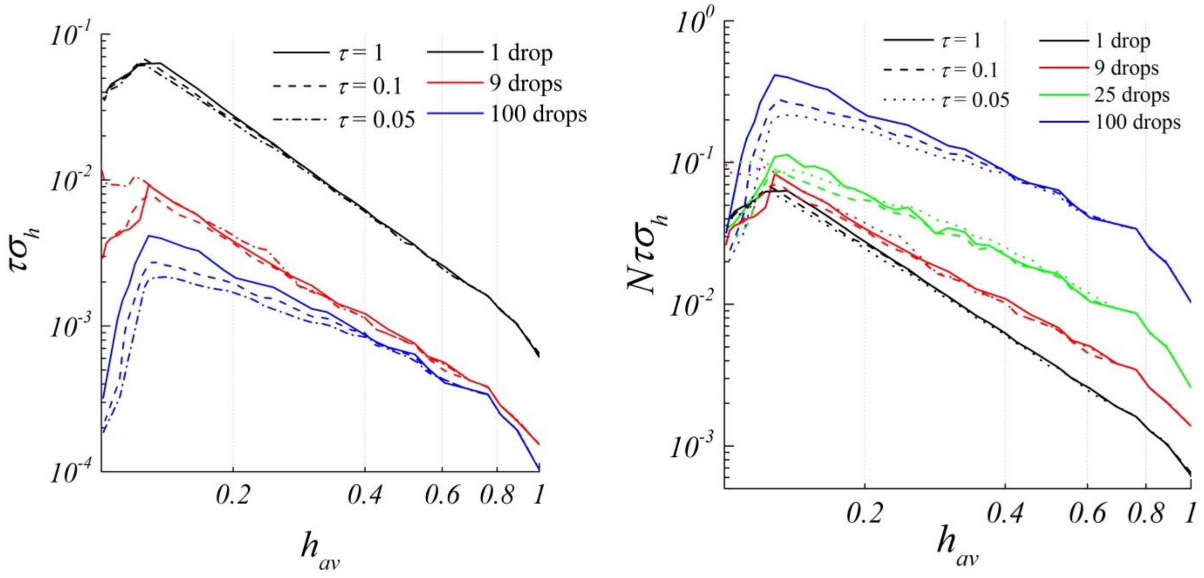

Figure 5.11: The plot of standard deviation of gap, σ_h scaled with τ^{-1} (left) and $(N\tau)^{-1}$ (right) shows that when the gap closes to a final average height of $h_{av,f} = 0.1$, $N\tau\sigma_h$ converges to a value of about 0.03. l_s/l for this simulation is 3.

Variation in RLT for a final gap $h_{av,f} = 0.01$ is shown in Figure 5.12 for $\tau = 1$ and 10. We find that reducing $h_{av,f}$ from 0.1 to 0.01, increases the final value of $N\tau\sigma_h$ from 0.03 to 0.3. This implies that for 10 times decrease in RLT, 10 times larger web tension would be required to achieve the same RLT variation.

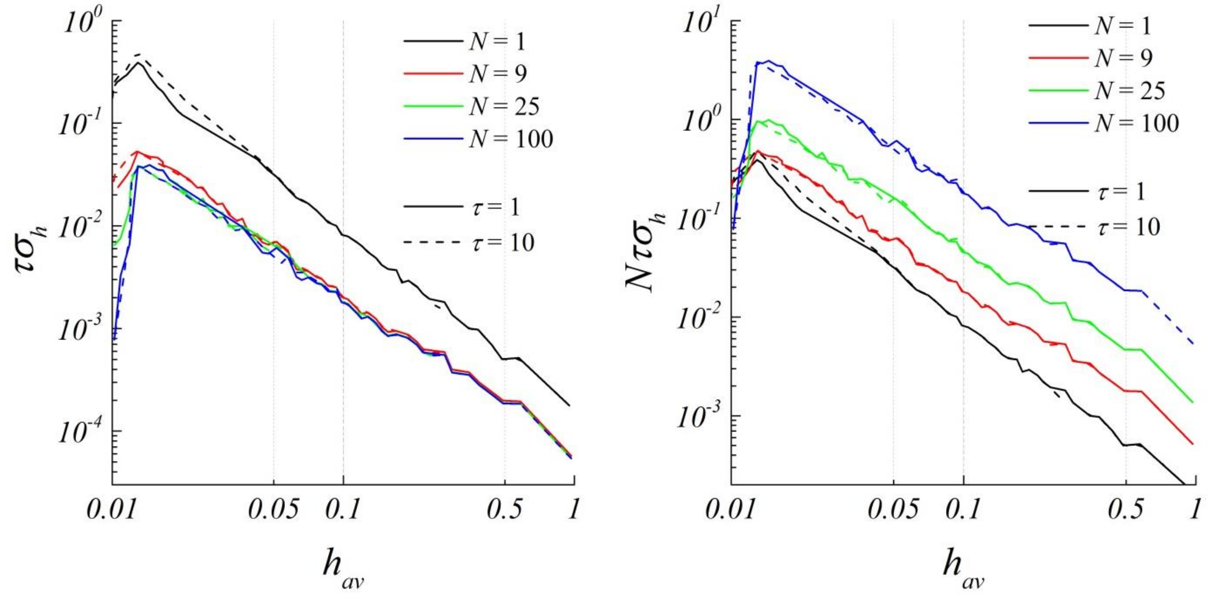

Figure 5.12: The plot of standard deviation of gap, σ_h scaled with τ^{-1} (left) and $(N\tau)^{-1}$ (right) shows that when the gap closes to a final average height of $h_{av,f} = 0.01$, $N\tau\sigma_h$ converges to a value of about 0.3. l_s/l for this simulation is 3.

5.3.3. Effect of Template Position on Web Deformation

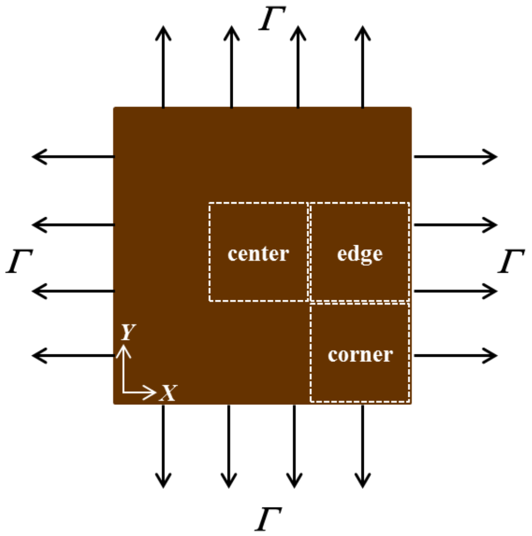

Figure 5.13: Schematic showing three template positions: center, edge and corner.

Web deformation in SFIL is simulated for three template positions on the substrate: center, edge and corner as shown in Figure 5.13. Results for web deformation with 1 droplet (left) and 100 droplets (right) and τ = 1 and 0.1 is shown in Figure 5.14. We find that the average deformation w_{avg} is largest when the template is positioned at the center and least when the template moves to the corner. Negative w_{avg} implies that on an average the web deforms away from the template as shown in Figure 5.5(b).

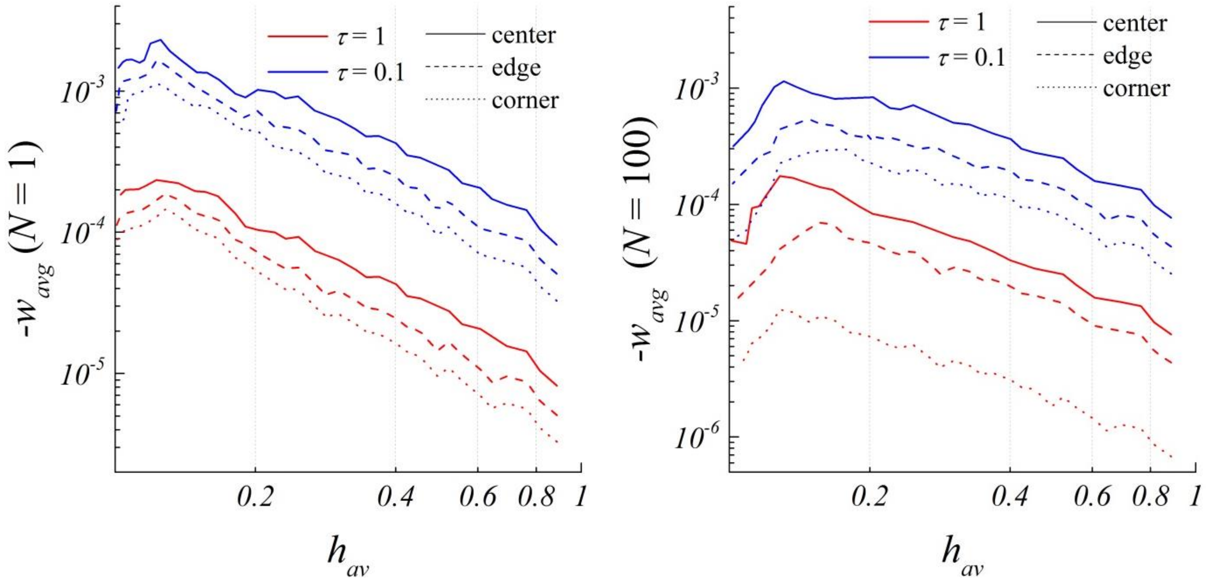

Figure 5.14: The plot of w_{avg} with h_{avg} for a single droplet (left) and 100 droplets (right) with the template at three template positions (center, edge and corner). The average web deformation is largest when the template is positioned at the web center and smallest when the template is at the corner.

The template aligns with two substrate edges in the corner position and one substrate edge at the edge position. Since the substrate edges are fixed, the web deforms less in the corner position on an average compared to the edge and center positions. Figure 5.15 shows the RLT variation σ_h for 1 droplet (a) and 100 droplets (b). For a single droplet, σ_h for different template position is not different significantly. However, for 100 droplets σ_h changes with template position. Since the substrate edges are fixed, σ_h is lower in the corner position compared to the center and edge positions as shown in Figure 5.15(b). σ_h at the center is smaller compared to the edge because the web deformation is radially symmetrical when the droplet is at the center. When scaled by τ, the plot of σ_h for different web tensions collapse as shown in Figure 5.15(right) suggesting that the RLT variation scales as τ^{-1}. This study suggests that for minimum

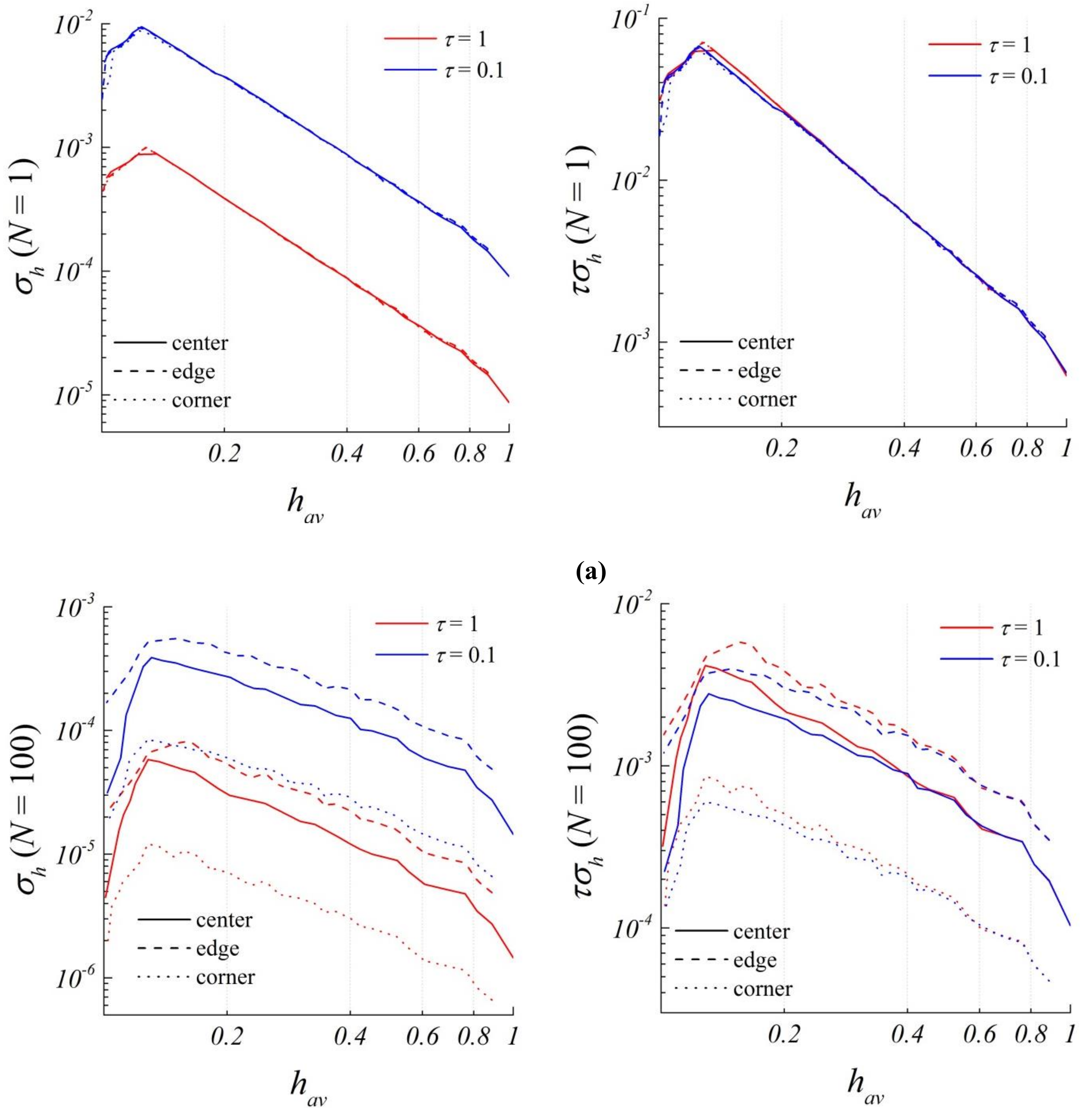

(a)

(b)

Figure 5.15: The plot of σ_h for (a) 1 droplet and (b) 100 droplets for three template positions: center, edge and corner. For a single droplet, the template position does not affect the RLT variation significantly. For 100 droplets, the variation in gap is smallest when the template is positioned at the corner and largest when it is at the edge. The plot of σ_h for different wen tensions collapse into one curve when scaled by τ as shown in the plots on the right.

RLT variation, the template must be placed at the corner. The center position provides the least variation after the corner position; however, the average web deformation of the substrate in the center position can be a magnitude larger than the edge position.

5.4. CONCLUSION

We have presented a model to study the fluid-structure interaction in the Step R2RNIL process with biaxial tension. We find very thin substrates can be modeled as membranes because of low rigidity. The fluid flow is modeled using the Reynold's lubrication equation while the deformation in flexible substrate is modeled using the membrane theory. The effect of web tension and number of droplets on the imprint time and RLT variation is studied. We find that as the number of droplets is increased, the web deformation reduces. The web deformation also reduces as the web tension is increased. The standard deviation of the gap σ_h during the nanoimprinting process is observed. σ_h increases as the gap between the template and the substrate closes until the end when σ_h reduces due change in pressure at the droplet merging and making contact with the template edge. We also found that for final average height $h_{av,f} = 0.1$ and $h_{av,f} = 0.01$, $N\tau\sigma_h$ converges to about 0.03 and 0.3 respectively. This implied that to smaller RLT requires higher web tension to maintain the same uniformity. The model predicts that for a droplet volume 6 pl, $\Gamma = 1000$ N/m and final RLT of 100 nm, σ_h is about 12 nm which is strongly supported by previous experimental results. The effect of template position on substrate is studied. The study shows that the average web deformation and variation in RLT are least when the template is at the corner since all the edges of the substrate are fixed. The average web deformation is largest when the template is positioned at the center of the substrate while the RLT variation is largest when the template is at the edge.

5.5. APPENDIX

The deformation of the flexible substrate can be described using plate theory as following

$$D\nabla^4 W - \Gamma\nabla^2 W = -P \tag{A.1}$$

where Γ is the web tension and D is the bending stiffness given by

$$D = \frac{Ed^3}{12\left(1-\nu^2\right)}. \tag{A.2}$$

Here E is the Young's modulus, d is the substrate thickness and ν is the Poisson ratio. Equation (A.1) can be non-dimensionalized using the characteristic values of the variables: $P_c = 2\hat{\gamma}/H_o$, $H_c = H_o$ and $W_c = H_o$ where H_o is the initial gap. The x and y coordinates are non-dimensionalized using the template width L. The dimensionless form of Equation (A.1) is given by

$$\frac{DH_o}{P_c L^4}\nabla^4 w - \frac{\Gamma H_o}{P_c L^2}\nabla^2 w = -p. \tag{A.3}$$

where, $p = P/P_c$, $h = H/H_c$ and $w = w/W_c$. For PET, the value of d = 100 - 125 μm, E = 2 - 2.7 GPa and ν = 0.37 – 0.44. For L = 10 cm, H_o = 1 μm, γ = 70 dyne/cm, Γ = 1000 N/m and small contact angles $\theta_{1,2}$, $DH_o/P_c L^4$ is ~O(10^{-11}) while $\Gamma H_o/P_c L^2$ is ~ O(10^{-6}). Clearly the first term is much smaller than the first term. Therefore, neglecting the first term, Equation (A.1) can be written as

$$\Gamma \nabla^2 W = P \tag{A.4}$$

This equation is referred to as the "membrane equation" since the rigidity of the substrate is completely neglected.

Chapter 6: Concluding Remarks

Models and simulations have been created for process design and optimization of various realizations of Nanoimprint Lithography (NIL) on rigid and flexible substrates. The main Roll-to-Roll Nanoimprint Lithography (R2RNIL) systems are identified and classified based on template-type and web handling. The underlying physics behind continuous pattern transfer with roller-based templates is not very well understood. Fluid flow, UV curing and template peel-off in roller-based NIL is modeled to understand the process and calculate the main process parameters. Based on this study, the main advantages, disadvantages and operational limits of different R2RNIL configurations are presented. Improvement in throughput and defect rate in NIL on rigid substrates can be achieved by understanding droplet spreading in different settings. A fluid flow model to simulate spreading of high density of droplets in Step and Flash Imprint Lithography (SFIL) is presented. Droplet spreading is simulated with different droplet sizes, droplet arrangements and template patterns to understand their effect on throughput and defectivity. A method to calculate bulk flow permeability in SFIL is introduced in order to account for anisotropic fluid flow through features on patterned templates. This study helps determine factors which have significant impact on throughput and defectivity and proposes optimum droplet arrangement and droplet dispensing scheme for SFIL. The fluid-structure interaction in stepper-based NIL on flexible substrate dictates the web deformation, residual layer thickness (RLT) variation and throughput of the process. The effect of web tension, droplet spreading and template position on this fluid-structure interaction is not very well understood. A model to simulate droplet spreading on flexible substrates is presented in order to study these effects and calculate RLT variation and throughput for Step R2RNIL with different web tensions and template positions. The main findings from this study and future direction for research are discussed below.

6.1. ROLL-TO-ROLL NANOIMPRINT LITHOGRAPHY

Based on the type of template and substrate handling, the main R2RNIL systems can be classified into Basic, Wrapped, Belt and Step R2RNIL. Basic, Wrapped and Belt configurations have a roller template while Step configuration has a stepper template. Basic, Belt and Step R2RNIL can be used for both rigid and flexible substrates whereas Wrapped R2RNIL can only be used for flexible substrates. The main steps involved in roller-based NIL are (i) merging of droplets to form a continuous film, (ii) simultaneous curing of imprint material and pattern transfer and (ii) resist peel-off for template detachment. Since roller-based NIL is a continuous process, these steps occur simultaneously and precise control of web speed, applied force and UV curing is required for high fidelity pattern transfer at high throughput. The fluid dynamics in these steps is studied for Basic R2RNIL and important process parameters such as optimum droplet size, droplet pitch, available area for UV exposure, required UV intensity, maximum web speed, the normal and shear forces on the substrate and the torque on the roller are calculated based on the input parameters and material properties. Modeling the merging of droplets reveals that small droplets or large droplet pitch can lead to incomplete merging and discontinuous resist layer. The viscoelasticity of the imprint material is described using a Maxwell model to calculate the normal and shear forces on the substrate and the torque on the roller. A theory for the mechanism of resist peel-off based on resist elasticity and the adhesion between the template and the resist is proposed. The total force and torque on the template is calculated based on fluid flow and resist peel-off. It is observed that UV intensity and web speed play a significant role in pattern quality for all roller-based configurations. High web speed reduces the time available for UV exposure and may lead to pattern collapse due to insufficient UV curing. For Wrapped and Belt, this can be compensated by increasing the UV intensity or available exposure area. However, in Basic R2R, the available area for UV curing is limited by the RLT. In this configuration, smaller RLT results in smaller exposure area. This limits the minimum RLT achievable with Basic R2R to about 100 nm. Many applications require sub-100 nm RLT which poses a huge disadvantage for Basic R2R setup. Wrapped R2R is recommended for flexible substrates over Basic and Belt configurations as this arrangement has demonstrated high pattern fidelity on large areas and its throughput is only limited by UV intensity requirement and system vibrations at high web speeds. Wrapped R2RNIL has been used for imprinting at web speed up to 30 m/min on a 250 mm wide area [31, 32] and a RLT of less than 70 nm [33]. Belt R2R configuration can pattern on both flexible and rigid substrates. The main challenges to overcome in this configuration are precise web-roller alignment and system vibrations. If these challenges are addressed, Belt R2R configuration can be used for high volume R2R nanofabrication. Basic R2R however does not have the capacity for high volume manufacturing as web speeds greater than 1 m/min and RLT smaller 100 nm are not possible with this configuration without use of high UV intensity.

Step R2RNIL takes advantage of the existing SFIL to provide very high resolution pattern transfer with low defectivity. However the throughput of Step R2RNIL is lower than the roller-based nanoimprint processes as the pattern transfer in Step R2RNIL takes place in discrete steps and template has to be lowered slowly and precisely on the substrate for complete feature filling. The maximum throughput reported using Step R2RNIL is 0.3 m^2/min [35] while that using roller-based NIL is 9 m^2/min [31, 32] for same size of patterned area. Since Step R2RNIL is based on the established SFIL process higher pattern fidelity can be anticipated. Step R2RNIL is recommended for applications where very low defect rate is desired such as flash memory. For applications, such as displays and color filters, in which low cost and high throughput are required and relatively high defectivity is tolerable, roller-based NIL can be used.

6.2. DROPLET SPREADING IN NANOIMPRINT LITHOGRAPHY ON RIGID SUBSTRATES

The throughput in NIL can be improved by analyzing droplet spreading under different process settings. Multi-drop spreading in SFIL is simulated by using lubrication theory to describe pressure and velocity field and Volume of Fluid (VOF) method to track fluid interface. The pressure field is solved using a parallel implementation of GMRES to reduce the computation time required to simulate several thousand droplets. It is found that imprint time required to reach the desired gap is longer for droplet arrangements with larger unfilled edge region. Hence, droplets in hexagonal arrangement, in which the unfilled edge is larger, require more time to reach a desired RLT compared to square arrangement. A modified droplet arrangement is proposed in which droplets arranged in a hexagonal arrangement are spaced further out to reduce the droplet-free edge region. Droplets in this arrangement require lower imprint time than in hexagonal droplet arrangement however imprint time for square arrangement remains the shortest. Ultimately, for the same size of droplets, the square arrangement is found to be the optimum arrangement for minimum imprint time. However, dispensing droplets in a perfect square arrangement is difficult as the inkjet dispenses droplets with a spatial error that cannot be neglected. The imprint time increases significantly for droplet placement errors of more than 0.01% relative to the width of the substrate. We find that the imprint time increases with the magnitude of droplet placement error and smaller droplets are found to be more sensitive to droplet placement error.

Directionality of patterns on a template can result in anisotropic flow in SFIL process. Fluid flow around features is taken into account by calculating bulk permeability for the template. We find that for line and space patterns on the template, the droplet spread faster in the direction parallel to the gratings due to increase in permeability in that direction while the flow in the direction normal to the patterns is slow leading to intermediate elliptical droplets and potential unfilled channel defects. The flow anisotropy and overall imprint time are found to increase with the pattern height. For a multi-patterned template, in which patterns with multiple directionalities may be present, a uniform droplet distribution in a square arrangement does not ensure minimum imprint time. Two drop pattern schemes are explored for SFIL with multi-patterned template: one in which all droplets have the same volume and other in which droplets have sufficient volume to fill the gap locally. It is found that dispensing droplets such that the droplets have sufficient volume to fill the gap locally lead to shorter imprint times. Isotropic patterns like cylinders and cones result in isotropic droplet spreading. For more complex patterns, empirical models for flow permeability are required to predict the flow profile. This computational tool can help make better design decisions when creating patterned templates and drop dispensing strategies that improve throughput and defect rate.

6.3. DEFECT CHARACTERIZATION AND GAS TRAPPING IN SFIL

Non-fill defects are formed when droplets start merging together. As the resist spreads, the defects reduce in size. These defects can be categorized into: unfilled edge defects (formed at the substrate edge) and unfilled pockets (formed between the resist). A model is proposed to predict the defect size and number of these defects for SFIL with pattern-free template based on gap height and imprint time. The model predicts that smaller droplets lead to smaller defects. However, the number of defects increases as the droplet size reduces. Defect characterization for SFIL with multi-patterned template is also presented. In addition to edge and pocket defects, unfilled channel defects are observed in patterned template. These channel defects run edge to edge and are formed due to anisotropic drop spreading. The size and count of each of these defects at different times can be predicted using these simulations. A model is proposed to study the diffusion of gas encapsulated between droplets into the resist. The model takes into account the initial droplet size and the effect of gas pressure on template velocity. The gas defects are modeled as cylinders and the time required for the gas to completely diffuse into the resist is observed. It is found that initially the drop size reduces due to hydrodynamic spreading of the resist. This increases the gas pressure inside until the pressure is so high that the resist cannot spread anymore. At this point, the defect size reduces as the gas diffuses into the resist. It is found that the imprint time can be diffusion–controlled or hydrodynamics-controlled based on a parameter α which scales as $\sim \mu D / k_H \gamma H_o$ where D is the gas diffusion constant, k_H is the Henry's law constant, μ is the resist viscosity, γ is the surface tension of the imprint resist and H_o is the initial resist gap. For values of $\alpha < 1\text{x}10^{-4}$, gas diffusion is slow and defect size is diffusion-controlled while for higher values, defect size is hydrodynamically-controlled. This model does not account for patterns on the template which may be important depending on the location of the defect and the type of pattern. It is important to note that the model used in these simulations assumes that template is flat when lowered on the droplets. In the actual process, the template is lowered with the center of the template making contact with the droplets first. This allows the droplets at the center of the substrate to merge first and spread out so that the gas can escape with less obstruction from the droplets. The observation of the effect of edge regions, droplet placement error and optimum droplet arrangement still hold as long as the template is lowered with net zero applied force.

6.4. RESIDUAL LAYER THICKNESS VARIATION IN STEP R2RNIL

Fluid-structure interaction in Step R2R is studied to understand the effect of web tension, droplet distribution and template position on throughput and RLT uniformity. We find that the flexible substrate can be modeled as a membrane since the substrate is about 100 μm thick and its rigidity is negligible. A model to simulate web deformation and droplet spreading in Step R2RNIL is presented. Fluid flow is modeled using the Reynold's lubrication equation while the deformation in flexible substrate is modeled using the membrane theory. It is found that that for a constant web tension, the web deformation reduces as the number of droplets is increased. The variation in the gap increases as the gap between the template and the substrate closes until the end when the variation reduces. This reduction is variation is due to merging of droplets which results in lowering of template velocity and droplet pressure. The effect of three template positions: center, edge and corner on web deformation is studied. The study shows that the average web deformation and variation in RLT are least when the template is at the corner since all the edges of the substrate are fixed. The average web deformation is largest when the template is positioned at the center of the substrate while the RLT variation is largest when the template is at the edge. Based on this study, the RLT variation and process throughput can be estimated.

6.5. FUTURE WORK

6.5.1. Gas Flow in Nanoimprint Lithography

For dynamic multi-drop simulations, it was assumed that there is no gas flow during droplet spreading. However, in some systems the dynamic flow and trapping of gas may be important to accurately determine the throughput and defects. Simultaneous gas and liquid flow in NIL can be described using the following equations

$$\frac{\partial H}{\partial T} = \nabla \cdot \left(\frac{S_L H^3}{12\mu_L} \nabla P_L \right) + \nabla \cdot \left(\frac{\left(1 - S_L\right) H^3}{12\mu_G} \nabla P_G \right), \tag{6.1}$$

$$\mathbf{U}_L = -\frac{H^2}{12\mu_L} \nabla P_L \tag{6.2}$$

$$\mathbf{U}_G = -\frac{H^2}{12\mu_G} \nabla P_G \tag{6.3}$$

and

$$P_L - P_G = \frac{\gamma\left(cos\,\theta_1 + cos\,\theta_2\right)}{H} \tag{6.4}$$

where H is the gap between substrate and template and S_L is the fraction of liquid in the gap between the template and the substrate. P_L and P_G are the liquid and gas pressure respectively. μ_L and μ_G are the liquid and gas viscosity respectively. $\mathbf{U_L}$ and $\mathbf{U_G}$ are the vertically averaged liquid and gas velocity. γ is the surface tension of the imprint. θ_1 and θ_2 are the contact angles of the fluid with the template and the substrate respectively. The dynamic two-phase flow in the gap can be simulated using the above equations to describe the pressure and fluid velocities and VOF method to track fluid as discussed in Chapter 3 and 4. The droplets spread and merge to create pockets of gas trapped between the resist. Once the gas is trapped, a three-dimensional version of the gas-diffusion model described in Chapter 3 can be used to track the gas diffusing into the resist. This model is computationally more expensive to simulate however it will give a more accurate estimate for the imprint time and defectivity. Since the gas viscosity (~10^{-5} Pa.s) is much lower than resist viscosity (10^{-3} Pa.s), the simulation can be simplified by neglecting the pressure gradient during hydrodynamic resist spreading.

6.5.2. Web Deformation with Uniaxial Web Tension

In this dissertation, the web tension in Step R2RNIL is assumed to be biaxial while in real systems the tension is applied only along one direction. A 1D model for a droplet spreading between a deformable superstrate and a substrate was proposed by Singhal *et al*. [135]. This model did not take into account the dynamic droplet spreading. Now that a base model has been created, gas trapping and uniaxial web tension can be incorporated in the model. The deformation of the flexible substrate is described using plate theory as following

$$D\nabla^4 W - \Gamma\nabla^2 W = -P \tag{6.5}$$

where Γ is the web tension and bending stiffness, $D = Ed^3 \big/ 12\left(1-\nu^2\right)$. Here E is the Young's modulus, d is the substrate thickness and ν is the Poisson ratio. For biaxial tension, the first term can be neglected due to negligible substrate rigidity and small thickness of the membrane (~100 μm). However, for uniaxial tension this is not the case. Assume a substrate with web tension Γ_{xx} acting in the x direction and fixed edges in the x direction as shown in the Figure 6.1. There is no tension acting in the y direction and the edges are free. Then Equation (6.5) can be written as

$$D\left(\frac{\partial^4 W}{\partial X^4} + \frac{\partial^4 W}{\partial Y^4}\right) - \Gamma_{xx}\frac{\partial^2 W}{\partial X^2} = -P \tag{6.6}$$

The rigidity in the x direction can be neglected because of the small substrate thickness and applied web tension in the x direction. The rigidity in the y direction is however still significant and must be taken into account. Equation (6.5) can be written as

$$D\frac{\partial^4 W}{\partial Y^4} - \Gamma_{XX}\frac{\partial^2 W}{\partial X^2} = -P \tag{6.7}$$

The six boundary conditions for solving these equations is given by

$$\frac{\partial W}{\partial Y}\Big|_{edge,Y} = 0 \tag{6.8}$$

$$\frac{\partial^3 W}{\partial Y^3}\Big|_{edge,Y} = 0 \tag{6.9}$$

$$W\Big|_{edge,X} = 0 \tag{6.10}$$

These equations can be used to determine RLT variation and throughout for Step R2RNIL with web tension in only one direction.

With the current capability to simulate several thousands of droplets under different process conditions, the model and simulations can be validated with realistic process settings used in NIL. Preliminary validation tests can be done by observing the defect rate and throughput for square droplet arrangement and pattern free template with net zero force on it. Once the model has been validated for pattern free template, the model can be tested for anisotropic pattern such as line and space patterns. Step R2RNIL can be carried out with different size of droplet and web tension with template at different positions to compare the results for final RLT variation and throughput from the simulations. Once these validations are complete, the multi-drop simulator will be ready for designing template patterns, droplet dispensing schemes and template control schemes for optimum pattern transfer and scale-up of nanoimprint lithography.

References

[1] P. Maury, D. Turkenburg, N. Stroeks, P. Giesen, I. Barbu, E. Meinders, A. van Bremen, N. Iosad, R. van der Werf, and H. Onvlee, "Roll-to-roll UV imprint lithography for flexible electronics," *Microelectronic Engineering,* vol. 88, pp. 2052-2055, 2011.

[2] R. Das, "Printed, Organic & Flexible Electronics Forecasts, Players & Opportunities 2016-2026," 2016.

[3] M. Malloy and L. C. Litt, "Technology review and assessment of nanoimprint lithography for semiconductor and patterned media manufacturing," *Journal of Micro-Nanolithography Mems and Moems,* vol. 10, 2011.

[4] S. Y. Chou, P. R. Krauss, and P. J. Renstrom, "Imprint of sub-25 nm vias and trenches in polymers," *Applied Physics letters,* vol. 67, pp. 3114-3116, 1995.

[5] A. L. Vig, T. Makela, P. Majander, V. Lambertini, J. Ahopelto, and A. Kristensen, "Roll-to-roll fabricated lab-on-a-chip devices," *Journal of Micromechanics and Microengineering,* vol. 21, 2011.

[6] M. G. Kang, H. J. Park, S. H. Ahn, and L. J. Guo, "Transparent Cu nanowire mesh electrode on flexible substrates fabricated by transfer printing and its application in organic solar cells," *Solar Energy Materials and Solar Cells,* vol. 94, pp. 1179-1184, 2010.

[7] S. H. Ahn, J. S. Kim, and L. J. Guo, "Bilayer metal wire-grid polarizer fabricated by roll-to-roll nanoimprint lithography on flexible plastic substrate," *Journal of Vacuum Science & Technology B,* vol. 25, pp. 2388-2391, 2007.

[8] P. C. Kao, S. Y. Chu, C. Y. Zhan, L. C. Hsu, and W. C. Liao, "Fabrication of organic light-emitting devices on flexible substrates using a combined roller imprinting and photolithography-patterning technique," *Journal of Vacuum Science & Technology B,* vol. 24, pp. 1278-1282, 2006.

[9] T. K. Whidden, D. K. Ferry, M. N. Kozicki, E. Kim, A. Kumar, J. Wilbur, and G. M. Whitesides, "Pattern transfer to silicon by microcontact printing and RIE," *Nanotechnology,* vol. 7, pp. 447-451, 1996.

[10] D. W. Wang, S. G. Thomas, K. L. Wang, Y. N. Xia, and G. M. Whitesides, "Nanometer scale patterning and pattern transfer on amorphous Si, crystalline Si, and SiO2 surfaces using self-assembled monolayers," *Applied Physics letters,* vol. 70, pp. 1593-1595, 1997.

[11] J. Haisma, M. Verheijen, K. vandenHeuvel, and J. vandenBerg, "Mold-assisted nanolithography: A process for reliable pattern replication," *Journal of Vacuum Science & Technology B,* vol. 14, pp. 4124-4128, 1996.

[12] M. Colburn, S. Johnson, M. Stewart, S. Damle, T. Bailey, B. Choi, M. Wedlake, T. Michaelson, S. V. Sreenivasan, J. Ekerdt, and C. G. Willson, "Step and Flash Imprint Lithography: A new approach to high-resolution patterning," *Emerging Lithographic Technologies Iii, Pts 1 and 2,* vol. 3676, pp. 379-389, 1999.

[13] T. C. Bailey, S. C. Johnson, S. V. Sreenivasan, J. G. Ekerdt, C. G. Willson, and D. J. Resnick, "Step and Flash Imprint Lithography: An efficient nanoscale printing technology," *Journal of Photopolymer Science and Technology,* vol. 15, pp. 481-486, 2002.

[14] C. Brooks, K. Selinidis, G. Doyle, L. Brown, D. LaBrake, D. J. Resnick, and S. V. Sreenivasan, "Development of template and mask replication using Jet and Flash Imprint Lithography," *Photomask Technology 2010,* vol. 7823, 2010.

[15] Z. M. Ye, R. Ramos, C. Brooks, P. Hellebrekers, S. Carden, and D. LaBrake, "High volume Jet and Flash Imprint Lithography for discrete track patterned media," *Alternative Lithographic Technologies Ii,* vol. 7637, 2010.

[16] S. Ahn, M. Ganapathisubramanian, M. Miller, J. Yang, J. Choi, F. Xu, D. J. Resnick, and S. V. Sreenivasan, "Roll-to-roll nanopatterning using Jet and Flash Imprint Lithography," *Alternative Lithographic Technologies Iv,* vol. 8323, 2012.

[17] J. G. Ok, H. S. Youn, M. K. Kwak, K. T. Lee, Y. J. Shin, L. J. Guo, A. Greenwald, and Y. S. Liu, "Continuous and scalable fabrication of flexible metamaterial films via roll-to-roll nanoimprint process for broadband plasmonic infrared filters," *Applied Physics letters,* vol. 101, 2012.

[18] C. H. Chuang, S. W. Tsai, J. F. Lin, and C. P. Chen, "Fabrication of multi-functional optical films by using a ultraviolet curing roll-to-roll system," *Japanese Journal of Applied Physics,* vol. 50, 2011.

[19] M. Moro, J. Taniguchi, and S. Hiwasa, "Fabrication of antireflection structure film by roll-to-roll ultraviolet nanoimprint lithography," *Journal of Vacuum Science & Technology B,* vol. 32, 2014.

[20] S. Ahn, M. Choi, H. Bae, J. Lim, H. Myung, H. Kim, and S. Kang, "Design and fabrication of micro optical film by ultraviolet roll imprinting," *Japanese Journal of Applied Physics Part 1-Regular Papers Brief Communications & Review Papers,* vol. 46, pp. 5478-5484, 2007.

[21] A. Bessonov, J. W. Seo, J. G. Kim, E. S. Hwang, J. W. Lee, J. W. Cho, D. J. Kim, and S. Lee, "Control over pattern fidelity and surface wettability of imprinted templates for flexible color filter manufacturing," *Microelectronic Engineering,* vol. 88, pp. 2913-2918, 2011.

[22] M. A. G. Lazo, R. Teuscher, Y. Leterrier, J. A. E. Manson, C. Calderone, A. Hessler-Wyser, P. Couty, Y. Ziegler, and D. Fischer, "UV-nanoimprint lithography and large area roll-to-roll texturization with hyperbranched polymer nanocomposites for light-trapping applications," *Solar Energy Materials and Solar Cells,* vol. 103, pp. 147-156, 2012.

[23] H. Tan, A. Gilbertson, and S. Y. Chou, "Roller nanoimprint lithography," *Journal of Vacuum Science & Technology B,* vol. 16, pp. 3926-3928, 1998.

[24] M. D. Fagan, B. H. Kim, and D. G. Yao, "A novel process for continuous thermal embossing of large-area nanopatterns onto polymer films," *Advances in Polymer Technology,* vol. 28, pp. 246-256, 2009.

[25] L. P. Yeo, S. H. Ng, Z. F. Wang, H. M. Xia, Z. P. Wang, V. S. Thang, Z. W. Zhong, and N. F. de Rooij, "Investigation of hot roller embossing for microfluidic devices," *Journal of Micromechanics and Microengineering,* vol. 20, 2010.

[26] S. Ahn, J. Cha, H. Myung, S. M. Kim, and S. Kang, "Continuous ultraviolet roll nanoimprinting process for replicating large-scale nano- and micropatterns," *Applied Physics letters,* vol. 89, 2006.

[27] S. H. Ahn and L. J. Guo, "High-speed roll-to-roll nanoimprint lithography on flexible plastic substrates," *Advanced Materials,* vol. 20, p. 2044, 2008.

[28] S. H. Ahn and L. J. Guo, "Large-area roll-to-roll and roll-to-plate nanoimprint lithography: A step toward high-throughput application of continuous nanoimprinting," *Acs Nano,* vol. 3, pp. 2304-10, 2009.

[29] A. Jeans, M. Almanza-Workman, R. Cobene, R. Elder, R. Garcia, F. Gomez-Pancorbo, W. Jackson, M. Jam, H. J. Kim, O. Kwon, H. Luo, J. Maltabes, P. Mei, C. Perlov, M. Smith, C. Taussig, F. Jeffrey, S. Braymen, J. Hauschildt, K. Junge, D. Larson, and D. Stieler, "Advances in roll-to-roll imprint lithography for display applications," *Alternative Lithographic Technologies Ii,* vol. 7637, 2010.

[30] J. J. Dumond, K. A. Mahabadi, Y. S. Yee, C. Tan, J. Y. Fuh, H. P. Lee, and H. Y. Low, "High resolution UV roll-to-roll nanoimprinting of resin moulds and subsequent replication via thermal nanoimprint lithography," *Nanotechnology,* vol. 23, p. 485310, Dec 2012.

[31] M. W. Thesen, M. Rumler, F. Schlachter, S. Grutzner, C. Moormannc, M. Rommel, D. Nees, S. Ruttloff, S. Pfirrmann, M. Vogler, A. Schleunitz, and G. Grutzner, "Enabling large area and high throughput roll-to-roll NIL by novel inkjetable and photo-curable NIL-resists," *Alternative Lithographic Technologies Vi,* vol. 9049, 2014.

[32] M. W. Thesen, D. Nees, S. Ruttloff, M. Rumler, M. Rommel, F. Schlachter, S. Grutzner, M. Vogler, A. Schleunitz, and G. Grutzner, "Inkjetable and photo-curable resists for large-area and high-throughput roll-to-roll nanoimprint lithography," *Journal of Micro-Nanolithography Mems and Moems,* vol. 13, 2014.

[33] C. L. Wu, C. K. Sung, P. H. Yao, and C. H. Chen, "Sub-15 nm linewidth gratings using roll-to-roll nanoimprinting and plasma trimming to fabricate flexible wire-grid polarizers with low colour shift," *Nanotechnology,* vol. 24, 2013.

[34] R. Inanami, T. Ojima, K. Matsuki, T. Kono, and T. Nakasugi, "Sub-100 nm pattern formation by roll-to-roll nanoimprint," *Alternative Lithographic Technologies Iv,* vol. 8323, 2012.

[35] S. H. Ahn, M. Miller, S. Q. Yang, M. Ganapathisubramanian, M. Menezes, V. Singh, F. Wan, J. Choi, F. Xu, D. LaBrake, D. J. Resnick, P. Hofemann, and S. V. Sreenivasan, "High volume nanoscale roll-based imprinting using Jet and Flash Imprint Lithography," *Alternative Lithographic Technologies Vi,* vol. 9049, 2014.

[36] T. Makela, T. Haatainen, and J. Ahopelto, "Roll-to-roll printed gratings in cellulose acetate web using novel nanoimprinting device," *Microelectronic Engineering,* vol. 88, pp. 2045-2047, 2011.

[37] K. J. Sohn, J. H. Park, D. E. Lee, H. I. Jang, and W. I. Lee, "Effects of the process temperature and rolling speed on the thermal roll-to-roll imprint lithography of flexible polycarbonate film," *Journal of Micromechanics and Microengineering,* vol. 23, 2013.

[38] J. J. Dumond and H. Y. Low, "Recent developments and design challenges in continuous roller micro- and nanoimprinting," *Journal of Vacuum Science & Technology B,* vol. 30, 2012.

[39] J. Zhang, M. Sahli, J. C. Gelin, and T. Barriere, "Roll manufacturing of polymer microfluidic devices using a roll embossing process," *Sensors and Actuators a-Physical,* vol. 230, pp. 156-169, 2015.

[40] P. Y. Yi, H. Wu, C. P. Zhang, L. F. Peng, and X. M. Lai, "Roll-to-roll UV imprinting lithography for micro/nanostructures," *Journal of Vacuum Science & Technology B,* vol. 33, 2015.

[41] J. Taniguchi, H. Yoshikawa, G. Tazaki, and T. Zento, "High-density pattern transfer via roll-to-roll ultraviolet nanoimprint lithography using replica mold," *Journal of Vacuum Science & Technology B,* vol. 30, 2012.

[42] N. Khusnatdinov, Z. M. Ye, K. Luo, T. Stachowiak, X. M. Lu, J. W. Irving, M. Shafran, W. Longsine, M. Traub, V. Truskett, B. Fletcher, W. J. Liu, F. Xu, D. LaBrake, and S. V. Sreenivasan, "High throughput Jet and Flash Imprint Lithography for advanced semiconductor memory," *Alternative Lithographic Technologies Vi,* vol. 9049, 2014.

[43] H. Takeishi and S. V. Sreenivasan, "Nanoimprint system development and status for high volume semiconductor manufacturing," *Alternative Lithographic Technologies Vii,* vol. 9423, 2015.

[44] W. Clemens, D. Lupo, K. Hecker, and S. Breitung, "White paper OE-A roadmap for Organic and Printed Electronics, Organic Electronics Association (OE-A)," 2009.

[45] S. V. Sreenivasan, "Nanoscale manufacturing enabled by imprint lithography," *Mrs Bulletin,* vol. 33, pp. 854-863, 2008.

[46] P. Y. Hao Wu, Linfa Peng, and Xinmin Lai, "Study on bubble defects in roll-to-roll UV imprinting process for micropyramid arrays. I. Experiments," *Journal of Vacuum Science & Technology B,* vol. 34, 2016.

[47] S. Chauhan, F. Palmieri, R. T. Bonnecaze, and C. G. Willson, "Feature filling modeling for Step and Flash Imprint Lithography," *Journal of Vacuum Science & Technology B,* vol. 27, pp. 1926-1932, 2009.

[48] X. D. Ye, Y. C. Ding, Y. G. Duan, H. Z. Liu, and B. H. Lu, "Effects of exposure time on defects and demolding force in soft ultraviolet nanoimprint lithography," *Journal of Vacuum Science & Technology B,* vol. 27, pp. 2091-2096, 2009.

[49] J. D. Morse, "Nanofabrication technologies for roll-to-roll processing," *Report from the NIST - NNN workshop,* 2011.

[50] M. Colburn, B. J. Choi, S. V. Sreenivasan, R. T. Bonnecaze, and C. G. Willson, "Ramifications of lubrication theory on imprint lithography," *Microelectronic Engineering,* vol. 75, pp. 321-329, 2004.

[51] S. Reddy and R. T. Bonnecaze, "Simulation of fluid flow in the Step and Flash Imprint Lithography process," *Microelectronic Engineering,* vol. 82, pp. 60-70, 2005.

[52] V. Sirotkin, A. Svintsov, S. Zaitsev, and H. Schift, "Viscous flow simulation in nanoimprint using coarse-grain method," *Microelectronic Engineering,* vol. 83, pp. 880-883, 2006.

[53] V. Sirotkin, A. Svintsov, H. Schift, and S. Zaitsev, "Coarse-grain method for modeling of stamp and substrate deformation in nanoimprint," *Microelectronic Engineering,* vol. 84, pp. 868-871, 2007.

[54] N. Kehagias, V. Reboud, C. M. S. Torres, V. Sirotkin, A. Svintsov, and S. Zaitsev, "Residual layer thickness in nanoimprint: Experiments and coarse-grain simulation," *Microelectronic Engineering,* vol. 85, pp. 846-849, 2008.

[55] S. Merino, A. Retolaza, A. Juarros, H. Schift, V. Sirotkin, A. Svintsov, and S. Zaitsev, "Refined coarse-grain modeling of stamp deformation in nanoimprint lithography," *Nsti Nanotech 2008,* vol. 1, pp. 368-370, 2008.

[56] V. Sirotkin, A. Svintsov, and S. Zaitsev, "Optimization of droplets for UV-NIL using coarse-grain simulation of resist flow," *Alternative Lithographic Technologies,* vol. 7271, 2009.

[57] S. Reddy, P. R. Schunk, and R. T. Bonnecaze, "Dynamics of low capillary number interfaces moving through sharp features," *Physics of Fluids,* vol. 17, 2005.

[58] S. Chauhan, F. Palmieri, R. T. Bonnecaze, and C. G. Willson, "Pinning at template feature edges for Step and Flash Imprint Lithography," *Journal of Applied Physics,* vol. 106, 2009.

[59] H. D. Rowland and W. P. King, "Polymer deformation and filling modes during microembossing," *Journal of Micromechanics and Microengineering,* vol. 14, pp. 1625-1632, 2004.

[60] H. D. Rowland, W. P. King, A. C. Sun, and P. R. Schunk, "Simulations of nonuniform embossing: The effect of asymmetric neighbor cavities on polymer flow during nanoimprint lithography," *Journal of Vacuum Science & Technology B,* vol. 23, pp. 2958-2962, 2005.

[61] H. D. Rowland, A. C. Sun, P. R. Schunk, and W. P. King, "Impact of polymer film thickness and cavity size on polymer flow during embossing: toward process design rules for nanoimprint lithography," *Journal of Micromechanics and Microengineering,* vol. 15, pp. 2414-2425, 2005.

[62] M. Neisser and S. Wurm, "ITRS lithography roadmap: 2015 challenges," *Advanced Optical Technologies,* vol. 4, pp. 235-240, 2015.

[63] Q. F. Xia and R. F. Pease, "Nanoimprint lithography 20 years on," *Nanotechnology,* vol. 26, 2015.

[64] S. M. Seo, T. I. Kim, and H. H. Lee, "Simple fabrication of nanostructure by continuous rigiflex imprinting," *Microelectronic Engineering,* vol. 84, pp. 567-572, 2007.

[65] H. Lim, K. B. Choi, G. Kim, S. Park, J. Ryu, and J. Lee, "Roller nanoimprint lithography for flexible electronic devices of a sub-micron scale," *Microelectronic Engineering,* vol. 88, pp. 2017-2020, 2011.

[66] S. W. Youn, M. Iwara, H. Goto, M. Takahashi, and R. Maeda, "Prototype development of a roller imprint system and its application to large area polymer replication for a microstructured optical device," *Journal of Materials Processing Technology,* vol. 202, pp. 76-85, 2008.

[67] J. T. Wu and S. Y. Yang, "A gasbag-roller-assisted UV imprinting technique for fabrication of a microlens array on a PMMA substrate," *Journal of Micromechanics and Microengineering,* vol. 20, 2010.

[68] C. Y. Chang, S. Y. Yang, and J. L. Sheh, "A roller embossing process for rapid fabrication of microlens arrays on glass substrates," *Microsystem Technologies-Micro- and Nanosystems-Information Storage and Processing Systems,* vol. 12, pp. 754-759, 2006.

[69] S. Y. Yang, F. S. Cheng, S. W. Xu, P. H. Huang, and T. C. Huang, "Fabrication of microlens arrays using UV micro-stamping with soft roller and gas-pressurized platform," *Microelectronic Engineering,* vol. 85, pp. 603-609, 2008.

[70] S. H. Ahn and L. J. Guo, "High-speed roll-to-roll nanoimprint lithography on flexible substrate and mold-separation analysis," *Advanced Fabrication Technologies for Micro/Nano Optics and Photonics Ii,* vol. 7205, 2009.

[71] K. S. Chen, K. S. Ou, and Y. M. Liao, "On the influence of roller misalignments on the web behavior during roll-to-roll processing," *Journal of the Chinese Institute of Engineers,* vol. 34, pp. 87-97, 2011.

[72] N. Unno and J. Taniguchi, "Fabrication of the metal nano pattern on plastic substrate using roll nanoimprint," *Microelectronic Engineering,* vol. 88, pp. 2149-2153, 2011.

[73] K. R. Carter and J. J. Wartkins, "Large-area, continuous roll-to-roll nanoimprinting with PFPE composite molds," 2013.

[74] H. Yoshikawa, J. Taniguchi, G. Tazaki, and T. Zento, "Fabrication of high-aspect-ratio pattern via high throughput roll-to-roll ultraviolet nanoimprint lithography," *Microelectronic Engineering,* vol. 112, pp. 273-277, 2013.

[75] R. Inanami, K. Matsuki, T. Ojima, T. Kono, and T. Nakasugi, "Challenges for pattern formation with sub-100nm residual-layer thickness by roll-to-roll nanoimprint lithography," *Alternative Lithographic Technologies Vi,* vol. 9049, 2014.

[76] S. Kobayashi, M. Shimizu, S. Tanaka, Y. Furutono, M. Hatano, K. Matsuki, R. Inanami, and S. Mimotogi, "The prospects of design for roll to roll lithography: Layout refinement utilizing process simulation," *Alternative Lithographic Technologies Vi,* vol. 9049, 2014.

[77] C. H. Liu, C. K. Sung, E. C. Chang, C. Y. Lo, and C. C. Fu, "Fabricating a silver soft mold on a flexible substrate for roll-to-roll nanoimprinting," *Ieee Transactions on Nanotechnology,* vol. 13, pp. 80-84, 2014.

[78] S. Sabik, J. de Riet, I. Yakimets, and E. Smits, "High resolution patterning for flexible electronics via roll-to-roll nanoimprint lithography," *Alternative Lithographic Technologies Vi,* vol. 9049, 2014.

[79] S. W. Tsai and Y. C. Lee, "Fabrication of ball-strip convex microlens array using seamless roller mold patterned by curved surface lithography technique," *Journal of Micromechanics and Microengineering,* vol. 24, 2014.

[80] Y. Chen and C. Stuart, "Roll in and roll out: A path to high-throughput nanoimprint lithography," *Acs Nano,* vol. 3, pp. 2062-2064, 2009.

[81] H. J. Park, M. G. Kang, S. H. Ahn, and L. J. Guo, "A facile route to polymer solar cells with optimum morphology readily applicable to a roll-to-roll process without sacrificing high device performance," *Advanced Materials,* vol. 22, p. E247, 2010.

[82] N. Kooy, K. Mohamed, and K. Ibrahim, "Patterning of microstructures on SU-8 coated flexible polymer substrate using roll-to-roll ultraviolet nanoimprint lithography," *Journal of Engineering Science,* vol. 9, pp. 71-78, 2013.

[83] M. Ogino, M. Hasegawa, K. Sakaue, S. Nagai, and A. Miyauchi, "Fabrication of 200-nm dot pattern on 15-m-long polymer sheet using sheet nanoimprint method," *Japanese Journal of Applied Physics,* vol. 52, 2013.

[84] Y. Otsubo, T. Amari, and K. Watanabe, "Rheological studies of ultraviolet curing with an oscillating plate rheometer," *Journal of Applied Polymer Science,* vol. 31, pp. 323-332, 1986.

[85] I. J. Hill and W. G. Sawyer, "Energy, adhesion, and the elastic foundation," *Tribology Letters,* vol. 37, pp. 453-461, 2010.

[86] E. Winkler, "Theory of elasticity and strength," *Theory of elasticity and strength,* 1867.

[87] Y. Otsubo, T. Amari, and K. Watanabe, "Rheological behavior of Epoxy Acrylate Prepolymer during UV curing," *Journal of Applied Polymer Science,* vol. 29, pp. 4071-4080, 1984.

[88] S. S. Lee, A. Luciani, and J. A. E. Manson, "A rheological characterisation technique for fast UV-curable systems," *Progress in Organic Coatings,* vol. 38, pp. 193-197, 2000.

[89] B. J. Love and F. Piguet-Ruinet, "Analyzing the dynamic chemorheology of curing resins: extraction of model parameters associated with cure advancement," *Journal of Applied Polymer Science,* vol. 106, pp. 3605-3609, 2007.

[90] F. A. Houle, A. Fornof, D. C. Miller, S. Raoux, H. Truong, E. Simonyi, C. Jahnes, and S. Rossnagel, "Chemical and mechanical properties of UV-cured nanoimprint resists and release layer interactions," *Emerging Lithographic Technologies Xii, Pts 1 and 2,* vol. 6921, pp. B9210-B9210, 2008.

[91] D. J. O'Brien, P. T. Mather, and S. R. White, "Viscoelastic properties of an epoxy resin during cure," *Journal of Composite Materials,* vol. 35, pp. 883-904, 2001.

[92] B. J. Love, F. P. Ruinet, and F. Teyssandier, "Chemorheology of photopolymerizable acrylates using a modified Boltzmann Sigmoidal model," *Journal of Polymer Science Part B-Polymer Physics,* vol. 46, pp. 2319-2325, 2008.

[93] X. K. Li, Y. S. Luo, Y. W. Qi, and R. Zhang, "On non-Newtonian lubrication with the upper convected Maxwell model," *Applied Mathematical Modelling,* vol. 35, pp. 2309-2323, 2011.

[94] J. A. Tichy, "Non-Newtonian lubrication with the convected Maxwell model," *Journal of Tribology-Transactions of the Asme,* vol. 118, pp. 344-348, 1996.

[95] C. W. Liu, C. H. Lee, and S. C. Lin, "Sub-wavelength gratings fabricated on a light bar by roll-to-roll UV embossing process," *Optics Express,* vol. 19, pp. 11299-11311, 2011.

[96] H. C. Scheer and H. Schulz, "A contribution to the flow behaviour of thin polymer films during hot embossing lithography," *Microelectronic Engineering,* vol. 56, pp. 311-332, 2001.

[97] H. C. Scheer, "Pattern definition by nanoimprint," *Micro-Optics 2012,* vol. 8428, 2012.

[98] Z. M. Ye, R. Ramos, C. Brooks, L. Simpson, J. Fretwell, S. Carden, P. Hellebrekers, D. LaBrake, D. J. Resnick, and S. V. Sreenivasan, "High density patterned media fabrication using Jet and Flash Imprint Lithography," *Alternative Lithographic Technologies Iii,* vol. 7970, 2011.

[99] G. M. Schmid, M. Miller, C. Brooks, N. Khusnatdinov, D. LaBrake, D. J. Resnick, S. V. Sreenivasan, G. Gauzner, K. Lee, D. Kuo, D. Weller, and X. M. Yang, "Step and Flash Imprint Lithography for manufacturing patterned media," *Journal of Vacuum Science & Technology B,* vol. 27, pp. 573-580, 2009.

[100] J. C. Taylor, T. Hostetler, P. Kornilovich, and K. Kramer, "Photonic crystals from Step and Flash Imprint Lithography," *Emerging Lithographic Technologies X, Pts 1 and 2,* vol. 6151, pp. L1510-L1510, 2006.

[101] M. Miller, G. Schmid, G. Doyle, E. Thompson, and D. J. Resnick, "Template replication for full wafer imprint lithography," *Microelectronic Engineering,* vol. 84, pp. 885-890, 2007.

[102] M. D. Stewart, S. C. Johnson, S. V. Sreenivasan, D. J. Resnick, and C. G. Willson, "Nanofabrication with Step and Flash Imprint Lithography," *Journal of Microlithography Microfabrication and Microsystems,* vol. 4, 2005.

[103] S. V. Sreenivasan, C. G. Willson, N. E. Schumaker, and D. J. Resnick, "Low-cost nanostructure patterning using Step and Flash Imprint Lithography," *Nanostructure Science, Metrology and Technology,* pp. 187-194, 2002.

[104] D. Lentz, G. Doyle, M. Miller, G. Schmid, M. Ganapathisuramanian, X. M. Lu, D. Resnick, and D. L. LaBrake, "Whole wafer imprint patterning using Step and Flash

Imprint Lithography: A manufacturing solution for sub 100 nm patterning," *Emerging Lithographic Technologies XI, Pts 1 and 2,* vol. 6517, pp. F5172-F5172, 2007.

[105] M. J. Chopra and R. T. Bonnecaze, "Impact of polymer curing on two-dimensional and three-dimensional shape change in nanoimprint lithography," *Journal of Micro-Nanolithography Mems and Moems,* vol. 14, 2015.

[106] M. Colburn, A. Grot, M. Amistoso, B. J. Choi, T. Bailey, J. Ekerdt, S. V. Sreenivasan, J. Hollenhorst, and C. G. Willson, "Step and Flash Imprint Lithography for sub-100-nm patterning," *Proc. SPIE 3997, Emerging Lithographic Technologies IV,* vol. 453, 2000.

[107] S. Murthy, M. Falcon, S. V. Sreenivasan, and D. Dance, "S-FIL (TM) technology: Cost of ownership case study," *Emerging Lithographic Technologies IX, Pts 1 and 2,* vol. 5751, pp. 964-975, 2005.

[108] S. V. Sreenivasan, C. G. Willson, N. E. Schumaker, and D. J. Resnick, "Cost of ownership analysis for patterning using Step and Flash Imprint Lithography," *Emerging Lithographic Technologies Vi, Pts 1 and 2,* vol. 4688, pp. 903-909, 2002.

[109] D. J. Resnick, W. J. Dauksher, D. Mancini, K. J. Nordquist, E. Ainley, K. Gehoski, J. H. Baker, T. C. Bailey, B. J. Choi, S. Johnson, S. V. Sreenivasan, J. G. Ekerdt, and C. G. Willson, "High resolution templates for Step and Flash Imprint Lithography," *Emerging Lithographic Technologies Vi, Pts 1 and 2,* vol. 4688, pp. 205-213, 2002.

[110] K. Usuki, S. Wakamatsu, T. Oomatsu, K. Kodama, and K. Kodama, "Approaches to rapid resist spreading on dispensing based UV-NIL," *Alternative Lithographic Technologies Iii,* vol. 7970, 2011.

[111] E. B. Fletcher, G. M. Schmid, S. Im, N. Khusnatdinov, Y. Srinivasan, W. Liu, and F. Y. Xu, "Drop pattern generation for imprint lithography with directionally-patterned templates," *US20150017329 A1,* 2015.

[112] A. Jain and R. T. Bonnecaze, "Fluid management in roll-to-roll nanoimprint lithography," *Journal of Applied Physics,* vol. 113, 2013.

[113] D. Morihara, Y. Nagaoka, H. Hiroshima, and Y. Hirai, "Numerical study on bubble trapping in UV nanoimprint lithography," *Journal of Vacuum Science & Technology B,* vol. 27, pp. 2866-2868, 2009.

[114] Y. Nagaoka, D. Morihara, H. Hiroshima, and Y. Hirai, "Simulation study on bubble trapping in UV nanoimprint lithography," *Journal of Photopolymer Science and Technology,* vol. 22, pp. 171-174, 2009.

[115] K. J. Nordquist, D. P. Mancini, W. J. Dauksher, E. S. Ainley, K. A. Gehoski, D. J. Resnick, Z. S. Masnyj, and P. J. Mangat, "Critical dimension and image placement issues for Step and Flash Imprint Lithography templates," *22nd Annual Bacus Symposium on Photomask Technology, Pts 1 and 2,* vol. 4889, pp. 1143-1149, 2002.

[116] Y. Hori, "Hydrodynamic lubrication," *Tokyo: Springer,* 2006.

[117] H. G. Rylander, "A theory of liquid-solid hydrodynamic film lubrication," *ASLE Transactions,* vol. 9, pp. 264-271, 1966.

[118] C. W. Hirt and B. D. Nichols, "Volume of fluid (VOF) method for the dynamics of free boundaries," *Journal of Computational Physics,* vol. 39, pp. 201-225, 1981.

[119] J. E. Pilliod and E. G. Puckett, "Second-order accurate volume-of-fluid algorithms for tracking material interfaces," *Journal of Computational Physics,* vol. 199, pp. 465-502, 2004.

[120] M. M., A. W., and B. A., "Simplified volume of fluid method (SVOF) for two-phase flows," *XVIII Polish National Conference of Fluid Mechanics,* vol. 12, 2008.

[121] E. G. Puckett, "A volume-of-fluid interface reconstruction algorithm that is second-order accurate in the max norm," *Communications in Applied Mathematics and Computational Science,* vol. 5, pp. 199-220, 2010.

[122] D. L. Youngs, "Time-dependent multi-material flow with large fluid distortion," *Numerical Methods for Fluid Dynamics* vol. 24, pp. 273–285, 1982.

[123] Y. Saad and M. H. Schultz, "GMRES: A generalized minimal residual algorithm for solving nonsymmetric linear systems," *Siam Journal on Scientific and Statistical Computing,* vol. 7, pp. 856-869, 1986.

[124] R. Mittal, H. Dong, M. Bozkurttas, F. M. Najjar, A. Vargas, and A. von Loebbecke, "A versatile sharp interface immersed boundary method for incompressible flows with complex boundaries," *Journal of Computational Physics,* vol. 227, pp. 4825-4852, 2008.

[125] P. S. Epstein and M. S. Plesset, "On the stability of gas bubbles in liquid-gas solutions," *Journal of Chemical Physics,* vol. 18, pp. 1505-1509, 1950.

[126] J. M. R. Marin, H. K. Rasmussen, and O. Hassager, "3D Simulation of Nano-Imprint Lithography," *Nanoscale Research Letters,* vol. 5, pp. 274-278, 2010.

[127] H. J. Lee, S. H. Lan, J. H. Song, M. G. Lee, J. Ni, and N. K. Lee, "Continuous roll-to-flat thermal imprinting process for large-area micro-pattern replication on polymer substrate," *Microelectronic Engineering,* vol. 87, pp. 2596-2601, 2010.

[128] P. H. Huang and S. Y. Yang, "Complete reversal imprinting for fabricating microlens arrays with faithful shape replication," *Journal of Vacuum Science & Technology B,* vol. 27, pp. 2781-2785, 2009.

[129] J. G. Ok, H. J. Park, M. K. Kwak, C. A. Pina-Hernandez, S. H. Ahn, and L. J. Guo, "Continuous patterning of nanogratings by nanochannel-guided lithography on liquid resists," *Advanced Materials,* vol. 23, p. 4444, 2011.

[130] M. K. Kwak, J. G. Ok, J. Y. Lee, and L. J. Guo, "Continuous phase-shift lithography with a roll-type mask and application to transparent conductor fabrication," *Nanotechnology,* vol. 23, 2012.

[131] X. M. Li, Y. C. Ding, J. Y. Shao, H. Z. Liu, and H. M. Tian, "Fabrication of concave microlens arrays using controllable dielectrophoretic force in template holes," *Optics Letters,* vol. 36, pp. 4083-4085, 2011.

[132] X. M. Li, H. M. Tian, J. Y. Shao, Y. C. Ding, and H. Z. Liu, "Electrically modulated microtransfer molding for fabrication of micropillar arrays with spatially varying heights," *Langmuir,* vol. 29, pp. 1351-1355, 2013.

[133] X. D. Wang, L. J. Ge, J. J. Lu, X. J. Li, K. Q. Qiu, Y. C. Tian, S. J. Fu, and Z. Cui, "Fabrication of enclosed nanofluidic channels by UV cured imprinting and optimized thermal bonding of SU-8 photoresist," *Microelectronic Engineering,* vol. 86, pp. 1347-1349, 2009.

[134] S. Singhal, M. J. Meissl, R. T. Bonnecaze, and S. V. Sreenivasan, "Inkjet-based deposition of polymer thin films enabled by a lubrication model incorporating nano-scale parasitics," *Physics of Fluids,* vol. 25, 2013.

[135] S. Singhal, R. Attota, and S. V. Sreenivasan, "Residual layer thickness control and metrology in Jet and Flash Imprint Lithography," *Metrology, Inspection, and Process Control for Microlithography Xxvi, Pts 1 and 2,* vol. 8324, 2012.

[136] M. M. K., "Investigation of a roll-to-roll nanoimprinting process utilizing inkjet based resist deposition " *Master's thesis,* 2011.